4-9-2020 10:00 AM

Characterization of Impactite Clay Minerals with Implications for Mars Geologic Context and Mars Sample Return

Christy M. Caudill
The University of Western Ontario

Supervisor
Dr. Gordon Osinski
The University of Western Ontario Co-Supervisor
Dr. Livio Tornabene
The University of Western Ontario

Graduate Program in Geology
A thesis submitted in partial fulfillment of the requirements for the degree in Doctor of Philosophy

Abstract

Geological processes, including impact cratering, are fundamental throughout rocky bodies in the solar system. Studies of terrestrial impact structures, like the Ries impact structure, Germany, have informed on impact cratering processes – e.g., early hot, hydrous degassing, autometamorphism, and recrystallization/devitrification of impact glass – and products – e.g., impact melt rocks and breccias comprised of clay minerals. Yet, clay minerals of authigenic impact origin remain understudied and their formation processes poorly-understood. This thesis details the characterization of impact-generated clay minerals at Ries, showing that compositionally diverse, abundant Al/Fe/Mg smectite clays formed through these processes in thin melt-bearing breccia deposits of the ejecta, as well as at depth. The inherent complexity of smectites – their formation, type, structure, and composition – makes their provenance difficult to discern; these factors may explain why impact-generated and altered materials, which comprise an appreciable volume and extent of Mars' ancient Noachian crust, are not generally recognized as a source of the enigmatic clays that are ubiquitous in those regions. Clay minerals can provide a defining window into a planet's geologic and climatic past as an indicator of water availability and geochemistry; the presence of clay minerals on Mars has been used to support the hypothesis of climatically "warm, wet" ancient conditions. Yet, climate modeling of Early Mars suggests that the likely nature of the climate was not conducive to long-term aqueous activity. We suggest that the omission of impact-generated materials in current models of Mars clay mineral formation leaves a fundamental gap in our understanding of Noachian crustal materials – materials that were continually recycled and completely transformed on a global scale over millennia on Mars. The opportunity to investigate clay-bearing impactites and strata-bound clay minerals will be presented to the upcoming NASA Mars 2020 and ESA ExoMars

rovers; this thesis offers caution in assigning clay mineral provenance until samples are returned to Earth from these missions. We furthermore suggest a methodological approach to augment current rover-based exploration frameworks to characterize potential impact-origin. Discerning clay species and provenance – and acknowledging the implications of that provenance – is central to understanding the geologic context of Mars, and thus its past climatic conditions and habitability potential.

Keywords
Mars, Earth analogues, impact cratering products, clay minerals, clay-bearing impactites

Lay Summary

Impact cratering is a fundamental geologic process throughout the solar system, one that serves as an external force to cycle and recycle crustal materials and produce new materials known as impactites. Impactites from terrestrial impact structures are known to comprise smectites (swelling, hydrated clay minerals). The heavily cratered, ancient Noachian region of Mars holds a diversity of alteration minerals, including widespread smectites. The presence of smectites on Mars is generally considered to indicate Earth-like paleoclimate conditions that supported long-term atmospheric stability and surface-stable liquid water. However, climate modeling of Early Mars suggests that the likely nature of the climate was not conducive to long-term aqueous activity. The work of this thesis may address the disconnect between the widespread clay minerals observed on Mars and the predictions of a "cold, dry" climate through the study of clay-bearing impactites. Impact processes can produce clay minerals even in the absence of an active hydrosphere and under very cold conditions; however, the production of clay minerals in impact craters is poorly-understood. Impact-generated clay minerals are not typically represented in current models of Mars clay mineral formation, and we suggest that this leaves a fundamental gap in our understanding of Noachian crustal materials that were continually recycled and completely transformed on a global scale over millennia. This thesis begins with extensive mapping of impactite deposits of Bakhuysen Crater, Mars. Next, two in-depth laboratory studies of clay-bearing impactites at the Ries impact structure provide a reference for impact-related clay minerals when investigating the provenance of materials on Mars. A main goal of this thesis is to incite new ways of thinking about the variety of complex processes – including impact cratering – that produced materials observed on the surface of Mars. Intellectual and exploration frameworks – i.e., science questions and resultant Mars

exploration strategies – were investigated through a simulated Mars rover mission: CanMars. The difficulties in properly characterizing geologic context and the inherent difficulty in identifying and adequately characterizing smectite clay minerals (relevant for upcoming Mars rover missions) calls for a methodological approach. This thesis augments current exploration frameworks with the broader goal of expanding current knowledge on the larger geologic context of Mars.

Land Acknowledgement

I acknowledge that Western University is located on the traditional lands of the Anishinaabek, Haudenosaunee, Lūnaapéewak, and Attawandaron peoples, on lands connected with the London Township and Sombra Treaties of 1796 and the Dish with One Spoon Covenant Wampum. With this, I respect the longstanding relationships that Indigenous Nations have to this land, as they are the original caretakers.

This land connected me to a fundamental truth, which is why this land acknowledgement is so important to me. It is about acknowledging the caretakers of this land – the life and spirit of this land, not simply its resources – and the historical and ongoing injustices that Indigenous Peoples (e.g. First Nations, Métis and Inuit) endure in Canada. But this land acknowledgement is also about the other – the non-humans, who are disadvantaged by the distinct dearth of a grammar of animacy in western culture that unwittingly conveys on us that only "humans" count as "persons", as described by Robin Kimmerer in *Braiding Sweetgrass*. We have inherited the most unfortunate of worldviews: that our perspective is the only perspective, that there are no other intelligences beside our own, other ways of being and knowing. We are blind to the wisdom around us. It is this truth – the truth that modern science works in a deeply-rooted reductionist framework, largely and disconcertingly invalidating other knowledge systems – that the land has awakened me to. Particularly, the tree people of the Anishinaabek land.

This journey comes come full circle for the little girl who connected so deeply with nature, with animals and every creature – though this truth of being was actively suppressed as a result of

cultural misinformation. Hurt people hurt people; deeply wounded societies do the same to their people. Yet, my experiences on this land healed me. This land connected me back to my truth. For that, I will be forever grateful for the people and the other beings here.

Thank you, Canadians, for living up to your reputation of warmth, inclusivity, openness, and kindness. Living here has shown me the great Canadian heart.

Co-Authorship Statement

Chapter 2: Data was collected and processed by Christy Caudill. Manuscript was written by Christy Caudill. Comments and editing were provided by Gordon Osinski and Livio Tornabene. The concept for this study came from observations and conversations with Livio Tornabene regarding Bakhuysen Crater deposits and impact melt-bearing deposits on Mars. A version of the work in this chapter is published in *Icarus*.

Caudill, C.M., G.R. Osinski, L.L. Tornabene (2018) Geological Mapping and Interpretation of Bakhuysen Crater, Mars, Icarus 314, 175-194.

Chapter 3: Data was collected and processed by Christy Caudill; spectral data was collected and processed with assistance from Rebecca Greenberger, and field assistance was provided by Haley Sapers, Lu Pan, Matthew Svennson, and Jen Ronholm. Rebecca Greenberger provided the spectral image for Figure 3.5. Bethany Ehlmann and Rebecca Greenberger graciously allowed use of their spectral processing lab and offered many valuable conversations regarding the spectral data, interpretations, and its implications. Roberta Flemming assisted with μXRD data manipulation and preparation. Marcel Kim assisted with laboratory sample preparation. Kim Law facilitated XRD laboratory space and instrumentation maintenance, and brought her lovely and strong presence to the lab. Manuscript was written by Christy Caudill. Comments and editing were provided by Gordon Osinski, Fred Longstaffe, Livio Tornabene, Rebecca Greenberger, and Bethany Ehlmann. Many helpful conversations with and guidance from Fred Longstaffe proved invaluable. A version of the work in this chapter has been submitted to *Meteoritics & Planetary Science.*

Chapter 4: Data was collected and processed by Christy Caudill. Marcel Kim assisted with laboratory sample preparation. Manuscript was written by Christy Caudill. Comments and editing were provided by Gordon Osinski, Fred Longstaffe, and Livio Tornabene.

Chapter 5: The concept for this paper grew from the CanMars field trials and post-mission meetings and analysis. Manuscript was written by Christy Caudill. Valuable input and ideas came from conversations with Anna Grau Galofre, Anna Mittelhoz, Tianqi Xie, Timothy Haltigin, Raymond Francis, and Gordon Osinski. Figure 5.1 was provided by Haley Sapers. Comments and editing were provided by Gordon Osinski, Raymond Francis, Livio Tornabene, Matthew Svensson, Eric Pilles, Timothy Haltigin, Victoria Hipkin, Dave Beaty, and Ken Williford. A version of the work in this chapter is published in *Planetary and Space Science.*

Caudill, C.M., Pontefract, A., Osinski, G. R., Tornabene, L. L., Xie, T., Mittelholz, A., Poitras, J., Simpson, S., Svensson, M., Grau, A. G., Godin, E., Pilles, E., Francis, R., Williford, K., Tuite, M., Battler, M., Hipkin, V., Haltigin, T., and the 2015 & 2016 Science Team members (2019) CanMars mission Science Team operational results: Implications for operations and the sample selection process for Mars Sample Return (MSR), Planetary and Space Science, 172, 43-56.

Acknowledgments

What an astounding life adventure has continued through this journey of pursuing a doctoral thesis. First and foremost, I would like to thank my thesis advisor, Dr. Gordon Osinski ("Oz") for providing me incredible and numerous opportunities and dedicated mentorship and guidance. I greatly respect and value the compassion, empathy, patience, and professionalism that you bring to a mentorship. We have always been on the same wavelength in terms of adventure and exploration; perhaps this was the reason you had such capacity to always allow me to be exactly who I was: a free spirit and a bit wild. It is not possible to overstate how meaningful that has been for me. I hold you as a dear friend and hope that more adventures await! I would also like to thank your family for holding space for me; I felt as though I would never be without a supportive place if ever I needed it.

To Dr. Livio Tornabene: thank you for being my advisor and connection to Western, and likely the force that brought me here. Your intellectual curiosity and unbridled enthusiasm is contagious – and it has been an inspiration for me from my first dabbling in Planetary Science. We go way back; you graciously offered many hours teaching me JMARS and planetary mapping techniques when I first started at the Lunar and Planetary Laboratory in 2009. You were really the first person to see potential in me that I didn't even believe was there. I am grateful that you've been in my path.

Of course, my family has always seen that potential and encouraged me every single step of the way. Through every battle that I have chosen to fight in the most unconventional of ways, you've

never criticized, doubted, or brought even a hint of negativity. I thank you and credit you – Mom, and my sisters Lisa and Jessica – for being my solid foundation. Thank you for being the incredible women that you are. Thank you for showing us the way, Mom. I hope that I am able to give justice to all your sacrifices and to our similar life dreams.

I also wish to thank Dr. Fred Longstaffe for his incredible, unique, and lovely presence. My work is exponentially better for your efforts and support. Many thanks to Dr. Alfred McEwen, who gave me the opportunity to start – and hugely grow – in Mars science; I have greatly appreciated that opportunity and the warm chats and encouragement as our paths have crossed over the years. Thank you to Raymond Francis for the incredible support, encouragement, and opportunities you provided, and mostly, your kind, open heart. Thanks to Bethany Ehlmann and Rebecca Greenberger for the chats, advice, and support.

To other incredible and cherished people that I met along the way, you have deeply enriched my life: Cassandra Marion, Jordan Hawkswell, Sarah Simpson, Haley Sapers, Matt Svensson, Alexandra Pontefract, and Tianqi Xie. I wish to thank Timothy Haltigin and Robbie Flemming for their support and friendship. James Wilkes and Kelly King: nothing but gratitude. The Sagers have been nothing short of family. Tanya Harrison – you inspire me with the incredible strength that is quiet, and lay unseen, even though the camera is often on you. Racel Sopoco: my soul sister – much love, and may we stay connected.

Lastly, a thank you to Mike Reaume: you changed my life forever by simply being your truth. Thank you for being my hero. I am free.

To the land of the Anishinaabek, to the trees; to the Utah sandstone; to the Lanzarote breeze …

Table of Contents

List of Tables

List of Figures

Chapter 1:

Chapter 2:

Chapter 3:

Chapter 4:

Chapter 5:

Chapter 6:

List of Appendices

List of Abbreviations and Symbols

ASU	Arizona State University
BB	Bunte Breccia
CTX	Context Camera
C/S	Chlorite/Smectite
DP	Degassing Pipe
d-spacing	distance-spacing – *XRD-derived distance between two adjacent mineral planes or layers yielding a value indicative of a mineral species*
EG	Ethylene Glycol-solvation
ESA	European Space Agency
HiRISE	High Resolution Imaging Science Experiment
HRSC	High Resolution Stereo Camera
I/S	Illite/Smectite
JPL	Jet Propulsion Laboratory
K/S	Kaolinite/Smectite
LROC WAC	Lunar Reconnaissance Orbiter Wide Angle Camera
LROC NAC	Lunar Reconnaissance Orbiter Narrow Angle Camera
MBB	Melt-Bearing Breccia
MEPAG	Mars Exploration Program Analysis Group
MOLA	Mars Orbiter Laser Altimeter
MRO	Mars Reconnaissance Orbiter
NASA	National Aeronautics and Space Administration
nm	nanometer

OMEGA	Observatoire pour la Mineralogie, l'Eau, les Glaces et l'Activite´
pXRD	powder X-ray Diffraction
R	Reichwete ordering
SWIR	Short-Wave Infrared
TES	Thermal Emission Spectrometer
THEMIS VIS	Thermal Emission Imaging Spectrometer (Visible subsystem)
THEMIS nTIR	Thermal Emission Imaging Spectrometer (nighttime imaging Thermal Infrared subsystem)
THEMIS dTIR	Thermal Emission Imaging Spectrometer (daytime imaging Thermal Infrared subsystem)
TI	Thermal Inertia
UA	University of Arizona
USGS	United States Geological Survey
VNIR	Visible and Near-Infrared
XRD	X-ray Diffraction
μm	micron
μXRD	micro-X-ray Diffraction
θ	theta – *angle of both the incoming beam and the beam diffracted from a mineral plane, or the constructive X-rays producing XRD patterns*

Chapter 1: Introduction and Background

1.1 Introduction

"Science is only one way of knowing, and its purpose is not to generate absolute truths but rather to inspire better and better ways of thinking about phenomena."
Wade Davis, *The Wayfinders*

A main goal of this work is to incite new ways of thinking about deciphering the materials on the surface of Mars and, thus, broadening our mind's potential for an accurate view of the past conditions of that planet. Building an ever more accurate record of past conditions and geologic processes is an avenue of study that provides insight into the potential for habitable environments in their own unique temporal and spatial context, throughout the solar system and beyond. Within this context, the narrow lens of this work focuses on specific materials that are common among all known terrestrial planets – impactites. Impactites are materials that have been created or modified by asteroidal or cometary impact into a rocky body. Impact cratering is the most ubiquitous geologic process in the solar system, one that serves as an external force to cycle and recycle crustal materials, such as the volatiles, accumulated over millennia. In addition to recycling materials, impact events also act to locally concentrate and differentiate crustal materials; the shock-induced heat and accommodated pore-space of crustal fracturing leads to the formation of hydrothermal systems in the presence of subsurface groundwater hydrosphere (Naumov, 2005; Osinski et al., 2013). It has been suggested that, on Earth, the hydrothermal environment offered the precise thermal and chemical dynamics – minerals as chemical precursors – to act as the "cradle of life" (Weiss et al., 2016); thermophilic archaea are thought to be the oldest organisms in the tree of life (Weiss et al., 2016), and in this hypothesis, those organisms may have come into being during the time of a potential peak of impact bombardment in our early solar system (~ 3.8 – 4.0 Gyr; Kring and Cohen, 2002). Hydrothermal environments

produce supergene (near-surface) and hypogene (subsurface) deposits of secondary clay mineral species, though unraveling the formation conditions of clay minerals is a complex undertaking. Not only are these materials formed in diagenetic-hydrothermal environments ("neoformation", or as precipitated from solution), but are also detrital minerals (present due to sedimentation, or environmental inheritance) and formed via weathering (retaining inherited structure while undergoing internal chemical substitution). Regardless of the particular formation process, clay minerals are the mineral markers of water-rock interaction over long spans of time. Thus, on Mars, the provenance of clay minerals is the subject of intensive study; their presence on the surface of Mars has been used as one line of evidence of an ancient climate supportive of surficial aqueous weathering, i.e., climatically "warm and wet Mars", much like that of Earth. However, this work and of others shows that the complexities of how, and magnitude of environment types where, clay minerals form forces a more expansive view on their geologic meaning and climatic context. Clay minerals are found in many different environments, and on Earth and Mars. On Earth, impactites are known to comprise clay minerals produced through various geologic processes, including: impact-induced hydrothermal activity, both local and metasomatic; devitrification (recrystallization) of glass (impact-produced melt) and subsequent alteration; and, autometamorphism (internal mineral alteration via constituent volatiles during the post-impact cooling phase) (Naumov, 2005; Osinski, 2005; Osinski et al., 2013). These impact-related processes are a focus for this work, as they have implications for clay mineral provenance on Mars – particularly considering that Martian clay minerals are observed in association with the heavily cratered, most ancient terrains.

This brings us to the fundamental importance of investigating planetary analogues on Earth to understand of the composition of these crustal materials and their importance as

indicators of climatic conditions in the past that were conducive to habitability. The first of two Mars analogue sites investigated in this thesis is the Ries impact structure, Germany. Arguably the best-preserved and exposed ejecta deposits on Earth are present at Ries; the clay-rich impactites are type-localities at Ries. The second Mars analogue site is the clay-rich sedimentary deposits of inverted paleochannels near Green River, Utah, US. This was the site of the CanMars simulated analogue mission, designed to assess the efficacy of discerning geologic context through remote rover-based operations. This thesis presents the results of the CanMars field trials, including: the CanMars operational construct, with tests and strategies for optimal Science Team operations and lessons-learned; the sol-by-sol operations and the effects of those on the participating team and the science return; the approaches employed to investigate the geologic context and choose and prioritize samples for cache and return; the efficacy of the instrument suite to assess geologic context and to identify and characterize samples, highlighting gaps in data needs; a summary of the in-simulation science return; and a summary of the post-mission site geologic validation.

This chapter will first discuss Mars' climate and geologic history, and proposed provenance of clay minerals, then describes how field geology on Earth provides insights and direction for research and experimentation – both theoretical and *in situ*. More specifically, and in summary, this work investigates: 1) presence of impactites on Mars through orbitally-derived remote-sensing instruments with comparisons to analogous materials on Earth and other planetary bodies; 2) comparison of impact-generated clay minerals to pre-impact clay minerals in the target stratigraphy at the Ries impact structure through novel, high-resolution mineralogic field and laboratory investigations; 3) Mars analogue mission simulations as a means to bridge the gap

between remote-science and laboratory validation of geologic assessments, prompting a better articulation of the science questions during Mars *in situ*, rover-based science.

1.2 Mars climatic and geologic history: the backstory of Noachian clay minerals

Three eras have been assigned to major geological time periods on Mars: Noachian (4.1 – 3.7 Ga), Hesperian (3.7 – 2.9 Ga), and Amazonian (2.9 Ga – present) (Hartmann and Neukum, 2001). Little is known about the Pre-Noachian period (4.5 – 4.1 Ga), beginning after the formation of the planetary body through accretion and the process of differentiation that lasted an estimated few tens of millions of years. Evidence of a remnant magnetic field indicates that an early Mars may have had an internal dynamo like on Earth: the convection system from the core which drove planetary dynamics like volcanism and created a magnetic field that potentially allowed for a sustained atmosphere (Dehant et al., 2007). Following accretion and proto-planet formation, impact events continued to modify the near-surface of the rocky and icy bodies of the solar system, provide water and other volatiles – elements and chemical compounds with a relative low boiling point/high vapor pressure, like water and carbon dioxide – and influence dynamical evolution. The impact flux is estimated to have been two orders of magnitude higher >3.5 Ga than in the time since (Hartmann, 1965; Fassett and Minton, 2013); a "Late Heavy Bombardment" may have occurred ~4.1 Ga, marked in Martian geologic history by the Hellas basin-forming impact (Frey, 2003). Impact cratering is a geological process present from the time of planetary formation, thus, relative age-dating on the surface of Mars and other rocky bodies is constrained by counting the number of impact craters retained on a given surface: oldest surfaces retain a high number of superimposed craters over time; younger geologic processes serve to modify (e.g., ice growth and subsequent sublimation or melting) or

"resurface" (e.g., volcanic lava flows) an area. Impact events have had a profound effect on the evolution of planets: geologic, climatic, and biological. The large basin-forming impacts of the Pre-Noachian to the Noachian Era (e.g., Isidis, 1352 km-diameter, Caprarelli and Orosei, 2015; Hellas, 2300 km, Leonard and Tanaka, 2001; Utopia, 3300 km, McGill, 1989; Fig. 1.1) served to recycle crustal materials, ballistically distributing material as ejecta (*Impact cratering* in following sections) around the planet. These impact events also influenced and sustained groundwater availability and circulation through massive brecciation of the crust and heat delivered through hydrothermal activity, elevated geothermal gradients, and shock metamorphism (Carr and Head, 2010; Kieffer and Simonds, 1980; Pierazzo, 2005).

The best evidence for stable liquid water on the surface of Mars is present in the morphology and mineralogy of the Noachian terrain, though evidence for a long-term "warm, wet" past climate remains elusive. Known by the regional name Noachis Terra (Fig. 1.1), this terrain dominates the southern highlands. Though marred by impact cratering and thus preserving the oldest crust on Mars, Noachian terrain is also characterized by high rates of erosion that formed vast valley networks and endowed all Noachian-aged surfaces with widespread weathering products (i.e., phyllosilicates, like smectite clay). The formation mechanism of the valley networks is of debate; the following mechanisms have been suggested: long-lived river systems supported by surficial run-off of precipitation (Craddock and Howard, 2002); groundwater seepage (Baker et al., 1990; Marra et al., 2014); sub-glacial channels (Wordsworth et al., 2015; Cassanelli and Head, 2019); and intermittent events like catastrophic flooding (Stepinski and Coradetti, 2004). Brief, ephemeral valley formation mechanisms may support punctuated events of climatic warming and atmospheric stability (Wordsworth et al., 2017). Large impact events could have forced such climatic cycling, injecting significant

atmospheric volatiles into the atmosphere and warmed the surface by several hundred K (Segura et al., 2002). However, the largest basin-forming impact events likely to appreciably effect global climate pre-date the valley networks (Fassett and Head, 2008a). Yet, basin-filling lakes are thought to have been common during the Noachian (Fassett and Head, 2008b), and likely extended into the Early Hesperian. Gale Crater, under investigation by NASA's Mars Science Laboratory (MSL) rover, provided a catch-basin for sedimentary materials, some deposited by deltas, streams, and lakes (though most were deposited by wind erosion). MSL data and remote observations suggest that although the fluvial events were likely transient, a lacustrine system could have persisted in the crater basin for a period of up to 10,000 years (Grotzinger et al., 2015). Analysis of the mudstones investigated in Gale Crater lacustrine deposits show they are comprised of the iron-rich smectite clay mineral Fe-saponite, and that episodic fluctuations in lake levels – closely linked with short-term atmospheric cycling – produced Al-rich, Fe^{3+}-bearing dioctahedral smectite (Fedo et al., 2017; Gwizd et al., 2018; Stein et al., 2017). The saponite clay mineral species was determined to be likely neoformation, syn-depositional, remnants of early-stage chemical alteration of basaltic parent rock transported from the rim of Gale Crater, or potentially formed *in situ* due to high Mg^{2+} activity in the lake water that concentrated due to evaporation during periods of atmospheric perturbations (Bristow et al., 2018). The Al-rich smectite is proposed to have formed from aqueous alteration near the time of deposition, driven by oxidation and elemental concentration and mobilization from evaporative periods (Bristow et al., 2018). These findings suggest that the clay minerals were formed at or near the paleosurface, and not a product of burial diagenesis, thus providing a powerful mineralogic indicator of paleoclimate.

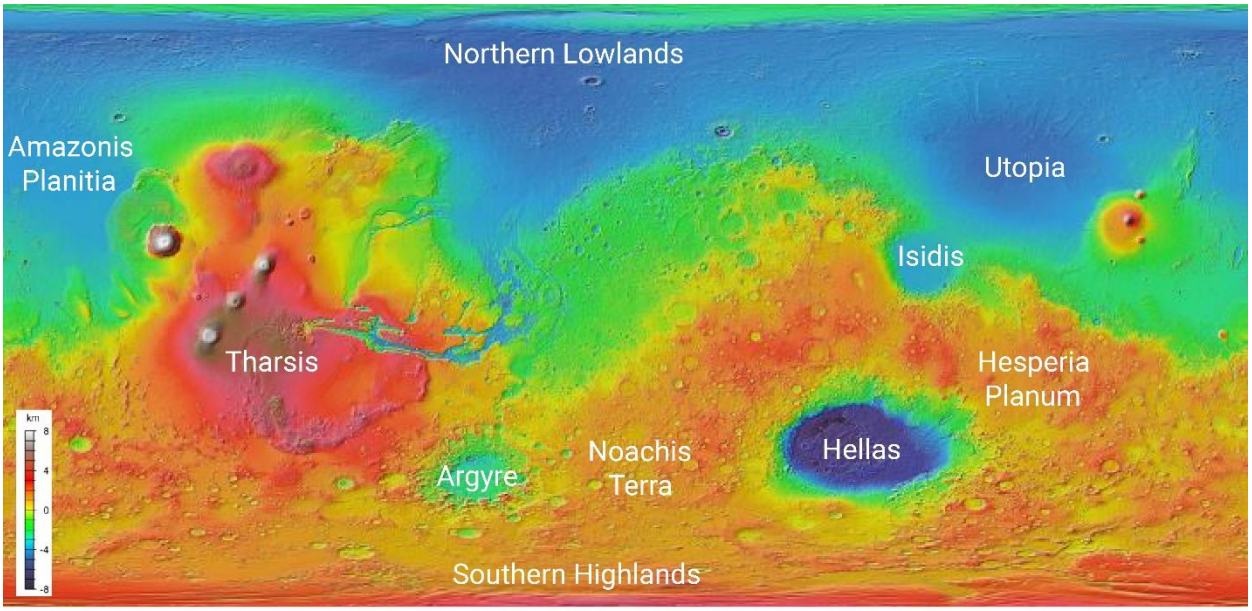

Figure 1.1. Map of Mars with major regions labeled, including the Noachian and the larger southern highlands terrain. The base map is a Mars Orbiter Laser Altimeter (MOLA) topographic map, colorized by elevation; image credits: NASA/Caltech-JPL/GSFC.

1.2.2 Clay minerals and their provenance in the ancient Noachian terrains

Clay minerals (along with other, amorphous hydrated silicates, e.g., silica impact glasses) (Table 1.1) are observed as widespread mineral phases on Mars, not simply as associated with fluvial features or in lacustrine basins, but concentrated in the heavily cratered Noachian highlands. Ehlmann and Edwards (2014) divided the occurrences of clay minerals on Mars into three types: in-place stratigraphy of clay-bearing units perhaps formed by *in situ* alteration; central to impact craters, in crater interiors and the ejecta; and clay-bearing sedimentary basin units. Clay minerals have an incredible range of formation environments and conditions (Wimpenny, 2018), and discerning clay mineral provenance even with the best of terrestrial laboratory analyses may not definitively describe formation processes or conditions (Tardy et al., 1987). Thus, the clay mineral weathering products of the Noachian are worthy of the significant

research that has thus far been compiled to elucidate on their origins (e.g., Ehlmann and Edwards, 2014; Bibring et al., 2006; Mustard et al., 2008; Ehlmann et al., 2009; Poulet et al., 2005). Hazen et al. (2013) shows that clay mineral formation throughout the solar system reflects the body's tectonic, geochemical, and biological processes, and that they present the opportunity on Mars to reveal the evolution of these processes.

Table 1.1. Clay minerals and other hydrated silicates detected on Mars from landed and orbital data sets, modified after (Ehlmann and Edwards, 2014 and references therin, except as indicated).

Mineral class	Mineral phase	Chemical formula
Phyllosilicates (clay minerals)	Fe/Mg smectites ~1.0 nm ferrian saponite [a] ~1.32 nm ferrian saponite (interpreted as interlayered with metal-hydroxyl groups) [a]	$(Ca, Na)_{0.3–0.5}(Fe, Mg, Al)_{2–3}(Al, Si)_4O_{10}(OH)_2 \cdot nH_2O$
	Al smectites (e.g., montmorillonite, beidellite) Al-rich, ferrous dioctahedral smectite [b]	$(Na, Ca)_{0.3–0.5}(Al, Mg)_2(Al, Si)_4O_{10}(OH)_2 \cdot nH_2O$
	Kaolin group minerals (e.g., kaolinite, halloysite)	$Al_2Si_2O_5(OH)_4$
	Chlorite	$(Mg, Fe^{2+})_5Al(Si_3Al)O_{10}(OH)_8$
	Serpentine	$(Mg, Fe)_3Si_2O_5(OH)_4$
	Al/K phyllosilicates (e.g., muscovite, illite)	$(K,H_3O)(Al,Mg,Fe)_2\ Al_xSi_{4–x}O_{10}(OH)_2$
Other hydrated silicates	Prehnite	$Ca_2Al(AlSi_3O_{10})(OH)_2$
	Analcime	$NaAlSi_2O_6 \cdot H_2O$
	Opaline silica	$SiO_2 \cdot nH_2O$

[a] See Bristow et al. (2015)
[b] See Bristow et al. (2018)

A brief introduction of the structure of clay minerals is also warranted here; smectites are a focus of this work as, regardless of the particular formation process, they are mineral markers of water-rock interaction over long spans of time. Clay minerals are minerals in the phyllosilicates group that are comprised of interconnected rings – or tetrahedra – of bonded silica and oxygen structures (SiO_4^{4-}; see Table 1.1) that give rise to (theoretically, potentially infinitely) long sheets of the basic structural unit of $Si_2O_5^{-2}$. Most phyllosilicates contain a hydroxyl ion (OH^-) located at the center of the silica rings with other bonded cations (e.g., Fe^{+2}, Mg^{+2}, Al^{+3}) resulting in an octahedral configuration. Smectite clay minerals have a high capacity to exchange cations and thus generally exist in a continuum composition rather than a distinct mineral phase. Adding further complexity to their potential compositions, smectites experience a structural change in the presence of water: H_2O molecules are absorbed between the tetrahedral and octahedral sheets, bound to the exchangeable cations or the clay mineral sheets, causing expansion or "swelling" (Brown and Brindley, 1980). A common, yet poorly-understood and under-characterized component of smectite is hydroxyl materials present as interlayers within the structure of the swelling smectite (Bamhisel, 1977); these materials are a product of weathering of metal oxides and clay minerals. The nature of hydroxy-interlayered materials remains challenging to identify, as do the conditions that are favorable for their formation (Georgiadis et al., 2019). Hydroxy-interlayered material is identified as a smectite component and characterized in this thesis through the use of a high-resolution treatment series, typically restricted to laboratory settings. Note that in Table 1.1, hydroxy-interlayered materials have been identified *in situ* on Mars though fantastically innovative rover instrumentation and data acquisition techniques (e.g., treatments to heat the materials). A trioctahedral ferrian smectite (saponite) with partial metal-hydroxy intercalation is the preferred interpretation of clay minerals observed by

the Mars Science Laboratory (MSL) CheMin and Sample Analysis at Mars (SAM) instruments via X-ray diffraction (XRD), derived from a pedogenic or lacustrine source (Bristow et al., 2015). However, more complex hydration and saturation treatments and cation manipulation that characterize the interlayered material – allowing an assessment of the detailed composition of the material and its origins – are currently only possible only in terrestrial laboratory settings. Interlayered materials and thus the complex nature of smectitic clay minerals often is unrecognized due to the difficulty in observation, characterization, and/or quantification of interlayer oligomers – this is compounded by the highly variable crystal-chemical composition, or "impurities" common among clay mineral species (Georgiadis et al., 2019). As discussed by Tardy et al. (1987), even an apparently monomineralic smectite, formed in any environment, may not be adequately evaluated as a product of the average chemical composition of millions of individual particles, covering a range of chemical formulas. This inherent difficulty in discerning specific clay mineral species from a given parent rock, or the specific conditions under which it altered, explains an extensive debate on the origin and formation conditions of the clay minerals on Mars, as well as at a long-studied Mars-analogue impact site – the Ries impact structure – as detailed in following sections.

It has been suggested that, given mounting evidence of only sporadic and transient periods of surface-water stability during the Noachian, the conditions may not have been sufficient for aqueous alteration of widespread materials on the surface (Tornabene et al., 2013). Tornabene et al. (2013) have proposed impact-related origins – as opposed to formation through atmosphere-water-rock interaction – for the widespread clay minerals observed in Noachian terrain. A major occurrence of clay minerals on Mars is in association with impact ejecta, and ejecta of large impact craters are globally disseminated during emplacement. The proximal ejecta

of the Isidis impact, for example, could have extended to nearly global scales (Tornabene et al., 2013 and references therein). While the alteration and resultant secondary mineral products of impactites produced at such a vast scale is not generally recognized as a source of the enigmatic Fe/Mg clay minerals dominant in the Noachian crust, it is accepted that they have been excavated by impact events. It is thought that these clay minerals were formed in subsurface environments – not formed as a result of surface-water-rock interaction as with deposits of Al-smectites – and represent excavated materials having formed at depth through hydrothermal or other processes (Ehlmann et al., 2009; Ehlmann and Edwards, 2014). Although crystal chemistry and bulk Fe/Mg-OH ratios of smectitic clay minerals have been constrained for the smectite occurrences on Mars (e.g., Ehlmann et al., 2011), assigning protoliths, and thus formation and/or alteration processes, is a difficult task in the absence of textural information (Michalski et al., 2015). The materials produced by impact cratering (detailed in the following section), as well as pre-impact materials that are excavated and recycled, may introduce complexity when discerning provenance of mineral phases in heavily cratered areas; indeed, this is a main hypothesis investigated by this thesis. The investigations of this work find that a number of complex clay mineral species (i.e., Al and Fe/Mg smectites) are generated as primary impact-related processes in impact-specific lithologies known as "impactites".

1.3 Impact cratering processes and products

1.3.1 Impact crater formation

The term impactite describes all rocks produced or affected by a hypervelocity impact (Grieve and Therriault, 2012). Fractured target rocks – sometimes present with post-impact hydrothermal alteration or pseudotachylite – as well as in-place brecciation, and deformation or

alteration in proximity to an identified impact crater are all clues to distinguish rocks affected *in situ* by impact cratering (French, 1998). Evidence of shock metamorphism provides an indication of impact-induced alteration (e.g., microscopic planar deformation features (PDFs), diaplectic glass; Stöffler, 1972; Stoffler, 1974; Stöffler and Grieve, 2007). The effects of impact shock are spectacular, as they metamorphose rock nearly instantaneously (Stöffler, 1972). In contrast to typical burial metamorphism deep within the Earth occurring at either constant temperature or constant pressure, the initial shock wave (Fig. 1.2) from an impact event causes a compression resulting in a sharp jump of pressure to several hundred gigapascals (GPa) and temperatures >10,000 K (Melosh, 2012). As described by Melosh (2012), the comparative temperatures and pressures within the Earth's core are ~350 GPa and ~5,000 K. The resultant effects on the target materials and the projectile are catastrophic: when shock pressures are sufficiently high, the projectile is vaporized and a substantial portion of the energy of the impact excavates the target to produce vapor condensates and high-speed ejecta. Material in the upper zone of the target is ejected on ballistic trajectories beyond the forming transient crater (Figs. 1.2a–b; Stöffler et al., 1975) – achieving a farther field of emplacement than the deeper zone of displaced rocks – and forms a continuous ejecta blanket (Pohl et al., 1977). The progressively deeper rocks from within the transient crater experience higher pressures and are thus shock-melted and produce completely reconstituted lithologies (Osinski et al., 2018). Impact melt rocks line the interior of the transient crater; the initial transient crater becomes the crater interior that houses melt-bearing "crater fill deposits". Impact melt rocks are also present as ejecta beyond the transient cavity and final crater rim (Fig. 1.2c). Unlike the initial ballistic ejecta, the impact melt-bearing ejecta deposits have been proposed to be emplaced as later ground-hugging, surface melt-rich flows that incorporate fragments of the deeper target rocks from which it was derived (Osinski et

al., 2011; Osinski and Pierazzo, 2012; Osinski et al., 2004). The initial ballistic ejecta is also a complex deposit, though, comprising "primary" ejecta from the excavated target and as much as ~69 vol% as "secondary" ejecta due to interaction with the substrate during emplacement (Hörz et al., 1983). Thus, the composition and morphology of a continuous ejecta blanket may vary considerably due to the entrainment of local weathering horizons and other surficial substrate (Oberbeck, 1975), as well as near-surface water or ice. For example, continuous ejecta blankets on Mars have a "fluidized" appearance that has been suggested to be a result of the entrainment of near-surface ice and/or other volatiles during emplacement (Fig. 1.3; Barlow, 2005; Mouginis-Mark, 1981).

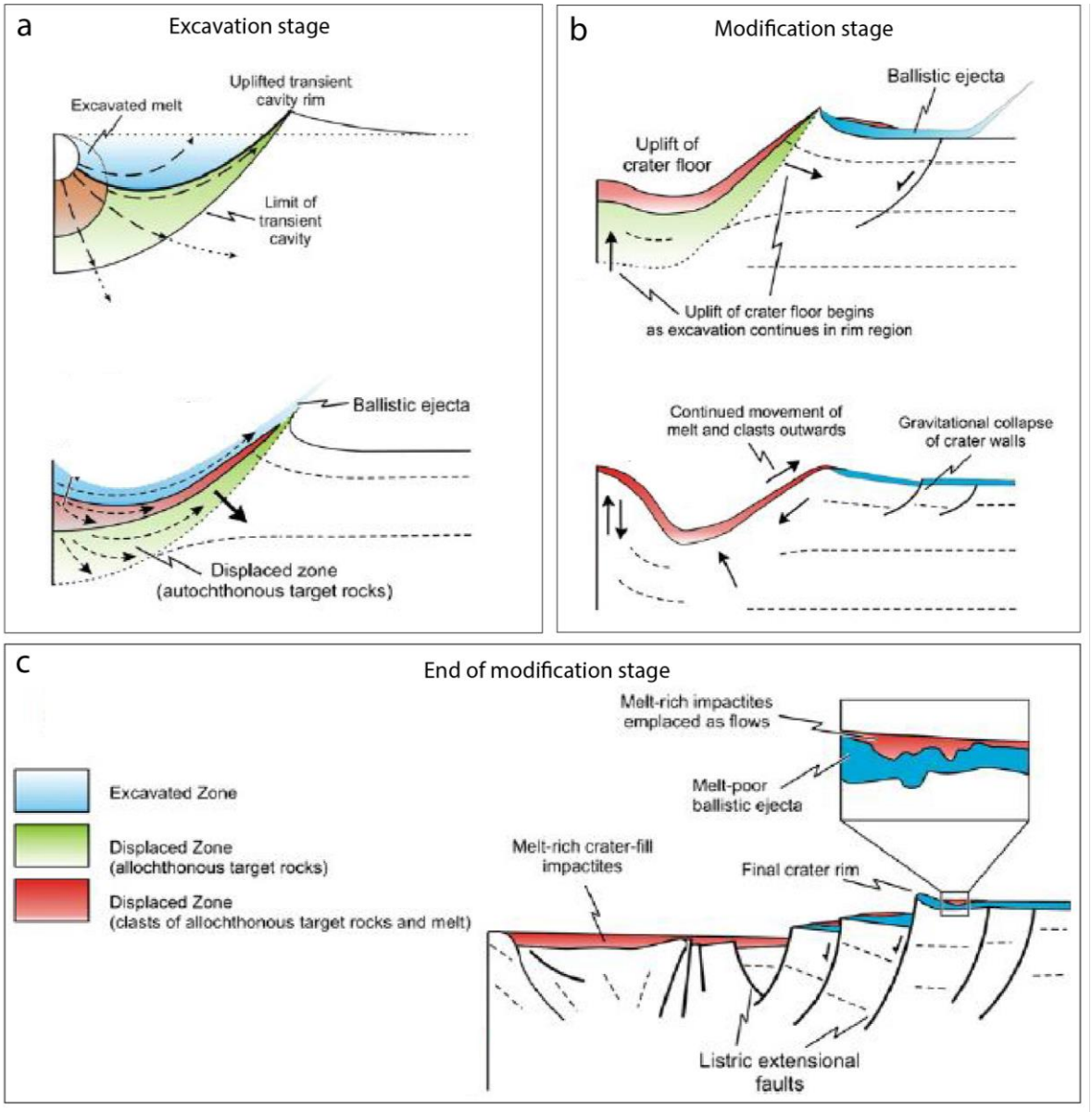

Figure 1.2. Schematic of impact crater formation for a complex crater, modified from Osinski et al. (2011). a) In the excavation stage, the transient crater is formed as the shock wave propagates through the subsurface target, displacing rocks along a downward and outward trajectory. b) In the modification stage, subsurface rebound causes the central interior of the crater to uplift and gravity collapse causes listric faulting to form crater walls and terraces. c) At the end of the modification stage, the final crater rim has been formed, the transient crater rim contains "crater-

fill" impactites, and a two-layer ejecta has been emplaced. The melt-poor ballistic ejecta (shown in blue) represents the continuous ejecta blanket.

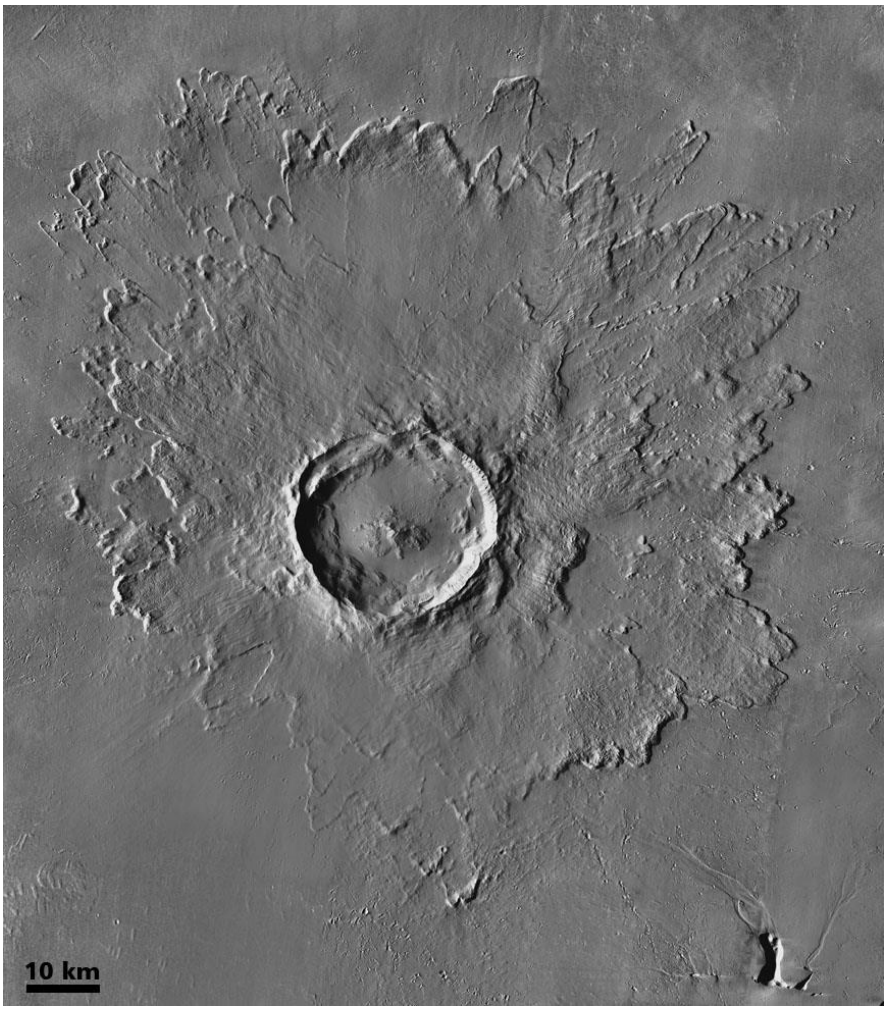

Figure 1.3. Ejecta deposits of Tooting Crater, Mars, located at 23.4N, 207.5E. The morphology typifies the layered, "fluidized" ejecta observed for many Martian craters, thought to form from a ground-hugging flow in a volatile-rich target (Mouginis-Mark and Garbeil, 2007). The base map is a Mars Orbiter Laser Altimeter (MOLA) map; image credits: NASA/Caltech-JPL/GSFC.

1.3.2 Impact ejecta and the Ries impact structure

The relationship between the two distinct ejecta impactites – the lower-most impact lithology of low-shock lithic breccia, and the upper-most melt-bearing breccia – have been well-studied at the Ries impact structure, Germany (e.g., Pohl et al., 1977; Hörz, 1982; Engelhardt et al., 1995; Osinski, 2004; Schaal and Horz, 1977). The ejecta deposits at Ries are a focus of this thesis, and particularly their study as an analogue to similar deposits on other rocky bodies. Indeed, the excellent exposures of ejecta deposits at the Ries, arguably the best-preserved deposits of their type on Earth, have been instructive regarding the formation processes and emplacement of impactites on Earth and elsewhere (Grieve and Therriault, 2012; Kenkmann and Schönian, 2006; Von Engelhardt, 1990). Figure 1.4a shows an outcrop of the two ejecta deposits in contact at the Aumühle quarry at Ries; at this and other exposures, the contact is observed as sharp and irregular, without mixing. The melt-bearing breccia deposits also infilled the topographic lows created by the underlying hummocky ejecta deposit, known at Ries as Bunte Breccia, hugging its contours during emplacement (Osinski, 2004; Osinski et al., 2011). This observed relationship indicates that the deposits were emplaced with some time separation, and not as a singular event, and further suggests that the melt-bearing breccias were a ground-hugging flow (Osinski, 2004). Among the strongest lines of evidence for this mode of emplacement is the typical flow texture of the glassy impact melt clasts, occurring with shock-metamorphosed crystalline rock fragments (e.g., Engelhardt, 1990; Osinski, 2003, 2004; Pohl et al., 1977; Engelhardt and Graup, 1984; Hörz, 1965; Engelhardt, 1997) (Figs. 1.4 d–e). The Bunte Breccia deposits consist of parautochthonous primary ejecta as lithics (Horz, 1979) including fragments of Jurassic and Triassic sedimentary rocks (described in detail in later chapters) and sparse crystalline material, but no impact glass, and secondary ejecta from surficial Miocene

sediments (Engelhardt et al., 1995; Oberbeck, 1975; Horz, 1979). Other, non-melt-bearing allochthonous breccias are more generally known as “lithic breccias” (Fig. 1.4b). Unlike the melt-bearing breccia, the Bunte Breccia materials did not experience appreciable shock-metamorphism, though they were mechanically deformed through transport (e.g., Fig. 1.4f); nor did the Bunte Breccia experience alteration by post-impact hydrothermal alteration as has been observed in the melt-bearing breccia (Osinski, 2005).

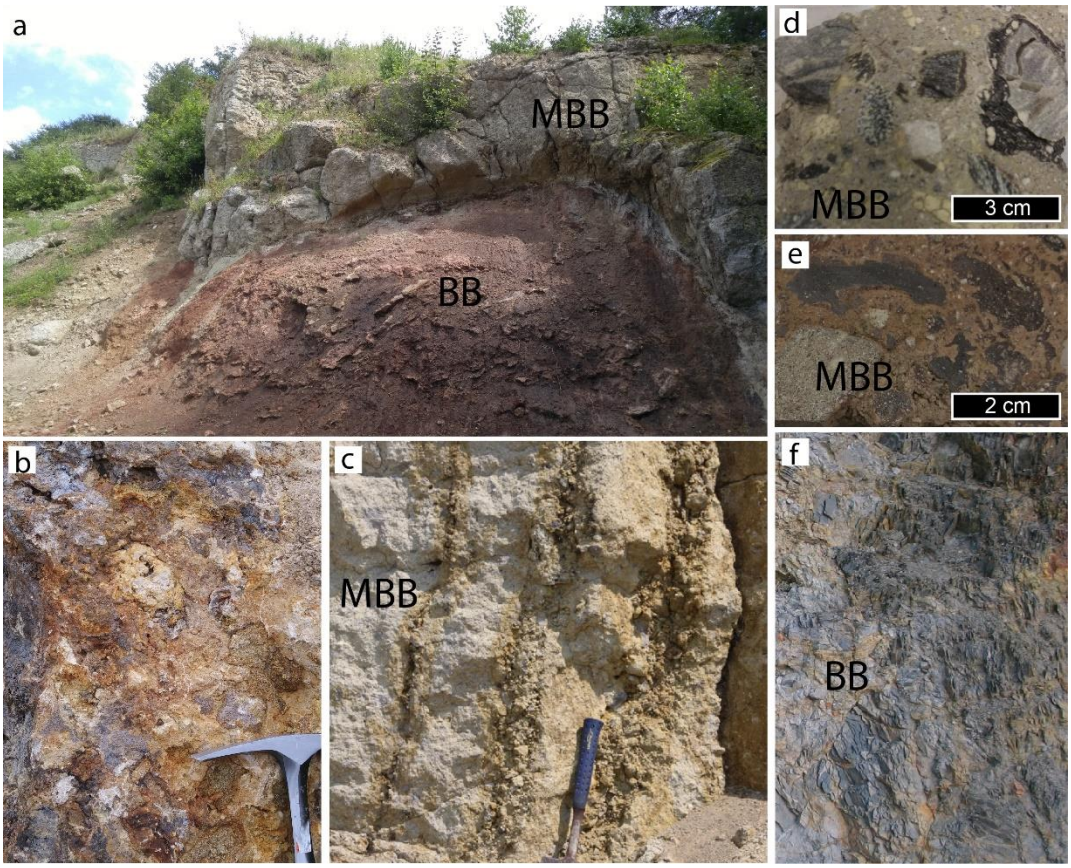

Figure 1.4. a) Ejecta deposits from the Ries impact structure, Aumühle quarry, are seen in sharp, irregular contact. Light-toned polymict melt-bearing breccia (MBB) unit overlies the dark-toned parautochthonous Bunte Breccia (BB). Height of outcrop is ~6 m. b) Wengenhousen quarry allochthonous lithic crystalline breccias (e.g., granite and gneiss) in the megablock zone, the region of the faulted crater rim in the Ries structure. c) Localized devolatilization formed vertical

degassing pipes; this process is suggested as the same that formed pitted terrains on Mars. d, e) Hand samples of typical melt-bearing breccia, showing flow-textured impact melt and angular crystalline basement-derived clasts. f) Shaley mudstones of the Bunte Breccia are shown from Aumühle quarry that were folded and deformed through emplacement yet retain original bedding planes.

1.3.3 Impact-generated hydrothermal systems

Hydrothermal alteration is a chemical weathering of rock occurring upon subsurface interaction with water that is at a greater temperature than the local geothermal gradient, in open fracture systems or porous rock, given an adequate and sustained heat source (Kirsimäe and Osinski, 2012). Impact events create these conditions, as they: (1) massively fracture and disaggregate the target rock, and; (2) impart kinetic energy to target from the shock waves of the impact that produce and sustain an elevated subsurface temperature (>90 °C) for potentially tens of thousands to millions of years in large (100 – 200 km-diameter) impacts (Abramov and Kring, 2007, 2004). Therefore, unsurprisingly, evidence for impact-induced hydrothermal systems has been identified in 70 of the ~200 impact craters on Earth (e.g., Osinski et al., 2013; Naumov, 2005). Osinski et al. (2013) identified six locations in and around impact craters that may form hydrothermal deposits, including: (1) crater-fill melt rock and breccias; (2) interior and (3) exterior of central uplifts; (4) crater rim; (5) post-impact lake sediments; and (6) ejecta deposits (Fig. 1.5). The ejecta deposits are surficial by nature, and so the heat that drives hydrothermal activity in these deposits is retained from emplacement of the melt-bearing unit (at temperatures of >750 – 900 °C; Osinski, 2004); this is in contrast to the immense, sustained subsurface heat imparted from the kinetic energy of the impact event.

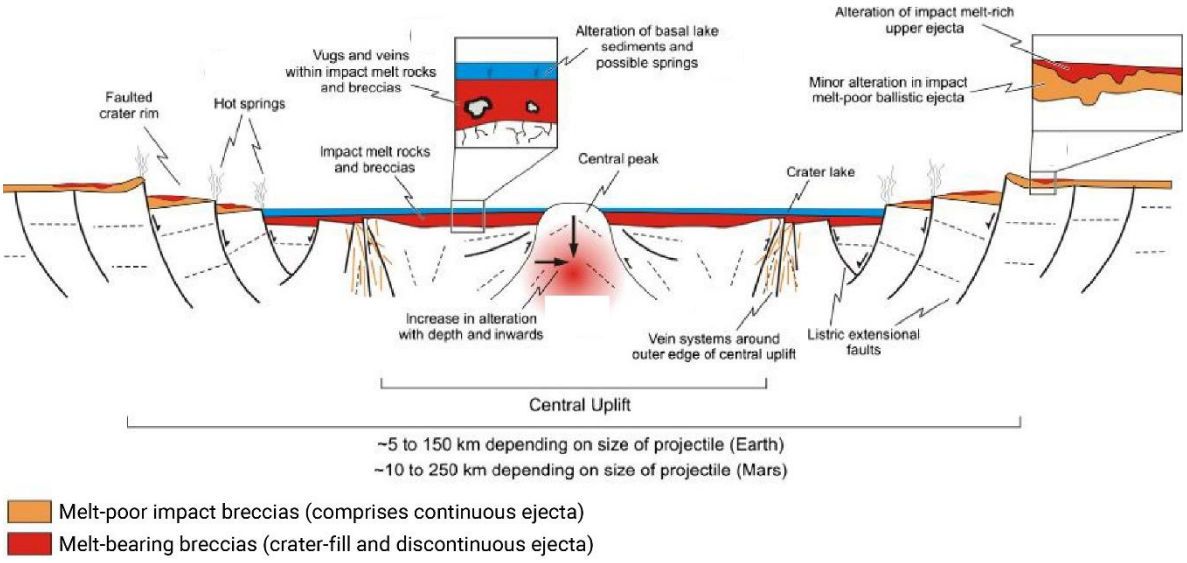

Figure 1.5. Locations of impact-generated hydrothermal systems within and surrounding a complex crater, modified from Osinski et al. (2013). Note the distribution of the melt-poor and melt-rich breccias as ejecta deposits.

The capacity for, and mineralogic evidence for the extent of, post-impact hydrothermal alteration in ejecta deposits at the Ries has generated substantial debate (e.g., Newsom et al., 1986; Osinski, 2003, 2005; Osinski et al., 2004; Muttik et al., 2008; Muttik et al., 2010; Muttik et al., 2011; Sapers et al., 2017). This debate, much like for deposits on Mars, is contentious in part due to the complexities of clay minerals, and specifically in discerning their formation environments and conditions. The Ries melt-bearing breccias contain considerable smectite clay minerals, ≥ ~70 vol% of the groundmass (Osinski et al., 2004). Some have suggested that hydrothermal activity was restricted to the crater fill deposits of the Ries (Muttik et al., 2008; Muttik, et al., 2010); the implications for the melt-bearing breccia of the ejecta deposits are that the clay minerals that comprise the bulk of this unit would be present as an ambient or low-temperature weathering product. In other words, the presence of the clay minerals is not due to

the nature of the impactite nor impact-related alteration, but simply a consequence of aqueous weathering that happens to all materials at Earth's surface. This idea was supported by bulk isotopic studies of the melt-bearing breccia of ejecta deposits showing that its dioctahedral smectite montmorillonite was precipitated from cool fluids (e.g., Muttik et al., 2010, 2008). However, both ejecta and crater-fill breccias contain localized, highly variable hydrothermal alteration products that include illite-smectite, calcite, zeolites, chlorite, and K-feldspar (Sapers et al., 2017; Osinski et al., 2004). Furthermore, platy montmorillonite from the ejecta deposits provided textural evidence (Osinski, 2005; Newsom et al., 1986), and complex trioctahedral smectites in altered glass clasts provided mineralogic evidence (Sapers et al., 2017) that are consistent with clay mineral formation through hydrothermal activity. Newsom et al. (1986) and Osinski et al. (2004) furthermore showed a greater complexity of clay minerals in the ejecta melt-bearing breccia, which comprise both montmorillonite and a "clayey groundmass". This "clayey" fraction of the groundmass is inconsistent with either surficial, aqueous smectite or hydrothermal smectite, instead formed through other impact-heat related processes: recrystallization/devitrification of metastable impact melt (Osinski et al., 2004). As shown by Sapers et al. (2017), a complex history of clay mineral formation within the Ries melt-bearing breccia is consistent with multiple alteration regimes that are highly spatially variable, including early devitrification and locally-restricted hydrothermal alteration with a later surficial weathering overprint. This thesis also investigates the complex smectite mineralogy of the Ries ejecta melt-bearing breccia and includes study of distinct features remnant of the earliest stages of post-impact cooling: degassing pipes.

1.3.4 Ries as a planetary analogue: degassing pipes and pitted deposits

Initial cooling through convection of the melt-bearing ejecta deposits at the Ries soon after emplacement is evidenced by venting structures known as “degassing pipes”. Degassing pipes are disseminated throughout the melt-bearing breccia deposits as quasi-vertical, chimney-like structures, typically <10 cm wide and several meters in vertical extent. The features are inferred to be conduits for volatile escape during ejecta cooling. Newsom et al. (1986) described the pipes as “elutriation pipes”, analogous to volcanic fumarole pipes; thus, they have been cited as one indication that the ejecta was emplaced as a density current similar to ignimbrites (Siegert et al., 2017). Engelhardt (1972) suggested that the degassing pipes represent a degassing of the host melt-bearing breccia, while Pietrek and Kenkmann (2016) proposed that their formation arose from degassing of the underlying Bunte Breccia. Chao et al. (1978) emphasized the role of hydrothermal activity in degassing pipe formation and related alteration.

One of the outcomes of this thesis is the first crater-wide investigation of degassing pipe exposures at the Ries structure, with a description of the complex smectitic mineralogy of the features and their related alteration. The motivation for this investigation is two-fold: (1) the degassing pipes are an obvious physical manifestation of the highly localized and spatially-restricted alteration that has been previously reported throughout melt-bearing breccia deposits (e.g., Sapers et al., 2017) and are, therefore, an avenue through which to further investigate impact-generated hydrothermal activity in the ejecta; and (2) it has been suggested that the degassing pipes at the Ries are analogous to crater-related pit clusters observed in impact melt-bearing deposits on Mars (Tornabene et al., 2012; Boyce et al., 2012), Ceres (Sizemore et al., 2017), and Vesta (Denevi et al., 2012). The work presented in this thesis shows the presence of secondary clay minerals in the degassing pipes; therefore, the results of this work may inform on

the presence of crustal volatiles and their interaction during the impact process on terrestrial bodies throughout the solar system.

1.3.5 Impactites on Mars and other bodies

An understanding of the products and processes of impact cratering are of paramount importance to deciphering the materials on other rocky bodies in the solar system, many of which bare the evidence of a geologic history dominated by impact cratering. With advancements in resolution and proliferation of remote-sensing data, the similarities between impactite types between rocky bodies (including Earth) have been recognized and are the subject of intensive study. Studies of geologic analogues – like Ries – have informed on the processes and products of impact cratering, including: an understanding of the geologic depths of exposures provided by cratering, fundamental to observing the crust of a body like Mars, without plate tectonics; the great distances from the host crater that impactites may be emplaced; and the extent to which ejecta and the immediately-impacted target are affected. As typified by the deposits at Ries (Grieve and Therriault, 2012), it is expected that a volatile-rich crust will form impact melt rocks and resultantly altered impactites as a consequence of impact cratering (Osinski et al., 2018; Osinski, 2006).

In the past decade, it has become clear that significant volumes of melt are produced from impacts into various volatile-rich target lithologies on Earth (see Osinski et al., 2008, 2018, and references therein), concomitant with recent documentation of impact melt materials on Mars (e.g., Morris et al., 2010; Cannon, 2015; Osinski et al., 2011; Skok et al., 2012; Tornabene et al., 2012). While the volume of impact melt produced varies based on the composition of the impactor and the target, planetary gravity and impactor size and velocity are the main factors

determining impact melt production on any rocky body (Osinski et al., 2012). On Mars, the crust is largely comprised of mafic silicates and it has been shown to have appreciable volatiles subsurface in the form of CO_2 and water ice (e.g., Stuurman et al., 2016; Orosei et al., 2018; Mellon et al., 2009); it has been suggested that substantial impact melt and other impactites were produced on Mars, forming much of the crustal materials, during the high cratering rates of the Noachian (Newsom, 1980; Schultz and Mustard, 2004; Schultz and Wrobel, 2012; Lorenz, 2000; Wrobel and Schultz, 2007). Impact melt-bearing deposits on Mars display a characteristically pitted appearance (Tornabene et al., 2012; Boyce et al., 2012). Tornabene et al. (2012) and Boyce et al. (2012) provide arguments for relationships between pits and the release of target volatiles during the impact process (as discussed in following chapters). Following the observation of widespread crater-related pitted material on Mars, similar pitted material was observed in the best-preserved impact craters on Vesta (Denevi et al., 2012) and Ceres (Sizemore et al., 2017). The pits are proposed to have formed via volatile loss following deposition, analogous to the degassing pipes at Ries (Boyce et al., 2012; Tornabene et al., 2012). In this contribution, we identify and map the ejecta deposits of a large impact crater on Mars (Bakhuysen Crater), and by morphologic indicators and comparisons to lunar and terrestrial impactites, suggest that the deposits most likely comprise impact melt-bearing breccia. Within these deposits are crater-related pitted materials, which we investigate at depth. Our mapping of the impactites of Bakhuysen Crater also shows a strong correlation between the putative melt-bearing breccia deposits and syn-impact fluvial features, further suggesting the role of volatiles the emplacement and formation of some Martian impactites (as discussed in following chapters).

As a ground-truth analogue study for the crater-related pits observed on other rocky bodies, we provide and synthesize the field and laboratory findings of the Ries degassing pipes

with special focus on the clay mineralogy, allowing assessments of the probable formation conditions. Additionally, we use the degassing pipe mineralogy as a hydrothermal alteration endmember of impact mineralogy and compare these to the clay mineral phases that comprise the melt-bearing breccia (≥ ~70 vol%) (Osinski et al., 2004) and terrigenous clay minerals preserved from the time of impact. Assessing the various formation conditions, and the depth of laboratory analyses necessary to confirm or best postulate on those conditions, we make recommendations as to best-practices when assessing clay mineral origin on Mars and other planetary bodies. Given the absence of contextualized samples from Mars, the method of confirming clay mineralogy – and thus, larger geologic and climatic history – must be understood through the lenses of: 1) Earth geologic analogues, and; 2) remote (i.e., Mars) rover-based instrumentation and missions developed with this specific goal. In this thesis– in addition to the analogue field site at Ries – we investigate specific geologic conditions likely to be encountered by future rover missions as a large-scale geologic ground-truthing endeavor (known as CanMars, detailed in the following section). Furthermore, we provide suggestions on structuring future rover mission operations to best meet goals of sample selection, which is of upmost importance in deciphering the mineralogy of ancient Mars and its past climatic conditions that may have supported life.

1.4 CanMars simulated analogue mission

The return of contextualized samples from Mars is in the planning stages for rover operations programs at both NASA and ESA; NASA's Mars 2020 (Williford et al., 2018) and ESA's ExoMars (Vago et al., 2017) rovers are being deployed as sample acquisition and cache missions, the first in a series of planned missions designed to return samples from the highly

debated – and potentially biologically significant – Noachian crust. It is acknowledged that sample return is a crucial next step in the exploration of Mars (McLennan et al., 2011; NASA, 2013; MEPAG, 2010), as orbital and *in situ* investigations are insufficient to fully provide geologic context (Haltigin et al., 2018;a topic investigated in some depth in following chapters) and assessments of past habitability; if *in situ* rover-based investigations discover evidence of preserved ancient life, return samples will be necessary for its confirmation. In advance of these missions, the CanMars Mars Sample Return Analogue Deployment (MSRAD) (Osinski et al., 2019, and detailed in following chapters) was developed to examine the intellectual frameworks and operational architecture of rover-based sample collection. CanMars was a complex, multi-year, multi-national effort producing the most realistic simulation of remote rover operations to-date. The simulation served as a testbed for strategies in conducting science operations for future missions, built on current MSL mission operations and traverse strategies. The mission scenario was closely-modeled after the technical constraints of MSL, including rover traverse limitations and resource costs as well as strict adherence to data uplink and downlink 'windows' and operational schedules. The Canadian Space Agency (CSA) Mars Exploration Science Rover (MESR) rover was deployed to a remote location – a clay-rich Mars geologic-analogue site near Green River, Utah, US (Tornabene et al., 2019) – and equipped with hardware and software built by MDA Maxar, as well as an array of spectrometers and imagers to mimic those that will be aboard Mars 2020 (Beegle et al., 2015; Wiens, R.C. et al., 2016; Allwood et al., 2015). The use of a remote Mars analogue site was a key priority for the exercise as it provided an opportunity to conduct post-mission field validation and laboratory analyses; this allowed an evaluation of the true efficacy of a remote rover mission in terms of science return. This thesis will discuss the tests and approaches employed to investigate the geologic context and choose and prioritize

samples for cache and return, as well as the efficacy of the instrument suite to assess geologic context, in particular consideration of the clay minerals present.

The level of realism of the CanMars mission scenario allowed us, as field geologists, to employ ground-truthing field investigations for planetary analogues – as at the Ries impact structure – to vet rover-based approaches to discern geological and climatic context. Through the laboratory validation of these field trails, and the detailed, intensive laboratory analyses of the clay-bearing impactites at the Ries impact structure provided in this work, we seek to incite new ways of thinking about deciphering the materials on the surface of Mars and adding to an ever more accurate view of Mars' past.

1.5 Thesis outline

The Mars science community is in an exciting time: orbiters and surface rovers are allowing scientists to investigate clay-rich deposits that may hold the key to understanding the evolution of the near-surface geology and climate – as well as life, if it ever existed on Mars. Discerning the origin of the clay minerals in the ancient, heavily-cratered terrains of Mars, and thus the implications for past habitability, is the subject of intense inquiry and the among the chief motivations of this thesis. This thesis examines the proposed provenance of Martian clay minerals, then describes how field geology on Earth provides insights and direction for research and experimentation – both theoretical and *in situ*. More specifically, this work investigates: 1) presence of impactites on Mars through orbitally-derived remote-sensing instruments with comparisons to analogous materials on Earth and other planetary bodies; 2) comparison of impact-generated clay minerals to pre-impact clay minerals in the target stratigraphy at the Ries impact structure through novel, high-resolution mineralogic field and laboratory investigations; 3) Mars analogue mission simulations as a means to bridge the gap between remote-science and

laboratory validation of geologic assessments, prompting a better articulation of the science questions during Mars *in situ*, rover-based science. A synopsis of this thesis by chapter is provided below.

Chapter 2: In this contribution, we identify and map the ejecta deposits of a large impact crater on Mars (Bakhuysen Crater), and by morphologic indicators and comparisons to lunar and terrestrial impactites, suggest that the deposits most likely comprise impact melt-bearing breccia. Within these deposits are crater-related pitted materials, suggested to be analogous to degassing pipe features at the Ries impact structure. Our mapping of the impactites of Bakhuysen Crater also shows a strong correlation between the putative melt-bearing breccia deposits and syn-impact fluvial features, further suggesting the role of volatiles the emplacement and formation of Martian impactites.

Chapter 3: We describe the first crater-wide investigation of degassing pipe exposures at the Ries impact structure as a ground-truthing study for the putatively analogous crater-related pitted material observed on other rocky bodies in the solar system. The field and laboratory findings are presented with a focus on the clay mineralogy and assessments of their probable formation conditions, as an avenue through which to further investigate impact-generated hydrothermal activity in ejecta deposits. We suggest that the degassing pipes are an obvious physical manifestation of the highly localized and spatially-restricted alteration that has been previously reported throughout melt-bearing breccia deposits at Ries, and extend these observations into the ejecta beyond the crater rim. We further suggest that the investigation of clay mineral

provenance at Ries provides insight into the potential for clay minerals on Mars produced through various impact-related processes.

Chapter 4: In this contribution, we use the degassing pipes and related mineralogy as an impact-hydrothermal alteration endmember and compare these to: (1) the clay mineral phases that comprise the melt-bearing breccia (≥ ~70 vol%) (Osinski et al., 2004), formed through a number of complex impact-related processes (e.g., recrystallization/devitrification, autometamorphism, hydrothermal), and (2) terrigenous clay minerals preserved from the time of impact. Assessing the various formation conditions, and the depth of laboratory analyses necessary to confirm or best postulate on those conditions, we make recommendations as to best-practices when assessing clay mineral origin for materials on Mars.

Chapter 5: The CanMars field trials provided an opportunity to conduct post-mission field validation and laboratory analyses, and thus, and an assessment of the efficacy of a remote rover mission in terms of science return. We provide recommendations on assessing mineralogy *in situ* in a clay-rich Mars geologic-analogue site as well as identifying and prioritizing samples for cache and return. This chapter will also present the science and operational results of the CanMars field trials, including: the CanMars operational construct, with tests and strategies for optimal Science Team operations and lessons-learned; the sol-by-sol operations and the effects of those on the participating team and the science return; the approaches employed to investigate the geologic context and choose and prioritize samples for cache and return; the efficacy of the instrument suite to assess geologic context and to identify and characterize samples, highlighting

gaps in data needs; a summary of the in-simulation science return; and a summary of the post-mission site geologic validation.

References

Abramov, O., and Kring, D.A., 2004, Numerical modeling of an impact-induced hydrothermal system at the Sudbury crater: Journal of Geophysical Research E: Planets, v. 109, doi: 10.1029/2003JE002213.

Abramov, O., and Kring, D. a., 2007, Numerical modeling of impact-induced hydrothermal activity at the Chicxulub crater: Meteoritics & Planetary Science, v. 42, p. 93–112, doi: 10.1111/j.1945-5100.2007.tb00220.x.

Allwood, A., Clark, B., Flannery, D., Hurowitz, J., Wade, L., Elam, T., Foote, M., and Knowles, E., 2015, Texture-specific elemental analysis of rocks and soils with PIXL: The Planetary Instrument for X-ray Lithochemistry on Mars 2020, *in* IEEE Aerospace Conference Proceedings, doi: 10.1109/AERO.2015.7119099.

Baker, V.R., Kochel, R.C., Laity, J.E., and Howard, A.D., 1990, Spring sapping and valley network development: Special Paper of the Geological Society of America, doi: 10.1130/SPE252-p235.

Bamhisel, R.L., 1977, Chlorites and Hydroxy Interlayered Vermiculite and Smectite, *in* Dixon, J. B., Weed, S. B., Kittrick, J.A. and Milford, M. H., White, J.L. (eds. . eds., Minerals in Soil Environments. SSSA, Madison, WI, USA, p. 331–356.

Barlow, N.G., 2005, A review of Martian impact crater ejecta structures and their implications for target properties: Large meteorite impacts III. Boulder, Colorado: Geological Society of America, p. 433–442, doi: 10.1130/0-8137-2384-1.433.

Beegle, L., Bhartia, R., White, M., Deflores, L., Abbey, W., Wu, Y.H., Cameron, B., Moore, J., Fries, M., Burton, A., Edgett, K.S., Ravine, M.A., Hug, W., Reid, R., et al., 2015, SHERLOC: Scanning habitable environments with Raman & luminescence for organics & chemicals, *in* IEEE Aerospace Conference Proceedings, v. 2015–June, doi: 10.1109/AERO.2015.7119105.

Bibring, J.-P., Langevin, Y., Mustard, J.F., Poulet, F., Arvidson, R., Gendrin, A., Gondet, B., Mangold, N., Pinet, P., Forget, F., Berthé, M., Bibring, J.-P., Gendrin, A., Gomez, C., et al., 2006, Global Mineralogical and Aqueous Mars History Derived from OMEGA/Mars Express Data: Science, v. 312, p. 400–404, doi: 10.1126/science.1122659.

Boyce, J.M., Wilson, L., Mouginis-Mark, P.J., Hamilton, C.W., and Tornabene, L.L., 2012, Origin of small pits in martian impact craters: Icarus, v. 221, p. 262–275, doi: 10.1016/j.icarus.2012.07.027.

Bristow, T.F., Bish, D.L., Vaniman, D.T., Morris, R. V., Blake, D.F., Grotzinger, J.P., Rampe, E.B., Crisp, J.A., Achilles, C.N., Ming, D.W., Ehlmann, B.L., King, P.L., Bridges, J.C., Eigenbrode, J.L., et al., 2015, The origin and implications of clay minerals from Yellowknife Bay, Gale crater, Mars: American Mineralogist, doi: 10.2138/am-2015-5077CCBYNCND.

Bristow, T.F., Rampe, E.B., Achilles, C.N., Blake, D.F., Chipera, S.J., Craig, P., Crisp, J.A., Des Marais, D.J., Downs, R.T., Gellert, R., Grotzinger, J.P., Gupta, S., Hazen, R.M., Horgan, B., et al., 2018, Clay mineral diversity and abundance in sedimentary rocks of Gale crater, Mars: Science Advances, doi: 10.1126/sciadv.aar3330.

Brown, G., Brindley, G.W., 1980, Crystal structures of clay minerals and their Xray identification: Journal of Mineralogical Society, p. 305–356., doi:

10.1016/j.jenvman.2011.05.031.

Cannon, K.M., 2015, Preserved glass-rich impactites on Mars: Geology, v. 43, http://geology.gsapubs.org/cgi/doi/10.1130/G36953.1.

Caprarelli, G., and Orosei, R., 2015, Probing the hidden geology of isidis planitia (mars) with impact craters: Geosciences (Switzerland), doi: 10.3390/geosciences5010030.

Carr, M.H., and Head, J.W., 2010, Geologic history of Mars: Earth and Planetary Science Letters, doi: 10.1016/j.epsl.2009.06.042.

Cassanelli, J.P., and Head, J.W., 2019, Assessing the formation of valley networks on a cold early Mars: Predictions for erosion rates and channel morphology: Icarus, doi: 10.1016/j.icarus.2018.11.020.

Chao, E.C.T., Cittner, R.H., and Schmidt-Kaler, H., 1978, Principle Exponents of the Ries Meteorite Crater in Southern Germany, *in* Bayerisches Geologisches Landesam, p. 84.

Craddock, R.A., and Howard, A.D., 2002, The case for rainfall on a warm, wet early Mars: Journal of Geophysical Research: Planets, v. 107, p. 5111, doi: 10.1029/2001JE001505.

Dehant, V., Lammer, H., Kulikov, Y.N., Grießmeier, J.M., Breuer, D., Verhoeven, O., Karatekin, Ö., Van Hoolst, T., Korablev, O., and Lognonné, P., 2007, Planetary magnetic dynamo effect on atmospheric protection of early earth and mars: Space Science Reviews, doi: 10.1007/s11214-007-9163-9.

Denevi, B.W., Blewett, D.T., Buczkowski, D.L., Capaccioni, F., Capria, M.T., De Sanctis, M.C., Garry, W.B., Gaskell, R.W., Le Corre, L., Li, J.-Y., Marchi, S., McCoy, T.J., Nathues, a, O'Brien, D.P., et al., 2012, Pitted terrain on Vesta and implications for the presence of volatiles.: Science (New York, N.Y.), v. 338, p. 246–9, doi: 10.1126/science.1225374.

Ehlmann, B.L., and Edwards, C.S., 2014, Mineralogy of the Martian Surface: Annual Review of

Earth and Planetary Sciences, v. 42, http://www.annualreviews.org/doi/abs/10.1146/annurev-earth-060313-055024.

Ehlmann, B.L., Mustard, J.F., Murchie, S.L., Bibring, J.-P., Meunier, A., Fraeman, A. a., and Langevin, Y., 2011, Subsurface water and clay mineral formation during the early history of Mars: Nature, v. 479, p. 53–60, doi: 10.1038/nature10582.

Ehlmann, B.L., Mustard, J.F., Swayze, G.A., Clark, R.N., Bishop, J.L., Poulet, F., Des Marais, D.J., Roach, L.H., Milliken, R.E., Wray, J.J., Barnouin-Jha, O., and Murchie, S.L., 2009, Identification of hydrated silicate minerals on Mars using MRO-CRISM: Geologic context near Nili Fossae and implications for aqueous alteration: Journal of Geophysical Research E: Planets, v. 114, doi: 10.1029/2009JE003339.

Engelhardt, W. v., 1972, Shock produced rock glasses from the Ries crater: Contributions to Mineralogy and Petrology, v. 36, p. 265–292, doi: 10.1007/BF00444336.

Engelhardt, W. Von, 1997, Suevite breccia of the Ries impact crater, Germany: Petrography, chemistry and shock metamorphism of crystalline rock: Meteoritics & Planetary Science, v. 32, p. 545–554, doi: 10.1111/j.1945-5100.1997.tb01299.x.

Engelhardt, W. V., Arndt, J., Fecker, B., and Pankau, H.G., 1995, Suevite breccia from the Ries crater, Germany: Origin, cooling history and devitrification of impact glasses: Meteoritics, v. 30, p. 279–293, doi: 10.1111/j.1945-5100.1995.tb01126.x.

Von Engelhardt, W., 1990a, Distribution, petrography and shock metamorphism of the ejecta of the Ries crater in Germany-a review: Tectonophysics, doi: 10.1016/0040-1951(90)90104-G.

Von Engelhardt, W., 1990b, Distribution, petrography and shock metamorphism of the ejecta of the Ries crater in Germany-a review: Tectonophysics, v. 171, p. 259–273, doi: 10.1016/0040-1951(90)90104-G.

von Engelhardt, W., and Graup, G., 1984, Suevite of the ries crater, Germany: Source rocks and implications for cratering mechanics: Geologische Rundschau, v. 73, p. 447–481, doi: 10.1007/BF01824968.

Fassett, C.I., and Head, J.W., 2008a, The timing of martian valley network activity: Constraints from buffered crater counting: Icarus, doi: 10.1016/j.icarus.2007.12.009.

Fassett, C.I., and Head, J.W., 2008b, Valley network-fed, open-basin lakes on Mars: Distribution and implications for Noachian surface and subsurface hydrology: Icarus, v. 198, p. 37–56, doi: 10.1016/j.icarus.2008.06.016.

Fassett, C.I., and Minton, D.A., 2013, Impact bombardment of the terrestrial planets and the early history of the Solar System: Nature Geoscience, doi: 10.1038/ngeo1841.

Fedo, C., Grotzinger, J., Gupta, S., Stein, N.T., Watkins, J., Banham, S., Edgett, K.S., Minitti, M., Schieber, J., Siebach, K., Stack-Morgan, K., Newsom, H., Lewis, K.W., House, C., et al., 2017, Facies analysis and basin architecture of the upper part of the Murray formation, Gale crater, Mars, *in* 48th Lunar and Planetary Science Conference, Woodlands, TX, p. abstract 1689.

French, B.M., 1998, Formation of Impact Craters: Traces of Catastrophe: A Handbook of Shock-Metamorphic Effects in Terrestrial Meteorite Impact Structures, p. 17–30.

Frey, H. V, 2003, Buried impact basins and the earliest history of Mars: Sixth Intern. Conf. Mars, Pasadena, Ca.,.

Georgiadis, A., Dietel, J., Dohrmann, R., and Rennert, T., 2019, What are the nature and formation conditions of hydroxy-interlayered minerals (HIMs) in soil? J. Plant Nutr. Soil Science, v. 000, p. 1–15, doi: 10.1002/jpln.201900283.

Grieve, R.A.F., and Therriault, A.M., 2012, Impactites: Their Characteristics and Spatial

Distribution, *in* Impact Cratering: Processes and Products, doi: 10.1002/9781118447307.ch7.

Grotzinger, J.P., Gupta, S., Malin, M.C., Rubin, D.M., Schieber, J., Siebach, K., Sumner, D.Y., Stack, K.M., Vasavada, A.R., Calef, F., Edgar, L., Fischer, W.F., Grant, J.A., Griffes, J., et al., 2015, Deposition, exhumation, and paleoclimate of an ancient lake deposit, Gale crater, Mars: Science, v. 350, http://www.sciencemag.org/cgi/doi/10.1126/science.aac7575.

Gwizd, S., Fedo, C., Grotzinger, J., Edgett, K., Rivera-Hernandez, F., and Stein, N., 2018, Depositional history of the Hartmann's Valley member, Murray formation, Gale crater, Mars, *in* 48th Lunar and Planetary Science Conference, Woodlands, TX, p. abstract 2150.

Haltigin, T., Lange, C., Mugnuolo, R., Smith, C., Haltigin, T., Lange, C., Mugnolo, R., Smith, C., Amundsen, H., Bousquet, P., Conley, C., Debus, A., Dias, J., Falkner, P., et al., 2018, iMARS Phase 2: A Draft Mission Architecture and Science Management Plan for the Return of Samples from Mars: Astrobiology, doi: 10.1089/ast.2018.29027.mars.

Hartmann, W.K., 1965, Secular changes in meteoritic flux through the history of the solar system: Icarus, doi: 10.1016/0019-1035(65)90062-X.

Hartmann, W.K., and Neukum, G., 2001, Cratering chronology and the evolution of Mars, *in* Space Science Reviews, v. 96, p. 165–194, doi: 10.1023/A:1011945222010.

Hazen, R.M., Sverjensky, D.A., Azzolini, D., Bish, D.L., Elmore, S.C., Hinnov, L., and Milliken, R.E., 2013, Clay mineral evolution: American Mineralogist, v. 98, p. 2007–2029, doi: 10.2138/am.2013.4425.

Horz, F., 1979, "Bunte Breccia" of the Ries crater: implications for lateral and vertical redistribution of large scale crater ejecta: Lunar and Planetary Institute,.

Hörz, F., 1982, Ejecta of the ries crater, Germany: Special Paper of the Geological Society of

America, doi: 10.1130/SPE190-p39.

Hörz, F., 1965, Untersuchungen an Riesgläsern: Beiträge zur Mineralogie und Petrographie, doi: 10.1007/BF01128707.

Hörz, F., Ostertag, R., and Rainey, D.A., 1983, Bunte Breccia of the Ries: Continuous deposits of large impact craters: Reviews of Geophysics, v. 21, p. 1667, doi: 10.1029/RG021i008p01667.

Kenkmann, T., and Schönian, F., 2006, Ries and Chicxulub: Impact craters on Earth provide insights for Martian ejecta blankets: Meteoritics and Planetary Science, v. 41, p. 1587–1603, doi: 10.1111/j.1945-5100.2006.tb00437.x.

Kieffer, S.W., and Simonds, C.H., 1980, The role of volatiles and lithology in the impact cratering process: Rev. Geophys., v. 18, http://onlinelibrary.wiley.com/doi/10.1029/RG018i001p00143/abstract.

Kirsimäe, K., and Osinski, G.R., 2012, Impact-Induced Hydrothermal Activity, *in* Impact Cratering: Processes and Products, p. 76–89, doi: 10.1002/9781118447307.ch6.

Kring, D.A., and Cohen, B.A., 2002, Cataclysmic bombardment throughout the inner solar system 3.9-4.0 Ga: Journal of Geophysical Research E: Planets, doi: 10.1029/2001je001529.

Leonard, G., and Tanaka, K., 2001, Geologic map of the Hellas region of Mars:, astropedia.astrogeology.usgs.gov.

Lorenz, R.D., 2000, Microtektites on Mars: Volume and Texture of Distal Impact Ejecta Deposits: Icarus, doi: 10.1006/icar.1999.6303.

Marra, W.A., Braat, L., Baar, A.W., and Kleinhans, M.G., 2014, Valley formation by groundwater seepage, pressurized groundwater outbursts and crater-lake overflow in flume

experiments with implications for Mars: Icarus, doi: 10.1016/j.icarus.2013.12.026.

Mars Exploration Program Analysis Group, 2010, Mars Science Goals , Objectives , Investigations , and Priorities : 2010: MEPAG Goals, p. 49.

McGill, G.E., 1989, Buried topography of Utopia, Mars: persistence of a giant impact depression: Journal of Geophysical Research, doi: 10.1029/JB094iB03p02753.

McLennan, S.M., Sephton, M.A., Allen, C., Allwood, A.C., Barbieri, R., Beaty, D.W., Boston, P., Carr, M., Grady, M., Grant, J., Heber, V.S., Herd, C.D.K., Hofmann, B., King, P., et al., 2011, Planning for Mars Returned Sample Science: Final report of the MSR End-to-End International Science Analysis Group (E2E-iSAG).:

Mellon, M.T., Arvidson, R.E., Sizemore, H.G., Searls, M.L., Blaney, D.L., Cull, S., Hecht, M.H., Heet, T.L., Keller, H.U., Lemmon, M.T., Markiewicz, W.J., Ming, D.W., Morris, R. V., Pike, W.T., et al., 2009, Ground ice at the Phoenix landing site: Stability state and origin: Journal of Geophysical Research E: Planets, doi: 10.1029/2009JE003417.

Melosh, H.J., 2012, The Contact and Compression Stage of Impact Cratering, *in* Impact Cratering: Processes and Products, doi: 10.1002/9781118447307.ch3.

Michalski, J.R., Cuadros, J., Bishop, J.L., Darby Dyar, M., Dekov, V., and Fiore, S., 2015, Constraints on the crystal-chemistry of Fe/Mg-rich smectitic clay minerals on Mars and links to global alteration trends: Earth and Planetary Science Letters, v. 427, p. 215–225, doi: 10.1016/j.epsl.2015.06.020.

Morris, A.R., Mouginis-Mark, P.J., and Garbeil, H., 2010, Possible impact melt and debris flows at Tooting Crater, Mars: Icarus, v. 209, p. 369–389, doi: 10.1016/j.icarus.2010.05.029.

Mouginis-Mark, P., 1981, Ejecta emplacement and modes of formation of martian fluidized ejecta craters: Icarus, v. 45, p. 60–76, doi: 10.1016/0019-1035(81)90006-3.

Mouginis-Mark, P.J., and Garbeil, H., 2007, Crater geometry and ejecta thickness of the Martian impact crater tooting: Meteoritics and Planetary Science, doi: 10.1111/j.1945-5100.2007.tb00594.x.

Mustard, J.F., Murchie, S.L., Pelkey, S.M., Ehlmann, B.L., Milliken, R.E., Grant, J. a, Bibring, J.-P., Poulet, F., Bishop, J., Dobrea, E.N., Roach, L., Seelos, F., Arvidson, R.E., Wiseman, S., et al., 2008, Hydrated silicate minerals on Mars observed by the Mars Reconnaissance Orbiter CRISM instrument.: Nature, v. 454, p. 305–309, doi: 10.1038/nature07097.

Muttik, N., Kirsimäe, K., and Vennemann, T.W., 2010, Stable isotope composition of smectite in suevites at the Ries crater, Germany: Implications for hydrous alteration of impactites: Earth and Planetary Science Letters, v. 299, p. 190–195, doi: 10.1016/j.epsl.2010.08.034.

Muttik, N., Kirsimäe, K., Newsom, H.E., and Williams, L.B., 2011, Boron isotope composition of secondary smectite in suevites at the Ries crater, Germany: Boron fractionation in weathering and hydrothermal processes: Earth and Planetary Science Letters, v. 310, p. 244–251, doi: 10.1016/j.epsl.2011.08.028.

Muttik, N., Kirsimäe, K., and Vennemann, T.W., 2010, Stable isotope composition of smectite in suevites at the Ries crater, Germany: Implications for hydrous alteration of impactites: Earth and Planetary Science Letters, v. 299, p. 190–195, doi: 10.1016/j.epsl.2010.08.034.

Muttik, N., Kirsimaee, K., Somelar, P., and Osinsk, G.R., 2008a, Post-impact alteration of surficial suevites in Ries crater, Germany: Hydrothermal modification or weathering processes? Meteoritics & Planetary Science, v. 43, p. 1827–1840, doi: 10.1111/j.1945-5100.2008.tb00646.x.

Muttik, N., Kirsimaee, K., Somelar, P., and Osinsk, G.R., 2008b, Post-impact alteration of surficial suevites in Ries crater, Germany: Hydrothermal modification or weathering

processes? METEORITICS & PLANETARY SCIENCE, v. 43, p. 1827–1840, doi: 10.1111/j.1945-5100.2008.tb00646.x.

NASA, 2013, Vision and Voyages for Planetary Science in the Decade 2013-2022: Washington, D.C., THE NATIONAL ACADEMIES PRESS.

Naumov, M. V., 2005, Principal features of impact-generated hydrothermal circulation systems: Mineralogical and geochemical evidence: Geofluids, v. 5, p. 165–184, doi: 10.1111/j.1468-8123.2005.00092.x.

Newsom, H.E., 1980, Hydrothermal alteration of impact melt sheets with implications for Mars: Icarus, v. 44, p. 207–216, doi: 10.1016/0019-1035(80)90066-4.

Newsom, H., Graup, G., Sewards, T., and Keil, K., 1986, Fluidization and hydrothermal alteration of the Suevite deposit at the Ries Crater, West Germany, and implications for Mars: Journal of Geophysical Research, v. 91, p. E239–E251, doi: http://dx.doi.org/10.1029/JB091iB13p0E239.

Oberbeck, V.R., 1975, The Role of Ballistic Erosion and Sedimentation in Lunar Stratigraphy: Reviews of Geophysics, v. 13, p. 337–362, doi: 10.1029/RG013i002p00337.

Orosei, R., Lauro, S.E., Pettinelli, E., Cicchetti, A., Coradini, M., Cosciotti, B., Di Paolo, F., Flamini, E., Mattei, E., Pajola, M., Soldovieri, F., Cartacci, M., Cassenti, F., Frigeri, A., et al., 2018, Radar evidence of subglacial liquid water on Mars: Science, doi: 10.1126/science.aar7268.

Osinski, G.R., 2006, Effect of volatiles and target lithology on the generation and emplacement of impact crater fill and ejecta deposits on Mars: Meteoritics & Planetary Science, v. 41, p. 1571–1586, doi: 10.1111/j.1945-5100.2006.tb00436.x.

Osinski, G.R., 2005, Hydrothermal activity associated with the Ries impact event, Germany:

Geofluids, v. 5, p. 202–220, doi: 10.1111/j.1468-8123.2005.00119.x.

Osinski, G.R., 2003, Impact glasses in fallout suevites from the Ries impact structure, Germany: An analytical SEM study: Meteoritics & Planetary Science, v. 38, p. 1641–1667, doi: 10.1111/j.1945-5100.2003.tb00006.x.

Osinski, G.R., 2004, Impact melt rocks from the Ries structure, Germany: An origin as impact melt flows? Earth and Planetary Science Letters, v. 226, p. 529–543, doi: 10.1016/j.epsl.2004.08.012.

Osinski, G.R., Battler, M., Caudill, C.M., Francis, R., Haltigin, T., Hipkin, V.J., Kerrigan, M., Pilles, E.A., Pontefract, A., Tornabene, L.L., Allard, P., Bakambu, J.N., Balachandran, K., Beaty, D.W., et al., 2019, The CanMars Mars Sample Return analogue mission: Planetary and Space Science, doi: 10.1016/j.pss.2018.07.011.

Osinski, G.R., Grieve, R.A.F., Bleacher, J.E., Neish, C.D., Pilles, E.A., and Tornabene, L.L., 2018, Igneous rocks formed by hypervelocity impact: Journal of Volcanology and Geothermal Research, v. 353, p. 25–54, doi: 10.1016/j.jvolgeores.2018.01.015.

Osinski, G.R., Grieve, R.A.F., Marion, C., and Chanou, A., 2012, Impact Melting, *in* Impact Cratering: Processes and Products, doi: 10.1002/9781118447307.ch9.

Osinski, G.R., Grieve, R.A.F., and Spray, J.G., 2008, Impact melting in sedimentary target rocks: An assessment, *in* Evans K. R., H.W., King D. K. Jr., Morrow J. R., and W.J.E.G.S., and Publication eds., The Sedimentary Record of Meteorite Impacts, . Boulder, Geological Society of America, p. 1–18.

Osinski, G.R., Grieve, R. a. F., and Spray, J.G., 2004, The nature of the groundmass of surficial suevite from the Ries impact structure, Germany, and constraints on its origin: Meteoritics & Planetary Science, v. 39, p. 1655–1683, doi: 10.1111/j.1945-5100.2004.tb00065.x.

Osinski, G.R., and Pierazzo, E., 2012, Impact Cratering: Processes and Products:, doi: 10.1002/9781118447307.

Osinski, G.R., Tornabene, L.L., Banerjee, N.R., Cockell, C.S., Flemming, R., Izawa, M.R.M., McCutcheon, J., Parnell, J., Preston, L.J., Pickersgill, A.E., Pontefract, A., Sapers, H.M., and Southam, G., 2013, Impact-generated hydrothermal systems on Earth and Mars: Icarus, v. 224, http://linkinghub.elsevier.com/retrieve/pii/S0019103512003491.

Osinski, G.R., Tornabene, L.L., and Grieve, R.A.F., 2011a, Impact ejecta emplacement on terrestrial planets: Earth and Planetary Science Letters, v. 310, http://linkinghub.elsevier.com/retrieve/pii/S0012821X11004675.

Osinski, G.R., Tornabene, L.L., and Grieve, R.A.F., 2011b, Impact ejecta emplacement on terrestrial planets: Earth and Planetary Science Letters, v. 310, p. 167–181, doi: 10.1016/j.epsl.2011.08.012.

Pierazzo, E., Artemieva, N.A., Ivanov, B.A., 2005, Starting conditions for hydrothermal systems underneath martian craters: Hydrocode modeling, *in* Kenkmann, T., Hörz, F., Deutsch, A. ed., Large Meteorite Impacts III, Boulder, Colorado, Geological Society of America, p. 443–457.

Pietrek, A., and Kenkmann, T., 2016, Ries Bunte Breccia revisited: Indications for the presence of water in Itzing and Otting drill cores and implications for the emplacement process: Meteoritics and Planetary Science, v. 51, p. 1203–1222, doi: 10.1111/maps.12656.

Pohl, J., Stöffler, D., Gall, H., and Ernstson, K., 1977, The Reis Impact Crater, *in* Impact and explosion cratering, p. 343–404.

Poulet, F., Bibring, J.-P., Mustard, J.F., Gendrin, a., Mangold, N., Langevin, Y., Arvidson, R.E., Gondet, B., Gomez, C., Berthé, M., Erard, S., Forni, O., Manaud, N., Poulleau, G., et al.,

2005, Phyllosilicates on Mars and implications for early martian climate: Nature, v. 438, p. 623–627, doi: 10.1038/nature04274.

Sapers, H.M., Osinski, G.R., Flemming, R.L., Buitenhuis, E., Banerjee, N.R., Tornabene, L.L., Blain, S., and Hainge, J., 2017, Evidence for a spatially extensive hydrothermal system at the Ries impact structure, Germany: Meteoritics & Planetary Science, v. 52, p. 351–371.

Schaal, R.B., and Horz, F., 1977, Shock Metamorphism of Lunar and Terrestrial Basalts: Proceedings of the Lunar Science Conference, v. 2, p. 1697–1729, http://articles.adsabs.harvard.edu/cgi-bin/nph-iarticle_query?1977LPSC....8.1697S&data_type=PDF_HIGH&whole_paper=YES&type=PRINTER&filetype=.pdf.

Schultz, P.H., and Mustard, J.F., 2004, Impact melts and glasses on Mars: Journal of Geophysical Research, v. 109, p. E01001, doi: 10.1029/2002JE002025.

Schultz, P.H., and Wrobel, K.E., 2012, The oblique impact Hale and its consequences on Mars: Journal of Geophysical Research: Planets, v. 117.

Segura, T.L., Toon, O.B., Colaprete, A., and Zahnle, K., 2002, Environmental effects of large impacts on Mars: Science, doi: 10.1126/science.1073586.

Siegert, S., Branney, M.J., and Hecht, L., 2017, Density current origin of a melt-bearing impact ejecta blanket (Ries suevite, Germany): Geology, doi: 10.1130/G39198.1.

Sizemore, H.G., Platz, T., Schorghofer, N., Prettyman, T.H., De Scantis, M.C., Crown, D.A., Schmedemann, N., Neesemann, A., Kneissl, T., Marchi, S., Shneck, P.M., Bland, M.T., Schmidt, B.E., Hughson, K.H.G., et al., 2017, Pitted terrains on (1) Ceres and implications for shallowsubsurface volatile distribution: Geophysical Research Letters, v. 44, p. 6570–6578, doi: doi:10.1002/2017GL073970.

Skok, J.R., Mustard, J.F., Tornabene, L.L., Pan, C., Rogers, D., and Murchie, S.L., 2012, A spectroscopic analysis of Martian crater central peaks: Formation of the ancient crust: Journal of Geophysical Research E: Planets, doi: 10.1029/2012JE004148.

Stein, N., Grotzinger, J.P., Schieber, J., Mangold, N., Newsom, H., Minitti, M., Sumner, D., Edgett, K.S., Stack, K., Fedo, C., Gupta, S., Hallet, B., Vasavada, A., and Fey, D., 2017, Candidate Desiccation Cracks in the Upper Murray Formation, Gale Crater, Mars: 48th Lunar and Planetary Science Conference,.

Stepinski, T.F., and Coradetti, S., 2004, Comparing morphologies of drainage basins on Mars and Earth using integral-geometry and neural maps: Geophysical Research Letters, doi: 10.1029/2004GL020359.

Stoffler, D., 1974, Deformation and transformation of rock-forming minerals by natural and experimental processes: II. Physical properties of shocked minerals.: Fortschritte Der Mineralogie, v. 51, p. 256–289.

Stöffler, D., 1972, Deformation and transformation of rock-forming minerals by natural and experimental shock processes I. Behavior of minerals under shock compression: Fortschritte der Mineralogie,.

Stöffler, D., Gault, D.E., Wedekind, J., and Polkowski, G., 1975, Experimental hypervelocity impact into quartz sand: Distribution and shock metamorphism of ejecta: Journal of Geophysical Research, doi: 10.1029/jb080i029p04062.

Stöffler, D., and Grieve, R.A.F., 2007, Impactites, *in* Metamorphic Rocks: A Classification and Glossary of Terms, Recommendations of the International Union of Geological Sciences,.

Stuurman, C.M., Osinski, G.R., Holt, J.W., Levy, J.S., Brothers, T.C., Kerrigan, M., and Campbell, B.A., 2016, SHARAD detection and characterization of subsurface water ice

deposits in Utopia Planitia, Mars: Geophysical Research Letters, doi: 10.1002/2016GL070138.

Tardy, Y., Duplay, J., and Fritz, B., 1987, Stability of smectites and illites as a function of temperature and chemical compostion, *in* Proc. Int. Meeting of Geochemistry of Earth Sciences and Processes of Mineral Formation, Granada, p. 461–494.

Tornabene, L.L., Battler, M., Choe, B.H., and Osinski, G.R., 2019, An orbit-based remote sensing geological assessment of the CanMars Mars Sample Return Analogue Deployment (MSRAD)landing site situated in the Henry Mountains Basin, near Hanksville, Utah: Planetary and Space Science, doi: 10.1016/j.pss.2019.04.006.

Tornabene, L.L., Osinski, G.R., McEwen, A.S., Boyce, J.M., Bray, V.J., Caudill, C.M., Grant, J.A., Hamilton, C.W., Mattson, S., and Mouginis-Mark, P.J., 2012, Widespread crater-related pitted materials on Mars: Further evidence for the role of target volatiles during the impact process: Icarus, v. 220, http://linkinghub.elsevier.com/retrieve/pii/S0019103512002047.

Tornabene, L.L., Osinski, G.R., McEwen, A.S., Wray, J.J., Craig, M.A., Sapers, H.M., and Christensen, P.R., 2013, An impact origin for hydrated silicates on Mars: A synthesis: Journal of Geophysical Research E: Planets, v. 118, p. 994–1012, doi: 10.1002/jgre.20082.

Vago, J.L., Westall, F., Pasteur Instrument Teams, Landing S, Coates, A.J., Jaumann, R., Korablev, O., Ciarletti, V., Mitrofanov, I., Josset, J.-L., De Sanctis, M.C., Bibring, J.-P., Rull, F., Goesmann, F., Steininger, H., et al., 2017, Habitability on Early Mars and the Search for Biosignatures with the ExoMars Rover: Astrobiology, v. 17, p. 471–510, doi: 10.1089/ast.2016.1533.

Weiss, M.C., Sousa, F.L., Mrnjavac, N., Neukirchen, S., Roettger, M., Nelson-Sathi, S., and

Martin, W.F., 2016, The physiology and habitat of the last universal common ancestor: Nature Microbiology, doi: 10.1038/nmicrobiol.2016.116.

Wiens, R.C., Maurice, S.R., and Rull, F., 2016, SuperCam Remote Sensing on the Mars 2020 Rover: Science Goals and Overview, *in* 3rd International Workshop on Instrumentation for Planetary Missions, p. 4136.

Williford, K.H., Farley, K.A., Stack, K.M., Allwood, A.C., Beaty, D., Beegle, L.W., Bhartia, R., Brown, A.J., de la Torre Juarez, M., Hamran, S.-E., Hecht, M.H., Hurowitz, J.A., Rodriguez-Manfredi, J.A., Maurice, S., et al., 2018, The NASA Mars 2020 Rover Mission and the Search for Extraterrestrial Life, *in* From Habitability to Life on Mars, doi: 10.1016/b978-0-12-809935-3.00010-4.

Wimpenny, J., 2018, Clay minerals, *in* Encyclopedia of Earth Sciences Series, doi: 10.1346/ccmn.1982.0300513.

Wordsworth, R., Kalugina, Y., Lokshtanov, S., Vigasin, A., Ehlmann, B., Head, J., Sanders, C., and Wang, H., 2017, Transient reducing greenhouse warming on early Mars: Geophysical Research Letters, doi: 10.1002/2016GL071766.

Wordsworth, R.D., Kerber, L., Pierrehumbert, R.T., Forget, F., and Head, J.W., 2015, Comparison of "warm and wet" and "cold and icy" scenarios for early Mars in a 3-D climate model: Journal of Geophysical Research E: Planets, doi: 10.1002/2015JE004787.

Wrobel, K.E., and Schultz, P.H., 2007, The significant contribution of impact glass to the martian surface record, *in* Seventh International Conference on Mars, Pasadena, California, p. 3093.

Chapter 2: Ejecta Deposits of Bakhuysen Crater, Mars [1]

2.1 Introduction

Impact cratering is a fundamental process and plays an important role in the geological evolution of the terrestrial planets (Melosh, 1989; Osinski and Pierazzo, 2012). It has been suggested that impact cratering was also important for the evolution of life (e.g., Cockell and Lee, 2002). The oldest basin-forming impacts on Earth are no longer observable at the surface due to subsequent geological processes (Werner, 2008); however, a record of large ancient basins and high cratering rates are preserved in Noachian-aged Martian terrains (~4.1 to 3.7 Ga). Noachian terrain also preserves widespread fluvial activity evidenced by channel networks (Carr, 1996) and abundant phyllosilicates (e.g., Bibring et al., 2006; Carter et al., 2013; Ehlmann et al., 2013, 2011; Ehlmann and Edwards, 2014; Viviano-Beck et al., 2014), with large impact events providing some means for hydrologic, crustal, and hydrothermal cycling without plate tectonics. Since phyllosilicates dominate the alteration mineralogy of terrestrial impact craters (e.g., Naumov, 2005; Osinski et al., 2013), resulting from complex impact- related alteration and weathering processes, an impact-related origin of the widespread phyllosilicates has been suggested for the heavily cratered Noachian surfaces on Mars (e.g., Tornabene et al., 2013).

The study of large impact structures provides a better understanding of the mineral, lithologic, and volatile composition of terrestrial crusts. This understanding is largely based on the ejecta deposits, which exhume and redistribute the target stratigraphy (Osinski et al., 2011; Tornabene et al., 2008 and references therein). However, the origin and emplacement of ejecta deposits is still widely debated, particularly for large impact structures. Indeed, among the three

[1] Caudill, C.M., G.R. Osinski, L.L. Tornabene (2018) Geological Mapping and Interpretation of Bakhuysen Crater, Mars, Icarus 314, 175-194.

largest craters on Earth – Chicxulub, Sudbury, Vredefort – only Chicxulub hosts abundant ejecta deposits (e.g., Kring, 2005; Sharpton et al., 1996). The lack of surface exposures and only limited drill core make study of the Chicxulub impact structure challenging. The better-exposed deposits at the smaller Ries impact structure (~24 km-diameter, Germany) and Haughton impact structure (~23 km-diameter, Canada) have been well-studied. The two main deposit types described at these terrestrial sites include a melt-poor or melt-free ballistically-emplaced impact breccia (Hörz, 1982; Morrison and Oberbeck, 1978; Osinski et al., 2005) overlain by discontinuous impact melt-bearing breccias (e.g., Osinski et al., 2011). Mars possesses numerous well-preserved impact craters, including several large structures (i.e., defined herein as craters with a diameter greater than 100 km), with opportunity for study afforded by abundant coverage of high-resolution (meter to sub-meter scale) remote sensing datasets.

On Mars, the majority of preserved ejecta deposits for craters ≥5km in diameter (~89%; Barlow, 2006, 2005) were apparently fluidized during emplacement in contrast to the typically blocky deposits present around lunar craters (e.g., Carr et al., 1977; Osinski et al., 2006; Horner and Greeley, 1982). Barlow et al. (2000) defined Martian layered ejecta based their highly sinuous shape and variable ejecta termini, including single, double, or multi-layered ejecta (SLE, DLE and MLE, respectively). The fluidized flow and layered ejecta morphologies have been suggested to result from the interaction of ejecta with target volatiles (Barlow, 2005, 2003; Barlow and Bradley, 1990; Boyce and Mouginis-Mark, 2006; Carr et al., 1977; Costard, 1989; Gault and Greeley, 1978; Komatsu et al., 2007; Mouginis-Mark, 1981, 1979; Oberbeck, 2009; Osinski, 2006; Wohletz and Sheridan, 1983), with the Martian atmosphere (Barnouin-Jha et al., 1999; Barnouin-Jha and Schultz, 1999, 1998, 1996; Schultz, 1992; Schultz and Gault, 1979), or both (e.g., Barlow, 2005; Komatsu et al., 2007); a dry, granular flow has also been proposed as

an emplacement mechanism (Barnouin-Jha et al., 2005; Wada and Barnouin-Jha, 2006). The presence of layered ejecta morphologies on Ganymede and Europa, which are airless planetary bodies, suggests that: (1) an atmosphere is not a required for their formation, and (2) fluidization cannot be facilitated purely by a dry flow (Boyce et al., 2010). Crustal volatile content is thought to be the major factor in the formation of layered ejecta on any rocky planetary body (Barlow, 2006, 2003; Carr et al., 1977; Gault and Greeley, 1978; Komatsu et al., 2007; Mouginis-Mark, 1987; Wohletz and Sheridan, 1983); although the mechanism by which separate layers form is still debated.

Previous studies have suggested that large coherent impact melt sheets would not form on Mars (Schultz and Mustard, 2004). This reasoning stems from the supposition that coherent impact melt rocks would not be generated in impact structures formed in volatile-rich sedimentary targets on Earth (Kieffer and Simonds, 1980), even though impacts into such targets should produce as much or more melt than impacts into crystalline rocks (Kieffer and Simonds, 1980). The apparent anomaly between observation and theory was attributed to the release of large amounts of vapor (e.g., H_2O, CO_2, SO_2), which was proposed to disperse the shock-melted sedimentary rocks (Kieffer and Simonds, 1980). In the past two decades it has become apparent that substantial volumes of impact melt are generated from impacts into volatile-rich sedimentary targets and retained within the host craters (see Osinski et al., 2008a; Osinski et al., 2008b and references therein). In other words, large volumes of melt are generated from impacts into volatile-rich targets on Earth (e.g., Graup, 1999; Osinski et al., 2008a; Osinski et al., 2008b; Osinski et al., 2005; Osinski and Spray, 2001) and, by analogy, Mars (e.g., Osinski, 2006).

It is notable that in-depth studies of ejecta deposits around large Martian craters are rare and the production of impact melt on Mars is still debated. One of the few craters to have

received attention is the ~125 × 150 km-diameter Hale Crater, where the ejecta deposits exhibit flow and pond morphologies typically observed around lunar craters (El-Maarry et al., 2013; Jones et al., 2011; Tornabene et al., 2012). A small number of other Martian craters have also been suggested to have preserved impact melt-bearing breccias surrounding the central uplifts and/or terraces, including Holden Crater (Tornabene et al., 2009), Toro Crater (Marzo et al., 2010), Ritchey Crater (Sun and Milliken, 2014), and Elorza Crater (Hopkins et al., 2017).

Of relevance to this investigation is the discovery of widespread crater-related pitted materials (see Tornabene et al., 2012 and references therein). The formation of these pitted materials have been suggested as a result of an impact into a volatile-rich target, with the escape of entrained volatiles eventually leading to the formation of the pitted surface texture (Boyce et al., 2012; Tornabene et al., 2012). The ~150 km diameter Bakhuysen Crater is the oldest and largest crater observed to date that hosts pitted materials as part of the ejecta and interior deposits (Tornabene et al., 2012). Beyond documenting that Bakhuysen Crater contains pitted materials, no detailed analysis has been conducted.

In this study, we present the results of the first detailed geomorphologic mapping and analysis of Bakhuysen Crater with a focus on the ejecta deposits (Fig. 2.1, Table 2.1). As outlined below, Bakhuysen Crater possesses some of the best-exposed impact melt-bearing deposits (as both ejecta and interior pitted material) for a crater >100 km in diameter on Mars. We show that Bakhuysen has two distinct ejecta units that share many attributes of impact ejecta deposits seen around complex craters on other planetary bodies (e.g., Earth, Moon, and Mercury). This provides important constraints as to the origin and emplacement of the Bakhuysen ejecta deposits and, by analogy, ejecta around other large impact craters on Mars. It

is clear that volatiles played a role during, and subsequent to, the emplacement of Bakhuysen ejecta.

2.2 Geologic and regional setting

Bakhuysen Crater is situated in Terra Sabaea (344.4°E, 23.3°S), regionally known as the southern highlands, which has been mapped as the oldest and most heavily cratered surface on Mars (e.g., Werner, 2008). The regional geology has been interpreted as cratered terrains with smooth lava plains, having wrinkle ridges generally overprinted by impact cratering materials, and reworked fluvial and alluvial terrain including valley and channel networks (Tanaka et al., 2014). It is located on a regional slope from the southern highlands toward Meridiani Planum (Fig. 2.1), with the northwestern crater rim being ~1.5 km lower in elevation than the southeastern rim (as measured from Mars Orbiter Laser Altimeter (MOLA); Smith et al., 1999). MOLA elevation data also show that Bakhuysen and its deposits over-print older impact craters and other topography, which is commonplace in the southern highlands terrain (Fig. 2.1). To the southeast of Bakhuysen Crater lies Scylla Scopulus, which is interpreted to be a rift valley related to the Hellas impact event (Grego, 2012).

2.3 Methods

This work presents a ~90,000 km^2 map of Bakhuysen Crater focusing on the ejecta deposits. Mapping of interior deposits have been included with brief interpretations as the understanding of the interior is crucial for interpretation of the ejecta deposits; however, detailed discussion of the interior has been intentionally omitted for brevity and focus. The mapping area is based on nearly full coverage with ~5–6-m/ pixel Context Camera data (CTX; Malin et al., 2007) and 136 individual and stereo pair High Resolution Imaging Science Experiment (McEwen et al., 2007, 2010) ~25–50 cm/pixel images. For the base map we used the

~100m/pixel Thermal Emission Imaging System (THEMIS; Christensen et al., 2004, 2001) daytime thermal infrared (dTIR) Sinus Sabaeus cartographically controlled mosaic; we also used the corresponding THEMIS nighttime thermal infrared (nTIR) controlled mosaic. THEMIS nTIR is useful as a proxy for thermal inertia, with the effects of topography and albedo largely mitigated, giving an indication of the physical properties of the surface materials (Fergason et al., 2006). The THEMIS mosaics were georeferenced in ESRI ArcMap 10.3 to the Mars 2000 geographical coordinate system using a best-fit ellipse, as was the Mars Global Surveyor Mars Orbiter Laser Altimeter (MOLA; Smith et al., 2001) Mission Experiment Gridded Data Records (MEGDRs) ~463-m/ pixel colorized global elevation mosaic. Higher level MOLA-derived data products were produced to aid mapping and interpretation, including a detailed surface slope map. The MOLA-derived slope map was created utilizing vectorized discrete topology data models in ESRI ArcMap. Multi-dataset overlays with THEMIS dTIR and nTIR also aided in mapping, including MOLA-derived global roughness RGB composite products; the MOLA Roughness 0.6 km-baseline composite corresponds to 2, 8, and 32 MOLA shot-to-shot distances, with calculated curvature values binned and correlated to elevation contour maps (Kreslavsky and Head, 2000). The various mapped units were distinguished based on a thermal inertia-proxy for surface roughness (e.g., blocky or hummocky, extent of primary or secondary craters) and texture (e.g., smooth or pitted). The overlay of the various data products guided mapping of the extent of the various ejecta units. Individual quantitative 32-bit THEMIS-derived thermal inertia (TI) stamps (Christensen et al., 2013) were used to aid mapping unit contacts, some of which were well-delineated thermophysically.

Table 2.1. Summary table of location and characteristics of Bakhuysen Crater.

Parameters	Bakhuysen crater characteristics
Location	Terra Sabaea (344.4°E, 23.3°S),
Diameter	~150 km (best fit circle)
Max. relief (rim to floor)	4084 m [1]
Max. relief / diameter ratio (d/D)	0.0272 [1]
Age	Late Noachian – Early Hesperian [2]

[1] Morphometric analyses and data obtained from Mars Global Surveyor Mars Orbiter Laser Altimeter (MOLA; (Smith et al., 2001) Mission Experiment Gridded Data Records (MEGDRs) ~463-m/pixel global elevation mosaic.
[2] Tornabene et al. (2012).

2.4 Geologic and regional setting

Bakhuysen Crater is situated in Terra Sabaea (344.4°E, 23.3°S), regionally known as the southern highlands, which has been mapped as the oldest and most heavily cratered surface on Mars (e.g., Werner, 2008). The regional geology has been interpreted as cratered terrains with smooth lava plains, having wrinkle ridges generally overprinted by impact cratering materials, and reworked fluvial and alluvial terrain including valley and channel networks (Tanaka et al., 2014). It is located on a regional slope from the southern highlands towards Meridiani Planum (Fig. 2.1), with the northwestern crater rim being ~1.5 km lower in elevation than the southeastern rim (as measured from Mars Orbiter Laser Altimeter (MOLA); Smith et al., 1999). MOLA elevation data also show that Bakhuysen and its deposits overprint older impact craters and other topography, which is commonplace in the southern highlands terrain (Fig. 2.1). To the southeast of Bakhuysen Crater lies Scylla Scopulus, which is interpreted to be a rift valley related to the Hellas impact event (Grego, 2012).

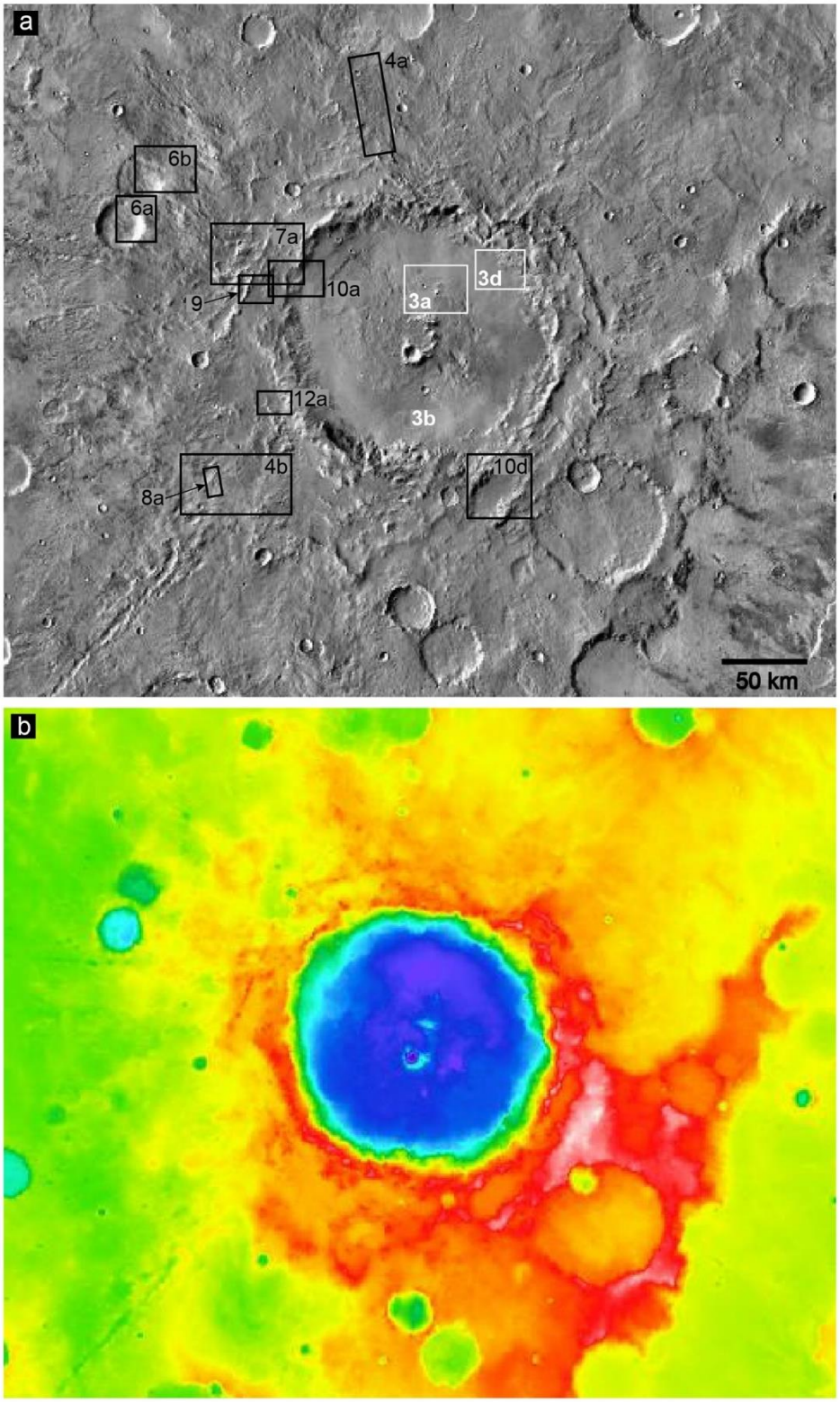

Figure 2.1. (a) Regional context of Bakhuysen Crater on a ~100m- pixel THEMIS daytime thermal infrared (dTIR) mosaic. Boxes indicate the locations of subsequent figures; white boxes

and numbers indicate interior deposits; black boxes indicate deposits beyond or near the crater rim. Note that the area for Fig. 2.3b is too small to be indicated by a box, but the location is shown by the position of the text “3b”. North is up. THEMIS image credits: NASA/JPL/ASU. (b) Regional topography of Bakhuysen Crater and surrounding terrains shown with Mars Orbiter Laser Altimeter (MOLA) ~ 463-m/pixel colorized global shaded relief mosaic. Red and white indicates topographic highs. MOLA image credits: NASA/Goddard Space Flight Center.

The quantitative TI data allowed for thermophysical constraints to be placed on the units based on the bulk numeric TI values; although it should be noted that we mapped the thermophysical properties of the units in relative terms instead of assuming a direct relationship between TI values and grain size. For this study, JMARS (Java Mission-planning and Analysis for Remote Sensing; Gorelick et al., 2003; Christensen et al., 2009) software package and ArcGIS software were used for dataset overlays and production of derived products. Individual images were stretched for a more instructive visual representation of the dynamic range of the data, which assisted in identifying compositional diversity in HiRISE false-color and IR images.

Although spectroscopic analysis is outside of the scope of this study, we used HiRISE false-color images as an indication of general compositional characteristics where such coverage was available. As confirmed through THEMIS, Thermal Emission Spectrometer (TES), and Observatoire pour la Mineralogie, l'Eau, les Glaces et l'Activite´ (OMEGA) spectral data, the HiRISE infrared-red-blue-green (IRB) color composite images exhibit specific colors that generally correlate with ferrous-bearing (Fe^{2+}) mafic materials (e.g., olivine, pyroxenes) and ferric-bearing (Fe^{3+}) altered or hydrated mineral phases (Delamere et al., 2010). Furthermore,

HiRISE IRB data provide additional context that helps to resolve possible morphological ambiguities of grayscale images alone (broadband red wavelength of HiRISE "RED" images).

For morphometric analyses, we primarily relied on Mars Express High Resolution Stereo Camera (HRSC) Level 4 Digital Terrain Model (DTM) data (Jaumann et al., 2007; Neukum and Jaumann, 2004). Six HRSC data products were used, covering all but the north-northeast portion of the ejecta, acquired as GIS-ready GeoTIFFs processed and made available by Freie Universität Berlin and the German Aerospace Center (DLR).

2.5 Observations

Figure 2.2 presents a geomorphological map of Bakhuysen Crater, ejecta deposits, and other features extending outward from the rim. First, the interior deposits are briefly described. In following sections, we focus on the two principal units observed in the ejecta of Bakhuysen Crater: Be1 (Bakhuysen ejecta unit 1) and Be2 (Bakhuysen ejecta unit 2). Other mapped units and features, including rim materials, channels, and associated structures, are described in Table 2.2.

2.5.1 Interior deposits

Bakhuysen crater floor deposits are dominated by pitted materials (p1; Fig. 2.3a), with individual pits having sub-rounded morphology with shared, irregular rims. Concentric crater floor fractures (lf) are also present within the pitted unit (Fig. 2.3a), and appear to be coeval with the pits. The pitted material comprises the stratigraphically lowest unit, with a potential exception of a relatively small (~1–2 km wide) bed- rock exposure (fb) downslope of a terrace ridge (Figs. 2.3b–c). The individual pits of p1 range in size, but are generally <50 m in diameter

(consistent with the pit size observed in Bakhuysen ejecta unit Be2, described in following sections). Much larger pits are observed within the pitted unit as well and are mapped as p2 due to their distinctive size. Unit p2 pits range from ~0.5–4 km in diameter (as measured utilizing the two 0.1 – 0.125 km/pixel HRSC DTMs covering Bakhuysen interior). The bottom of the large pits, particularly in the southeastern crater floor, are often lined with well-formed, dark linear dunes while the walls of the pits have abundant dust devil tracks. Interestingly, the p2 pits are confined to a concentric configuration (see Fig. 2.2) around the incomplete ringed peak cluster central uplift structure. Later materials cover the pitted unit from the crater rim (e.g., Fig. 2.3d), creating both gradual and sharp contacts.

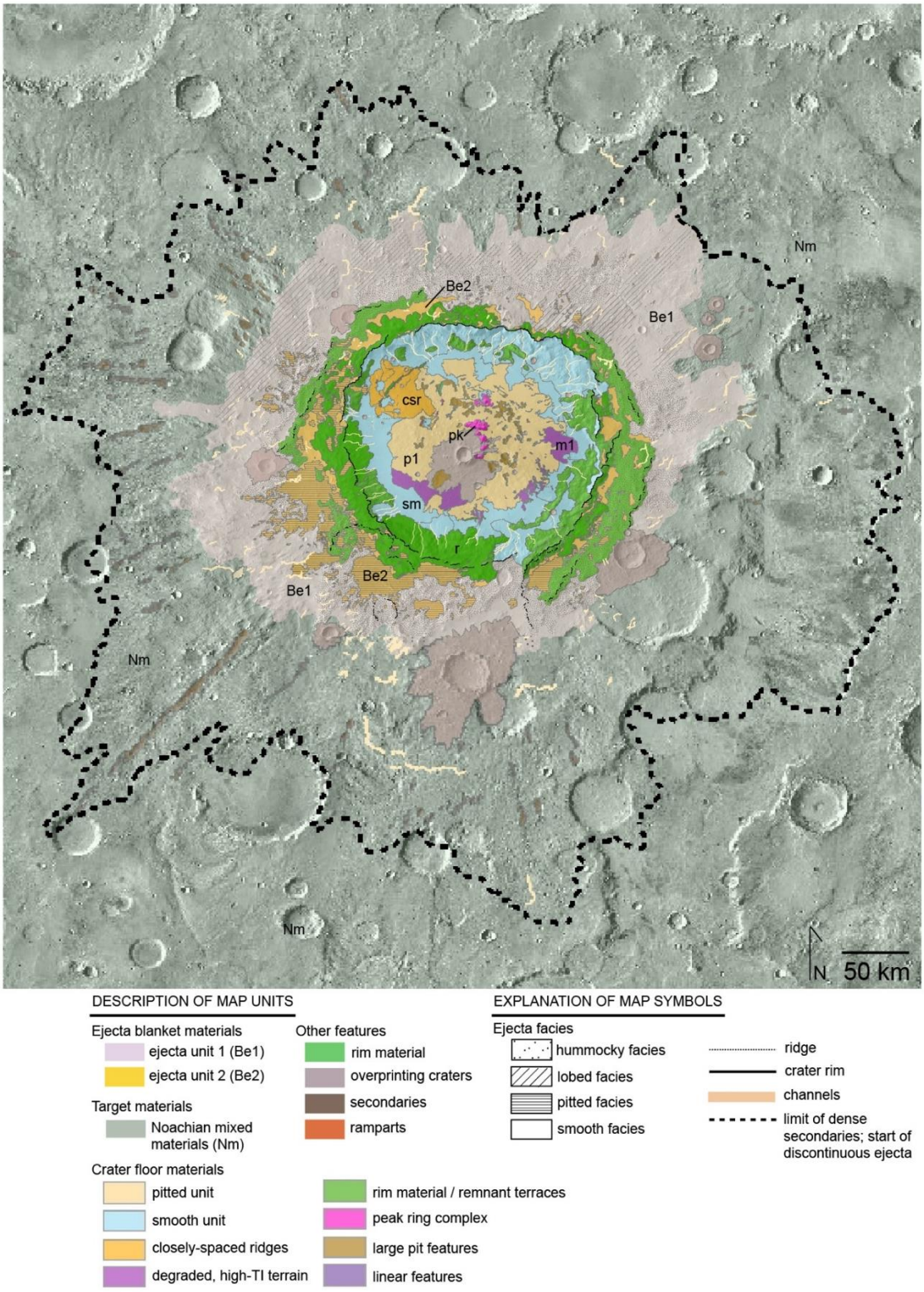

Figure 2.2. Interpretive geomorphological map of Bakhuysen Crater rim and ejecta deposits. The units are mapped at 1:125,000. The base map is a THEMIS dTIR centered on Bakhuysen Crater

(344.4°E, 23.3°S). The regional geology is largely volcanic, having smooth topography with wrinkle ridges, and heavily degraded and altered impact materials with fluvial and basin sedimentary deposits (Tanaka et al., 2014). The two main mapped units are Be1 and Be2 ejecta units, with hummocky rim (r) material, interior deposits, overprinting craters, and channels also included. THEMIS (base map shown here) image credits: NASA/JPL/ASU.

Table 2.2. Description of map units.

Ejecta Blanket Material	**Unit Name**	**Description**	**Interpretations**
Be1	ejecta unit 1; hummocky, smooth, and crenulated facies	Lowermost, continuous unit defined primarily by km-scale regional roughness. Remnant lobes (and sparse potential distal ramparts) are oriented radially from the crater, primarily seen in the NE-E ejecta and more rarely in the SW. Hummocky facies (rocky at CTX –scale (6-m/pixel)), crenulated (semi-lobed) facies, and smooth (less rocky than hummocky facies at CTX-scale) are characteristic (Fig. 2). Channel features are often observed overprinting Be1 and along ejecta unit contacts. *Type locality: 13.598 E, -22.942 (hummocky and smooth facies are present, with cross-cutting channels)*	Represents the continuous ejecta blanket. Comprises the lowermost ejecta layer and was the first layer of ejecta to be emplaced via ballistic sedimentation and radial flow (cf., Oberbeck, 1975). Lobes and multiple facies indicate a variety of flow regimes caused differential emplacement of ejecta. Topographically higher terrain to the SE (between Scylla Scopulus trough and Bakhuysen) appears to have caused a foreshortening of the continuous ejecta. Secondaries are far more extensive in the NW portions of the ejecta.
Be2	ejecta unit 2; pitted and smooth facies	Topmost ejecta unit defined by an isolated, patchy distribution present in topographic lows, having near equipotential surfaces. Pitted and smooth facies are characteristic; pitted facies is dominate in this unit (Fig. 7) which grades into the smooth facies (Fig. 8). The majority of this unit is observed in the SW ejecta where pre-existing craters are present directly outside the crater rim. Occurs at extents of less than one crater radii (up to ~0.7 crater radii). The deposits are limited to ~0–5° slopes. Kilometer-scale lobate deposits of Be2 are seen on slopes of crater rim (Fig. 9). Another flow feature extends tens of kms (Fig. 13). *Type locality: 13.86E, -24.251*	Represents the topmost ejecta deposit and overlies the Be1 hummocky, continuous ejecta. Be2 is interpreted as late-stage flows of melt-rich material emplaced during the modification stage of crater formation (cf., Osinski et al., 2011), having similarities to lunar and terrestrial melt-bearing ejecta deposits (Figs. 12, 13).
Target Materials	**Unit Name**	**Description**	**Interpretations**

Nm	Noachian mixed materials	Smooth surface with some wrinkle ridges. Some areas have a mottled texture. Channels or sinuous depressions cut into Nm, which are overprinted by Bakhuysen Crater deposits.	Early (eNh) and primarily Middle (mNh) Noachian terrains as mapped by Tanaka et al. (2014). eNh is among the oldest Martian crust, consisting mostly of impact breccias and melts, igneous rocks, and some sedimentary sequences. Grabens and rifts are associated with crustal extension, with widespread volcanism concentrated south of the Tharsis region. mNh has a higher proportion of volcanic and sedimentary material, which may reflect climatic conditions allowing for channelization and surface run-off (Irwin and Grant, 2013).
Rim Materials	**Unit Name**	**Description**	**Interpretations**
r	rim materials	Hummocky or blocky textured material (at CTX 6-m/pixel scale) associated with the rim of the crater (Figs. 2, 9a–d).	The structural rim of Bakhuysen is defined by the head of the scarp of the first set of terrace blocks (cf., Robbins et al., 2014). The blocky material was highly fragmented during crater formation and represents slumped blocks of material inside the crater rim and remobilized near-rim ejecta deposits on the outer rim. The hummocky-textured rim unit is mapped to distinguish the structural rim and slump blocks, excluding talus and other smooth rim materials.
Crater Floor Materials	**Unit Name**	**Description**	**Interpretations**
p1	pitted unit	Pitted crater floor unit, found in the topographically lowest portions of the crater floor. Pits have sub-rounded morphology with shared, irregular rims. Concentric crater floor fractures (lf) are also present, apparently coeval with pits. Pits are generally < 50m in diameter and are clustered in groups having similar diameters.	Crater SFD technique applied to the pits (within p1 as well as the pits in Be2 ejecta unit) show that these do not have the typical isochron slopes observed for primary or secondary craters; it is clear the individual pit features are not primary or secondary craters. The pits are interpreted to be a surficial expression of degassing of volatiles which become entrained or overlain by hot impact melt-bearing deposits (e.g., Tornabene et al., 2012). This unit may therefore represent impact-generated melt-rich or otherwise hot, volatile-rich crater fill deposits. This unit appears to be more degraded by wind erosion where it is exposed in the SE crater floor, which is likely responsible for the gradual change in morphology of features in this unit. (See m1 unit, which was also degraded and exposed by wind erosion. Dark aeolian deposits are also concentrated in the SE crater floor.) The extents of this unit are difficult to discern due to post-impact sedimentation, however an exposure of the crater floor (fb) may suggest that the pitted fill deposits generally extended to the lower crater interior terraces.
p2	large pit features	Pits mapped as p1 range from ~0.6 to > 4 km in diameter, measured from pit rim to rim using HRSC 100-125m/pix DTM data. Pit feature morphology defined as circular to irregular rim geometry with steep slopes. Pit bottoms are often lined with well-formed dunes and pit sides often display dust devil tracks, particularly in the SE crater floor. Dense pit clusters with shared rims are common.	These large, concentric pits (Fig. 2) are interpreted here as indicating subsurface structure as described generally by Tornabene et al. (2012). The structure, if it were to be expressed at the surface in the form of uplift, would have formed a ‘proto-basin,’ or transitional peak ring structure (Baker et al., 2011), consistent with other Martian craters of the same size. The peak ring (pk) features are also arranged as an arcuate ridge, likely representing a structure described previously as a 'central peak cluster' or a 'ringed peak cluster' (Baker et al., 2011). Based on the central structures, Bakhuysen likely represents a transition between a peak-ring cluster basin and a proto-basin.
fb	fractured bedrock	A highly fragmented and fractured bedrock exposure (Fig. 3c) is present at the base on a remnant crater terrace, bounded by pitted material toward the crater interior and smooth material from the rim (Fig. 3b).	This unit is potentially an exposure of the crater floor due to post-impact structural modification. (Note that this feature is too small to be visible in map in Fig. 2).
sm	smooth unit	Smooth material at CTX-scale. Talus slopes usually grade into sm, but sm extends from the rim to up to 40 km toward crater center. Unit is the youngest stratigraphically of the	Rim-emanating channels transported variably-sized material to comprise sm unit alluvial fans (Fig. 3d). Alluvial fans generally deposit larger fraction material towards the apex and finer material toward the base, leaving fine tails of

		interior deposits, as it is mapped cross-cutting the main pitted unit (p3), csr, and crater floor channel features (cfc). The gradient of this unit is ~9% as measured with HRSC 100m/pixel DTM data from the break in slope of the rim. Talus material and heavily channeled slopes emanating from crater wall. Some slopes have dust avalanches (slope streaks; type locality: 17.067E, -23.133). At HiRSE-scale, polygonal and boulder features (~10-20 m-scale) are apparent particularly at the distal, flatter reaches of the unit; sm crater wall slopes are smooth even at HiRISE-scale.	material and boulders (Fig. 3e). The polygonal features are tan-colored in HiRISE IRB false-color (which may indicate they are phyllosilicate-rich) and appear to be more competent than the darker intermittent fractures (potentially infilled with basaltic dust) (Fig. 3f). The polygons are interpreted as desiccation features, indicative of the volatile saturation of the sm unit during emplacement of the fans.
csr	closely-spaced ridges	Consists of semi-parallel sinuous ridges, variably spaced at ~ 30m with occasional broader channels or elongate depressions particularly at the lower elevations of unit extents. The unit has an overall lobate shape. The ridges are lighter-toned than the darker, lower-lying intermittent regions. Bulk TI values of 338 for the 39 km^2 sample area of the unit. From the break in slope of the rim materials, the slope gradient of this unit is ~ 5% (as measured with HRSC 125m/pixel DTM data).	The deposit is sourced from the Be2 unit, beyond the crater rim; the material flows down into the crater, forming an overall slumped deposit with pressure ridges (Fig. 15) which are similar to features observed in ejecta flows (Fig. 14e). We suggest this is an impact melt-bearing or otherwise super-heated, volatile-rich impact flow.
m1	degraded, channeled, high TI terrain	Highly degraded unit with sparse, degraded channel features. Layer contact strongly delineated in THEMIS Night IR.	Represents the oldest generation of channel-dissected terrain in crater interior, heavily degraded by wind erosion. Channel features are sparsely present. The layer is observed at various levels of erosion. Thermophysical data sampling suggest compaction and variably-sized coherent material. Emplacement of the crater floor units was followed by a period of heavy aeolian activity which scoured and revealed older bedrock, preferentially in the SE crater floor.
pk	peak complex	Central peak complex.	Represents an incomplete ringed-peak structure (Baker et al., 2011). Sparse smaller mounds outside of the main ringed-peak are located within p1 and p2 clusters, which may represent subsurface structure and a transition to a peak ring morphology.
cfc	crater floor channel features	Channel-like features on crater floor, distinct from linear depression features (ld) features as having higher sinuosity. Cross-cutting relationships are uncertain but the features appear to be most likely cut by the sm unit, having muted morphologies and without obvious sources or drainages.	Sparse, well-formed sinuous channels that are likely fluvially formed. Timing and emplacement are uncertain.
lf	linear fractures	Fracture-like features observed solely in pitted units and appear to be coeval with pits. Together, individual ld features form concentric geometries relative to the crater rim.	Represents concentric crater-fill fractures (Fig. 3a), commonly observed in Martian crater-related pitted material (Tornabene et al., 2012).
Other features		**Description**	**Interpretations**
secondaries		Chains of shallow, herringbone-shaped depressions present in a radial pattern from the crater (Fig. 2). “Dense secondaries” are also mapped by the dashed line to indicate the beginning of the discontinuous ejecta which is mappable. *Type locality: 13.248E, -21.958, 13.25E, -24.073*	The largest secondary crater chains are mapped within the field of secondary craters, which represents the beginning of the discontinuous ejecta. Often, the discontinuous ejecta shows clear pre-existing structures (usually wrinkle ridges) overprinted locally by channels.

overprinting craters	Younger craters which overprint Bakhuysen deposits (Fig. 2).	
ridges	Structural ridges are seen primarily SE and NW of Bakhuysen crater rim and are overprinted by ejecta deposits (Fig. 2).	Concentric ridges bounding the flat areas beyond the Bakhuysen crater rim are not associated with the structural rim of the crater and must be pre-existing. Bakhuysen may be a 'bulls-eye' crater within an older structure. The flat areas between the crater rim and the ridges (as well as the pre-existing craters to the SW) appear to have allowed for a pooling of Be2 ejecta deposits.
channels	Numerous, sinuous – semi-sinuous channel-like features cut Be1 and are seen largely in a radial direction from the crater rim (Figs. 3d–f and 14).	Fluvial networks formed around impact craters have been suggested to have resulted from impact-induced elevated geothermal gradients, the interaction of available water with impact melt sheets, and the mobilization of ground ice and/or groundwater through the kinetic energy of impact events.

Deeply incising, rim-emanating channels lead into talus slopes and smooth crater floor material (sm). In some locations, pitted lobes are present at the crater wall slopes, cross-cut by the smooth material (Fig. 2.3d). The smooth material often terminates in alluvial fans (Figs. 2.3d–e), and widespread polygons and sparse boulders are observed at the distal portions of the fans (Fig. 2.3f). The polygons are generally ~10 m across with dark-toned, recessive boundaries.

The two other crater floor units are stratigraphically between p1 and sm, bounded by the pitted unit toward the crater interior and covered by smooth materials toward the crater rim. The degraded, channeled, high-TI unit (m1) is present in the southeast crater floor. It is apparently a highly erosional surface, observed as isolated outcrops of higher-standing terrain relative to the surrounding units. Dark wind streaks and dunes are also concentrated in the southeast crater floor. In the northwest crater interior, the closely-spaced ridges unit (csr) comprises semi-parallel and sinuous ridge features somewhat uniformly spaced at ~30 m. Slope measurements of crater interior deposits, including csr, sm, and m1 units (acquired with HRSC DTM products). The smooth units have the steepest slopes of the interior deposits at ~ 9% gradients (~5°, where the

slope in degrees is the arctangent of the gradient ratio). The m1 and csr units have much more shallow gradients, at 3% (~2°) and 5% (~3°), respectively.

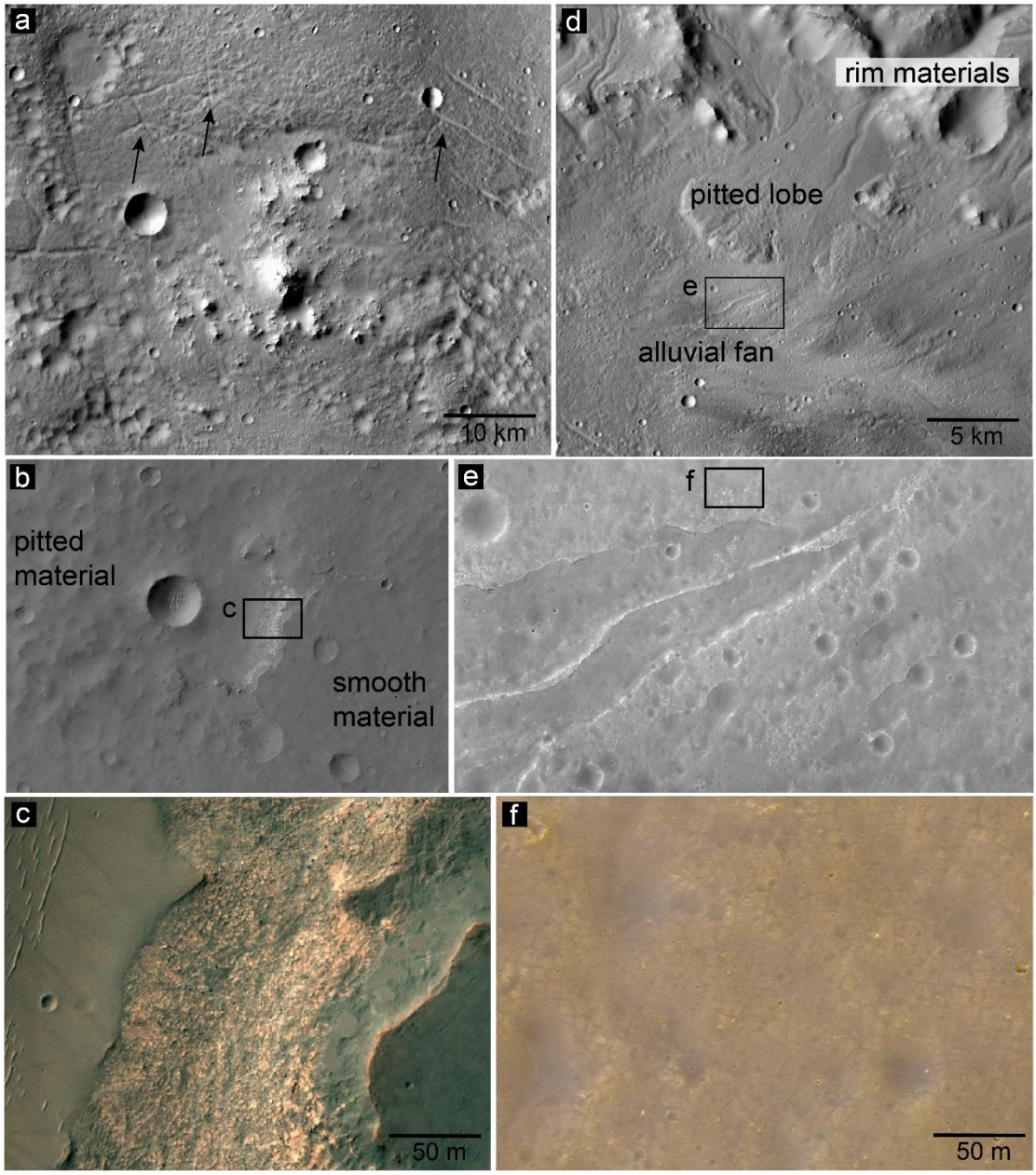

Figure 2.3. (a) Bakhuysen crater floor pitted deposits (p1). Black arrows indicate linear features (ld) that are apparently coeval with pits. (CTX image B16_015984_1569_XN_23S344; CTX image credits: NASA/JPL/MSSS.) (b) Bedrock exposure downslope of a terrace ridge. The higher-standing material at the top of the ridge is smooth material (sm), and the exposure is overlain by pitted material (p1) towards the crater interior. (HiRISE image ESP_044981_1560;

HiRISE image credits: NASA/JPL/UA.) (c) Subset of (b) in HiRISE false-color RBG product (3-bandpass color image consisting of RED, BG, and synthetic blue images) showing brecciation of mostly light-toned materials. (d) Interior crater rim materials, a pitted lobe, and overprinting smooth (sm) alluvial fan are shown on CTX image B04_011382_1575_XN_22S343W. e) From the subset in d, HiRISE image ESP_011382_1575 shows sharp contacts of the tail of the fan. f) Subset of (e) in HiRISE false-color RGB showing the polygonal features and boulders in tail of smooth (sm) fans. Lighter-toned polygons are bounded by darker, recessive features.

2.5.2 Ejecta unit Be1

The Be1 ejecta unit comprises the majority of the continuous ejecta (Fig. 2.2). This unit is defined by a distinctive regional hummocky morphology which is in contrast to the otherwise smooth pre-impact terrain dominated by volcanic materials (Nm). While regionally hummocky (rocky at km-scale based on TI), Be1 unit is sub-divided into characteristic facies, including a general hummocky facies (rocky at m-scale as observed in HiRISE imagery), a crenulated (semi-lobed) facies, and a smooth facies. The Be1 unit exhibits a few degraded ejecta lobes with cross-cutting channels.

Channels are commonly associated with the Bakhuysen ejecta and are observed as cross-cutting Be1 and underlying terrain. Primarily, these are small features, tens of meters across and a few kilometers in length. One channel in the northern ejecta extends >50 km from the near crater rim, cuts into the Be1 unit, and apparently terminates in the topographic low of a crater which pre-dates Bakhuysen (Fig. 2.4a). While ~150 individual channels in and near Bakhuysen ejecta were mapped (Fig. 2.2), the some of the largest channels are observed at the contact

between the two ejecta units (Figs. 2.4b–d); in the southwest ejecta, a deeply incising channel at the contact between the ejecta units cross- cuts Be1 and extends ~70 km into, and beyond, Be1 (Figs. 2.4b–c).

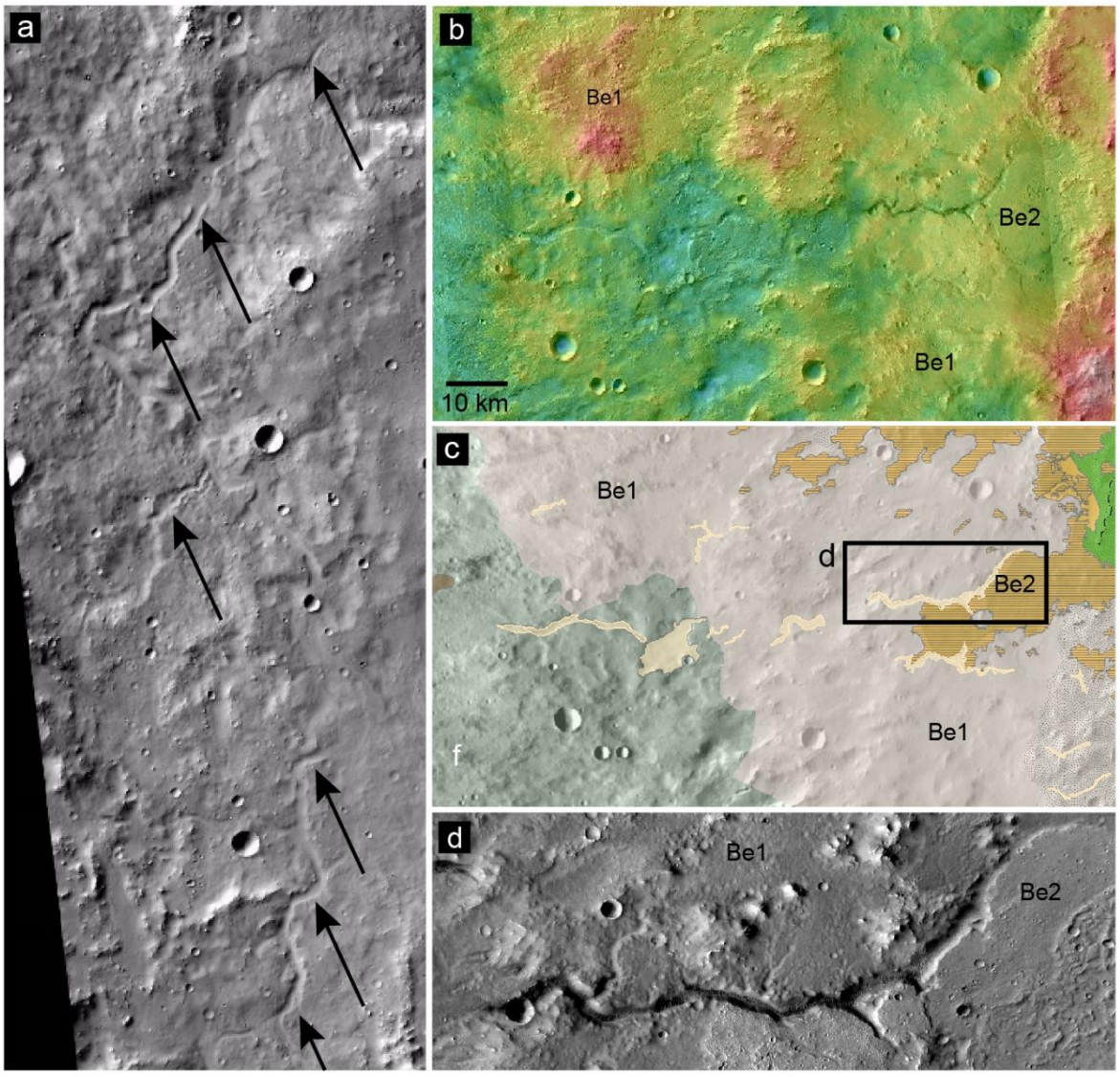

Figure 2.4. a) A ~1 km-wide channel is shown cross-cutting the northern Be1 ejecta unit and extending >50 km into the Be1 unit. See Figure 2.1 for location context. CTX image

B18_016762_1610_XN_19S345W. CTX image credits: NASA/ JPL/MSSS. (b) and (c) The largest channel observed in the ejecta is shown on HRSC DTM (H4174_0000_DT4 ~75m/ pixel) overlay on THEMIS dTIR with accompanying interpretive map. Channels are mapped in peach. The channel is present at a contact between Be1 (mapped in purple) and Be2 (mapped in orange) ejecta units, and extends to an apparent length of ~70 km. See Figure 2.1 for location context and image references. Refer to Figure 2.2 for map units and legend. Black box indicates the location of panel d. HRSC image credits: ESA/ Freie Universitaet and the German Aerospace Center (DLR). THEMIS dTIR image credits: NASA/JPL/ASU. d) Close-up of the channel at the ejecta contacts shown on THEMIS dTIR.

The spatial extent of the Be1 unit was delineated first by large-scale change in surface roughness as seen with MOLA-derived global roughness RGB composite and THEMIS dTIR image overlays. CTX and THEMIS dTIR overlays then guided the finer-scale mapping of the unit extent. The Be1 ejecta displays an obvious, kilometers-scale roughness due to the hummocky nature of the unit (Fig. 2.5a). In general, the surface of Be1 becomes smoother with increasing radial distance, where the dense field of secondaries are present in the discontinuous ejecta. The well-formed secondary crater chains, which begin roughly at the mapped extent of Be1, extend radially outward from and are relatively well-distributed around Bakhuysen though are denser in the north-western ejecta. The hummocky nature of the Be1 terrain is also seen in terms of slope variations, as derived from MOLA at the ~463-m/pixel scale (Fig. 2.5b). As seen in Figure 2.5, the change in both roughness and slope with distance from the crater rim correlate to demarcate the extent of the Be1 ejecta unit. (Although the smooth facies characterizes a

portion of the Be1 unit, it is defined as smooth at the m-scale yet within the broader, km-scale hummocky expression of the unit; this is demonstrated in Figure 2.5a.) Be1 is not thermophysically distinct from the over- printed terrain, though the thermophysical contrast between Be1 and the ejecta unit which overlies it (Be2; Figs. 2.5c–d) is stark, as discussed in later sections.

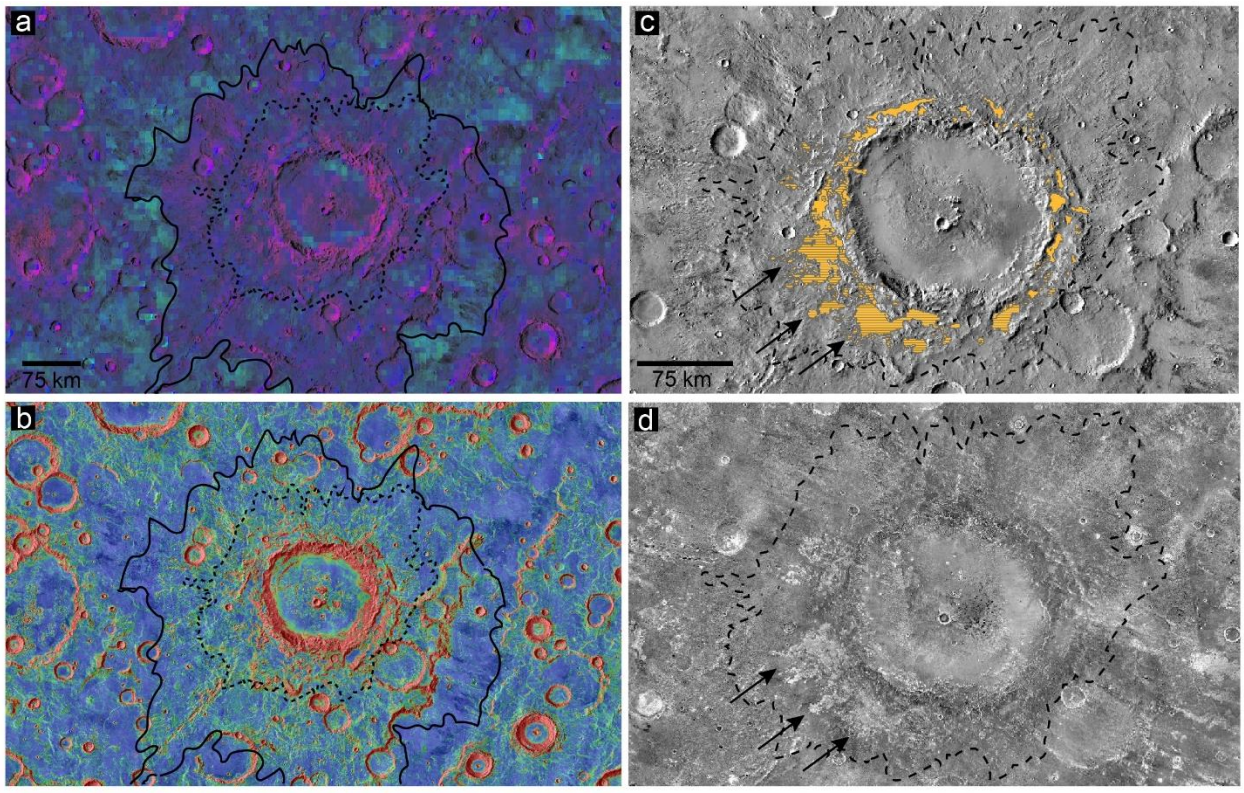

Figure 2.5. a) MOLA Roughness 0.6 km-baseline RGB composite map (Kreslavsky and Head, 2000) centered on Bakhuysen Crater. Pinks and purples indicate rough terrain; green-blues indicate smoother terrain. A local color stretch was applied. Interior dashed line represents the continuous ejecta (Be1) extent; outer solid line indicates the dense secondaries field and transition to discontinuous ejecta. Note that Be1 is consistently rough due to its hummocky

nature; Be2 has large flat areas (smooth terrain) though the well-formed secondaries appear as rough features. b) MOLA-derived slope map, with blue areas indicating slopes ~ <3° (see Methods section for more information) and red areas indicating slopes ~ >14°. The terrain is generally more flat in the discontinuous ejecta. Note also the correlation between the near-rim topographic lows (blue) in the south and southwest and the mapped Be2 unit (panel c). c) THEMIS dTIR with mapped Be2 ejecta unit overlay in orange with dashed line representing the continuous ejecta (Be1) extent. Be2 deposits have excellent correlation to bright white areas observed in the THEMIS nTIR mosaic (panel d). The best exposures of Be2 is indicated by black arrows. THEMIS image credits: NASA/JPL/ASU. d) THEMIS night thermal inertia mosaic (nTIR) mosaic showing Bakhuysen Crater and near ejecta, where bright white region correlate well to the Be2 unit as shown by black arrows. North is up in all images.

A broad, ~10 km-wide deposit is observed ~85 km northwest of Bakhuysen crater rim and ~15 km outside of the mapped extent of Be1, into the discontinuous ejecta. As seen in Fig. 2.6a, channelized features are observed above the rim of an existing ~25 km-diameter crater, leading to a flow of material into the crater and broad, lobate deposits covering approximately a quarter of the crater floor. HiRISE color (Fig. 2.6c) and anaglyph data products show that the distal portions of the larger flow deposit are light-toned with polygonal fractures. The crater wall above the deposit is deeply incised with levees at the lateral margins (Fig. 2.6d). Another ~25 km-diameter crater to the north (See Figure 2.1 for context boxes) also has narrow channel features cutting the degraded crater rim (Fig. 2.6b). The flow deposit and channels are only observed on the sides of the craters nearest to Bakhuysen rim.

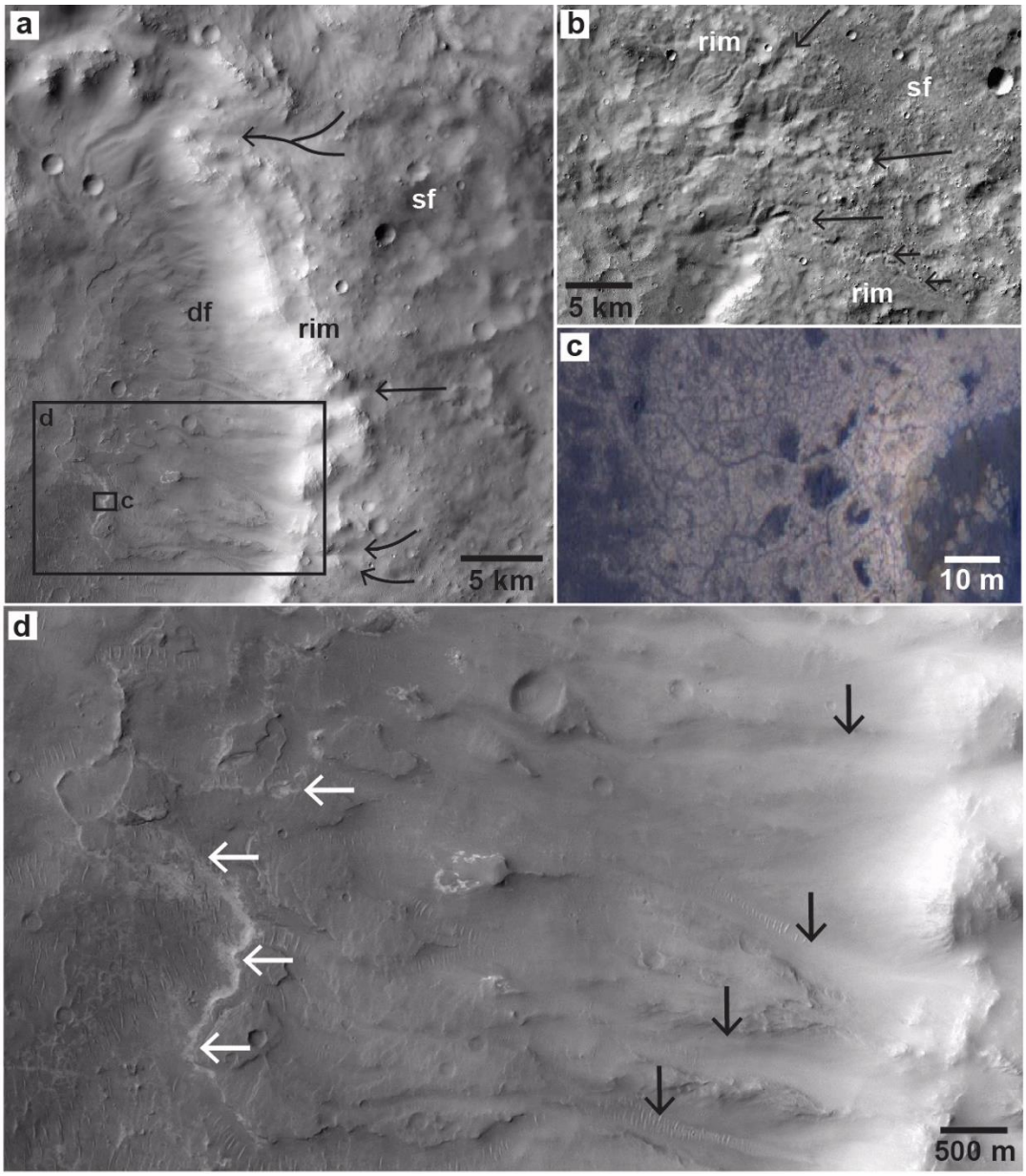

Figure 2.6. a) Distal flow covers the wall and floor of a pre-existing ~25 km-diameter impact crater located ~85 km northwest of Bakhuysen Crater rim in the discontinuous ejecta. Flow directions indicated by black arrows, where the eastern crater rim was breached, shown on CTX image F03_036937_1577_XN_22S347W. Black boxes are given for context for panel d. See Figure 2.1 for location context of this panel. CTX image credits: NASA/JPL/MSSS. b) Another ~25 km-diameter crater nearly overlaps the crater shown in panel a. See Figure 2.1 for location

context. Black arrows indicate channels in the crater rim and wall. c) Close-up of the light- toned extents of the deposit in panel a, shown in HiRISE image ESP_045957_1575 false color IRB. Polygonal features are apparent in the light-toned material. d) Close up of the flow seen in panel a shown in HiRISE image ESP_045957_1575. White arrows indicate the light-toned deposits at the extent of the flow. Black arrows indicate the deeply incised crater wall. HiRISE image credits: NASA/JPL/UA.

A 3 km-diameter crater excavated into the Be1 ejecta unit ~30 km northwest of Bakhuysen crater rim and may provide a unique exposure of Bakhuysen ejecta material (Fig. 2.7a). The southern wall of the crater is well-exposed and shows a highly fractured light-toned block ~100 m across (Figs. 2.7b–c). The block is exposed at ~80m depth from the current surface. Smaller fragments (~5 m-wide) of light-toned brecciated material are also observable in the crater wall at depths of up to ~100 m.

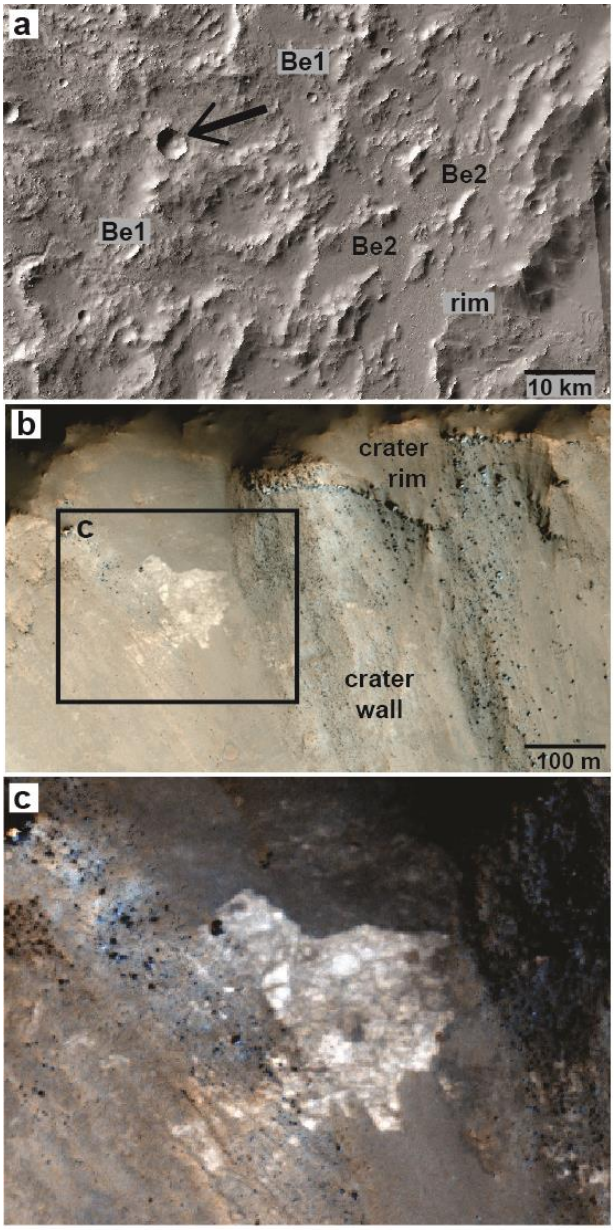

Figure 2.7. a) Black arrow indicates a ~3 km-diameter crater within Be1 ejecta unit, ~30 km northwest of Bakhuysen crater rim shown on CTX image mosaic: B18_016617_1562_XI_23S345W, D15_033258_1562_XN_23S345W, G22_026744 _1589_XN_21S346W, G21_026533_1573_XN_22S345W, B17_016195_1563 _XN_23S345W. See Figure 2.1 for location context. CTX image credits: NASA/JPL/ MSSS. b) Wall of the ~3 km-diameter crater indicated in panel a shown with HiRISE ESP_044902_1575 false-color

RGB. A ~100 m wide, light-toned and apparently highly fractured, possibly monomict block is observable in the crater wall. Down is north. Black box inset shows location context for panel c. c) HiRISE ESP_044902_1575 false color RGB image is stretched to optimize the color contrast and show the fractured texture of the block. Other potential, smaller block fragments of various sizes may be in the crater wall but are at the limit of resolution. HiRISE image credits: NASA/JPL/UA.

2.5.3 Ejecta unit Be2

The topmost ejecta unit, Be2, is defined by an isolated, patchy distribution of deposits having near-equipotential surfaces, are present in near-crater rim topographic lows, and have a dominantly pitted texture (Figs. 2.2 and 2.4c–d). The contacts with the underlying Be1 unit are generally sharp (Fig. 2.8); the stratigraphic superposition of Be2 is apparent in Figure 2.8c. Pitted and smooth facies are present. The dominant pitted facies is characterized by ubiquitous pit features that are clustered with shared, irregular rims and a sub-rounded morphology (Fig. 2.8). The pit walls do not always form a distinctive closed depression and the pits are often elongate (not perfectly circular). HiRISE IRB false- color imagery (Fig. 2.8b) of the pitted Be2 material shows that the pits are generally yellow-orange along rims with intermittent blue-gray material in between them. The individual pits range in size but are most frequently ~60 m in diameter. The pitted facies grades into the smooth facies (Fig. 2.9).

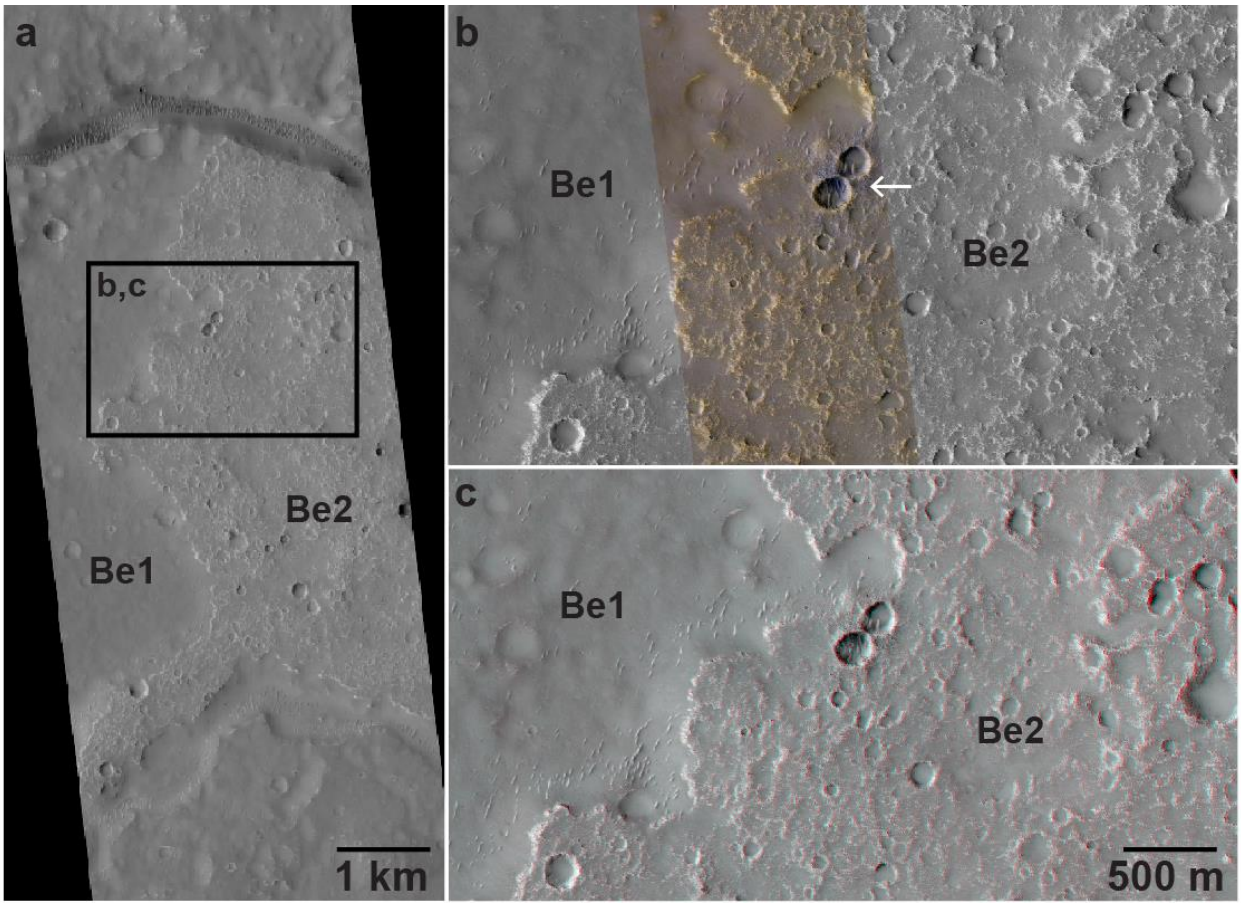

Figure 2.8. Images showing the sharp contact between ejecta unit Be1 and overlying Be2 ejecta unit. North is up in all panels. See Figure 2.1 for location context. a) Image showing a subset of the best preserved, most extensive deposit of the Be2 unit. HiRISE image ESP_031056_1555. b) The typical pit morphology of Be2 pitted facies shown with HiRISE ESP_031056_1555 false-color IRB data. (This products is a 3-bandpass image consisting of IR, RED and BG data; in this product, mafic or ferrous-bearing materials can appear blueish, and ferric materials, like dust, often appear yellowish). The pit rims are generally tan-orange with adjacent, intermittent blue-gray mate- rial. Pit interiors are generally blue-gray. Two relatively fresh overprinting primary impact craters are also seen in the Be2 unit, indicated by white arrow, having bright blue ejecta around the crater interiors and rims. c) Stratigraphical superposition is well observed in the

HiRISE anaglyph pair (ESP_031056_1555_ESP_031201_1555). HiRISE image credits: NASA/JPL/UA.

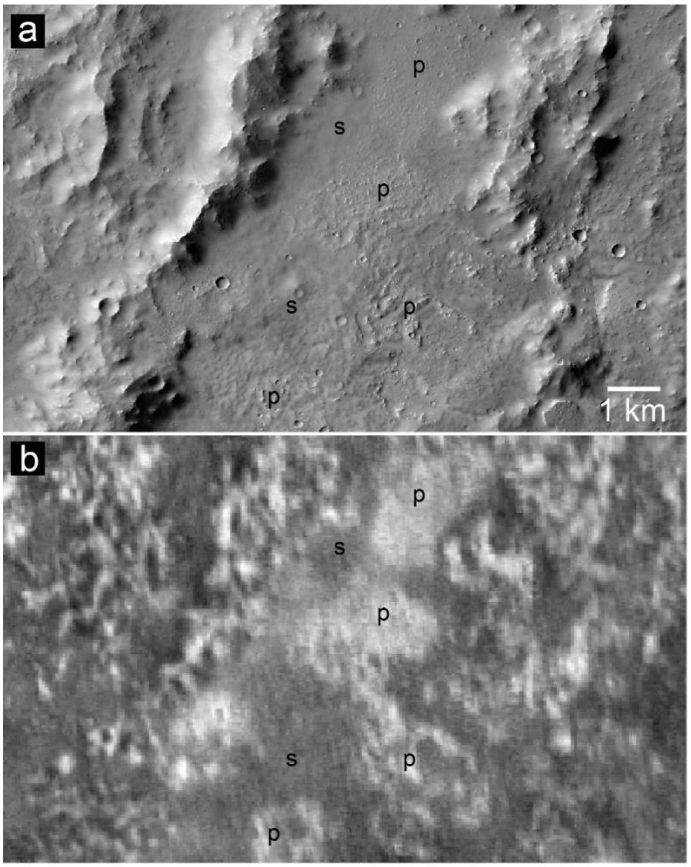

Figure 2.9. a) The smooth (s) and pitted (p) facies of Be2 is shown in a topographic low just outside the crater rim. See Figure 2.1 for context. While the pitted facies dominate this unit, locally, pockets of pitted material are separated by smoother regions with gradational contacts. Shown on CTX-D15_033258_ 1562_XN_23S345W; CTX image credits: NASA/JPL/MSSS. b) The pitted facies of Be2 correlates very well with THEMIS nTIR, seen as bright white. The same extents are shown in both panels. Note the smooth facies are dark in THEMIS nTIR, generally

indicating that this material is finer grained or less consolidated. THEMIS image credits: NASA/JPL/ASU.

The Be2 unit is most prevalent in the southwestern portion of the ejecta (Figs. 2.2 and 2.4c–d). Elevation profiles derived from HRSC data (~50–125 m/pixel) indicate that the best-preserved Be2 pitted facies, including a ~25 × 10 km^2 deposit, occupies pre-existing circular depressions (see Figs. 2.1b and 2.5c). Most Be2 deposits occupy topographic lows and exhibit a near flat surface as seen in MOLA-derived slope map of the ejecta (slopes < ~3°; blue regions in Fig. 2.5b). In this way, the Be2 unit can be described as "ponded". Within these ponded deposits, both pitted and smooth textures are present, at HiRISE (~25–50 cm/ pixel) and CTX (~6 m/pixel) scales (Fig. 2.9), which we mapped as two different facies of the same unit. The pitted facies comprise the majority of Be2, with pockets of pitted material locally separated by smoother regions by gradational contacts (Fig. 2.9). The margins of Be2 were delineated based primarily on MOLA-derived slope data, as both the smooth and pitted facies are relatively flat, largely present in the near- rim ejecta between the rim and preexisting ridges outside of the crater rim (Fig. 2.2, Table 2.2).

The Be2 unit contrasts with the dominantly hummocky texture of Be1 which it overlies; Be1 has a range of variable slopes up to ~>14° (Fig. 2.5b). The contacts between the two main ejecta units are strongly delineated in THEMIS nTIR, where Be2 deposits correlate very well to a higher thermophysical signature relative to unit Be1 (Fig. 2.4). There is a bulk TI difference of

$\sim$40 J m$-$2 K$-$1s$^{-1/2}$ (based on THEMIS Quantitative TI data). Correlation between THEMIS nTIR and Be2 is shown in Figure 2.5d.

In two locations, lobate-shaped deposits of Be2 are observed on either side of the crater rim (Fig. 2.10). They can be traced to larger "ponds" of Be2 pitted material, which then flowed from the topographic high of the rim. These km-scale (1–5 km-wide) deposits appear to be degraded, so the shape is difficult to discern with visible imagery. However, they are bright in THEMIS nTIR (e.g., Figs. 2.10a and 2.10d) where the lobate shape is more apparent.

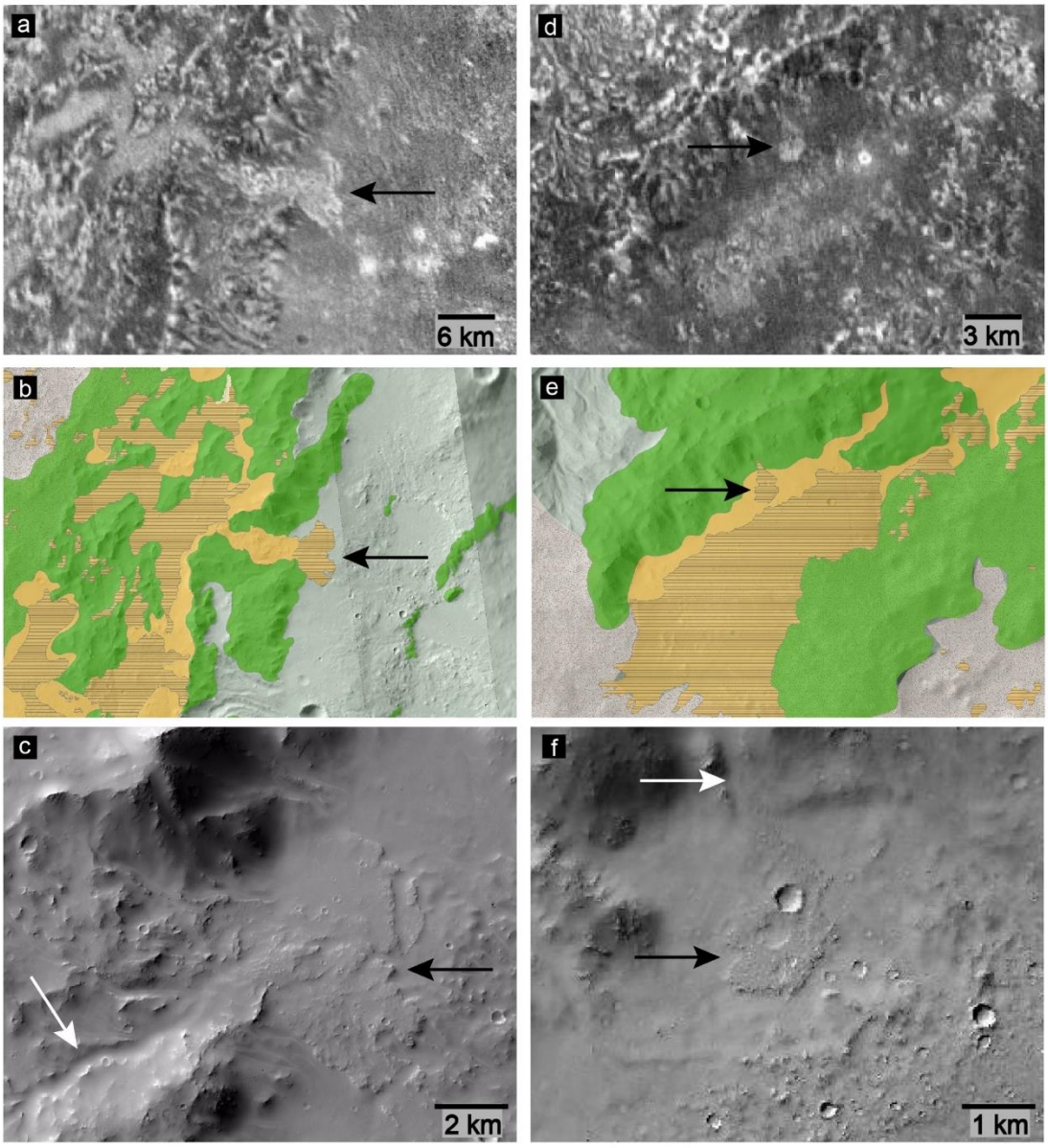

Figure 2.10. a) and (b) THEMIS nTIR mosaic, showing Be2 deposits as relatively bright white, and corresponding geomorphological map of Bakhuysen rim shown on CTX image B18_016617_1562_XI_23S345W. Mapped units include rim materials (green) and Be2 deposits (orange) with pitted facies shown with a lined texture. The ponded Be2 ejecta deposits shown are topographically above the lobate deposit, outside of the crater rim, also seen as bright white in panel a. See Figure 2.1 for location context. THEMIS image credits: NASA/JPL/ASU. c) Zoom

image of the lobate deposit in panels a and b shown on HiRISE image ESP_048950_1575. White arrow indicates a channel. HiRISE image credits: NASA/JPL/UA. d) and (e) CTX image F20_043781_1554_XN_24S343W and corresponding geomorphological map of crater rim material (green) and Be2 ejecta (orange) with pitted facies indicated by lined texture. A lobate, pitted deposit is observed on the southern slope of Bakhuysen crater rim. Black arrows indicate same location in both panels. See Figure 2.1 for location context. (f) Zoom image of the lobate Be2 deposit in panels d and e shown on HiRISE image ESP_043781_1555.

The pits of the pitted facies of Be2 are morphologically distinct from impact craters, and we provide a quantitative analysis on the size-frequency distribution to test this distinction. As part of this study, we quantified the size and distribution of the pits to assist in determining their origin. Individual pits within the pitted facies were counted and binned. To determine if they were primary impact craters, we compared the size-frequency distribution results to previous crater counts within Bakhuysen interior pitted deposits (Tornabene et al., 2012). The pits were differentiated from overprinting craters based on pit morphology including sub-rounded and shared rims, clustering of same-sized pits, and lack of ejecta material and upraised rims (see also Tornabene et al., 2012). Pits in three 2.5 km^2 rectangular areas in the pitted facies of Be2 ejecta were mapped using CraterTools and CraterStats (Kneissl et al., 2011) ArcMap add-in tools (http://www.geo.fu-berlin.de/en/geol/fachrichtungen/planet/software/), for a total mapped area of 7.5 km^2 area. The digitized pits were then plotted in a logarithmic, cumulative chart which is normalized to the measurement area, shown in Fig. 2.11, overlain on a Hartmann-style incremental diagram with previous Bakhuysen interior deposit crater counts (Tornabene et al.,

2012). The pits have a size range of 30 to 100m in diameter. When compared to general crater distributions, the pits have a very narrow size range and are far smaller, more numerous, and generally more clustered. Fig. 2.11 shows that these pits plot at and above geometric saturation level on a size-frequency plot.

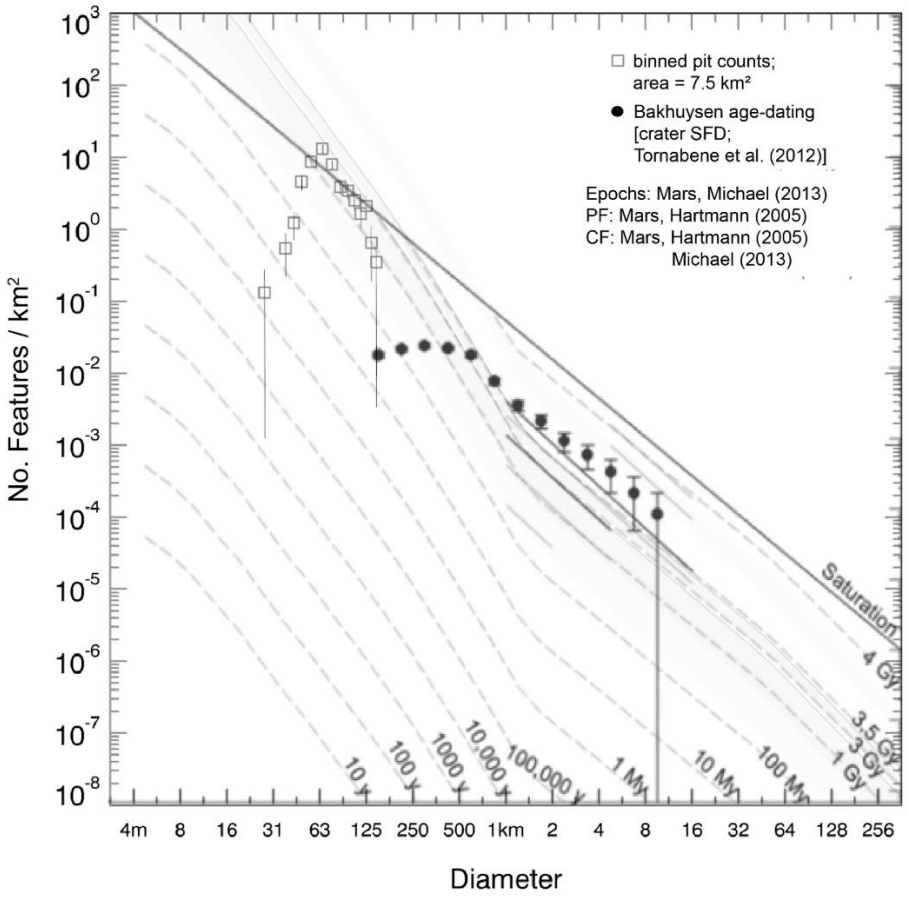

Figure 2.11. A Hartmann-style log diagram with incremental isochrons (Hartmann, 2005), showing a modeled crater retention age for Bakhuysen interior pitted deposits (Tornabene et al., 2012) as black, filled circles. The white squares show the pit-size frequency distribution, gathered by similar means. Both the digitized pits and the age-dating craters were plotted in a logarithmic, cumulative chart which is normalized to the measurement area. The pits were

binned as described by Neukum (1983) and Hartmann and Neukum (2001) with calculated error bars as described by Kneissl et al. (2011).

2.6 Interpretations and Discussion

In the following sections, we discuss the two major units comprising Bakhuysen ejecta in terms of their relative stratigraphic relationships and surficial textures as well as their morphological and thermophysical properties. Interior deposits are briefly discussed as they relate to the ejecta deposits and the overall formation and evolution of deposits in and near Bakhuysen. In terms of classification, we note that Bakhuysen ejecta morphology has been previously classified by Robbins and Hynek (2012) as "radial" (Rd) and by Barlow (2017) as "single layer ejecta with radial pattern" (SLERSRd) in their global catalogues. This contribution provides the first detailed study of the ejecta deposits of the Bakhuysen Crater, which clearly shows that Bakhuysen ejecta morphology is more subdued and eroded compared to younger, better- preserved ejecta on Mars (e.g., Tooting Crater; Mouginis-Mark, 2015; Piatek et al., 2016). As demonstrated above and as discussed further below, Bakhuysen possesses two layers of ejecta, one being continuous (unit Be1) and one discontinuous (unit Be2). We use the observed characteristics for comparison of the ejecta units to potentially similar deposits on other rocky bodies to place constraints on their emplacement.

2.6.1. Unit Be1

The predominantly hummocky expression and distribution of the Be1 unit is consistent with deposits produced by ballistic sedimentation and radial flow, where a turbulent, ground hugging flow of ejected material is emplaced radially around the crater (Hörz, 1982; Hörz et al., 1983; Oberbeck, 1975). The radial component of the flow terminates in degraded lobes having variable runout distances from the crater rim. The presence and distribution of the Be1 facies (hummocky, semi- lobed, and smooth) suggest local differential emplacement, perhaps due to interaction with pre-existing topography or near-surface materials, or a variation in the composition of the exhumed materials. Distal ejecta flows (Fig. 2.6) are suggestive of relatively thin ejecta deposits behaving as a ground-hugging flow at distances of ~1 crater radii, infilling preexisting depressions and forming streamlined deposits. Be1 ejecta deposits appear to have been foreshortened by pre-existing topography in the southeastern quadrant (e.g., Figs. 2.1 and 2.2), where lobes and distal flows are absent.

The distal ejecta flows observed in the northwestern portion of Bakhuysen ejecta (Fig. 2.6; See Fig. 2.1 for context) are in a region of apparent transition from continuous (Be1) to discontinuous, distal ejecta. Large chains of secondaries with well-preserved herringbone-patterns emerge beyond Be1 as the unit thins, but some buried secondaries are apparent beneath Be1. Thinning of the Be1 unit indicates the advanced erosion and thus gradational boundaries of the ejecta. The distal flows are interpreted as having been emplaced as primary ejecta deposits, and may indicate entrainment of volatile-rich target material into the ejecta flow. This was also the interpretation of distal ejecta flows from Hale Crater, which are morphologically comparable to the distal flow observed in Bakhuysen, showing streamlined features and distinct leveed lateral margins, terminate in multilobate forms, and pool in low-lying pre-existing craters (Grant and Wilson, 2017). Grant and Wilson (2017) suggested that these flows are present at Hale as a

result of a substantially ice-rich pre-impact target, with dewatering of excavated and entrained materials of the ejecta. Such entrainment in ejecta flow has been evidenced by deposits of the terrestrial Chicxulub impact structure.

The Chicxulub impact structure offers a good terrestrial comparison to the morphologies observed in Bakhuysen continuous ejecta. Field investigations of the Chicxulub ejecta deposits showed that shear localized in bedding plains of rapidly stacking ejecta deposits transition from a turbulent flow to friction-controlled flow (Kenkmann and Schönian, 2006). The Coulomb friction rule describes intergranular shear stress on these planes in mass movement flows, with pore-fluid pressure acting locally to reduce friction and enhance fluidization (Iverson and Vallance, 2001). Therefore, incorporation of clay-rich target material into the ballistic Chicxulub ejecta during deposition enhanced fluidized flow, moving ejecta-entrained materials to much greater distances that would be accommodated by dry, volatile-poor bedrock (Schönian et al., 2004). The flows slowed variably throughout the ejecta and resulted in lobe and rampart formation (Schönian et al., 2004). This suggests that at Bakhuysen, the ejecta runout is likely due to variable entrainment of target material, potentially including volatile-rich target material, as well as effects from pre-existing topography.

Osinski (2006) and Barlow et al. (2007) describe continuous ejecta blankets observed on Mars as being analogous to the Bunte Breccia at the Ries impact structure, Germany, which is comprised of shocked and unshocked allochthonous clasts of target materials. A key characteristic of the Bunte Breccia is the unsorted nature and the presence of ~25 m to 1 km-sized blocks, transported up to ~35 km from the Ries crater rim (Pohl et al., 1977). The Be1 terrain at Bakhuysen is also hummocky or blocky at the meter to kilometer scale and we have documented an exposure of megablocks (up to ~100 m wide) in the wall of a super- posed crater

(Fig. 2.7) ~30 km from the rim of Bakhuysen. We suggest that the megablocks represent Bakhuysen ejecta that was later exposed, presenting a unique opportunity to observe ejecta blocks in such detail as they are rarely observed on Mars. Another notable example of impact megablocks has been observed in Hargraves Crater ejecta, exposed in Nili Fossae through crustal deformation and erosion (McEwen et al., 2010).

2.6.2. Unit Be2

2.6.2.1 Pitted material

The characteristic feature of the best preserved Be2 deposits is the pitted texture (Fig. 2.8). We suggest that the pits were formed syn-impact and furthermore are consistent with widespread crater-related pitted material as previously described (Boyce et al., 2012; Bray et al., 2009; Jones et al., 2011.; McEwen et al., 2007; Mouginis-Mark et al., 2007; Tornabene et al., 2007, 2012) based on the pit morphology, pond-and- flow emplacement of the unit, and stratigraphic superposition. The ubiquitous pits in the Be2 unit were distinguished from primary or secondary impact craters due to a characteristic lack of ejecta, shared pit rims that are semi-circular to polygonal (and in some cases, coalesce to form linear features), roughly consistent pit diameters at local scales, and are often observed as pit clusters. The distinctive morphology of these pits is also as observed in the pitted unit of the crater interior. Figure 2.11 shows the pits in the ejecta unit and crater interior unit plotted against crater counts of Bakhuysen deposits, showing that the pits can be clearly distinguished from impact craters based on their density and clustering; Figure 2.11 demonstrates that these features are at, or above, geometric saturation level, implying that if these features were impact craters, the surface of the assessed unit would have a model age that is over ~4 Ga. However, the pitted ejecta unit overlies material that is

clearly not saturated in craters (e.g., Fig. 2.8). This is consistent with the pitted features being a primary texture of the impact-related deposits, and not impact craters.

In the best exposures of Be2, in the southwestern ejecta, Bakhuysen pitted ejecta deposits are clearly more than just a thin coating, having deep pits and relatively well-defined pit rims (e.g., Fig. 2.8). The pits themselves are generally better defined than those observed in association with other Martian impacts, and may represent a highly eroded end member of Martian crater-related pitted deposits. The pit rims are excellently exposed and generally free of overlying aeolian bedforms; the pit interiors are however somewhat infilled with dunes which obscure the bedrock of the pit floors (Figs. 2.8b–c). This is shown in HiRISE false-color IRB color (Fig. 2.8b), where the rims have a spectral characteristic that is distinct from the bulk of the unit and the material between the rims, indicating a potential compositional or mineralogical difference. Bedrock exposure of the pit rims is consistent with the increased quantitative THEMIS TI values with respect to the underlying Be1 unit (Fig. 2.5d). Crater-related ponded, pitted materials generally are observed as having a relatively low TI compared to their surroundings as the low-lying deposits and pits themselves act as traps for aeolian deposits (Tornabene et al., 2016). While the ponded, pitted deposits in Bakhuysen ejecta (Be2) exist in regional topographic lows (Figs. 2.1b and 2.4b), they are now subtly elevated through the erosion of surrounding, less resistant units, as seen in the HiRISE anaglyph in Figure 2.8c. This is in stark difference to the Be2 unit in the northeastern ejecta (Fig. 2.2), which is dominated by the smooth facies having intermittent pitted material, comparatively low TI, and no evidence of erosion by wind activity as observed in the southwestern pitted facies. The smooth facies could represent dust or otherwise covered pitted deposits which would explain the gradational contact between pitted and smooth textures (e.g., Fig. 2.9), though pits may not have been formed at all

in the smooth facies. We further suggest that exposure of the pitted facies, and indeed a unique exposure of crater-related pitted material, are a product of scouring through wind erosion. Despite the potential degradation state of the deposits at Bakhuysen, the pitted facies of unit Be2 are most consistent with being crater-related pitted material as seen in other well-preserved Martian craters as described by Tornabene et al. (2007a, 2012), Marzo et al. (2010), Morris et al. (2010), Jones et al. (2011), and El-Maarry et al. (2013).

Previous studies have shown that crater-related pitted materials, having a range of degradation states, display both ponded and flow-like morphologies and infill topographic lows in crater interiors and the proximal ejecta blankets on Mars (e.g., Tornabene et al., 2012). Mojave, Tooting, and Hale craters represent the best-preserved pitted deposits thus far observed, with pitted flows interpreted as originating from the ponded deposits (Jones et al., 2011; McEwen et al., 2007; Morris et al., 2010; Mouginis-Mark et al., 2007; Tornabene et al., 2007, 2012). Figure 2.12 shows a comparison of pitted materials with the best-preserved examples of ponds and flow-like morphologies in Mojave, Tooting, and Hale craters to Bakhuysen Be2 deposits. Though the pits in these examples are remarkably similar, morphologic variances are likely due to differential degradation and impactites themselves influenced by variable target materials. Tornabene et al. (2012) concluded that the flow features and topographic controls of impact-related pitted material associated with impact craters on Mars was most consistent with volatile-rich impact melts based on the distribution, morphology, and textures of ponded deposits.

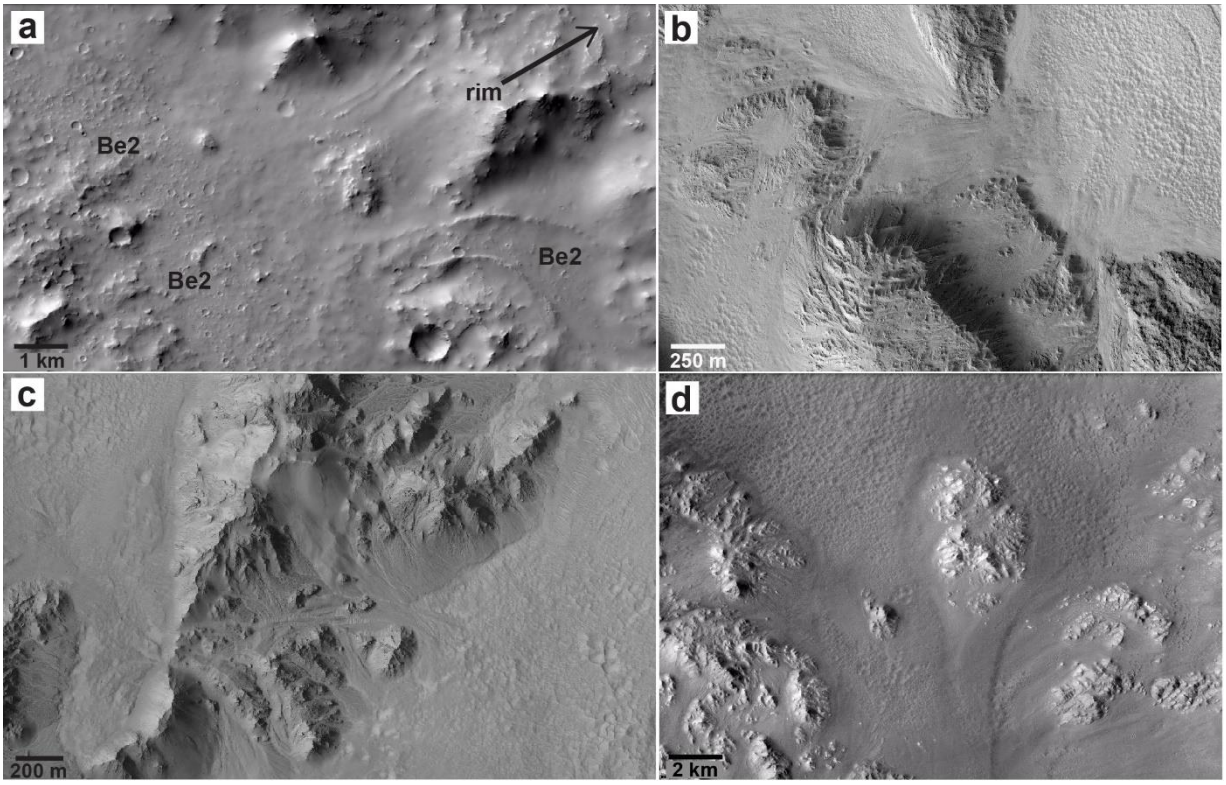

Figure 2.12. a) Bakhuysen Be2 deposits with degraded flow features and pitted flows downslope from crater rim. CTX image B18_016617_1562_XI_23S345W. See Figure 2.1 for context. b) Tooting Crater pitted flows, originating from ponded, pitted deposits in the crater interior. HiRISE image PSP_005771_2035. HiRISE image credits: NASA/JPL/UA. c) Mojave Crater pitted flows, originating from ponded, pitted deposits in the crater interior. HiRISE image PSP_002167_1880. d) Hale Crater pitted flows, originating from ponded, pitted deposits in the crater interior. CTX P05_002932_1445_XI_35S035W. CTX image credits: NASA/JPL/MSSS.

2.6.2.2 Be2 classification as an impact melt-bearing deposit

The presence of ponded impact melt stratigraphically above the continuous ejecta blanket has been observed as a common ejecta morphology around many lunar and terrestrial craters (e.g., Bray et al., 2010; Hawke and Head, 1977; Osinski et al., 2011). An excellent lunar example is in the ~83 km-diameter Tycho Crater, which has numerous isolated ponds and flows of impact melt (Fig. 2.13a). Importantly, the final emplacement and remobilization of lunar impact melt is described as being largely dependent on pre-existing topography (Bray et al., 2010; Neish et al., 2014; Krüger et al., 2016; Morris et al., 2000). The stratigraphic relationship of melt-rich and melt-poor to melt-free breccias has also been observed terrestrial ejecta deposits, as seen at the Ries impact structure, Germany (Fig. 2.13b). Although small-scale mixing occurs as the flows entrain materials during transport, large-scale mixing does not occur between the ejecta layers around lunar (Hörz et al., 1983; Osinski et al., 2011) or terrestrial craters (Hörz et al., 1983; Newsom et al., 1986) resulting in sharp, distinctive contacts. Figure 2.12 shows the sharp contacts of ejecta layers in Bakhuysen (Figs. 2.5d, 2.8, and 2.13c), and further compares the spatial distribution and scale of ponded deposits with those in lunar Tycho and King craters (Figs. 2.13a and 2.13d). The ponded nature of Be2 is consistent with emplacement by flow which was influenced by topography. We suggest that local topography was the main control on the deposition of unit Be2 based on the following lines of evidence: 1) the strong correlation between pre-existing topographic lows and the presence of Be2; 2) the lack of Be2 deposits in the topographic highs of the northeastern and southeastern ejecta (Figs. 2.1b and 2.4c); and 3) the relatively uniform distribution of secondaries.

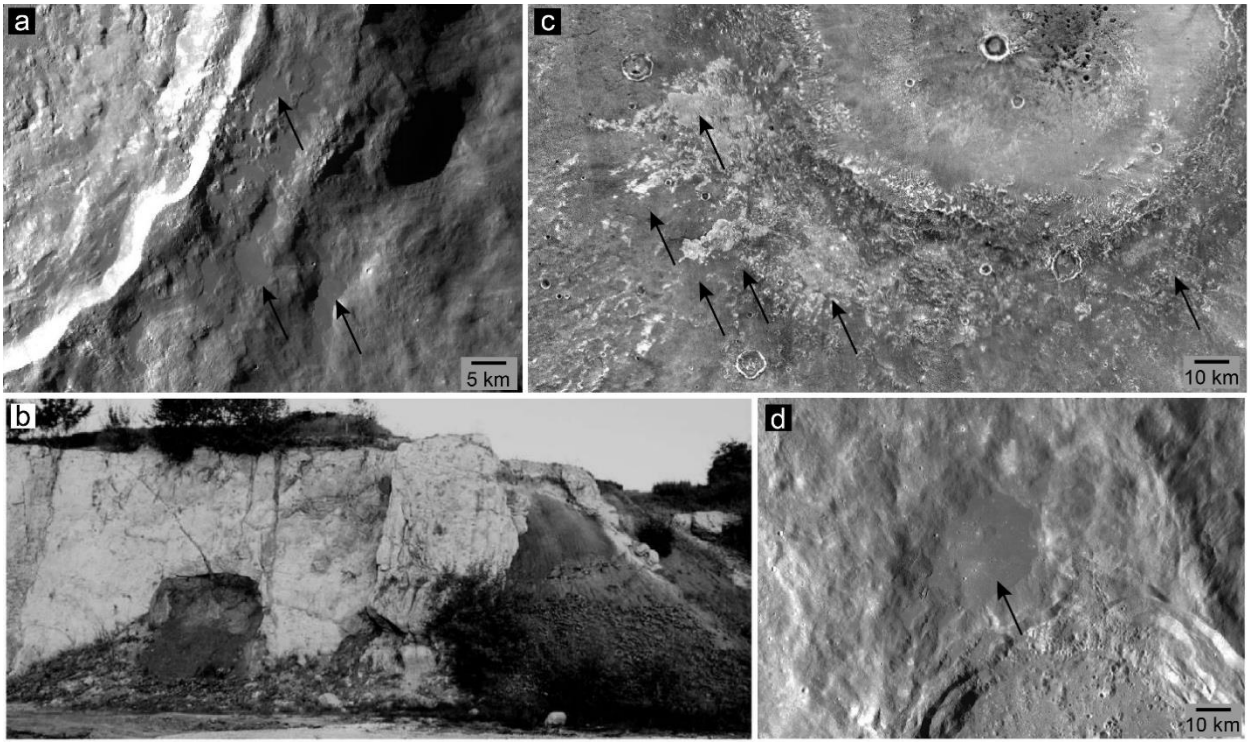

Figure 2.13. a) Tycho Crater southeastern rim and ejecta. Black arrows indicate melt ponds. Shown on 100 m/pixel LROC WAC global mosaic (Robinson et al., 2010). b) Ejecta deposits from the Ries impact structure, Amuhule quarry, are seen in sharp, irregular contact. The light-toned, melt-bearing "suevite" unit overlies the dark-toned, hummocky Bunte Breccia. Localized devolatilization at this contact has been suggested as the same process that forms pitted terrains on Mars. Height of outcrop is ~9.5 m. Modified from Osinski (2006). c) THEMIS nTIR data showing Bakhuysen ponded Be2 deposits (indicated by black arrows) in stark contact with Be1. See Figure 2.1 indicator box for location reference. THEMIS image credits: NASA/JPL/ASU. d) Impact melt pond in King Crater ejecta indicated by black arrow, north of the crater rim. Shown on LROC WAC global mosaic.

Tornabene et al. (2012) also noted the similarities of crater-related pitted material on Mars to lunar ponded impact, but made an important distinction: lunar impact melt pools have smooth, near-equipotential surfaces often with entrained hummocky crater fill, but are pit-free. Another important distinction between lunar and Martian ejecta is that the blocky lunar ejecta is produced from a dry target, whereas the fluidized, and therefore layered, Martian ejecta is accepted to result from the volatile content of the target; it therefore stands to reason that the lack of pitted material in lunar impact melt flows is a result of the volatile-poor upper lunar crust (Tornabene et al., 2012).

Lunar impact melt deposits are typically observed as having flow textures that are commonly seen in terrestrial lava flows, such as rugged flow features or pressure ridges, rafted plates, and stratigraphically stacked flows (Keszthelyi et al., 2004, 2000). Impact melt flows around lunar craters have been described as driven by inflation of a waning influx of melt and cooling flow fronts, causing lobate breakouts, as seen in a Giordano Bruno flow (Fig. 2.14a) (Bray et al., 2010). As lunar impact melt is understood through terrestrial lava flow analogues, it is useful to morphologically define a lava flow, which displays steep margins, a continuous top, and forms a succession of breakout lobes (Keszthelyi et al., 2000). Pressure ridges within a melt pond represent late-stage flow with a series of ridges both perpendicular to the direction of flow and at the edges of flow, as observed in volcanic deposits as well as lunar impact melt flows (Fig. 2.14b). Fluctuations in the effusion rate lead to rafted plates (Fig. 2.14c), where solidified crust forms on a relatively stagnant flow which is disrupted by a later surge (Keszthelyi et al., 2000). Though rafted plate morphology has been observed in lunar impact melt (Carter et al., 2012), lava flows on Mars show a unique platy-ridged morphology due to the viscosity and

effusive nature of basalts (Keszthelyi et al., 2000). Keszthelyi et al. (2000) modeled that Martian basaltic lava flows have very long runout lengths and form relatively thin deposits. Figure 2.14d shows the best-preserved deposit of Be2, which appears to be a series of lengthy flows (tens of kms) sourced from topographically higher pitted, ponded Be2 deposits. The deposit is comprised of stacked flows (Figs. 2.14d–e), where the topographically highest flow shows potential pressure ridges and digitate textures (Fig. 2.14e) similar to those observed in lunar impact melt flows. As described in Giordano Bruno (Bray et al., 2010), stacked flows and digitate textures in Bakhuysen ejecta may have resulted from a temporary, upslope ponding of portions of the impact melt by topographic obstacles, perhaps released by movement along faults during initial crater modification stages. The ejecta flow shown in Figure 2.14 is furthermore characterized by morphology consistent with rafted plates (Fig. 2.14f), supporting that initial surges and movement of melt may have been accommodated. The observations in the best preserved Be2 ejecta deposit indicates the analogous nature of lunar and terrestrial melt flows to the morphology of Bakhuysen deposits.

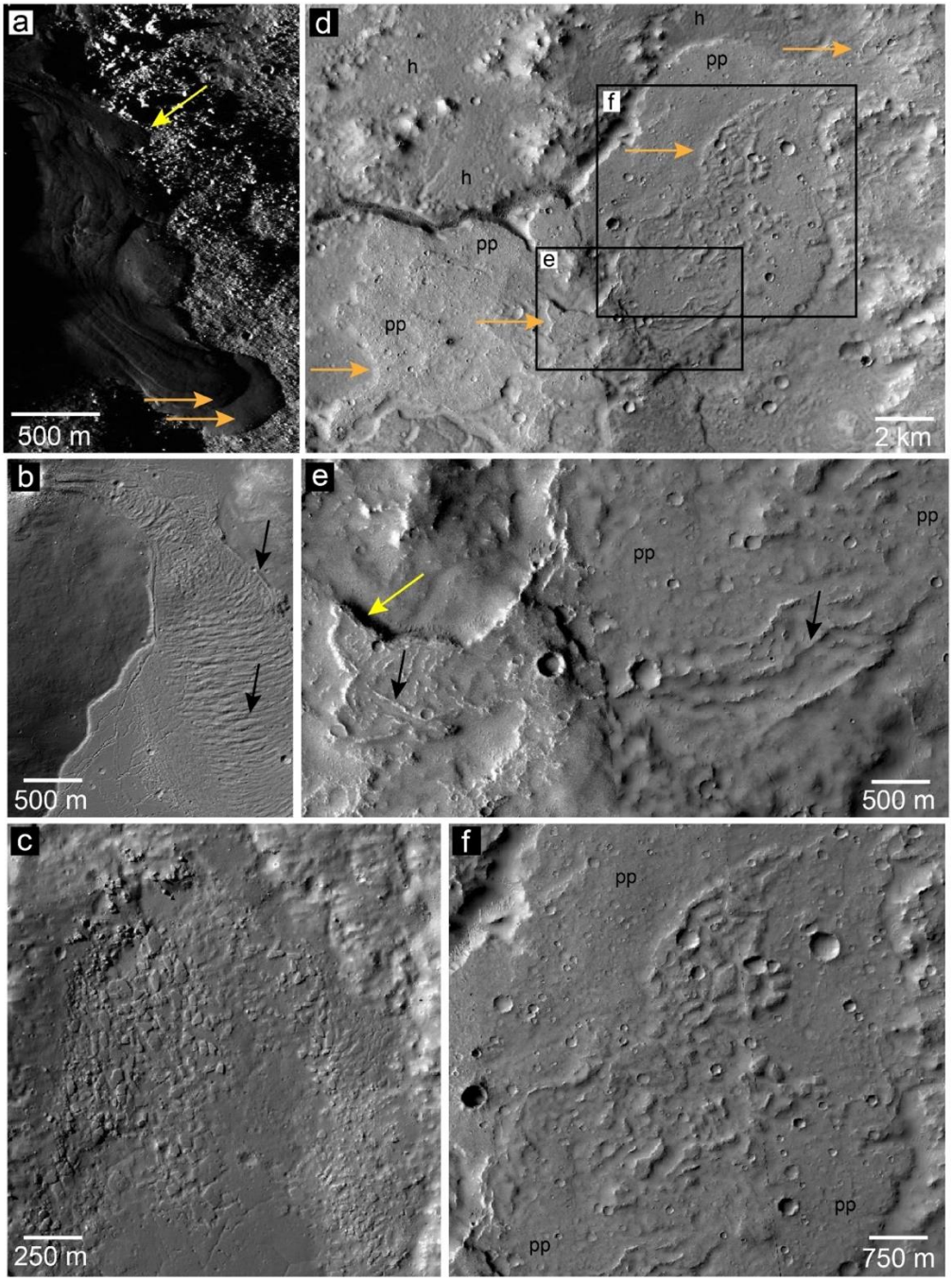

Figure 2.14. a) An example of a lobate flow of lunar impact melt mapped near Giordano Bruno crater rim. Shown on LROC NAC M101476840L at low sun angle. Multiple, stratigraphically stacked flow fronts are indicated by orange arrows, and digitate texture is indicated by yellow arrow. LROC image credits: NASA/GSFC/Arizona State University. b) Tycho Crater impact

melt flow displaying pressure ridges and ponding, shown on LROC NAC M1144842159. Arrows indicate the various directions of the ridges which indicate main flow direction over time. c) Tycho Crater impact melt flow displaying rafted plates, also a common morphology in lunar impact melt. Shown on LROC NAC M119916367. d) View of a sequence of Bakhuysen pitted flows of Be2 into ponded Be2 deposits, indicated by orange arrows. Shown on CTX images D10_031056_1559_XN _24S346W and D15_033258_1562_XN_23S345W. For location context, see Figures 2.1 and 2.4. Be1 unit corresponds to the hummocky "h" regions; Be2 unit corresponds to the pitted ponds "pp". (A zoom image of the Be1 (h) and Be2 (pp) contact seen in panel a is shown in Fig. 2.7.) Black boxes indicate regions for panels (e) and (f). e) Stratigraphically highest portion of the flow shown on HiRISE images ESP_037293_1555-ESP_036726 _1555. Yellow arrow indicates a digitate texture as compared to the lunar flow in panel a. Black arrows indicate potential pressure ridges, as compared to features observed in lunar impact melt deposits (panel b). f) Portion of the Be2 flow showing textures analogous to rafted plates as seen in panel c. Shown on CTX image D10_031056_1559_XN_24S346W and D15_ 033258_1562_XN_23S345W.

Bakhuysen crater interior deposits and features, including flows and concentric fractures, may further support the analogies between Be2 impactites and lunar impact melt flows. The flow deposit in the crater interior (csr) displays ridges much like those in the ejecta flow (Fig. 2.14e), similar to pressure ridge morphology observed in Tycho impact melt flows (Fig. 2.14b). The csr deposit is observed as being sourced from Be2, beyond the crater rim, and flowing into the crater (Figs. 2.10a–c; Fig. 2.15). We suggest that the morphology of the deposit is reflective of the

viscosity and rheology of the material as well as the transport distance and the topography. The behavior of these deposits is consistent with an impact melt-bearing or otherwise super-heated, volatile-rich impactite deposited in the crater interior and as near-rim ejecta (cf., Osinski et al., 2011). In the interior pitted unit, concentric fractures (Fig. 2.3a) appear to have been coeval with the pits. Pit-associated fractures are commonly observed in Martian pitted material (e.g., Tooting Crater; Mouginis-Mark and Garbeil, 2007). The fractures are similar to contraction fractures of impact melt deposits (Heather and Dunkin, 2003; Tornabene et al., 2012) caused by volume loss of hot, young impact melt deposits on crater floors.

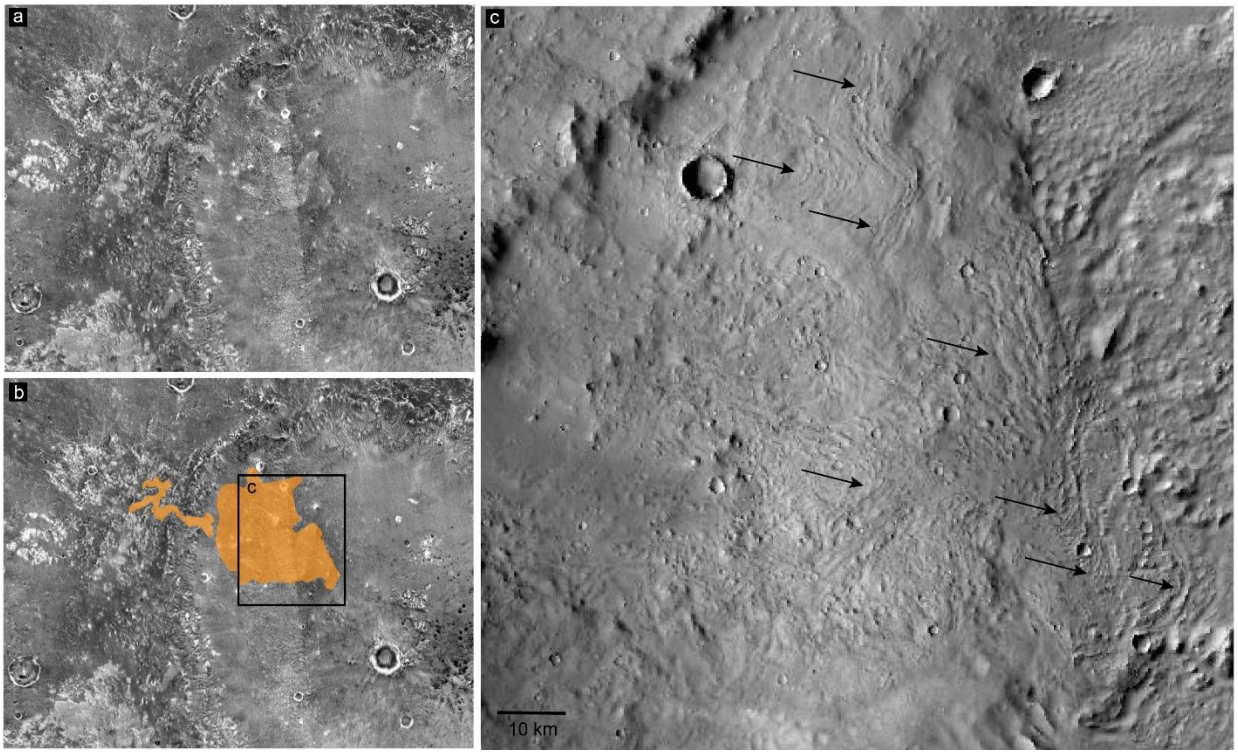

Figure 2.15. a) Northwestern crater rim shown with THEMIS night thermal inertia mosaic (nTIR; THEMIS image credits: NASA/JPL/ ASU). Be2 ejecta deposits and the csr interior unit

are relatively bright white in nTIR, observed as ponds and flows. The flow mapped in (b) shows that the origin of csr is beyond the crater rim in Be2. c) Subset of c shows the deposit in CTX image F20_043570_1569 _XN_23S344W. Black arrows indicate the ridges that are unique to this unit in the interior, but are similar to those observed in Be2 ejecta flows (Fig. 2.14e).

In summary, we suggest that the overlying Be2 ejecta unit is most consistent with a melt-bearing impactite based on the following lines of evidence: 1) morphological, thermophysical, and textural differences between the two Bakhuysen ejecta units; 2) the stratigraphical relationships, relative distribution, and pond-and-flow morphology of Be2, which are consistent with observations from terrestrial and lunar impact deposits, and; 3) textures of Be2 flow features, which are comparable to those commonly observed in lunar impact melt flows, and that are consistent with observed basaltic flows on Mars.

2.6.2.3. Implications of impact melt-bearing deposits on Mars

Based on field studies at the Haughton and Ries impact structures, Osinski (2006) suggested that impact melting-bearing lithologies should be common on terrestrial bodies having a volatile-rich subsurface; this is further supported by modeling and other terrestrial studies (Kieffer and Simonds, 1980; Osinski et al., 2008a; Stewart and Ahrens, 2005; Wohletz and Sheridan, 1983). The propensity of impact melts to weather to clay minerals, as well as the enhanced devitrification of mafic glass likely to comprise Martian impact melts, have both been suggested as factors in the lack of identification of impact melts as a major Martian crustal component (Farrand et al., 2016; Minitti et al., 2002; Schultz and Mustard, 2004). Difficulties in

distinguishing between impact melt rocks versus endogenic igneous rocks is also another likely factor (Osinski et al., 2018).

Our documentation of Bakhuysen ejecta deposits thus supports the view that impacts into volatile-rich targets likely produce significant impact melt rock or melt-bearing breccias. The variably volatile-rich Martian crust served an important role in the formation of impact melt, and other crater-related fluvial and mass flow features may have resulted (e.g., Tornabene et al., 2012), as are detailed in following sections. Still, the lack of identification and acknowledgment of the potential of impact-melt bearing ejecta on Mars has led to these deposits being omitted in current Martian ejecta classifications schemes.

Bakhuysen, as well as many other craters on Mars, possess ponds and flows atop and embaying hummocky ejecta materials that are consistent with being melt-rich deposits superposing the melt-poor ballistically-emplaced ejecta (Osinski et al., 2011; Tornabene et al., 2012). We interpret the two ejecta units as constituting "two layers", even if one – the melt-rich ejecta – is often discontinuous. This suggests that Bakhuysen, and many other well-studied and well-preserved craters on Mars not classified as layered ejecta in global catalogues (e.g., Zumba, Resen, Noord, Zunil, Mojave, Hale; Robbins and Hynek, 2012), could be classified as double layer ejecta (DLE) craters. It is important to note, however, that given the state of erosion of Bakhuysen, we cannot rule out the possibility that this crater originally displayed the multiple layer ejecta (MLE) morphology. Given the strict definition of what constitutes a DLE, i.e., two 'layers' of continuous ejecta (see Barlow et al., 2000), and the consistent observation of a melt-rich ejecta unit atop a melt-poor one here, and at other well-preserved craters (e.g., Hopkins et al., 2017; Marzo et al., 2010; Osinski et al., 2011; Sun and Milliken, 2014; Tornabene et al., 2009, 2012), there are certain ambiguities with the current ejecta classification scheme for Mars

that leads to some degree of confusion. This ambiguity suggests that a re- assessment of crater ejecta classification and nomenclature is needed.

2.6.3. Ejecta emanating channels

The release of target volatiles and consequent fluvial dissection as related to impact events on Mars have been suggested based on the presence of fluvial features emanating from, and cross-cutting, ejecta deposits at Hale Crater (Jones et al., 2011), Lyot Crater (Harrison et al., 2010), Mojave Crater (Tornabene et al., 2012). Fluvial networks formed around impact craters have been suggested to have resulted from impact-induced elevated geothermal gradients (Brakenridge, 1990; Gulick, 1998), the interaction of available water with impact melt sheets (Newsom, 1980), and/or the mobilization of ground ice and/or groundwater through the kinetic energy of impact events, with subsequent channel and valley formation (McEwen et al., 2007; Morgan and Head, 2009; Tornabene et al., 2012, 2013; Osinski et al., 2013; Tornabene et al., 2008). However, channels in the hummocky ejecta of the ~3-km Zumba crater are observed exclusively where it is clearly associated with ponded and pitted materials in the ejecta (see Fig. 13 in Tornabene et al., 2012), which suggests the deposition of these materials are associated with the release of volatiles from ejecta. In support of this hypothesis, Morris et al. (2010) mapped fluidized debris flows in Tooting Crater and suggested that dewatering of the ejecta blanket as being the most likely source of volatiles. Similarly, Jones et al. (2011a) proposed that the Hale Crater-forming impact generated extensive channel systems primarily by melting of both ejecta-entrained subsurface ice and ice in contact with non-ambient ejecta materials. Simulations of channels and flow deposits produced by the Hale impact are consistent with an estimated ~10% water by volume substrate (El- Maarry et al., 2013; Jones et al., 2011; Schultz and Wrobel, 2012). More recent mapping of flow features in the distal discontinuous ejecta of

Hale Crater also suggests that their formation was the result of impact-induced release of volatiles (El-Maarry et al., 2013; Grant and Wilson, 2017a; Jones et al., 2011).

The numerous channels mapped in association with the Bakhuysen ejecta are consistent with an origin through the release of target volatiles from the ejecta deposits themselves. Many impact craters postdate Bakhuysen deposits and are not cut by channels, suggesting that channel formation was restricted to the time in which Bakhuysen formed. Channels are most often observed near the contacts between Bakhuysen ejecta units and this is especially true for the largest channels (Fig. 2.4). Figure 2.16 shows the source region for one channel (also shown in Figs. 2.4b–d), with the Be2 material having flowed ("f") southwest, away from the higher elevation of the rim into the topographically lowest pitted ponds ("pp"). (Note that the Be2 flow mapped in Figures 2.14d–f is the pitted pond in Figure 2.16.) The pitted ponds are fed step-wise by overflow (indicated by "f" in Fig. 2.16b) of higher topography pools of impact melt-bearing material. The flows are indicated by both curvilinear structures and channelized features. The star in both images indicates the apparent source region for the channel, which is adjacent to the largest pitted pond at the bottom of the overflow; the channel then formed along the contact between the ejecta units (where "h" indicates the hummocky terrain of the Be1 unit).

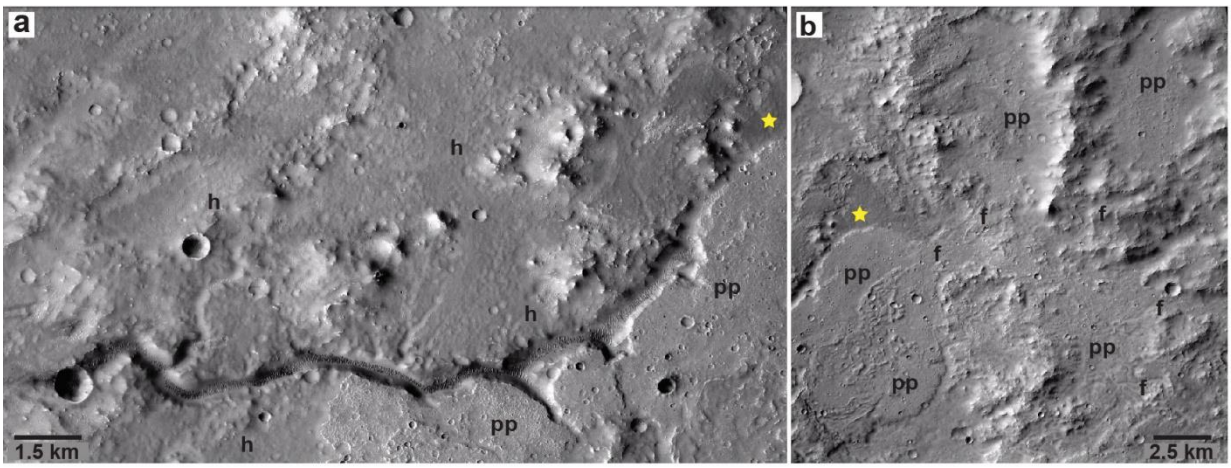

Figure 2.16. a) The largest mapped channel in Bakhuysen ejecta, which occupies the contact between the Be1 and the most extensive exposure of Be2 ejecta. Be1 unit corresponds to the hummocky "h" regions; Be2 unit corresponds to the pitted ponds "pp". Shown on CTX (Malin et al., 2007) image D10_031056_1559_XN_24S346W. Figure 2.8a location box is shown. See Figures 2.4b–c for a map of the extent of the main channel observed in this figure and Figure 2.1 for context. b) Source region for the large channel indicates by star in both panels. The source is fed down-slope from higher topography pitted ponds ("pp"). Shown on CTX image D15_033258_1562_XN _23S345W. CTX image credits: NASA/JPL/MSSS.

Furthermore, the extensive network of cross-cutting channels in Bakhuysen continuous ejecta (Figs. 2.4 and 2.16), some of which appear to also be sourced from the contact between the pitted (Be2) and continuous ejecta (Be1) units, suggests that the Bakhuysen impact event mobilized subsurface volatiles and resulted in the formation of fluvial features. Given the pitted material represents an impact melt-bearing impactite (Tornabene et al., 2013; Tornabene, 2007),

it stands to reason that the increased temperatures and hence greater capacity to melt ice would have caused a release of volatiles preferentially at this contact.

The rim-emanating channels in the interior of the crater may support an impact-induced concentration and release of volatiles as a channel formation mechanism. As in the ejecta, the rim channels originate from Be2 ejecta unit, beyond the rim where the origin is observable. There is no evidence to suggest that the channels emanate from the craters walls; though some ice or water-rich substrate may have been exposed by crater excavation, the rim-emanating channels do not appear to be associated with wall exposures. However, alluvial fans are present in the crater floor which are younger than the pitted impactites and represent later post-impact sedimentation. Stratigraphic relationships of the crater interior deposits (e.g., Fig. 2.3d) may suggest that the rim-emanating channels were formed the result of dewatering of impactites or otherwise related to the volatile concentration and release via impact-induced heating and mechanical transport; the channels from the rim were then exploited by later alluvial processes.

2.7. Conclusions

Our mapping and geomorphological analysis indicates that Bakhuysen possesses two distinct ejecta units. The Be1 unit is the lowermost ejecta unit, having features consistent with emplacement via ballistic sedimentation and radial flow. The unit is largely hummocky and has a radial component that terminates in degraded lobes. Distal flow features beyond the continuous ejecta, as well as many channel features cross-cutting Be1, may indicate that the pre-impact target was ice-rich, resulting in volatile-rich ejecta deposits (e.g., Grant and Wilson, 2017). We suggest that the pitted material ubiquitous in the Be2 ejecta unit is also an indication of the availability of volatiles in the ejecta (e.g., Tornabene et al., 2012). The Be2 unit is interpreted as the uppermost, melt-bearing ejecta unit based on morphological (e.g., embayment relationships

and pond-and-flow) and thermophysical evidence, stratigraphical superposition, surficial pitted and flow textures, and analogies to lunar and terrestrial impactites. For example, our observations of pressure ridges, rafted plates, and stratigraphically stacked flows observed in Be2, as seen in lunar impact melts (e.g., Bray et al., 2010) and Martian lavas, is suggestive of impact melt flows. Such melt-bearing deposits overlying ballistic ejecta are common around lunar and Mercurian impact craters, have been sparsely identified on Mars and, although rare on Earth, have been well-studied at the Ries terrestrial impact structure. This supports previous work (e.g., Carter et al., 2012; Neish et al., 2014; Osinski et al., 2011) which suggests that given similarities in volatile content and subsurface stratigraphy, similar mechanisms of multi-unit ejecta emplacement may extend to impact cratering processes on other comparable rocky bodies.

Large fluvial features (km-wide and tens of kms in length) emanate from the contact between the two ejecta units. Coupled with the presence of pitted material in Be2, we suggest this indicates an exhumation of crustal volatiles through the impact event and a subsequent release of those volatiles due to the emplacement of higher temperature, melt- bearing impact ejecta. The preservation and exposure of impact deposits is key for observing such associated features, investigating their origin, and determining a clear relationship to the crater. Bakhuysen Crater possesses unique exposures and preservation of multi-unit ejecta and, therefore, presents a unique opportunity to study ejecta deposits, with preserved pitted material and channels.

References

Barlow, N.G., Sharpton, V., Kuzmin, R.O., 2007. Impact Structures on Earth and Mars. In: Chapman, M. (Ed.), The Geology of Mars: Evidence from Earth-Based Analogs. Cambridge University Press, pp. 47–56.

Barlow, N.G., 2017. Revision of the “Catalog of Large Martian Impact Craters” and comparison to other Martian crater databases. In: Proceedings of the 48th Lunar and Planetary Science Conference, #1562.

Barlow, N.G., 2006. Impact craters in the northern hemisphere of Mars: Layered ejecta and central pit characteristics. Meteorit. Planet. Sci. 41, 1425–1436.

Barlow, N.G., 2005. A review of Martian impact crater ejecta structures and their im- plications for target properties. Large Meteor. impacts III. Boulder, Color. Geol. Soc. Am. 384, 433–442.

Barlow, N.G., 2003. Martian impact crater ejecta morphologies as indicators of the dis- tribution of subsurface volatiles. J. Geophys. Res. 108, 1–10.

Barlow, N.G., Boyce, J.M., Costard, F.M., Craddock, R.a., Garvin, J.B., Sakimoto, S.E.H., Kuzmin, R.O., Roddy, D.J., Soderblom, L., 2000. Standardizing the nomenclature of Martian impact crater ejecta morphologies. J. Geophys. Res. 105 (E11), 26733–26738.

Barlow, N.G., Bradley, T.L., 1990. Martian impact craters: Correlations of ejecta and in- terior morphologies with diameter, latitude, and terrain. Icarus 87, 156–179.

Barnouin-Jha, O.S., Baloga, S., Glaze, L., 2005. Comparing landslides to fluidized crater ejecta on Mars. J. Geophys. Res. E Planets 110, 1–22.

Barnouin-Jha, O.S., Schultz, P.H., 1999. Interactions between an impact generated ejecta curtain and an atmosphere. Int. J. Impact Eng. 23, 51–62.

Barnouin-Jha, O.S., Schultz, P.H., 1998. Lobateness of impact ejecta deposits from atmospheric interactions. J. Geophys. Res. 103, 739–756.

Barnouin-Jha, O.S., Schultz, P.H., 1996. Ejecta entrainment by impact-generated ring vortices: theory and experiments. J. Geophys. Res. 101 (E9), 21099–21115. Bibring, J.-P.,

Langevin, Y., Mustard, J.F., Poulet, F., Arvidson, R., Gendrin, A., Gondet, B., Mangold, N., Pinet, P., Forget, F., Berthé, M., Bibring, J.-P., Gendrin, A., Gomez,

C., Gondet, B., Jouglet, D., Poulet, F., Soufflot, A., Vincendon, M., Combes, M., Drossart, P., Encrenaz, T., Fouchet, T., Merchiorri, R., Belluci, G., Altieri, F., Formisano, V., Capaccioni, F., Cerroni, P., Coradini, A., Fonti, S., Korablev, O., Kottsov, V., Ignatiev, N., Moroz, V., Titov, D., Zasova, L., Loiseau, D., Mangold, N., Pinet, P., Douté, S., Schmitt, B., Sotin, C., Hauber, E., Hoffmann, H., Jaumann, R., Keller, U., Arvidson, R., Mustard, J.F., Duxbury, T., Forget, F., Neukum, G., 2006. Global mineralogical and aqueous mars history derived from OMEGA/Mars express data. Science 312, 400–404.

Boyce, J., Barlow, N., Mouginis-Mark, P., Stewart, S., 2010. Rampart craters on Ganymede: their implications for fluidized ejecta emplacement. Meteorit. Planet. Sci. 45, 638–661.

Boyce, J.M., Mouginis-Mark, P.J., 2006. Martian craters viewed by the thermal emission imaging system instrument: double-layered ejecta craters. J. Geophys. Res. 111, E10005.

Boyce, J.M., Wilson, L., Mouginis-Mark, P.J., Hamilton, C.W., Tornabene, L.L., 2012. Origin of small pits in martian impact craters. Icarus 221, 262–275.

Brakenridge, G.R., 1990. The origin of fluvial valleys and early geologic history, aeolis quadrangle, Mars. J. Geophys. Res. Lett. 95, 17289–17308.

Bray, V.J., Tornabene, L.L., Keszthelyi, L.P., McEwen, A.S., Hawke, B.R., Giguere, T.A., Kattenhorn, S.A., Garry, W.B., Rizk, B., Caudill, C.M., Gaddis, L.R., van der Bogert, C.H., 2010. New insight into lunar impact melt mobility from the LRO camera. Geophys. Res. Lett. 37, L21202. http://dx.doi.org/10.1029/2010GL044666.

Bray, V.J., Tornabene, L.L., McEwen, A.S., Mattson, S., 2009. Measurement of smallscale pits in the Corinito crater. In: Proceedings of the Lunar and Planetary Science Conference, pp.

1389.

Carr, M.H., 1996. Water on Mars. Oxford University Press ISBN 10: 0195099389. Carr, M.H., Crumpler, L.S., Cutts, J.a., Greeley, R., Guest, J.E., Masursky, H., 1977. Martian impact craters and emplacement of ejecta by surface flow. J. Geophys. Res. 82, 4055–4065.

Carter, J., Poulet, F., Bibring, J.P., Mangold, N., Murchie, S., 2013. Hydrous minerals on Mars as seen by the CRISM and OMEGA imaging spectrometers: updated global view. J. Geophys. Res. E Planets 118, 831–858.

Carter, L.M., Neish, C.D., Bussey, D.B.J., Spudis, P.D., Patterson, G.W., Cahill, J.T., Raney,

R.K., 2012. Initial observations of lunar impact melts and ejecta flows with the Mini- RF radar. J. Geophys. Res. E Planets 117, E00H09. http://dx.doi.org/10.1029/ 2011JE003911.

Christensen, P.R., Bandfield, J.L., Hamilton, V.E., Ruff, S.W., Kieffer, H.H., Titus, T.N., Malin, M.C., Morris, R.V, Lane, M.D., Clark, R.L., Jakosky, B.M., Mellon, M.T., Pearl, J.C., Conrath, B.J., Smith, M.D., Clancy, R.T., Kuzmin, R.O., Roush, T., Mehall, G.L., Gorelick, N., Bender, K., Murray, K., Dason, S., Greene, E., Silverman, S., Greenfield, M., 2001. Mars global surveyor thermal emission spectrometer experiment: in- vestigation description and surface science results. J. Geophys. Res. 106871, 823–23823.

Christensen, P.R., Engle, E., Anwar, S., Dickenshied, S., Noss, D., Gorelick, N., Weiss- Malik, M., 2009. JMARS – A Planetary GIS, in: American Geophysical Union, Fall Meeting 2009. p. IN22A–06.

Christensen, P.R., Fergason, R.L., Edwards, C.S., Hill, J., 2013. Themis-derived thermal inertia mosaic of mars: product description and science results. In: Proceedings of the 44th Lunar

and Planetary Science Conference, #2822.

Christensen, P.R., Jakosky, B.M., Kieffer, H.H., Malin, M.C., Mcsween, H.Y., Nealson, K., Mehall, G.L., Silverman, S.H., Ferry, S., Caplinger, M., Ravine, M., 2004. The Thermal Emission System (THEMIS) for the Mars 2001 Odyssey Mission. Space Sci. Rev. 110, 85–130.

Cockell, C.S., Lee, P., 2002. The biology of impact craters–a review. Biol. Rev. Camb. Philos. Soc 77, 279–310.

Costard, F.M., 1989. The spatial distribution of volatiles in the Martian hydrolithosphere. Earth Moon Planets 45, 265–290.

Delamere, W.A., Tornabene, L.L., McEwen, A.S., Becker, K., Bergstrom, J.W., Bridges, N.T., Eliason, E.M., Gallagher, D., Herkenhoff, K.E., Keszthelyi, L., Mattson, S., McArthur, G.K., Mellon, M.T., Milazzo, M., Russell, P.S., Thomas, N., 2010. Color imaging of Mars by the High Resolution Imaging Science Experiment (HiRISE). Icarus 205, 38–52.

Ehlmann, B.L., Berger, G., Mangold, N., Michalski, J.R., Catling, D.C., Ruff, S.W., Chassefière, E., Niles, P.B., Chevrier, V., Poulet, F., 2013. Geochemical consequences of widespread clay mineral formation in Mars' ancient crust. Space Sci. Rev. 174, 329–364.

Ehlmann, B.L., Edwards, C.S., 2014. Mineralogy of the Martian surface. Annu. Rev. Earth Planet. Sci. 42, 291–315.

Ehlmann, B.L., Mustard, J.F., Murchie, S.L., Bibring, J.-P., Meunier, A., Fraeman, A.a., Langevin, Y., 2011. Subsurface water and clay mineral formation during the early history of Mars. Nature 479, 53–60.

El-Maarry, M.R., Dohm, J.M., Michael, G., Thomas, N., Maruyama, S., 2013. Morphology and evolution of the ejecta of Hale crater in Argyre basin, Mars: results from high resolution

mapping. Icarus 226, 905–922.

Farrand, W.H., Rogers, A.D., Wright, S.P., Glotch, T.D., 2016. Partially devitrified glass as a component of the Martian surface layer: thermal infrared evidence. In: Proceedings of the 47th Lunar Planetary Science Conference, #1956.

Fergason, R.L., Christensen, P.R., Kieffer, H.H., 2006. High-resolution thermal inertia derived from the Thermal Emission Imaging System (THEMIS): Thermal model and applications. J. Geophys. Res. E Planets 111, E12004. http://dx.doi.org/10.1029/ 2006JE002735.

Gault, D.E., Greeley, R., 1978. Exploratory experiments of impact craters formed in vis- cous-liquid targets: analogs for Martian rampart craters? Icarus 34, 486–495.

Gorelick, NS., Weiss-Malik, M., Steinberg, B., Anwar, S., 2003. JMARS: a multimission data fusion application. In: Proceedings of the Lunar and Planetary Science, pp. 2057. Graup, G., 1999. Carbonate-silicate liquid immiscibility upon impact melting: Ries Crater, Germany. Meteorit. Planet. Sci. 34, 425–438.

Grant, J.A., Wilson, S.A., 2017. The nature and emplacement of distal aqueous-rich ejecta deposits from Hale crater. Mars. Meteorit. Planet. Sci. 1–18.

Grego, P., 2012. Mars and How to Observe it. Springer Science & Business Media. Gulick, V.C., 1998. Magmatic intrusions and a hydrothermal origin for fluvial valleys on Mars. J. Geophys. Res. 103 (E8), 19365–19387.

Harrison, T.N., Malin, M.C., Edgett, K.S., Shean, D.E., Kennedy, M.R., Lipkaman, L.J., Cantor, B.A., Posiolova, L.V, 2010. Impact-induced overland fluid flow and channe- lized erosion at Lyot Crater, Mars. Geophys. Res. Lett. 37, L21201. http://dx.doi.org/ 10.1029/2010GL045074.

Hartmann, W.K., 2005. Martian cratering 8: Isochron refinement and the chronology of Mars.

Icarus. 174 (2), 294–320.

Hawke, B.R., Head, J.W., 1977. Impact melt on lunar crater rims. Impact Explos. Cratering 1, 815–841.

Heather, D.J., Dunkin, S.K., 2003. Geology and stratigraphy of King crater, lunar farside. Icarus 163, 307–329.

Hopkins, R.T., Tornabene, L.L., Osinski, G.R., 2017. The central uplift of Elorza Crater: insights into its geology and possible relationships to the Valles Marineris and Tharsis regions. Icarus 284, 284–304.

Horner, V.M., Greeley, R., 1982. Pedestal craters on Ganymede. Icarus 51, 549–562. Hörz, F., 1982. Ejecta of the Ries Crater, Germany in Geological Implications of Impacts of Large Asteroids and Comets on the Earth, Special Paper of the Geological Society of America. doi:10.1130/SPE190.

Hörz, F., Ostertag, R., Rainey, D.A., 1983. Bunte Breccia of the Ries: continuous deposits of large impact craters. Rev. Geophys. 21 (8), 1667–1725.

Irwin, R.P., Grant, J.A., 2013. Geologic map of MTM –15027, –20027, –25027, and –25032 quadrangles, Margaritifer Terra region of Mars: U.S. Geological Survey Science Investigations Map 3209, pamphlet 11 p., 1, scale 1:1,000,000. U.S. Geol. Surv. 3209.

Iverson, R.M., Vallance, J.W., 2001. New views of granular mass flows. Geology 29 (2), 115–118.

Jaumann, R., Neukum, G., Behnke, T., Duxbury, T.C., Eichentopf, K., Flohrer, J., Gasselt, S.v., Giese, B., Gwinner, K., Hauber, E., Hoffmann, H., Hoffmeister, A., Khler, U., Matz, K.D., McCord, T.B., Mertens, V., Oberst, J., Pischel, R., Reiss, D., Ress, E., Roatsch, T., Saiger, P., Scholten, F., Schwarz, G., Stephan, K., Whlisch, M., 2007. The high-resolution stereo

camera (HRSC) experiment on Mars Express: Instrument as- pects and experiment conduct from interplanetary cruise through the nominal mis- sion. Planet. Space Sci. 55, 928–952.

Jones, A.P., Baker, V.R., Melosh, H.J., Berman, D.C., 2011. A geomorphic analysis of Hale crater, Mars: the effects of impact into ice-rich crust. Icarus 211, 259–272.

Kenkmann, T., Schönian, F., 2006. Ries and chicxulub: impact craters on earth provide insights for Martian ejecta blankets. Meteorit. Planet. Sci. 41 (10), 1587–1603. Keszthelyi, L., Mcewen, A.S., Thordarson, T., 2000. Terrestrial analogs and thermal models for Martian flood lavas. J. Geophys. Res. E Planets 105, 15027–15049.

Keszthelyi, L., Thordarson, T., McEwen, A., Haack, H., Guilbaud, M.N., Self, S., Rossi, M.J., 2004. Icelandic analogs to Martian flood lavas. Geochem. Geophys. Geosyst. 5. http://dx.doi.org/10.1029/2004GC000758.

Kieffer, S.W., Simonds, C.H., 1980. The role of volatiles and lithology in the impact cratering process. Rev. Geophys. 18 (1), 143–181.

Kneissl, T., Van Gasselt, S., Neukum, G., 2011. Map-projection-independent crater size-frequency determination in GIS environments - New software tool for ArcGIS. Planet. Space Sci. 59, 1243–1254.

Komatsu, G., Ori, G.G., Di Lorenzo, S., Rossi, A.P., Neukum, G., 2007. Combinations of processes responsible for Martian impact crater “layered ejecta structures” empla- cement. J. Geophys. Res. E Planets 112 (E6). http://dx.doi.org/10.1029/ 2006JE002787.

Kreslavsky, M.A., Head Iii, J.W., 2000. Kilometer-scale roughness of mars- results from MOLA data analysis. J. Geophys. Res. 105711 695-626.

Kring, D.A., 2005. Hypervelocity collisions into continental crust composed of sediments and an underlying crystalline basement: comparing the Ries (24km) and Chicxulub (180km)

impact craters. Chemie der Erde - Geochem. 65 (1), 1–46.

Krüger, T., van der Bogert, C.H., Hiesinger, H., 2016. Geomorphologic mapping of the lunar crater Tycho and its impact melt deposits. Icarus 273, 164–181.

Malin, M.C., Bell, J.F., Cantor, B.A., Caplinger, M.A., Calvin, W.M., Clancy, R.T., Edgett, K.S., Edwards, L., Haberle, R.M., James, P.B., Lee, S.W., Ravine, M.A., Thomas, P.C., Wolff, M.J., 2007. Context camera investigation on board the mars reconnaissance orbiter. J. Geophys. Res. E Planets 112, E05S04. http://dx.doi.org/10.1029/ 2006JE002808.

Marzo, G.A., Davila, A.F., Tornabene, L.L., Dohm, J.M., Fairn, A.G., Gross, C., Kneissl, T., Bishop, J.L., Roush, T.L., McKay, C.P., 2010. Evidence for hesperian impact-induced hydrothermalism on mars. Icarus 208, 667–683.

McEwen, A.S., Banks, M.E., Baugh, N., Becker, K., Boyd, A., Bergstrom, J.W., Beyer, R.A., Bortolini, E., Bridges, N.T., Byrne, S., Castalia, B., Chuang, F.C., Crumpler, L.S., Daubar, I., Davatzes, A.K., Deardorff, D.G., DeJong, A., Alan Delamere, W., Dobrea, E.N., Dundas, C.M., Eliason, E.M., Espinoza, Y., Fennema, A., Fishbaugh, K.E., Forrester, T., Geissler, P.E., Grant, J.A., Griffes, J.L., Grotzinger, J.P., Gulick, V.C., Hansen, C.J., Herkenhoff, K.E., Heyd, R., Jaeger, W.L., Jones, D., Kanefsky, B., Keszthelyi, L., King, R., Kirk, R.L., Kolb, K.J., Lasco, J., Lefort, A., Leis, R., Lewis, K.W., Martinez-Alonso, S., Mattson, S., McArthur, G., Mellon, M.T., Metz, J.M., Milazzo, M.P., Milliken, R.E., Motazedian, T., Okubo, C.H., Ortiz, A., Philippoff, A.J., Plassmann, J., Polit, A., Russell, P.S., Schaller, C., Searls, M.L., Spriggs, T., Squyres,

S.W., Tarr, S., Thomas, N., Thomson, B.J., Tornabene, L.L., Van Houten, C., Verba, C., Weitz, C.M., Wray, J.J., 2010. The high resolution imaging science experiment (HiRISE) during MRO's primary science phase (PSP). Icarus 205, 2–37.

McEwen, A.S., Eliason, E.M., Bergstrom, J.W., Bridges, N.T., Hansen, C.J., Delamere, W.A., Grant, J.A., Gulick, V.C., Herkenhoff, K.E., Keszthelyi, L., kirk, R.L., Mellon, M.T., Squyres, S.W., Thomas, N., Weitz, C.M., 2007. Mars reconnaissance orbiter's high resolution imaging science experiment (HiRISE). J. Geophys. Res. E Planets 112, E05S02. http://dx.doi.org/10.1029/2005JE002605.

Melosh, H.J., 1989. Impact Cratering: A Geologic Process, Research supported by NASA. Oxford University Press Oxford Monographs on Geology and Geophysics No11, New York, pp. 253. http://dx.doi.org/10.1103/PhysRevB.46.10411.

Minitti, M.E., Mustard, J.F., Rutherford, M.J., 2002. Effects of glass content and oxidation on the spectra of SNC-like basalts: applications to Mars remote sensing. J. Geophys. Res. Planets 107, 1–14.

Morgan, G.A., Head, J.W., 2009. Sinton crater, Mars: evidence for impact into a plateau icefield and melting to produce valley networks at the Hesperian-Amazonian boundary. Icarus 202, 39–59.

Morris, A.R., Head, J.W., Margot, J., Campbell, D.B., Sciences, G., Astronomy, N., 2000. Impact melt distribution and emplacement on Tycho: a new look at an old question. In: Proceedings of the Lunar and Planetary Science Conference, #1828.

Morris, A.R., Mouginis-Mark, P.J., Garbeil, H., 2010. Possible impact melt and debris flows at Tooting Crater, Mars. Icarus 209, 369–389.

Morrison, RH, Oberbeck, V.R., 1978. A composition and thickness model for lunar impact crater and basin deposits. In: Proceedings of the Lunar and Planetary Science Conference. 3, (A79-39253 16-91). pp. 3763–3785.

Mouginis-Mark, P., 1981. Ejecta emplacement and modes of formation of Martian flui- dized

ejecta craters. Icarus 45, 60–76.

Mouginis-Mark, P., 1979. Martian fluidized crater morphology: variations with crater size, latitude, altitude, and target material. J. Geophys. Res. 84 (B14), 8011–8022.

Mouginis-Mark, P.J., 1987. Water or ice in the Martian regolith?: clues from rampart craters seen at very high resolution. Icarus 71, 268–286.

Mouginis-Mark, P.J., 2015. Geologic map of Tooting crater, Amazonis Planitia region of Mars, U.S. Geological Survey Astrogeology Science Center. USGS Numbered Series #3297.

Mouginis-Mark, P.J., Tornabene, L.L., Boyce, J.M., McEwen, A.S., 2007. Impact melt and water release at tooting crater, Mars. In: Proceedings of the 7th International Conference on Mars. Abstract, pp. 3039.

Naumov, M.V., 2005. Principal features of impact-generated hydrothermal circulation systems: mineralogical and geochemical evidence. Geofluids 5, 165–184.

Neish, C.D., Madden, J., Carter, L.M., Hawke, B.R., Giguere, T., Bray, V.J., Osinski, G.R., Cahill, J.T.S., 2014. Global distribution of lunar impact melt flows. Icarus 239, 105–117.

Neukum, G., Jaumann, R., 2004. HRSC: The high resolution stereo camera of Mars Express. In: Wilson, Andrew (Ed.), Mars Express: The Scientific Payload. ESA Publications Division, Noordwijk, Netherlands, pp. 17–35 Scientific Coordination: Agustin Chicarro. ESA SP-1240ISBN 92-9092-556-6, 2004.

Newsom, H., Graup, G., Sewards, T., Keil, K., 1986. Fluidization and hydrothermal al- teration of the Suevite deposit at the Ries Crater, West Germany, and implications for Mars. J. Geophys. Res. 91, E239–E251.

Newsom, H.E., 1980. Hydrothermal alteration of impact melt sheets with implications for Mars. Icarus 44, 207–216.

Oberbeck, V.R., 2009. Layered ejecta craters and the early water/ice aquifer on Mars. Meteorit. Planet. Sci. 44, 43–54.

Oberbeck, V.R., 1975. The role of ballistic erosion and sedimentation in lunar strati- graphy. Rev. Geophys. 13, 337–362.

Osinski, G.R., Spray, J.G., 2001. Impact-generated carbonate melts: evidence from the Haughton structure, Canada. Earth Planet. Sci. Lett. 194, 17–29.

Osinski, G.R., Grieve, Collins, G.S., Marion, C., Sylvester, P., 2008a. The effect of target lithology on the products of impact melting. Meteorit. Planet. Sci. 43, 1939–1954. Osinski, G.R., Spray, J.G., Grieve, R.A.F., 2008b. Impact melting in sedimentary target rocks: an assessment. In: Evans, Kevin R., Horton Jr.J.Wright, King Jr.David T., Morrow, Jared R. (Eds.), The Sedimentary Record of Meteorite Impacts. Special Paper of the Geological Society of America, 437, http://dx.doi.org/10.1130/2008. 2437(01).

Osinski, G.R., 2006. Effect of volatiles and target lithology on the generation and em- placement of impact crater fill and ejecta deposits on Mars. Meteorit. Planet. Sci. 41, 1571–1586.

Osinski, G.R., Pierazzo, E., 2012. Impact Cratering: Processes and Products. John Wiley & Sons, Ltd, Chichester, UK. http://dx.doi.org/10.1002/9781118447307.

Osinski, G.R., Spray, J.G., Lee, P., 2005. A case study of impact-induced hydrothermal activity: the Haughton impact structure, Devon Island, Canadian High Arctic. Meteorit. Planet. Sci. 40, 1789–1812.

Osinski, G.R., Tornabene, L.L., Banerjee, N.R., Cockell, C.S., Flemming, R., Izawa, M.R.M., McCutcheon, J., Parnell, J., Preston, L.J., Pickersgill, A.E., Pontefract, A., Sapers, H.M., Southam, G., 2013. Impact-generated hydrothermal systems on Earth and Mars. Icarus 224, 347–363.

Osinski, G.R., Tornabene, L.L., Grieve, R.A.F., 2011. Impact ejecta emplacement on ter- restrial planets. Earth Planet. Sci. Lett. 310, 167–181.

Osinski, G.R., Grieve, R.A.F., Bleacher, J.E., Neish, C.D., Pilles, E.A., Tornabene, L.L., 2018. Igneous rocks formed by hypervelocity impact. J. Volcanol. Geotherm. Res. http://dx.doi.org/10.1016/j.jvolgeores.2018.01.015.

Piatek, J.L., Tornabene, L.L., Barlow, N.G., Osinski, G.R., Robbins, S.J., 2016. Visible and thermophysical characteristics of the best-preserved martian craters, part 2: ther- mophysical mapping of Resen and Noord. In: Proceedings of the 47th Lunar and Planetary Science Conference, #2879.

Pohl, J., Stöffler, D., Gall, H., Ernstson, K., 1977. The Ries impact crater. In: Proceedings of the Impact and Explosion Cratering, pp. 343–404.

Robbins, S.J., Hynek, B.M., 2012. A new global database of Mars impact craters ≥1 km:

1. Database creation, properties, and parameters: Mars crater database construction.

J. Geophys. Res. Planets 117 (E05004). http://dx.doi.org/10.1029/2011JE003966. Robinson, M.S., Brylow, S.M., Tschimmel, M., Humm, D., Lawrence, S.J., Thomas, P.C., Denevi, B.W., Bowman-Cisneros, E., Zerr, J., Ravine, M.A., Caplinger, M.A., Ghaemi, F.T., Schaffner, J.A., Malin, M.C., Mahanti, P., Bartels, A., Anderson, J., Tran, T.N.,

Eliason, E.M., McEwen, A.S., Turtle, E., Jolliff, B.L., Hiesinger, H., 2010. Lunar re- connaissance orbiter camera (LROC) instrument overview. Space Sci. Rev. 150, 81–124.

Schönian, F., Stöffler, D., Kenkmann, T., Wittmann, A., 2004. The fluidized Chicxulub ejecta blanket, Mexico: Implications for Mars. In: Proceedings of the Lunar and Planetary Science Conference, #1848.

Schultz, P.H., 1992. Atmospheric effects on ejecta emplacement. J. Geophys. Res. 97, 11623–

11662.

Schultz, P.H., Gault, D.E., 1979. Atmospheric effects on Martian Ejecta emplacement. J. Geophys. Res. Solid Earth 84, 7669–7687.

Schultz, P.H., Mustard, J.F., 2004. Impact melts and glasses on Mars. J. Geophys. Res. 109 (E01001). http://dx.doi.org/10.1029/2002JE002025.

Schultz, P.H., Wrobel, K.E., 2012. The oblique impact Hale and its consequences on Mars. J. Geophys. Res. Planets 117, E04001. http://dx.doi.org/10.1029/2011JE003843. Sharpton, V.L., Marin, L.E., Carney, J.L., Lee, S., Ryder, G., Schuraytz, B.C., Sikora, P.,

Spudis, P.D., 1996. A model of the Chicxulub impact basin based on evaluation of geophysical data, well logs, and drill core samples. In: The Cretaceous-Tertiary Event and Other Catastrophes in Earth History, pp. 55–74.

Smith, D.E., Zuber, M.T., Frey, H.V., Garvin, J.B., Head, J.W., Muhleman, D.O., Pettengill, G.H., Phillips, R.J., Solomon, S.C., Zwally, H.J., Banerdt, W.B., Duxbury, T.C., Golombek, M.P., Lemoine, F.G., Neumann, G.a., Rowlands, D.D., Aharonson, O., Ford, P.G., Ivanov, A.B., Johnson, C.L., McGovern, P.J., Abshire, J.B., Afzal, R.S., Sun, X., 2001. Mars orbiter laser altimeter: experiment summary after the first year of global mapping of Mars. J. Geophys. Res. Planets 106, 23689–23722.

Smith, D.E., Zuber, M.T., Solomon, S.C., Phillips, R.J., Head, J.W., Garvin, J.B., Banerdt, W.B., Muhleman, D.O., Pettengill, G.H., Neumann, G.A., Lemoine, F.G., Abshire, J.B., Aharonson, O., Brown, DavidC., Hauck, S.A., Ivanov, A.B., McGovern, P.J., Zwally, H.J., Duxbury, T.C., 1999. The global topography of Mars and implications for sur- face evolution. Science. 284 (5419), 1495–1503.

Stewart, S.T., Ahrens, T.J., 2005. Shock properties of H2O ice. J. Geophys. Res. E Planets 110,

1–23.

Sun, V.Z., Milliken, R.E., 2014. The geology and mineralogy of Ritchey crater, Mars: evidence for post-Noachian clay mineral formation. J. Geophys. Res. E Planets 119, 810–836.

Tanaka, K.L., Robbins, S.J., Fortezzo, C.M., Skinner, J.A., Hare, T.M., 2014. The digital global geologic map of Mars: chronostratigraphic ages, topographic and crater morphologic characteristics, and updated resurfacing history. Planet. Space Sci. 95, 11–24.

Tornabene, L.L., McEwen, A.S., Osinski, G.R., Mouginis-Mark, P.J., Williams, R.M.E., Wray, J.J., Grant, J.A., 2007. Impact melting andthe role of sub-surface volatiles: Implications for the formation of valleynetworks and phyllosilicate-rich lithologies on early Mars. In: Proceedings of the Seventh International Conference Mars, pp. 3288–3291.

Tornabene, L.L., Ling, V., Osinski, G.R., Boyce, J.M., Harrison, T.N., McEwen, A.S., 2013. A revised global depth-diameter scaling relationship for Mars based on pitted impact melt-bearing craters. In: Proceedings of the 44th Lunar and Planetary Science Conference, #2592.

Tornabene, L.L., Moersch, J.E., McSween, H.Y., Hamilton, V.E., Piatek, J.L., Christensen, P.R., 2008. Surface and crater-exposed lithologic units of the Isidis based as mapped by coanalysis of THEMIS and TES derived data products. J. Geophys. Res. E Planets 113. http://dx.doi.org/10.1029/2007JE002988.

Tornabene, L.L., Osinski, G.R., McEwen, A.S., 2009. Parautochthonous megabreccias and possible evidence of impact-induced hydrothermal alteration in Holden Crater, Mars. In: Proceedings of the Lunar and Planetary Science Conference, #1766.

Tornabene, L.L., Osinski, G.R., McEwen, A.S., Boyce, J.M., Bray, V.J., Caudill, C.M., Grant,

J.A., Hamilton, C.W., Mattson, S., Mouginis-Mark, P.J., 2012. Widespread crater-related pitted materials on Mars: Further evidence for the role of target vola- tiles during the impact process. Icarus 220, 348–368.

Tornabene, L.L., Piatek, J.L., Hansen, K.T., Hutchinson, S.J., Barlow, N.G., Osinski, G.R., Robbins, S.J., McEwen, A.S., 2016. Visible and thermophysical characteristics of the best preserved Martian Craters, Part 1: detailed morphological mapping of Resen and Nord. In: Proceedings of the Lunar and Planetary Science Conference, #2879.

Viviano-Beck, C.E., Seelos, F.P., Murchie, S.L., Kahn, E.G., Seelos, K.D., Taylor, H.W., Taylor, K., Ehlmann, B.L., Wisemann, S.M., Mustard, J.F., Morgan, M.F., 2014. Revised CRISM spectral parameters and summary products based on the currently detected mineral diversity on Mars. J. Geophys. Res. E Planets 119, 1403–1431.

Wada, K., Barnouin-Jha, O.S., 2006. The formation of fluidized ejecta on Mars by granular flows. Meteorit. Planet. Sci. 41, 1551–1569.

Werner, S.C., 2008. The early Martian evolution-Constraints from basin formation ages. Icarus 195, 45–60.

Wohletz, K.H., Sheridan, M.F., 1983. Martian rampart crater ejecta: experiments and analysis of melt-water interaction. Icarus 56, 15–37.

Chapter 3: Origin of the degassing pipes at the Ries impact structure and implications for impact-induced alteration on planetary bodies

3.1 Introduction

Meteorite impact craters are the most ubiquitous geological landform on rocky bodies throughout the solar system and provide insight into the subsurface composition of planetary crusts. Early studies of impact craters in the Canadian Shield demonstrated that significant volumes of impact melt can be generated and emplaced within and around the host crater (Grieve et al., 1977). Historically, it was thought that only small amounts of impact melt were generated from volatile-rich sedimentary targets on Earth (e.g., Kieffer and Simonds, 1980), which led to the assumption that impact melts would be rare on Mars (e.g., Pope et al., 2006). However, in the past decade, it has become clear that significant volumes of melt are produced from impacts into various volatile-rich target lithologies on Earth (see Osinski et al., 2008, 2018, and references therein), concomitant with recent documentation of impact melt materials on Mars (e.g., Cannon and Mustard, 2015; Tornabene et al., 2012; Boyce et al., 2012). Impact melt-bearing deposits in Martian craters display a characteristic pitted appearance (Fig. 3.1) (Tornabene et al., 2012). Tornabene et al. (2012) and Boyce et al. (2012) provide arguments for relationships between pits and the release of target volatiles during the impact process (e.g., Fig. 3.1). Following the observation of widespread crater-related pitted material on Mars, similar pitted material was observed in the best-preserved impact craters on Vesta (Denevi et al., 2012) and Ceres (Sizemore et al., 2017). The pits are proposed to have formed via volatile loss following deposition, analogous to the degassing pipes in impact melt-bearing deposits at the Ries impact structure, Germany (Boyce et al., 2012; Tornabene et al., 2012).

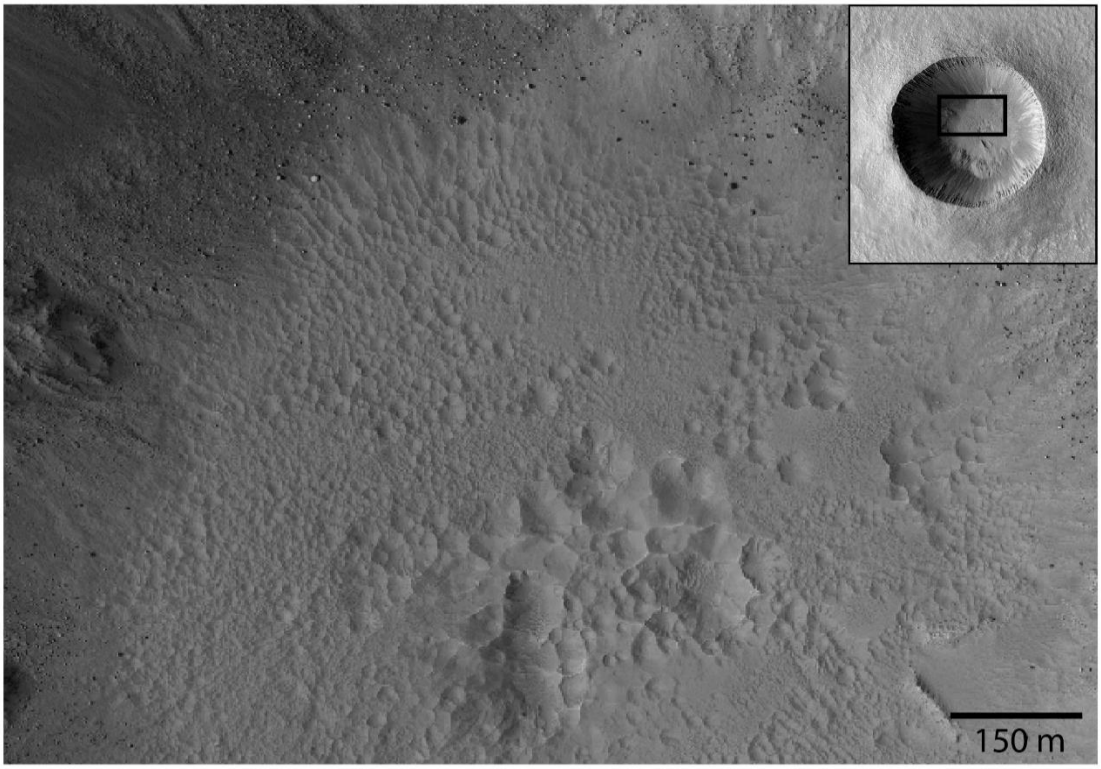

Figure 3.1. Crater-related pitted materials on the floor of Zumba Crater, Mars (HiRISE image PSP_003608_1510_RED). Inset of Zumba Crater shown for reference. The largest pits are near the center of the crater fill, with smaller pits toward the crater wall. Aeolian deposits are common in the pit floors. HiRISE image credits: NASA/Caltech-JPL/UA-LPL.

The Ries impact structure has arguably the best-preserved and exposed ejecta on Earth. The melt-bearing ejecta deposits at the Ries host degassing pipe structures – disseminated, quasi-vertical, chimney-like structures, typically <10 cm wide and several meters in vertical extent – that are inferred conduits for volatile escape during ejecta cooling. Newsom et al. (1986) described the pipes as “elutriation pipes”, analogous to volcanic fumarole pipes; thus, they have been cited as

one indication that the ejecta was emplaced as a density current similar to ignimbrites (Siegert et al., 2017). Engelhardt (1972) suggested that the degassing pipes represent a degassing of the host melt-bearing breccia, while Pietrek and Kenkmann (2016) proposed that their formation arose from degassing of the underlying Bunte Breccia. Chao et al. (1978) emphasized the role of hydrothermal alteration in degassing pipe formation and related alteration.

Despite the suggestion that the degassing pipes at Ries represent an analogue for crater-related pitted deposits on Mars, Vesta, and Ceres (Boyce et al., 2012; Tornabene et al., 2012), detailed field and laboratory analyses have yet to be published. Newsom et al. (1986) most thoroughly described the associated alteration as a light brown coating of "undetermined Fe-oxide or hydroxide" and noted a lack of hydrothermal clay mineral alteration. Thus, they proposed that these phases formed under low-temperature (<100° C), under-saturated conditions. Newsom et al. (1986) also recognized various potential sources for volatiles and/or fluidization pressure for degassing pipe formation and mineralization, including trapped and/or incorporated gas during the emplacement of the melt-bearing breccia unit, hydrous melt phases within the melt-bearing breccia, and gases released due to heating of the volatile-rich underlying Bunte Breccia deposits. The present work provides the first crater-wide field and laboratory study of degassing pipes at the Ries structure with a focus on the alteration mineralogy of the degassing pipe interiors. Based on the mineral assemblages observed, we expand the conditions of formation to include a likely higher temperature of formation. We also identify the role of the host melt-bearing breccia deposits in providing a source for the volatiles and cations required to produce the alteration phases associated with the degassing pipes.

3.2 Ries impact structure

The 24 km-diameter (Pohl et al., 1977) Ries impact structure, Germany (Fig. 3.2a), has been dated at 14.808 ± 0.021 Ma (Schmieder et al., 2018). The target is comprised of a 500 – 800 m thick, predominately Mesozoic sedimentary sequence overlying a crystalline basement having a variety of gneisses, amphibolites, and granites (Graup, 1978). The Ries structure preserves two distinct types of ejecta deposits. The basal and continuous ejecta unit is the Bunte Breccia, comprising largely unshocked materials derived from the sedimentary target substrate (Hörz et al., 1983). Impact melt-bearing breccias overlie the Bunte Breccia, deposited at a high temperature (> 900 °C; Osinski et al., 2004) within the inner ring (as part of the crater-fill deposits) and beyond the inner ring and crater rim (i.e., as ejecta; Stoffler et al., 2013; Engelhardt, 1990). The fine-grained groundmass of the melt-bearing breccias contains compositionally heterogeneous glasses (~20 – 30 vol%) and smectitic clay minerals (≥ ~70 vol%) (Osinski et al., 2004). Both ejecta and crater-fill impactites of melt-bearing breccia contain localized, highly variable hydrothermal alteration products that include illite-smectite, calcite, zeolites, chlorite, and K-feldspar (Sapers et al., 2017; Osinski et al., 2004). The melt-bearing ejecta, emplaced as a discontinuous unit, varies in thickness from several meters to 250 m (Engelhardt, 1990; Engelhardt, 1997).

The extent of post-impact hydrothermal alteration in ejecta deposits at Ries has generated substantial debate; the melt-bearing breccias are mineralogically complex, with highly heterogenous alteration and a surficial ambient-temperature alteration overprint. Some have suggested that hydrothermal activity was restricted to the crater fill deposits (e.g., Muttik et al., 2008; Muttik et al., 2010); however, platy montmorillonite (Osinski, 2005; Newsom et al., 1986) and complex trioctahedral smectites in altered glass clasts within the melt-bearing breccias of the ejecta (Sapers et al., 2017) are consistent with clay mineral formation through hydrothermal

activity. As the degassing pipes (e.g., Figs. 3.2b–c) are a physical remnant of early hydrothermal activity in the melt-bearing impact breccias at Ries, an understanding of their mineralogy and conditions of formation should provide deeper insight into post-impact hydrothermal systems.

The crater-fill melt-bearing breccias are ~270 m thick, based on sampling from the Nördlingen 1973 drill core (Bayerisches Geologisches Landesamt, 1974). The crater-fill breccias are more intensely altered than the ejecta breccias with complete replacement of primary impact-generated glasses. This relatively intense alteration is due to the increased melt volume in the crater fill and the presence of a post-impact, crater-filling lake that increased the longevity of the hydrothermal system (Osinski, 2005). We have documented degassing pipes (Fig. 3.2) in quarry exposures of melt-bearing breccia in the ejecta – inside (Aumühle; Fig. 3.3) and outside of the crater rim (Otting and Altenbürg) – and, for the first time, in drill cores of ejecta (Otting and Wörnitzoshtheim) and in crater-fill breccias (Nördlingen 1973, Fig. 3.4). Study locations are provided in Figure 3.2 (see Appendix A.1 and Table A.1 for full field descriptions).

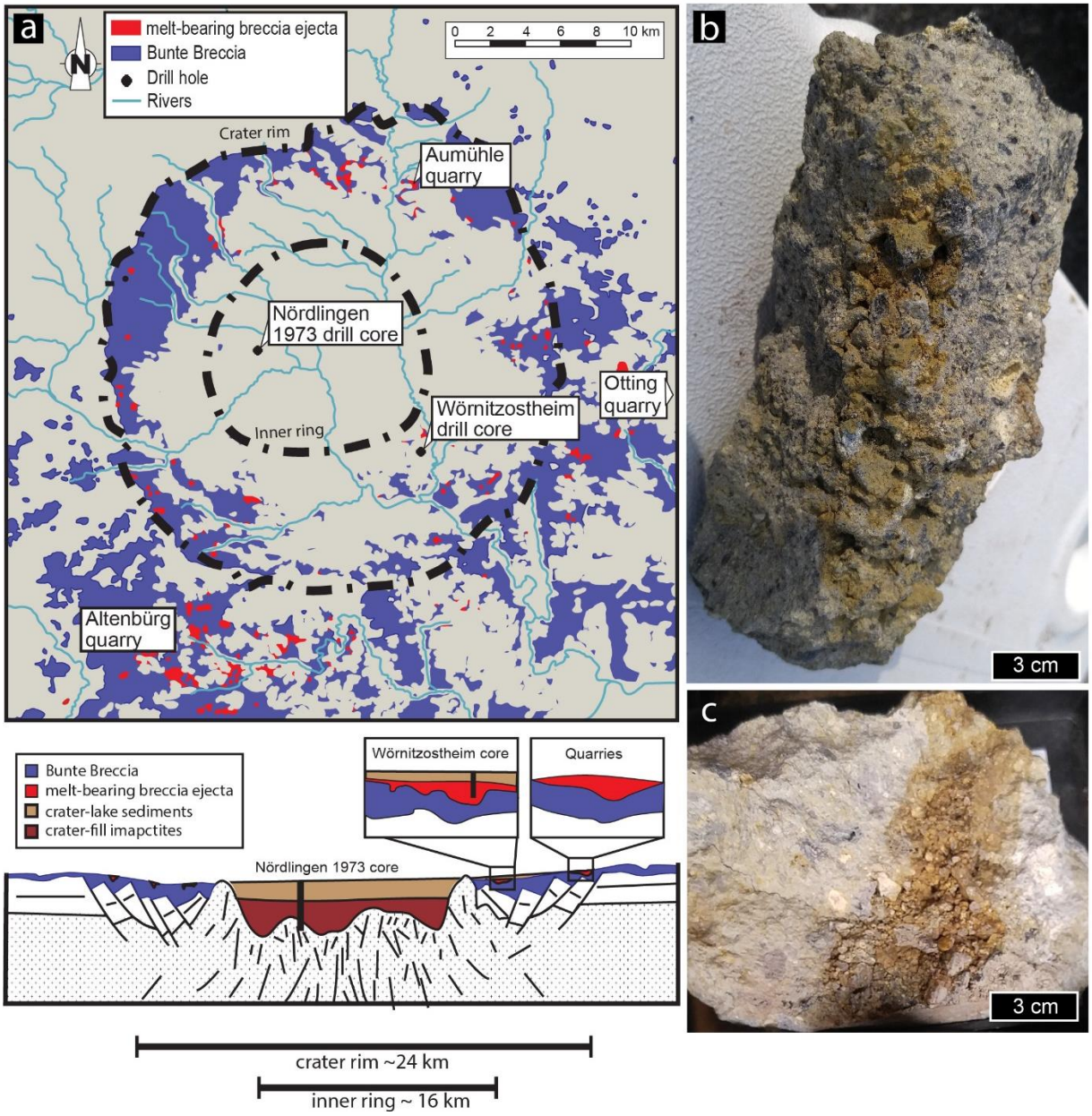

Figure 3.2. a) Geological map of Ries impactites (modified after Hüttner and Schmidt-Kaler, 1999). The crater rim and inner ring are indicated by broken black lines. Sampling areas in quarries and drill core are shown. The Otting drill core is from the Otting quarry. See Appendix A.1 and Table A.1 for location descriptions. b) Hand sample of a degassing pipe cross-section from Otting quarry; alteration is shown as the orange-brown material. c) Hand sample of a degassing pipe cross-section from Aumühle quarry.

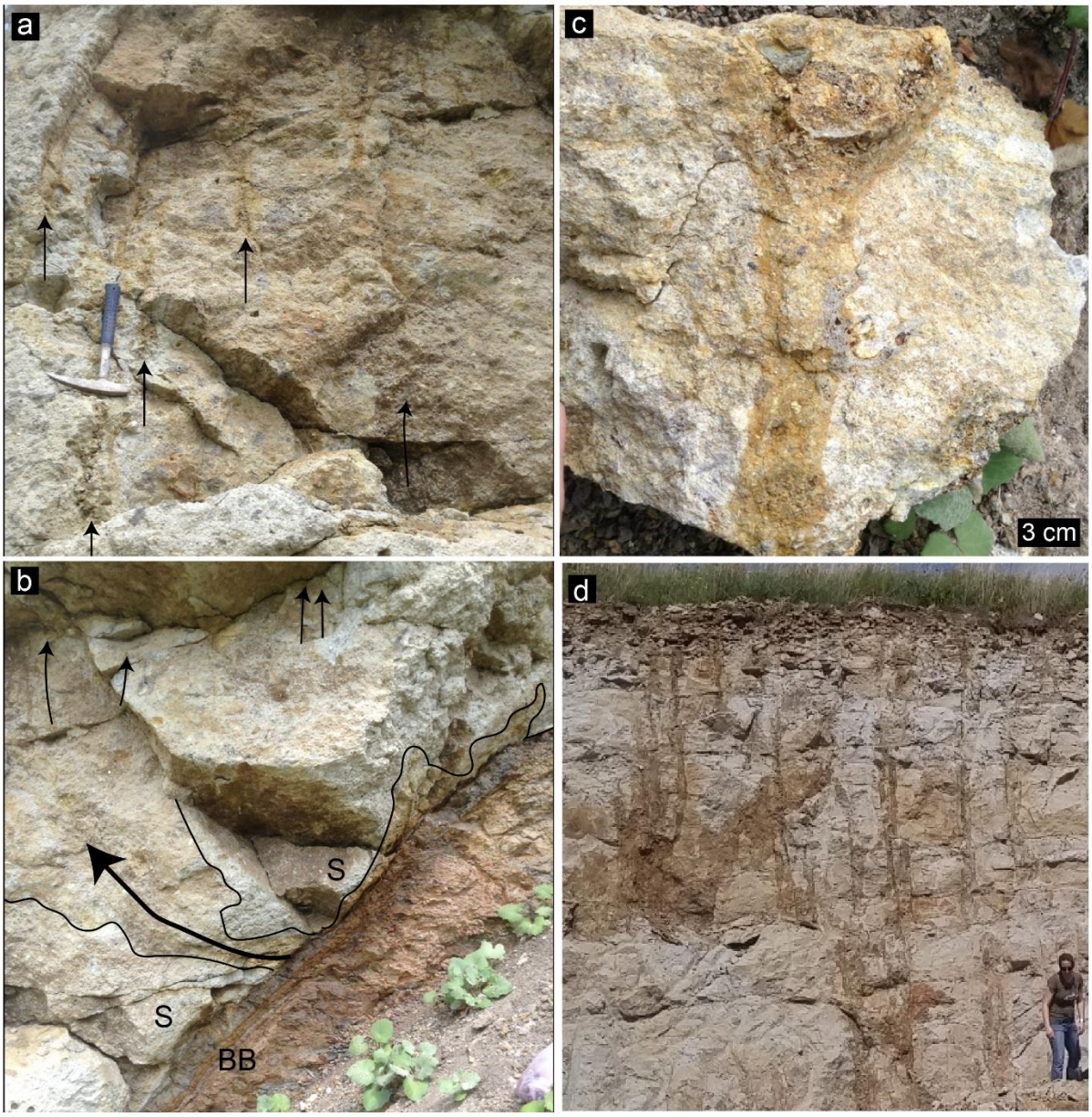

Figure 3.3. a) Aumühle quarry wall outcrop. Black arrows show the vertical flow direction of degassing pipes and “proto-pipes” (indicative of fluid flow preceding the formation of a degassing pipe) in melt-bearing breccia at Aumühle quarry. Hammer for scale. b) Contact between Bunte Breccia (BB; lower) and suevite (S; upper) at the Aumühle quarry, ~2 m below the degassing pipes shown in (a) (shown at the same scale as (a)). Fluid flow emanates from the Bunte Breccia in alteration pathways that connect to proto-pipes and eventually degassing pipes.

The alteration is outlined by black lines, with flow directionality indicated by the large arrow. Smaller arrows show proto-pipes. c) Hand sample of a degassing pipe from Aumühle quarry, which begins with a proto-pipe from fluid flow, expressed as brownish alteration without structure, fines, or clasts. Note the large glass clast at the top of the hand sample, which causes fluid flow divergence around the clast. d) Outcrop of degassing pipe-hosted suevite at Aumühle quarry, showing the scale of alteration haloes associated with the pipes. Person for scale.

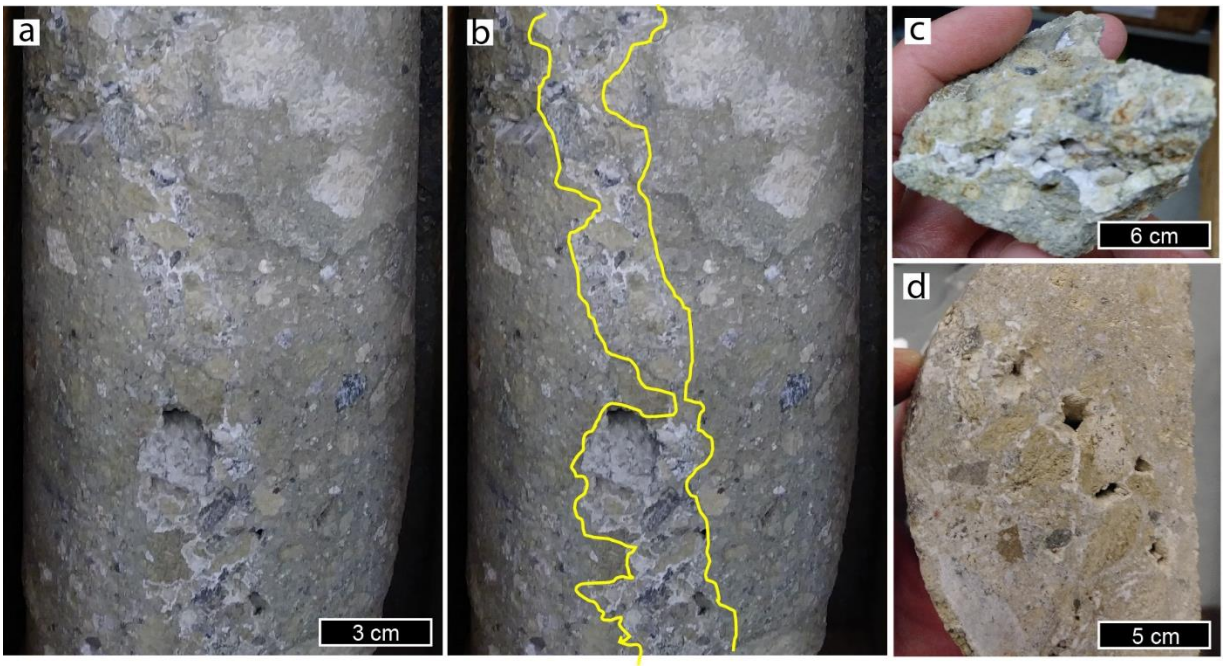

Figure 3.4. a) Nördlingen 1973 drill core with typical degassing pipe morphology (clast-rich/fine-poor interiors lined with very fine-grained materials). This section represents a drill depth of 332 – 336 m (~ 10 m below the top of the suevite unit). The alteration of the degassing pipe is a white crystalline material. b) A yellow overlay outlines the degassing pipe (white alteration) as seen from the uncut drill core exterior. c) Hand sample of the degassing pipe interior from (a). Zeolites are the dominant alteration product and occur as botryoidal clinoptilolite with bladed clinoptilolite infilling veins and capping the botryoidal forms. d) View from a cut surface of the core, looking down at the degassing pipe, showing the void spaces.

3.3. Methods

3.3.1. Powder X-ray Diffraction (pXRD)

The interiors of 28 degassing pipes were sampled for analysis. Scraped/disaggregated, powdered sample material was isolated to the <2 μm size-fraction by suspension and centrifugation, and separate aliquots were saturated with $CaCl_2$ and KCl. A subset of these samples was further separated to the <0.2 μm size-fraction. Ca-saturated samples were analyzed at 54% relative humidity (RH) and then glycolated. K-saturated samples were analyzed at 0% RH (110^o C), followed by 54% RH analyses, and then dehydrated by heating at 300^o C and 550^o C. Samples were analyzed after each treatment using a Rigaku Rotaflex RU-200B series X-ray diffractometer, equipped with a rotating anode (Co K- α source operated at 160 mA and 45 kV) and a graphite monochromator. Scans were performed from 2 to 42º 2θ at a step size of 0.02º 2θ. Nördlingen core degassing pipe samples were powdered and analyzed without clay size-fraction separation; mineral phases for the Nördlingen core samples were identified using the Bruker AXS EVA software interface with the mineral database provided by the International Centre for Diffraction Data (ICDD).

Smectite compositions and the type and amount of interstratified clay minerals were identified by modeling XRD patterns based on theoretical calculations built into the modeling software Sybilla (unpublished software). The percentage of layers for each clay mineral phase constituent, as well as the octahedral and interlayer iron content, can be adjusted via fit parameters. The Reichwete (R) ordering of layer interstratification was also adjusted – indicating the probability of finding a given layer depending on a preceding layer – to obtain better fits of the measured pattern to a simulated pattern. These fitting parameters yield the weight percentage of each constituent mineral phase.

3.3.2 Hyperspectral imaging and point spectrometry

Hyperspectral imaging of outcrops and core were acquired with a Headwall Photonics co-boresighted system custom-built for the California Institute of Technology. Images were acquired of outcrops at Aumühle, Altenbürg, and Otting quarries and of Otting, Wörnitzostheim, and Nördlingen core samples imaged under laboratory conditions at the ZERIN RiesKrater Museum, Germany. Data from the shortwave infrared (SWIR) sensor were used in this study and cover 1.0-2.6 μm with 640 spatial pixels, 285 spectral bands, and 6 nm spectral resolution. Field measurements used the sun as the incident light source, while laboratory measurements used a halogen light. Outcrops and samples propped vertically were scanned by rotating the imaging spectrometer on a motor-controlled stage. Spatial resolution depends on distance from the target but typically was on the order of several cm's in the field and sub-mm in the laboratory. (Spectral parameters and further details regarding processing imaging spectrometry are provided in Appendix A.2 and Table A.2.)

Spectral imaging was complemented by an ASD TerraSpec handheld point spectrometer with provided light source, collecting data over the 1.0-2.5 μm (SWIR) ranges. Corrections for normalizing the spectrum are computed at the instrument-level, as the background is removed by taking the ratio between the reflectance spectrum and the convex hull. Spectral resolution is 9.8 nm at 1400 nm wavelength and 8.1 nm at 2100 nm.

3.3.3 Petrography and Electron Microprobe Analysis (EMPA)

Thirteen polished thin sections of degassing pipe cross-sections were examined in both transmitted and reflected light, and a subset of eight samples were carbon-coated and analyzed using the JEOL JXA-8530F Hyperprobe at the Earth and Planetary Materials Analysis (EPMA)

laboratory at the University of Western Ontario. Wavelength dispersive X-ray spectrometry (WDS) was employed to obtain quantitative geochemical data and produce element maps. Element map data were collected at 15 kV accelerating voltage, 100 nA probe current, and 10 ms dwell time. Ca, Fe, K, Mg, Na were collected using WDS while Si, Al, P, Ti, and Zr were collected using an energy dispersive X-ray spectrometer (EDS). Quantitative spot analyses of glasses and clay minerals were collected using WDS at 15 kV accelerating voltage, 10 nA probe current, and 5 um spot size.

3.4 Mineralogy Results

3.4.1 Ejecta degassing pipes

3.4.1.1 Reflectance spectroscopy

In situ field and laboratory short-wave infrared (SWIR) reflectance spectral analysis provided an outcrop-scale spatial representation of the degassing pipe mineralogy and highlighted the variation of mineral phases between the degassing pipes and background melt-bearing breccia (e.g., Figs. 3.5a–b). The SWIR data indicates the presence of hydrated and hydroxylated mineral phases and that the degassing pipes and alteration halos are compositionally distinct from the host melt-bearing breccia. Spectra derived from laboratory point reflectance spectrometry show hydration (H_2O)-related absorptions present at ~1.4 μm and ~1.9 μm (Fig. 3.5d) – these wavelengths are masked from the field imaging spectrometry data due to atmospheric interaction (Fig. 3.5e). When individual spectra are extracted from the scene and compared to USGS library spectra (Fig. 3.5c), metal-hydroxyl bonding (ν-OH) is indicated by 2.2–2.3 μm features (Figs. 3.5c–d; Bishop et al., 2008; Clark et al., 1990). The matrix of the melt-bearing breccia is spectrally characterized by a sharp 2.21 μm absorption feature (Fig. 3.5e), resulting from either Al-OH or Si-

OH bonds, or contributions from both; an Si-OH bond is expected due to the glassy nature of the silicate impact melt. In spectra from the degassing pipes, when present, the 2.21 μm feature is typically accompanied by an additional shoulder or weak Al, Fe/Mg-OH band at 2.24 – 2.29 μm. As shown in Figure 3.5b, most of the areas with degassing pipes display spectral characteristics that are distinct from that of the host melt-bearing breccia. Specifically, the degassing pipes most often have 2.285 μm – 2.320 μm features (Fig. 3.5e), indicative of Fe/Mg-OH bearing minerals (e.g., Fe-montmorillonite, nontronite, or saponite; Hunt, 1977).

Point spectrometry data shows that cations of the degassing pipe interiors are a mix of Al, Mg, and Fe (Table 3.1). Mg is more often observed in Altenbürg and Otting degassing pipes, and the data from Aumühle (e.g., Fig. 3.5b) indicates that Fe is spectrally dominant within the degassing pipes in this location. Absorptions at ~1.41 μm (OH, H_2O) and ~2.39 μm (v-OH) also vary in center wavelength based on the octahedral cation (Fig. 3.5d; Bishop et al., 2008; Clark et al., 1990). Point spectrometry data on hand samples from Otting and Altenbürg quarries, and Otting and Wörnitzoshtheim drill cores, shows some dominant absorptions at ~ 1.39, 2.30–2.31, and ~ 2.38 μm (Fig. 3.5d). This indicates that a low Fe/Mg ratio is favored, as the v-OH band shifts from the 2Fe–OH band (2.285 μm) towards the 3Mg–OH bending and stretching vibrations at 2.32 μm (Bishop et al., 2008). All point spectrometry data collected from the Wörnitzoshtheim cores show a 2.30–2.31 μm feature, representative of the dominant v-OH bond in this degassing pipe. Point spectrometry sampling from Aumühle quarry degassing pipes did not produce the Mg-OH-indicative 2.30 – 2.32 μm feature; 54% of the sampling at Aumühle had a dominant 2.21 μm feature; 39% are dominated by 1.43 μm and 2.29 μm features, as for Fe-rich nontronite (due to 2Fe-OH bonding) (Bishop et al., 2008; Figs. 3.5d–e). Sixty percent of the spectrometry point sampling from Otting quarry samples show a dominant 2.30–2.31 μm v-OH bond; 10% are

dominated by 2.29 μm; 30% are dominated by a 2.203 – 2.211 μm feature. A continuum of smectitic clay mineral compositions from all degassing pipe sample locations is likely, depending on Al, Fe, and Mg substitutions in the octahedral sites.

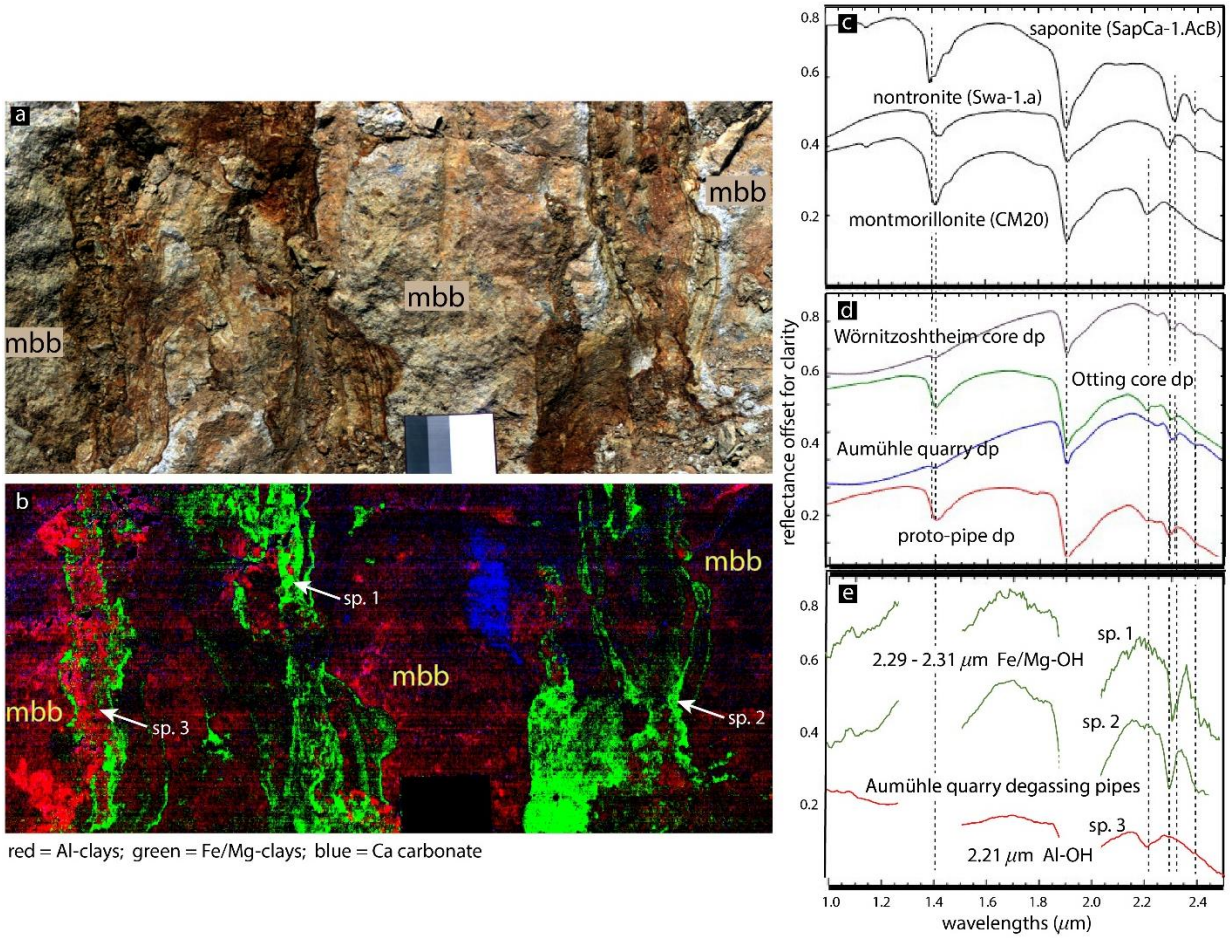

Figure 3.5. a) Field VNIR image (approximate true color) of *in situ* Aumühle quarry degassing pipes within the melt-bearing breccia unit. Spectralon calibration target shown for scale (30.5 cm width). b) Corresponding field SWIR mineral/phase spectral parameter map stretched so that the deepest absorption features (maximum 8%) corresponding to each parameter are shown; shadows have been masked. See Table A.2 for band depth (BD) parameter calculations. Red (BD2210 parameter tracking Al-OH infrared absorptions) highlights Al clay minerals; the melt-bearing lithology in the background is characterized a ~2.2 μm feature. (Note, however, that thresholds have been applied to the BD2210 parameter to highlight regions where the feature is present above background levels.). The ~2.2 μm feature also corresponds to the degassing pipes. Fe/Mg-OH bearing minerals are mapped as green (BD2300 parameter tracking the range of Fe-OH and Mg-

OH infrared absorptions. Blue (BD2340 parameter tracking C-O combination features in carbonates) highlights calcite. c) USGS library spectra (Clark et al., 2007) of Al, Fe, and Mg-smectites are shown for comparison. d) Laboratory-measured SWIR spectra of samples from Ries ejecta degassing pipes. e) Individual *in situ* SWIR spectra from spectral image in panel (b) representing the exposed degassing pipe interiors. The location of individual spectra are shown in (b) (e.g., sp. 1 = spectrum 1). Spectral gaps around ~1.4 μm and ~1.7–2.0 μm in field data have been masked out due to interference from atmospheric water vapor. Guidelines in (C-E) are at ~2.2 μm (Al-OH), ~2.29 μm (Fe^{3+}-OH), and ~2.32 μm (Mg-OH).

3.4.1.2 Powder X-ray diffraction (pXRD)

The pXRD data supports the spectral data, and further shows that the degassing pipes interiors and alteration halos comprise highly complex smectitic clay minerals. Table 3.1 provides a summary of the mineralogical compositions of the degassing pipes at studied locations.

The <2 μm size-fraction-separated Ca-saturated samples show very strong 001 reflections with d-spacings that confirm smectite composition. The *d*(001) of ~ 1.5 nm for 54% RH, air-dried samples, with an observed range of 1.461 – 1.597 nm, is observed at ~6º 2θ (Fig. 3.6a). When treated with ethylene glycol (EG)-solvation, the shifted 001 reflection (~5.2º 2θ) shows a d-spacing of ~1.7nm (Fig. 3.6b); this is a swelling/expansion consistent with the low layer charge (higher CEC) indicative of smectites (Brown and Brindley, 1980) that absorb two layers of ethylene glycol. Peaks at 0.85 – 0.86 nm also represent glycolated smectites. Importantly, the 001 peaks are broad, “drawn-out”, low-asymmetry peaks, with irrational higher-order 00l reflections; this is indicative of hydroxy interlayering in a complex, disordered structure, as monomineralic material

would instead produce ordered patterns with sharp peaks. A pure montmorillonite would produce *d*(001) of 1.66 nm – 1.71 nm for EG samples. Samples from Altenbürg and Otting quarry degassing pipes and the Wörnitzoshtheim core degassing pipes show a higher *d*(001), up to 1.75 nm. Sherman and Vergo (1988) found a similar range for Ca-saturated and glycolated (Fe^{2+},Fe^{3+}) trioctahedral saponites, and dioctahedral nontronites and (Fe^{2+},Fe^{3+})-bearing montmorillonites. By comparison of the d-spacing ranges of that study, Altenbürg and Otting are most consistent with an Fe-rich saponite. Analysis of the 060 plane of several Aumühle samples (0.1522 nm) indicates that the smectites could be either nontronite or saponite. The EG-solvated Aumühle samples were at the lower-end of the *d*(001) range at 1.62 nm, which could be explained by an interlayering with an Mg-complex which decreases d-spacing upon hydration (Brown and Brindley, 1980). The d-spacing observed in several Aumühle samples is consistent with as much as 40% interlayered chlorite/smectite (Brown and Brindley, 1980).

Further separation of the Ca-saturated <2 μm size-fraction to <0.2 μm shows a 001 peak that is smaller in ratio to the 002 – 004 peaks and is broader and slightly more asymmetric (Figs. 3.6c–d). A sharper 001 peak in the <2 μm size-fraction suggests that hydroxy interlayered material with crystallites between 2 μm and ≤0.2 μm caused peak broadening (Figs. 3.6c–d).

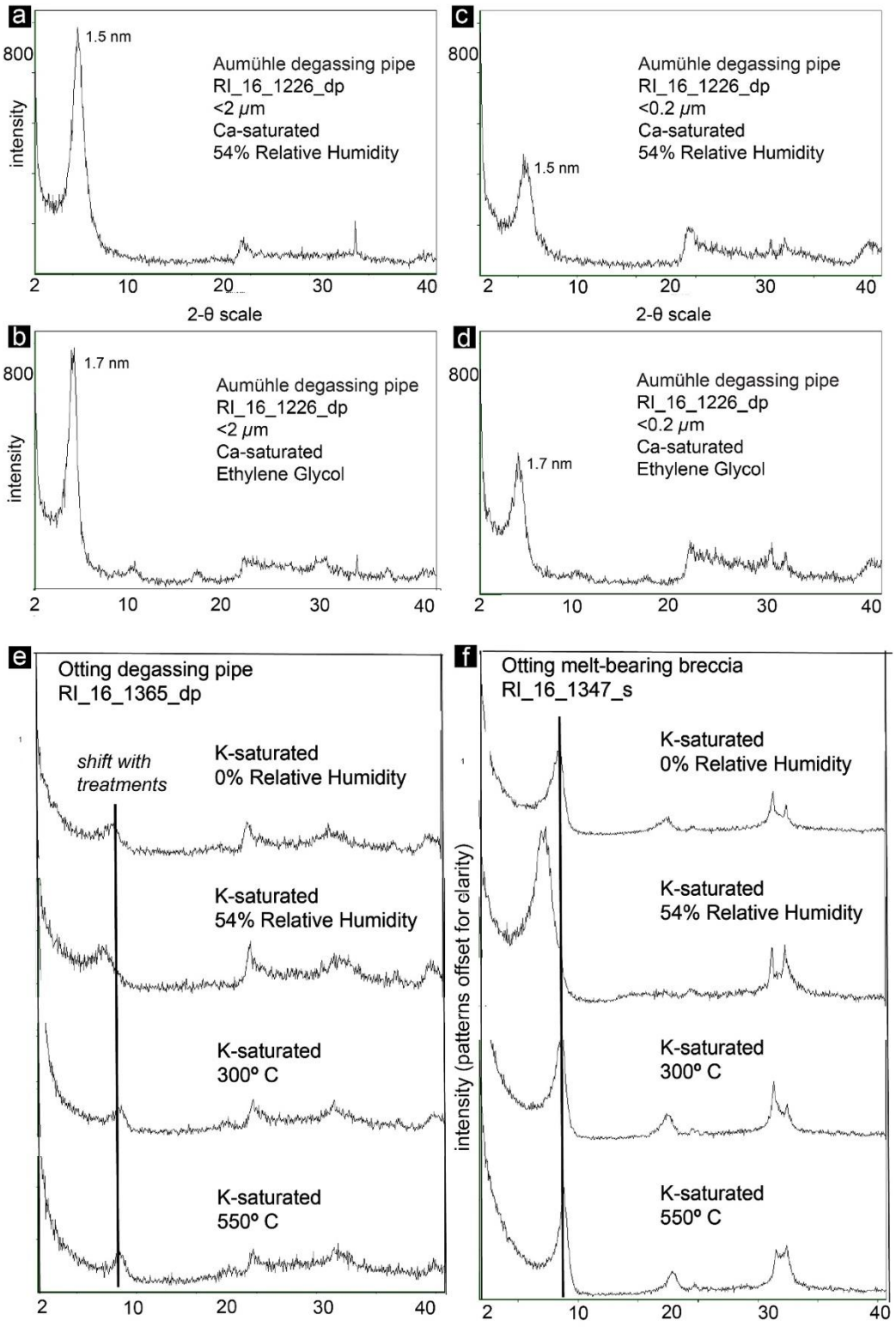

Figure 3.6. a–d) pXRD patterns are shown for ejecta degassing pipe clay-size fraction separates from Aumühle quarry, all Ca-saturated. The patterns represent two treatments as indicated,

performed in the order of hydration (54% relative humidity) then glycolated. The change in diffraction pattern appears most strongly about the basal (001) position. a) The *d*(001) of the <2 μm size-fraction shows 1.5 nm for 54% RH, air-dried samples. b) When treated with ethylene glycol (EG)-solvation, the *d*(001) shifts to 1.7nm. c) Further separation to the <0.2 μm size-fraction a broader and slightly more asymmetric 001 peak. d) When treated with ethylene glycol (EG)-solvation, the *d*(001) shifts to 1.7nm. e) Ejecta degassing pipe XRD patterns are shown for clay-size fraction (<2 μm), K-saturated separates from Otting quarry. The patterns represent four treatments, performed in the order of top to bottom. The change in diffraction pattern appears most strongly about the basal (001) position, with the shift in successive treatments as shown. With increasing heating, the 001 peak shifts toward higher 2θ but does change in intensity nor sharpen. f) XRD patterns for a K-saturated, clay-size fraction (<2 μm) from the host melt-bearing breccia. The 001 peak swells considerably with treatment (54% RH) as compared to the degassing pipe samples in (a). Comparatively, the host melt-bearing breccia patterns are sharper peaks and “cleaner”.

Table 3.1. Clay mineralogy is derived from XRD data; cation chemistry and percent and type of interlayered material is given as a relative composition of Al, Fe, and Mg, derived from EMPA WDS and XRD pattern modeling; *v*-OH is derived from reflectance (point) spectrometry, described as the percent of samples measured with given dominant *v*-OH absorption features. Modeled compositions are provided for those sample types modeled with Sybilla software; otherwise this field is left blank. Degassing pipe modeled compositions are listed as a representative of a range of samples from each quarry; XRD patterns of samples from other locations were not modeled).

Sample location	Mineralogy	Cation chemistry	Dominant *v*-OH (μm)	Modeled compositions [a]
Degassing pipe interiors in quarry exposures	poorly crystalized, turbostratically-stacked smectites, highly (randomly) interlayered with hydroxy or chloritic materials (Ca EG 1.461 – 1.597 nm)	Al/Fe/Mg	Al-OH Fe-OH Mg-OH	–
Altenbürg	mixed dioctohedral and trioctahedral clay minerals in intermediate/continuum compositions (nontronite, saponite, montmorillonite); most samples consistent with C/S	60/40 Al/Fe with ≤20% Mg:Al+Fe+Mg	42% 2.203–2.211 (Al-OH); 21% ~ 2.29 (Fe-OH); 26% 2.30–2.31 (Mg-OH)	mixed-layer dioctahedral; mixed-layer trioctahedral smectites; up to 20% interlayered chlorite (C/S); small amounts of illite possible (R1)
Aumühle	Fe-smectites with few trioctahedral samples; likely all smectites are in intermediate/continuum forms; remaining Fe are portioned to Fe-oxides as identified with μXRD	100% –5% Al:Fe; with ≤20% Mg:Al+Fe+Mg	54% 2.203–2.211 (Al-OH); 38% ~ 2.29 (Fe-OH)	mixed-layer dioctahedral; mixed-layer trioctahedral smectites; up to 3% interlayered chlorite (R1)
Otting	mixed dioctohedral clay minerals with intermediate forms; remaining Mg suggests Mg-chlorite interlayers and/or Mg + Fe in the octahedral sites	~45% Al:Fe; with ≤45% Mg:Al+Fe+Mg	30% 2.203–2.211 (Al-OH); 10% ~ 2.29 (Fe-OH); 60% 2.30–2.31 (Mg-OH)	mixed-layer dioctahedral; mixed-layer trioctahedral smectites; up to 30% interlayered chlorite and 1% kaolinite (C/S, R1)
Aumühle Alteration halos	Fe-oxides and mixed dioctohedral clay minerals in intermediate forms		100% ~ 2.29 (Fe-OH)	–
Otting core	Intermediate/mixed smectites; Low Fe/Mg ratio favored band shift from the 2Fe–OH band (2.285 μm) towards the 3Mg–OH bending and stretching vibrations at 2.31 μm		45% 2.203–2.211 (Al-OH); 27% ~ 2.29 (Fe-OH); 27% 2.30–2.31 (Mg-OH)	–
Wörnitzoshtheim core	Fe-smectite with chlorite and goethite		100% 2.30–2.31 (Mg-OH)	–
Nördlingen 1973 core (crater fill breccias)	botryoidal clinoptilolite with bladed clinoptilolite ± illite and Fe-oxides		weak 2.21 Al-OH weak 2.36 Mg-OH downslope toward 2.5	–

Melt-bearing breccia	comparatively well-ordered, higher crystallinity dioctohedral smectites with turbostratic stacking; some samples are interlayered with hydroxy and/or chloritic materials, some show a strong illitic component; kaolinite sometimes present	89% 2.203–2.211 (Al-OH); 11% 2.30–2.31 (Mg-OH)	dioctahedral smectite with kaolinite and illite (K/S, R1)

[a] Abbreviations are defined as follows: C/S = chlorite/smectite; K/S = kaolinite/smectite; R = Reichweite ordering; Ca EG = Ca-saturated, ethylene glycol-solvated samples.

The changes in diffraction patterns for the Ca and K-saturated samples occur most strongly about the basal (001) position; the 001 peaks are used for interpretation of the superstructure smectitic peaks. When the degassing pipe clay separates (<2 μm) are K-saturated and dehydrated, a broad, asymmetric *d*(001) peak is produced which collapses predictably to ~1.0 nm (e.g., Fig. 3.6e), though maximum variation is observed at 1.12 nm. Rehydration of the K-saturated material at 54% relative humidity produced smectite-like re-expansion of the 001 peak to ~1.2 nm (e.g., Fig. 3.6e) with maximum variation observed at 1.31 nm. The broad, low-intensity, low-angle asymmetric peak shape remains upon heating to 550º C, shifting toward higher 2θ. The failure of the 001 peak to completely collapse upon heating and dehydration to a narrow 1.0 nm peak indicates that interlayering is propping open the clay mineral structure. Mg-complexes (i.e., saponites or chlorites) dehydrate less readily than montmorillonites as water is retained with Mg^{+} (Brown and Brindley, 1980), resulting in a higher d-spacing. The cation exchange capacity (CEC) is reduced, hindering both contraction (upon heating) and full expansion (upon hydration). The low peak-height ratio between 001 and higher order 00l peaks are also indicative of a high component of interlayered cations.

A summary of the mineralogy is provided in Table 3.1 for degassing pipe samples from studied locations, as well as samples from the host melt-bearing breccia. The groundmass of the

melt-bearing breccias of the ejecta are dominated by fine-grained clay minerals (up to ~70 vol%; Osinski, 2004); montmorillonite is consistent with the platy-textured clay mineral of the groundmass, which is cross-cut by a finer-grained "clayey" material, suggestive of a hydrothermal alteration overprint (Newsom et al., 1986; Osinski, 2004). Sapers et al. (2017) compared the finer-grained clay minerals of the melt-bearing breccia groundmass of the surficially-exposed ejecta (Aumühle quarry) to those at depth (Wörnitzoshtheim core) and suggested that they were mineralogically consistent; these workers further observed that this alteration was localized and spatially restricted in the surficially-exposed deposits. We sought to investigate if the finer-grained clay minerals of the host melt-bearing breccias were different from the degassing pipe interiors in terms of clay mineralogy and interlayer type and abundance, and therefore alteration histories. When K-saturated, melt-bearing breccia separates produced XRD patterns with a comparatively higher peak-height ratio between 001 and higher order 00l peaks (e.g., Fig. 3.6f). Upon heating, the broader 001 peaks collapse to sharp 001 peaks. In some samples, heating to 550 °C produces a collapse at ~0.7 nm and ~0.358 nm due to a kaolinite component. By comparison, the degassing pipe material is highly interlayered, having muted (low intensity), broad peaks (e.g., Fig. 3.6e) that indicate a more disordered, poorly-crystallized material. The sharper 001 peaks and "cleaner" overall patterns produced by the melt-bearing breccia (e.g., Fig. 3.6f) samples suggest a clay mineral phase having more ordered cations in distinct sites, like illite, and which is better crystalized.

The types and amount of interstratified material and the smectite composition was identified by modeling the pXRD patterns. A heterogeneous composition of the clay minerals from all three ejecta melt-bearing breccia quarries were modeled, yielding a best-fit of mixed-layer dioctahedral and mixed-layer trioctahedral smectites with up to 30% interlayered chlorite and

small amounts of kaolinite (<5%) (Table 3.1). Modeling of Aumühle degassing pipes (sample 1229) yielded a best fit of 85% double-layer trioctahedral smectite (SS) with 3% chlorite and 12% kaolinite, and a moderately high degree of disorder (R1, where R (Reichweite ordering) describes the layer nearing-neighbor effects), and high interlayered Fe. Analysis of the 060 plane of this sample (0.1522 nm) indicates that the smectites could be either nontronite or saponite. Modeling from Altenbürg (sample 00008) produced a three-layer smectite (100% chlorite/double-layer smectite, C/SS R1) having very low octahedral and interlayered Fe content. Chlorite/smectite (C/SS R1) as modeled from Otting (e.g., sample 1343) also indicated that little interlayer space or octahedral vacancies were filled by Fe.

By comparison, the background melt-bearing breccia samples produced XRD patterns that were more representative of an Al-clay mineral: a hydroxyl-interlayered montmorillonite with kaolinite and/or illite (Table 3.1). The melt-bearing breccia patterns generally display sharper, better defined peaks, and less asymmetry. Modeling of melt-bearing breccia from the Aumühle quarry (sample 1347) produced a best-fit with a moderately disordered, three-layer, kaolinite/smectite (KSS R1) with high interlayer and octahedral Fe.

3.4.1.3 Electron Microprobe Analysis (EMPA)

The Wavelength dispersive X-ray spectrometry (WDS) data from a subset of degassing pipes studied in thin sections support the idea that the interiors are lined with complex and interlayered smectitic clay minerals, likely in continuum compositions between mineral end-members on Al, Fe, and Mg substitutions in the octahedral sites. The geochemical point data obtained from WDS integrates a ~5 μm analysis spot; the data obtained by each spot analysis necessarily integrates the geochemistry from the clay-size fraction (<2 μm) and the finer-grained

component (<0.2 μm size-fraction crystallites). As shown in Figure 3.7, the smectites range from Al-rich to Al-poor as Fe and Mg increase. An Fe-rich composition of Aumühle quarry degassing pipe samples (shown as black points in Fig. 3.7) is consistent with a continuum from montmorillonite to nontronite, as observed in the spectral data. In some Aumühle samples, the Mg content is as much as ~ 20% (as a normalized Al/Fe/Mg ratio), which was not observed in the spectral data. Geochemical data from Altenbürg cluster in a zone that indicates as much as ~ 20% Mg and as much as ~ 50% Fe (Fig. 3.7). Otting quarry samples also indicate a compositional mixture, with as much as ~ 45% Mg but much less Fe than observed at Aumühle. Intermediate compositions between montmorillonite and nontronite or saponite are indicated by Si/Al ratios (0.31) for degassing pipe samples from all quarry locations, ranging from 0.26 – 0.42. This range is consistent with smectites having an intimate mixture of other materials (e.g., hydroxy material, very fine-grained chlorites or zeolites). Illite can also alter the Al/Si ratio of smectites, but the lack of K (0.04 K/Al) observed indicates that an illitic component is unlikely.

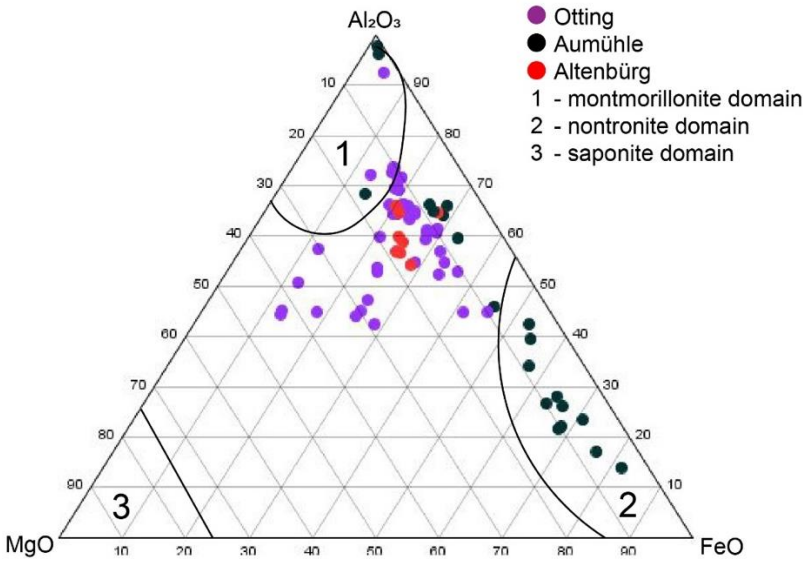

Figure 3.7. EMPA WDS geochemical data for Otting, Altenbürg, and Aumühle quarry degassing pipe thin sections plotted as an Al_2O_3/MgO/FeO ternary diagram. Mineral nodes are provided. The degassing pipe data plots as general continuum compositions between discrete mineral phases. Aumühle data points (black) have an Fe-dominant composition. Otting data points (purple) have the most Mg, at ~ 45% as a normalized Al/Fe/Mg ratio. Altenbürg data points (red) are tightly clustered at ~ 60/40 Al/Fe with <20% Mg.

Backscattered electron imaging supports the spatial relationships similar to those observed from the *in situ* SWIR spectroscopy and further shows the morphologies of the crystallites comprising the degassing pipe alteration. Figure 3.8 shows BSE images and WDS element maps from degassing pipes, with Fe and Mg-rich clay minerals infilling vesicles and pore space. The space-filling alteration shown from an Altenbürg degassing pipe (Figs. 3.8a–b) has two distinct textures: a bladed texture (implying a relatively longer formation period) that apparently formed subsequent to and concurrent with "fuzzy" very fine-grained (sub-μm), or nanocrystalline clay-phase. The bladed-textured clay minerals are Fe-rich (Figs. 3.8b–c), and the very fine-grained clay

minerals are Mg-rich (Figs. 3.8b–d). These differing textures provide support to the analysis from the <2 and <0.2 μm size-fraction separates – that the material at the smaller size-fraction is distinct, and more amorphous or highly disordered (Fig. 3.6). Furthermore, the BSE imaging and WDS element maps indicate that the smaller size-fraction material is of Mg-rich composition, in support of a saponitic or chloritic nature. The overall presence of Al, Fe, and Mg is consistent with a compositional continuum of the clay minerals.

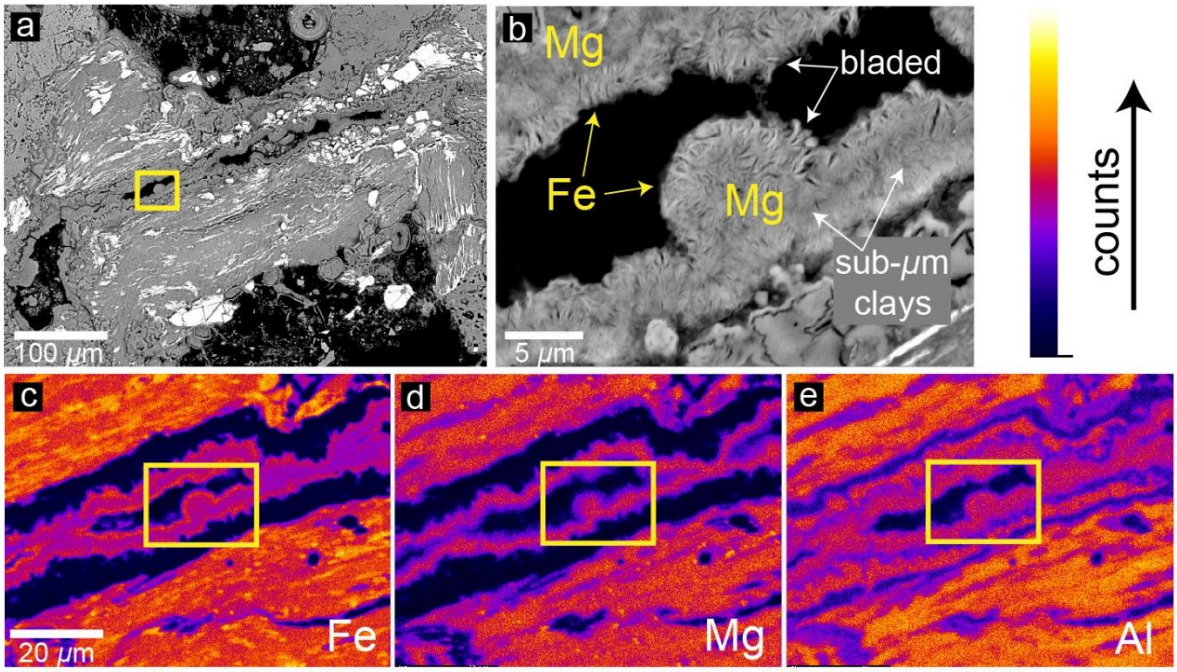

Figure 3.8. a) Backscattered electron image an Altenbürg degassing pipe in thin section (sample 00013). Yellow box indicates the area shown in (b). b) Subset of (a) shown by yellow box, magnified to show clay mineral textures. Fe and Mg-rich clay minerals infill vesicles and pore space. Fe-rich clay minerals are associated with larger, fibrous crystallites; Mg-rich clay minerals are associated with a very fine-grained (sub-μm) "fuzzy" texture. c) WDS Fe-specific map displaying qualitative Mg abundances, with yellow box to indicate subset image of (b). d) WDS Mg-specific map. e) WDS Al-specific map.

In summary, the Al/Fe/Mg smectitic clay minerals lining the ejecta quarry degassing pipes are a heterogeneous compositional continuum of end-member minerals (e.g., nontronite, saponite, and montmorillonite) characterized by high degree of disorder, complex interlayering, and very little and/or ill-defined other mineral phases at the <2 μm size-fraction. The amount of interlayered

material is variable, but XRD and EMPA data indicate that it is comprised of Mg-rich material, consistent with a Mg-rich phyllosilicate or other complex Mg-hydroxy material. The XRD pattern modeling indicates that the interlayered material is of a chloritic composition; the 001 peak structure of the XRD pattern is interpreted to be "propped open" by chloritic material as it fails to collapse upon 550º C heating treatments. The observed variability of chemical compositions of the modeled clay minerals are due to cations occupying vacancies in three non-independent sites within the mineral structure (i.e., tetrahedral, octahedral, interlayer), giving rise to a number of possible end-members in a solid solution series (e..g., Fritz, 1983).

3.4.2 Crater-fill degassing pipes

In addition to the analyses of the degassing pipes within the ejecta deposits, we provide the first known description of a degassing pipe in the Nördlingen 1973 core, located within the crater-fill melt-bearing breccia deposits. Consistent with degassing pipe morphology, the interiors provide vertically-oriented void spaces that are clast-rich and fines-poor, lined with fine-grained material that coats the pipe walls and entrained clasts (Fig. 3.4). Zeolites are the dominant alteration product observed in the Nördlingen core pipes, as determined by pXRD (Fig. 3.9a), occurring as white, botryoidal clinoptilolite with bladed clinoptilolite infilling veins and capping the botryoidal forms (Fig. 3.4). Other mineral phases include illite, gypsum, and jarosite, with less-certain peak matching to montmorillonite and chlorite (Fig. 3.9a). Yellow-brown-orange alteration was present, localized to glass clasts sparsely entrained throughout the Nördlingen core degassing pipe. Mineral phases specifically from these color zones was determined by pXRD to be jarosite and goethite, with additional clay mineral phases (Fig. 3.9b). Laboratory short-wave infrared (SWIR) reflectance spectra was performed on the white alteration and compared to standard USGS spectra (Fig. 3.9c). The data show hydration bands present at ~1.4 μm, ~1.9 μm, and a slope toward

~2.5 μm (Fig. 3.9d). Zeolites have a characteristically smaller ~1.4 μm hydration feature, a deeper, sharper ~1.9 μm hydration feature, and a ~2.5 μm indicative feature (Clark et al., 1990; Cloutis et al., 2002), producing a negative slope from ~ 2.2 μm (Fig. 3.9d). Subtle, yet consistent features are present in the spectra at 2.205 and 2.357 μm; the spectra were matched to the USGS illite spectra (Fig. 3.9a). Spectral features of jarosite are not observed.

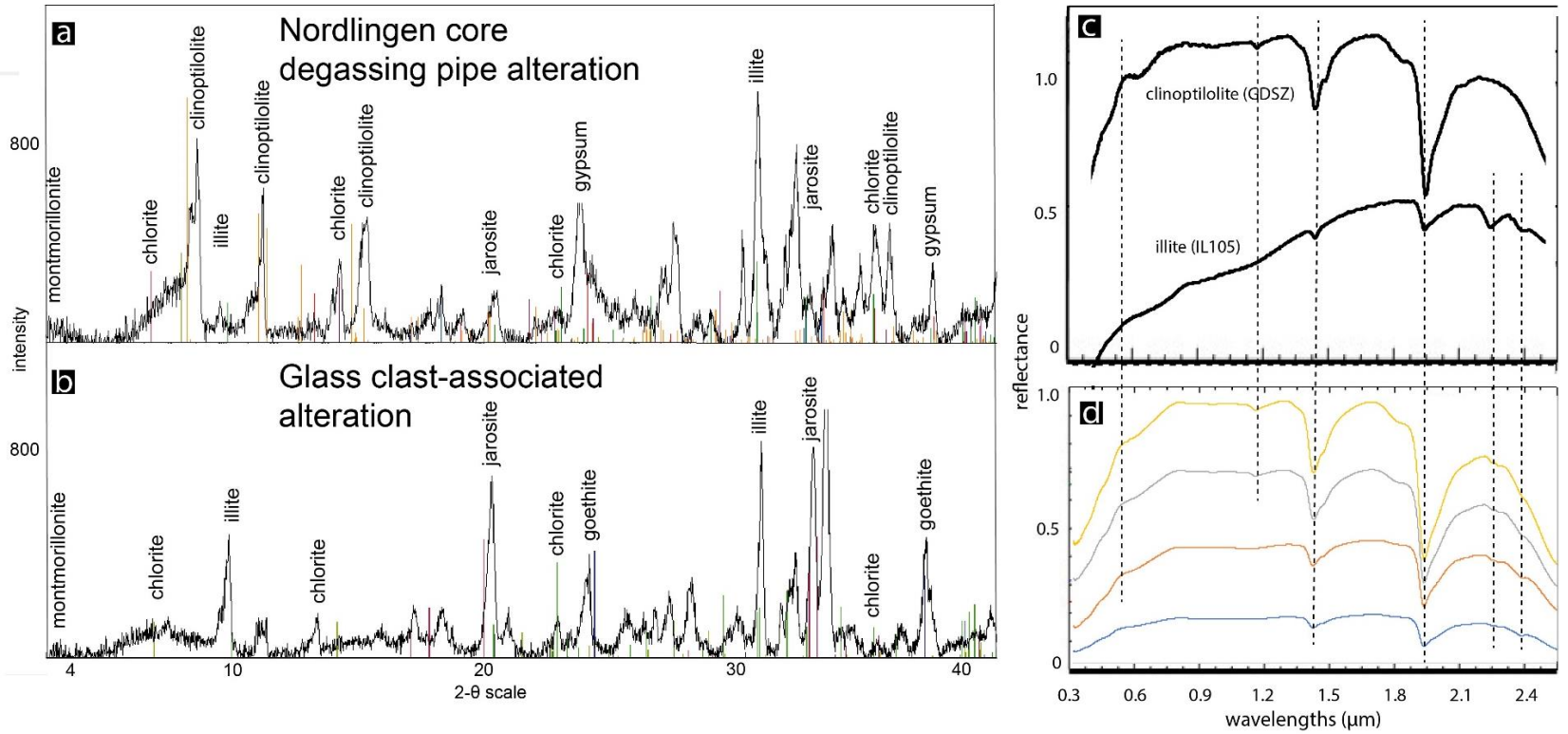

Figure 3.9. a) pXRD pattern from the white alteration lining the interior of the Nördlingen 1973 core degassing pipe (Fig. 3.3). Clinoptilolite is the dominant mineral phase, with minor smectites and sulfates. b) pXRD pattern from the yellow-orange-brown alteration surrounding glass clasts entrained in the degassing pipes, showing Fe-oxyhydroxides, sulfates, and clay minerals. c) USGS spectra (Clark et al., 2007) for clinoptilolite and illite as compared to (d) VIS-SWIR ASD point spectra of samples from Nördlingen

1973 core degassing pipe. The blue Nördlingen spectra is most similar to illite; the yellow Nördlingen spectra is most similar to clinoptilolite; all spectra suggest a mixing of mineral phases. Spectra are offset for clarity.

3.5 Discussion

The Al/Fe/Mg smectitic clay minerals lining the ejecta quarry degassing pipes are a variable, heterogeneous compositional continuum of end-member minerals (e.g., nontronite, saponite, and montmorillonite) and contain hydroxy-interlayer material of a chloritic nature. Although Aumühle quarry degassing pipe interiors are comprised primarily of Fe-rich smectites (Figs. 3.5 and 3.7), XRD pattern modeling (Table 3.1) and WDS geochemical data (Fig. 3.8) indicate that up to 3% chlorite may be present, with up to 20% Mg (as a ratio of Al/Fe/Mg cations) present in some samples. This is an interesting finding, as these proportions of Mg-rich material are not observed in the reflectance spectral data at Aumühle. The 2.32 μm feature commonly associated with saponite is rarely observed in the reflectance data from Aumühle, and the spectral shape of chlorite and the indicative 2.35 μm feature is even more rarely observed, though small amounts of these minerals may be present. A band shift is observed in the data from the 2Fe–OH band (2.285 μm) towards the 3Mg–OH bending and stretching vibrations at 2.315 μm, and may account for the Mg in the continuum-composition clay minerals. Baldermann et al. (2014) synthesized saponites having octahedral substitutions of Mg, Fe^{2+}, and Fe^{3+} cations, and found that their spectral features exhibited mainly dioctahedral Fe^{3+}-OH features, suggesting this was due to the oxidation of the samples; this scenario is plausible for ferric iron-dominated degassing pipe alteration, as at Aumühle. The chloritic component of degassing pipe clay minerals is present in varying amounts as interlayered within the smectites; it also may be possible that the reflectance spectra do not deconvolve the interlayer constituents as is possible with the XRD data and therefore the chloritic component is not readily observed.

This work describes, for the first time, the complex smectitic clay mineral composition of the alteration lining the degassing pipes: what were the volatile and cation sources for these clay

minerals? Newsom et al. (1986) suggested various potential volatile sources within the melt-bearing breccias for degassing pipe formation, including volatiles trapped and/or incorporated during the emplacement of the melt-bearing breccia unit, basement rock inclusions, hydrous melt phases, and gases released due to heating of the volatile-rich underlying Bunte Breccia deposits. Other workers (e.g., Pietrek and Kenkmann, 2016) have suggested that their formation arose solely as a degassing of the Bunte Breccia. At Aumühle quarry, where the Bunte Breccia/melt-bearing breccia contact is exposed, a mineralization pathway clearly emanated from the Bunte Breccia and into the impact melt-bearing breccia, eventually forming degassing pipes (e.g., Fig. 3.3). Clearly, where an underlaying volatile-rich source exists (e.g., Bunte Breccia), a degassing of that unit will likely occur. However, we suggest that any volatile source that is available will be involved in the formation of degassing pipes and other early impact-hydrothermal activity, including mineral-bound, interstitial, meteoric, or even ground-ice in the case of Mars. Indeed, the observation of degassing pipes in the Wörnitzoshtheim core and the Nördlingen core show that the volatile-rich Bunte Breccia is not a necessary source of volatiles for their formation; we further suggest that the cation sources for the clay minerals lining the degassing pipes and associated alteration may have been derived from the melt-bearing breccia itself. The sedimentary-derived Bunte Breccia is an unlikely cation source for Fe/Mg smectites that line the degassing pipes; the alteration of impact melt and the clasts of the crystalline basement – having clinopyroxenes, amphiboles, feldspars and biotite – generally produces Mg-smectites, nontronites, and mixed di-trioctahedral smectites (Banfield and Eggleton, 1990). The hydrous melt phases would most likely be an important source for volatiles and cations, as suggested by Newsom et al. (1986); commonly, vesicular glass clasts within the melt-bearing breccia contain a considerable volatile content (~6 wt %), and rarely have been observed to contain up to ~20% by weight H_2O (Osinski, 2003). At Aumühle, degassing

pipes were observed to often bisect glass clasts, producing red-brown alteration halos; smaller glass clasts are often entrained within degassing pipes, providing obvious cation sources.

The Navarupta-Katmai fumarole pipes, Alaska, were formed – at 200 – 400 °C (Fisher and Schmincke, 1985) – by focused gas ascent due to a fluidization pressure differential that originated from interstitial water trapped during emplacement, liberated in part by devitrification of glass (Hildreth and Fierstein, 2012). At Ries, the ejecta was emplaced at temperatures of >750 – 900 °C (Osinski et al., 2004) and heat was initially lost quickly through convective cooling in the form of degassing until the temperature of the deposit fell below 100 °C; during this early cooling phase, hydroxides and hydroxyl groups were liberated (at ~ 650 – 1000 °C; Deer et al., 1998) from melt-bearing breccia materials and likely served as contributory volatile sources.

This work supports previous findings of the bulk melt-bearing breccia secondary alteration (Sapers et al., 2017), and that post-impact hydrothemal activity in Ries melt-bearing breccia deposits were much more extensive than previously thought (e.g., Muttik et al., 2008; Muttik et al., 2010). The alteration assemblages comprising ejecta degassing pipe interiors are compositionally distinct from the secondary alteration of the surrounding melt-bearing breccia deposits; this study confirms that montmorillonite comprises the groundmass, based on the Ca saturation and ethylene glycol treatment series and concomitant XRD patterns and 001 peak shifts (e.g., Fig. 3.6). The Al-smectite, typical of metasomatic argillic alteration, is rich in K and has other lower temperature clay minerals like kaolinite, illite, illite-smectite, and halloysite. However, hydroxy interlayered materials and a hydrated nanocrystalline clay-phase (i.e., “fuzzy-textured clay minerals, Fig. 3.8) are present in both the melt-bearing breccia groundmass and in the lining of the degassing pipes, in both surfically-exposed deposits and those in drill core; we interpret that studying these deposits, surficially and at depth, formation process other than

surficial weathering and hydrothermal needs to be considered. We suggest that the early hot, hydrous ejecta alteration (as described by Schwenzer and Kring, 2013) likely includes autometamorphism (internal mineral alteration and recrystallization of molten rock through strictly endogenous volatiles during the post-impact cooling phase (e.g., Naumov, 2005; Osinski, 2005; Osinski et al., 2013) and devitrification/recrystallization (as described for closed-system alteration of volcanic glass-bearing deposits; e.g., Drewes, 1963). However, the degassing pipes are an obvious physical manifestation of the highly localized and spatially-restricted hydrothermal or degassing alteration that has been previously reported throughout melt-bearing breccia deposits within the crater rim (e.g., Sapers et al., 2017). This study extends observation of secondary hydrothermal alteration to ejecta deposits outside of the crater rim (Otting and Altenbürg quarries). This study's findings of the smectite mineralogy comprising the melt-bearing breccia groundmass and the degassing pipe interiors in the ejecta at Ries could have implications for the presence of these phases – and the necessary volatiles to form these minerals and features – on other rocky bodies in the solar system.

3.6 Planetary Implications

Tornabene et al. (2012) described widespread pitted material in and around impact craters on Mars (e.g., Fig. 3.1); dense clusters of pits were observed to occur within ponded and flow-like deposits as quasi-circular depressions that scale with crater diameter (~10 m – 3 km in diameter). Both Tornabene et al. (2012) and Boyce et al. (2012) provide geologic and morphologic evidence, including a conceptual model, that supports that these deposits are consistent with impact melt-bearing deposits, similar in emplacement and lithologic character to the melt-bearing breccias at Ries. These impact deposits types with pitted material have also

been observed associated with the best-preserved impact craters on Vesta (Denevi et al., 2012) and Ceres (Sizemore et al., 2017). These workers have suggested that the degassing pipes at Ries may represent the pit features in vertical cross-section, and that both features were a likely consequence of a impact-induced degassing following impact into a volatile-rich crust. Boyce et al. (2012) also drew this analogy, and suggested an explosive gas (high flow rate) formation model that would explain both Martian pit and Ries degassing pipe features.

It is important to note the problem of scale when comparing the degassing pipes at Ries to crater-related pit features on other planetary bodies: the observed difference in size is an order of magnitude. Any structures at the size of Ries degassing pipes are below the resolution of HiRISE; however, it has been postulated that the individual pipes coalesce into larger collapse features, and the pits are a surficial expression of pipes – a surface that have not been preserved at Ries. It is possible that larger pits would have formed at the surface of pipes, given the density of the degassing pipes observed at Aumühle (~5 per m; Table A.1) coupled with the "spouting, fountaining, and explosive-like conditions at the top of the pipes" proposed during formation (Boyce et al., 2012). The varying conditions on other planetary bodies may also explain the potential problem of scale. As noted by Boyce et al. (2012) the lower acceleration due to gravity and atmospheric pressure of Mars as compared to Earth may have extended the duration of flow, caused increased pit erosion at the surface, and resulted in an increased surficial growth of the features. We suggest that field studies on terrestrial analogues such as the Navarupta-Katmai fumarole pipes are necessary for further comparative study of degassing pipes to investigate: the surficial expression as relative to the size of the pipes at depth; evidence for explosive activity at the surface of the pipes; the potential for pipe coalescence; the role of volatiles and resultant mineralization, and; the origin of pipes in the middle of a unit and at unit contacts.

If indeed these are analogous features with similar formation mechanisms, the hydrothermal origin of degassing pipe alteration mineral assemblages would support the role of volatiles in the formation of crater-related pitted deposits. Our work at Ries shows that the thinner and less voluminous impact melt-bearing breccia deposits in Ries ejecta (e.g., Aumühle) developed degassing pipe mineralization – smectite-dominated – that is distinct from alteration developed in the more voluminous crater fill deposits in the Nördlingen core – primarily consisting of zeolites. The volume of ponded impact melt – and thus increased relative heat capacity of the deposit – and the source for volatiles and cations likely contribute to both the type of mineralization and the localized presence of degassing pipes within impact melt-bearing deposits. It has been suggested that the volume of impact melt may also dictate pit size: pitted material on Mars, present at scales large enough for individual pits to be observed in HiRISE imagery, may be present at those scales due to the volume of impact melt produced. In fact, due to the relatively well-preserved state of many Martian impactites (e.g., Caudill et al., 2018), the pitted material may provide observations of degassing pipe surface morphology that is not preserved on Earth.

Field observations of degassing pipes reveal that they may originate from within the host melt-bearing breccia deposit itself, and can be formed and mineralized from local volatile and cation sources; this may be key when considering the volatile origin and formation of crater-related pitted features on Vesta. The presence of crater-related pits on Ceres has been used to support the presence and local abundance of ground ice (Sizemore et al., 2017); the same has been suggested for crater-related pitted materials on Mars (Tornabene et al., 2012). The crust of Vesta, however, is likely devoid of such a volatile resevior. Our work on the degassing pipes at Ries – showing that an underlying volatile-rich source like that of the Bunte Breccia or other

volatile reservior may not be necessary, and may support the assertion that Vestan pits could have formed due to mineral-bound volatiles within crustal materials. The mineral-bound volatiles that formed Vestan pits have been proposed to be sourced from exogenic chondritic material implanted into the Vestan surface (Denevi et al., 2012) and, specfically, H-rich zones of more ancient regolith detected by the Gamma Ray Spectrometer suite on the Dawn orbiter (Prettyman et al., 2012). However, the volatile estimate for fluidization and formation of degassing pipes at Ries – 34 gm of water per cm^2 of melt-bearing breccia, from an estimated 1.4 wt % of water (Newsom et al., 1986) – are an order of magnitude greater than the potential volatile availability on even the most H-rich zones on Vesta (400 μgm/gm, or 0.0025 wt %; Prettyman et al., 2012). The H content of the Vestan crust would be sufficient to form the relatively thin film of secondary mineralization that lines Ries degassing pipe interiors (~20 μm thickness), but it is unclear if the volatiles present would provide the gas pressure to form degassing pipes. The pressure at which ignimbrite degassing pipes form is based on the sorting of material, the average grain size, and the loose-packed bulk density, and fluidization depends on the solid/fluid density ratio of the bed (Wilson, 1980); degassing will cause preferential pathway formation even when the density ratio is high, as fluid escapes in the form of bubbles. Although the extent of fluidization to form and mineralize degassing pipes in impact melt-bearing deposits depend on the source material and its volatile content, these deposits on terrestrial planets throughout the solar system likely share similar formation mechanisms; thus, these deposits likely share similar features, like degassing pipes, where sufficient volatiles are present. Whether or not sufficient volatiles are present within the Vestan crust for the formation of such features is likely to remain of some debate.

In closing, we note that the spatial extent and nature of impact-generated hydrothermal activity and impact-related alteration is still under investigation at the Ries impact structure despite the depth of study at the site. This should serve as a cautionary tale when discerning clay mineral provenance remotely, via landed robotic or satellite assets. The techniques used in this study to discern the interlayered clay mineral composition (e.g., clay-size-fraction separations, cation and dehydration treatments, and low-2θ XRD) are presently only practical in a laboratory setting, although imaging spectroscopy did identify and distinguish Fe, Mg, and Al-smectites in field measurements. Detailed XRD experiments, as completed in this study, are not possible to acquire via field or rover-based instrumentation. For the NASA Mars 2020 and ESA ExoMars rover missions, an incredible opportunity may be presented to observe a variety of clay-bearing materials and lithologies. For the Mars 2020 rover, this includes within the deltaic environment in Jezero Crater, Jezero's crater rim and ejecta blanket, and the larger Early/Middle Noachian Isidis impact basin, investigating impact megabreccia and other potentially impact-hydrothermally-altered rocks; indeed, if degassing pipes were observed in Jezero Crater (potentially exposed in its deeply-incised crater rim and terraces), they may represent an astrobiologically-significant target. As shown by the morphologic and mineralogic characterization in this study, degassing pipes would have accommodated pore space and provided water and nutrients for early chemolithoautotrophic life (e.g., Westall et al., 2015) if present, with subsurface protection from harmful effects of radiation and oxidation. If pipe structures are discovered, this study could provide a comparative analysis for a potential impact-related origin. For the ExoMars rover, clay-rich stratigraphies in Oxia Planum are planned as the exploration target. The impact-related alteration products observed from this work and others (e.g., Osinski, 2005; Sapers et al., 2017) at Ries structure could have implications for the origin of clay mineral phases identified in the early Martian crust as predicted

by Tornabene et al. (2013); the exploration of Mars 2020 and ExoMars rover missions may investigate the impact-related or other potential origin of clay minerals. However, we suggest that, since science payload of these rovers do not have the advantage of the high-resolution laboratory analytical techniques as were used in this study, caution should be exercised when ruling out any particular origin hypothesis for clay minerals (e.g., volcanic or impact-hydrothermal alteration products; formation under elevated or ambient temperature) until collected samples are returned to Earth.

References

Baldermann, A., Dohrmann, R., Kaufhold, S., Nickel, C., Letofsky-Papst, I., and Dietzel, M., 2014, The Fe-Mg-saponite solid solution series – a hydrothermal synthesis study: Clay minerals, doi: 10.1180/claymin.2014.049.3.04.

Banfield, J.F., and Eggleton, R.A., 1990, Analytical transmission electron microscope studies of plagioclase, muscovite, and K-feldspar weathering: Clay minerals & Clay minerals, doi: 10.1346/CCMN.1990.0380111.

Bayerisches Geologisches Landesamt, ed. 1974., 1974, Die Forschungsbohrung N€ordlingen 1973: Geologica Bavarica, v. 72.

Bishop, J.L., Lane, M.D., Dyar, M.D., and Brown, A.J., 2008, Reflectance and emission spectroscopy study of four groups of phyllosilicates: smectites, kaolinite-serpentines, chlorites and micas: Clay minerals, doi: 10.1180/claymin.2008.043.1.03.

Boyce, J.M., Wilson, L., Mouginis-Mark, P.J., Hamilton, C.W., and Tornabene, L.L., 2012, Origin of small pits in martian impact craters: Icarus, v. 221, p. 262–275, doi:

10.1016/j.icarus.2012.07.027.

Brown, G., Brindley, G.W., 1980, Crystal structures of clay minerals and their Xray identification: Journal of Mineralogical Society, p. 305–356., doi: 10.1016/j.jenvman.2011.05.031.

Cannon, K.M., and Mustard, J.F., 2015, Preserved glass-rich impactites on Mars: Geology, v. 43, p. 635–638, doi: 10.1130/G36953.1.

Caudill, C.M., Osinski, G.R., and Tornabene, L.L., 2018, Ejecta deposits of Bakhuysen Crater, Mars: Icarus, v. 314, p. 175–194.

Chao, E.C.T., Cittner, R.H., and Schmidt-Kaler, H., 1978, Principle Exponents of the Ries Meteorite Crater in Southern Germany, *in* Bayerisches Geologisches Landesam, p. 84.

Clark, R.N., King, T.V. V., Klejwa, M., Swayze, G. a., and Vergo, N., 1990, High spectral resolution reflectance spectroscopy of minerals: Journal of Geophysical Research, v. 95, p. 12653, doi: 10.1029/JB095iB08p12653.

Clark, R.N., Swayze, G.A., Wise, R., Livo, K.E., Hoefen, T.M., Kokaly, R.F., Sutley, S.J., Survey, U.S.G., and Title, S., 2007, USGS Digital Spectral Library splib06a: U.S. Geological Survey, p. Digital Data Series 231, http://speclab.cr.usgs.gov/spectral.lib06.

Cloutis, E.A., Asher, P.M., and Mertzman, S.A., 2002, Spectral reflectance properties of zeolites and remote sensing implications: , J. Geophys. Res., v. 107, doi: 10.1029/2000JE001467.

Deer, W.A., Howie, R.A., and Zussman, J., 1998, Rock-forming minerals, volume 2B (second edition): double-chain silicates:

Denevi, B.W., Blewett, D.T., Buczkowski, D.L., Capaccioni, F., Capria, M.T., De Sanctis, M.C., Garry, W.B., Gaskell, R.W., Le Corre, L., Li, J.-Y., Marchi, S., McCoy, T.J., Nathues, a, O'Brien, D.P., et al., 2012, Pitted terrain on Vesta and implications for the presence of volatiles.: Science (New York, N.Y.), v. 338, p. 246–9, doi: 10.1126/science.1225374.

Drewes, H., 1963, Geology of the Funeral Peak Quadrangle, California, on the east flank of Death Valley: Geological Survey professional paper, p. 1–75.

Engelhardt, W. v., 1972, Shock produced rock glasses from the Ries crater: Contributions to Mineralogy and Petrology, v. 36, p. 265–292, doi: 10.1007/BF00444336.

Engelhardt, W. Von, 1997, Suevite breccia of the Ries impact crater, Germany: Petrography, chemistry and shock metamorphism of crystalline rock: Meteoritics & Planetary Science, v. 32, p. 545–554, doi: 10.1111/j.1945-5100.1997.tb01299.x.

Engelhardt, W., 1990, Distribution, petrography and shock metamorphism of the ejecta of the Ries crater in Germany-a review: Tectonophysics, v. 171, p. 259–273, doi: 10.1016/0040-1951(90)90104-G.

Fisher, R. V., and Schmincke, H.U., 1985, Pyroclastic Rocks: Geological Magazine, doi: 10.1017/S0016756800031332.

Fritz, B., 1983, Simulation of Clay minerals-Solutions Interactions by Using Solid Solution Models, *in* Smectite alteration, Proceedings of a Workshop Convened at The Shoreham Hotel, Washington, D.C., p. 45–47.

Graup, G., 1978, Das Kristallin im Nordlinger Ries. € Petrographische Zusammensetzung und

Auswurfmechanismus der kristallinen Trummermassen; Struktur des kristallinen € Untergrundes und Beziehungen zum Moldanubikum: Stuttgart: Enke Verlag, p. 190.

Grieve, R. a F., Dence, M.R., and Robertson, P.B., 1977, Cratering processes-As interpreted from the occurrence of impact melts, *in* Impact and explosion cratering: Planetary and terrestrial implications, p. 791–814.

Hildreth, W., and Fierstein, J., 2012, The Novarupta-Katmai Eruption of 1912 — Largest Eruption of the Twentieth Century: Centennial Perspectives: US Geological Survey Professional Paper, p. 259.

Hörz, F., Ostertag, R., and Rainey, D.A., 1983, Bunte Breccia of the Ries: Continuous deposits of large impact craters: Reviews of Geophysics, v. 21, p. 1667–1725, doi: 10.1029/RG021i008p01667.

Hunt, G.R., 1977, SPECTRAL SIGNATURES OF PARTICULATE MINERALS IN THE VISIBLE AND NEAR INFRARED: GEOPHYSICS, v. 42, p. 501–513, doi: 10.1190/1.1440721.

Hüttner, H., and Schmidt-Kaler, R., 1999, Die Geologische Karte des Rieses 1:50 000: Geologica Bavarica, v. 104, p. 7–76.

Kieffer, S.W., and Simonds, C.H., 1980, The role of volatiles and lithology in the impact cratering process: Rev. Geophys., v. 18, http://onlinelibrary.wiley.com/doi/10.1029/RG018i001p00143/abstract.

Muttik, N., Kirsimäe, K., and Vennemann, T.W., 2010, Stable isotope composition of smectite in

suevites at the Ries crater, Germany: Implications for hydrous alteration of impactites: Earth and Planetary Science Letters, v. 299, p. 190–195, doi: 10.1016/j.epsl.2010.08.034.

Muttik, N., Kirsimäe, K., Somelar, P., and Osinsk, G.R., 2008, Post-impact alteration of surficial suevites in Ries crater, Germany: Hydrothermal modification or weathering processes? Meteoritics & Planetary Science, v. 43, p. 1827–1840, doi: 10.1111/j.1945-5100.2008.tb00646.x.

Newsom, H., Graup, G., Sewards, T., and Keil, K., 1986, Fluidization and hydrothermal alteration of the Suevite deposit at the Ries Crater, West Germany, and implications for Mars: Journal of Geophysical Research, v. 91, p. E239–E251, doi: http://dx.doi.org/10.1029/JB091iB13p0E239.

Osinski, G.R., Grieve, R.A.F., Collins, G.S., Marion, C., 2008, The effect of target lithology on the products of impact melting: Meteorit. Planet. Sci., v. 42, p. 1939–1954, file:///Files/31/31191bb2-4df2-42d5-afe5-26cdd7ed49d7.pdf.

Osinski, G.R., 2005, Hydrothermal activity associated with the Ries impact event, Germany: Geofluids, v. 5, p. 202–220, doi: 10.1111/j.1468-8123.2005.00119.x.

Osinski, G.R., 2003, Impact glasses in fallout suevites from the Ries impact structure, Germany: An analytical SEM study: Meteoritics & Planetary Science, v. 38, p. 1641–1667, doi: 10.1111/j.1945-5100.2003.tb00006.x.

Osinski, G.R., 2004, Impact melt rocks from the Ries structure, Germany: An origin as impact melt flows? Earth and Planetary Science Letters, v. 226, p. 529–543, doi: 10.1016/j.epsl.2004.08.012.

Osinski, G.R., Grieve, R. a. F., and Spray, J.G., 2004, The nature of the groundmass of surficial suevite from the Ries impact structure, Germany, and constraints on its origin: Meteoritics & Planetary Science, v. 39, p. 1655–1683, doi: 10.1111/j.1945-5100.2004.tb00065.x.

Pietrek, A., and Kenkmann, T., 2016, Ries Bunte Breccia revisited: Indications for the presence of water in Itzing and Otting drill cores and implications for the emplacement process: Meteoritics and Planetary Science, v. 51, p. 1203–1222, doi: 10.1111/maps.12656.

Pohl, J., Stöffler, D., Gall, H., and Ernstson, K., 1977, The Ries impact crater, *in* Impact and explosion cratering, p. 343–404.

Pope, K.O., Kieffer, S.W., and Ames, D.E., 2006, Impact melt sheet formation on Mars and its implication for hydrothermal systems and exobiology: Icarus, v. 183, p. 1–9, doi: 10.1016/j.icarus.2006.01.012.

Prettyman, T.H., Feldman, W.C., McSween, H.Y., Dingler, R.D., Enemark, D.C., Patrick, D.E., Storms, S.A., Hendricks, J.S., Morgenthaler, J.P., Pitman, K.M., and Reedy, R.C., 2012, Dawn's gamma ray and neutron detector, *in* The Dawn Mission to Minor Planets 4 Vesta and 1 Ceres, v. 9781461449, p. 371–459, doi: 10.1007/978-1-4614-4903-4_14.

Sapers, H.M., Osinski, G.R., Flemming, R.L., Buitenhuis, E., Banerjee, N.R., Tornabene, L.., Blain, S., and Hainge, J., 2017, Evidence for a spatially extensive hydrothermal system at the Ries impact structure, Germany: Meteoritics & Planetary Science, v. 52.

Schmieder, M., Kennedy, T., Jourdan, F., Buchner, E., and Reimold, W.U., 2018, A high-precision40Ar/39Ar age for the Nördlinger Ries impact crater, Germany, and implications for the accurate dating of terrestrial impact events: Geochimica et Cosmochimica Acta, v.

220, p. 146–157, doi: 10.1016/j.gca.2017.09.036.

Schultz, P.H., and Mustard, J.F., 2004, Impact melts and glasses on Mars: Journal of Geophysical Research, v. 109, p. E01001, doi: 10.1029/2002JE002025.

Siegert, S., Branney, M.J., and Hecht, L., 2017, Density current origin of a melt-bearing impact ejecta blanket (Ries suevite, Germany): Geology, doi: 10.1130/G39198.1.

Sizemore, H.G., Platz, T., Schorghofer, N., Prettyman, T.H., De Scantis, M.C., Crown, D.A., Schmedemann, N., Neesemann, A., Kneissl, T., Marchi, S., Shneck, P.M., Bland, M.T., Schmidt, B.E., Hughson, K.H.G., et al., 2017, Pitted terrains on (1) Ceres and implications for shallowsubsurface volatile distribution: Geophysical Research Letters, v. 44, p. 6570–6578, doi: doi:10.1002/2017GL073970.

Stoffler, D., Artemieva, N.A., Wunnemann, K., Reimold, W.U., Jacob, J., Hansen, B.K., and Summerson, I.A.T., 2013, Ries crater and suevite revisited—Observations and modeling Part I: Observations: Meteorit. Planet. Sci, v. 48, p. 515–589.

Tornabene, L.L., Osinski, G.R., McEwen, A.S., Boyce, J.M., Bray, V.J., Caudill, C.M., Grant, J.A., Hamilton, C.W., Mattson, S., and Mouginis-Mark, P.J., 2012, Widespread crater-related pitted materials on Mars: Further evidence for the role of target volatiles during the impact process: Icarus, v. 220, http://linkinghub.elsevier.com/retrieve/pii/S0019103512002047.

Tornabene, L.L., Osinski, G.R., McEwen, A.S., Wray, J.J., Craig, M.A., Sapers, H.M., and Christensen, P.R., 2013, An impact origin for hydrated silicates on Mars: A synthesis: AN IMPACT ORIGIN FOR HYDRATED SILICATES: Journal of Geophysical Research:

Planets, v. 118, http://doi.wiley.com/10.1002/jgre.20082.

Westall, F., Foucher, F., Bost, N., Bertrand, M., Loizeau, D., Vago, J. L., Kminek, G., Gaboyer, F., Campbell, K. A., Bréhéret, J. G.,Gautret, P., Cockell, C. S., 2015 Biosignatures on Mars: What, Where, and How? Implications for the Search for Martian Life: Astrobiology, 15(11): 998–1029.

Wilson, C.J.N., 1980, The role of fluidization in the emplacement of pyroclastic claws: An experimental approach: Journal of Volcanology and Geothermal Research, doi: 10.1016/0377-0273(80)90106-7.

Chapter 4: Exploring the origin of clay minerals on Mars: A case study of pre- and syn-impact formation at the Ries impact structure, Germany

4.1 Introduction

The origin of clay minerals on Mars is the subject of ongoing debate. The large amounts of these hydrated minerals identified in ancient terrains has been used to invoke the existence of a warmer, wetter paleoclimate – one that may have been highly conductive to past habitability (e.g., Nisbet and Sleep, 2001; Zahnle et al., 2007). It has been suggested that warm, wet conditions were restricted to the earliest period of Martian history (the Noachian Era, ~4.5 – 3.7 Ga), and thus, phyllosilicate-forming environments involving surficial water-rock interaction are largely responsible for these mineral phases observed in Noachian terrains (~4.5 – 3.7 Ga; Poulet et al., 2005; Bibring et al., 2006). Indeed, expansive valley systems interpreted to have been carved by running water, are also observed in Noachian terrains and have been used as additional evidence to invoke a past climate that supported surface-stable liquid water, mobilized by run-off, and even precipitation (Bibring et al., 2006; Ehlmann et al., 2008; Mustard et al., 2005). However, this origin hypothesis for clay minerals on Mars – with long-term, ambient-temperature, surface-water interaction in the presence of an atmosphere – is not well-supported by climate modeling (Wordsworth et al., 2015; Wordsworth, 2016; Hynek, 2016; Squyres and Kasting, 1994). Several factors may have led to unfavorable conditions for Early Mars to attain and sustain temperatures necessary for surface-water stability during the Noachian, including: sun luminosity was only 75% that of today (Gough, 1981); the inefficiency of CO_2 as a primary greenhouse gas (Wordsworth et al., 2013; Forget et al., 2013); and strongly chaotic obliquity cycles of Mars likely forced ice ages and prevented long periods of climatic stability (Laskar et al., 2004).

It is notable that the majority of orbital clay mineral detections on Mars are in Noachian-aged crust that is also the most heavily impact-cratered terrain; the preferential association of clay minerals with this Noachian cratered terrain is commonly interpreted as being due to the exposure of pre-existing bedrock clay minerals by the impact process (Fairén et al., 2010; Ehlmann et al., 2013). However, there is growing evidence that impact events can also result in the generation of new secondary hydrated phases, including clay minerals (e.g., Sapers et al., 2017; Osinski et al., 2004; Osinski, 2005; Naumov, 2005; Osinski et al., 2013). Discerning the origin of secondary phases in impact craters is, however, complicated by several factors associated with crater formation: (1) impact events also exhume pre-existing target rocks and disseminate them via ejecta deposits; (2) in larger, complex impact craters, pre-existing target rocks are exposed from depth in central uplifts; and (3) the crater interior depression acts as a sedimentary catchment basin for non-impact-related, transported materials (e.g., Osinski et al., 2012; Kenkmann et al., 2012). As such, elucidating mineral provenance, and thus past processes, in heavily impacted and otherwise geologically complex terrains is difficult (Tornabene et al., 2013). Understanding the origin of clay minerals, and thus, the highly variable alteration histories, is important for NASA's upcoming Mars 2020 mission; the Mars 2020 landing site is within the clay-rich Jezero Crater basin, and an extended mission may investigate the materials of the crater rim and into the ejecta deposits (Farley et al., 2018; Williford et al., 2018). The next ESA Mars rover mission, ExoMars, will also be exploring ancient Noachian clay-bearing terrain: layered, stratigraphically-bound Al/Fe/Mg smectites in Oxia Planum (Quantin-Nataf et al., 2019; Carter et al., 2019).

The well-preserved Ries impact structure, Germany, has long been studied as an analogue for impact cratering processes on Mars (e.g., Pohl et al., 1977; Hörz, 1982; Engelhardt et al., 1995; Osinski, 2004; Schaal and Horz, 1977; Sturm et al., 2013) and provides an excellent site to

investigate pre- and syn/post-impact clay minerals. Indeed, it contains some of the best-preserved and exposed impact ejecta deposits on Earth. The continuous ejecta deposits, known as the Bunte Breccia (e.g., Morrison and Oberbeck, 1978; Hörz, 1982; Hörz et al., 1983), preserve clay-rich Miocene sediments and limestones from the time of impact and are largely free from impact alteration, aside from brecciation through transportation, having low levels of shocked material (< 10 GPa) and very little, if any, incorporated impact melt (Hörz et al., 1983). The discontinuous ejecta deposits that overlay the Bunte Breccia (e.g., Figs. 3.1a–c), as well as materials of the crater fill within the inner crystalline ring (Fig. 3.1d), are comprised of impact melt-bearing breccias in various states of impact-induced alteration (Stähle, 1972; Stahle and Otterman, 1977; Newsom et al., 1986; Osinski, 2005; Sapers et al., 2017). The extent of post-impact hydrothermal alteration in ejecta deposits at the Ries has generated substantial debate; the melt-bearing breccias are mineralogically complex, with highly heterogenous alteration and a surficial ambient-temperature alteration overprint. Some have suggested that hydrothermal activity was restricted to the crater fill deposits (e.g., Muttik et al., 2008; Muttik, et al., 2010); however, platy montmorillonite (Osinski, 2005; Newsom et al., 1986) and complex trioctahedral smectites in altered glass clasts within the melt-bearing breccias (Sapers et al., 2017) are consistent with clay mineral formation through localized hydrothermal activity. It has been suggested that complex Al-clays in the groundmass represent crystalline rock flour (Engelhardt and Graup, 1984) or were formed through post-impact hydrothermal alteration of fine-grained glass (Engelhardt, 1972; Stähle, 1972; Newsom et al., 1986, 1990). Osinski et al. (2004) noted that the chemical heterogeneity, lack of Na (typical of hydrothermal montmorillonite), textural evidence, and cross-cutting relationships of multiple phases of the groundmass clays are inconsistent with a hydrothermal origin for up to ~ 70 vol% of melt-bearing breccia groundmass. Instead, Osinski et al. (2004) offers evidence for an

impact melt origin for the groundmass material, including flow-textures, “budding off” clay globules, and quench-textured crystallites. Secondary hydrothermal montmorillonite – displaying platy, open-space-filling textures – overprints and cross-cuts the finer-grained “clayey” groundmass, and comprises only <10 – 30 vol% of the groundmass by comparison (Newsom et al., 1986; Osinski et al., 2004). The nature and formation of the complex, geochemically heterogenous “clayey groundmass” remains enigmatic, yet comprises a majority of the melt-bearing breccia groundmass.

This work seeks to further investigate the clay minerals of the Ries melt-bearing breccia matrix to better understand clay mineral formation processes in impactites, particularly in the understudied ejecta deposits. We compare these impactite clay minerals to pre-impact clay minerals excavated and preserved in the Bunte Breccia deposits. In this comparison, we expound on the variety of formation conditions and, thus, end-member types of clay minerals in impactites. We then extend this understanding to the clay minerals observed on Mars; crucially, ejecta deposits on Mars are typically an underappreciated but likely a volumetrically important and spatially-extensive part of the crust. Importantly, this work reveals the difficulty in discerning clay mineral formation based on mineralogy alone, particularly in the absence of high-resolution laboratory techniques with multiple supportive datasets. This is of particular concern for discerning the formation and origin of clay minerals on Mars *in situ* given the inherent limitations of orbital and rover-based instruments and techniques. It is our hope that this and other in-depth field studies at the Ries will provide context and laboratory analyses as a baseline for clay mineral composition of impact-related materials, aiding in the interpretation of the provenance of clay-bearing materials investigated on the surface of Mars.

4.2 Ries impact structure

The 24 km-diameter (Pohl et al., 1977) Ries impact structure, Germany (Fig. 4.1d), has been dated at 14.808 ± 0.021 Ma (Schmieder et al., 2018). The pre-impact stratigraphy from which the Bunte Breccia is derived comprises ~600 m of sediments, including ~25 m of unconsolidated Middle Miocene sands, marls, and clays, 190 m of Upper Jurassic limestone, 65 m of Middle and Lower Jurassic claystones and sandstones, and 300 m of Triassic sandstones and claystones (Engelhardt et al., 1995). The polymict Bunte Breccia is interpreted to have formed as ballistic ejecta comprising materials from the sedimentary sequence. During emplacement and ground-flow of the ballistic ejecta to radial extents of up to ~45 km (Huttner, 1969), local materials (weathering horizons, other surficial substrate, and water present at the time of impact) were entrained as "secondary ejecta", comprising ~69 vol% on average of the deposit (Hörz et al., 1983). Bunte Breccia is the basal ejecta unit, volumetrically comprising the majority of the Ries ejecta deposits, up to >90% of the ejecta deposits outside of the crater rim (Hörz et al., 1983). The clays within the Bunte Breccia are detrital terrigenous clay minerals and other minerals derived from the weathering of the lithologies in the Bohemian Massif (320 – 580 Ma) during the Cadomian Orogeny in the Central European Basin (Wemmer, 2008). These deposits are locally overlain by impact melt-bearing ejecta deposits (Figs. 4.1a–c), also known as "suevite". The melt-bearing breccia was deposited at a high temperature (>900 °C) and contains highly-shocked and melted materials; this is in contrast to the Bunte Breccia which has very little evidence of shock (Osinski, 2004). It has been proposed that the melt-bearing breccias were emplaced as a flow (Siegert et al., 2017; Osinski, 2004), evidenced by flow-textured silicate impact melts (with calcite and clay minerals) quenched after emplacement (Osinski et al., 2004) with the deposits conforming to underlying topography (e.g., Fig. 4.1c). This flow behavior is similar to impact melt ponds

observed on the ejecta of craters on other bodies (e.g., Osinski et al., 2011; Tornabene et al., 2012). The complex clayey groundmass hosts lithics, minerals, and angular clasts derived from the deeper crystalline basement comprised of a variety of gneisses, amphibolites, and granites (Graup, 1978; Engelhardt, 1990).

In summary, although an impactite, the Bunte Breccia is representative of pre-impact materials in this study, as it has not undergone substantial impact-related shock metamorphism of post-impact alteration (Hörz, 1982; Hörz et al., 1983); it is considered here to serve as the preserved near-surface sedimentary sequence at the time of impact. However, the clay minerals from the overlying, discontinuous melt-bearing deposit are secondary, formed from impact-related processes or produced afterward through post-impact non-impact related ambient weathering processes. We therefore examined samples in this study from the Bunte Breccia and the melt-bearing breccia as a comparative study of clay minerals formed prior to (and present at) the time of impact, and those of impact- and post-impact origin.

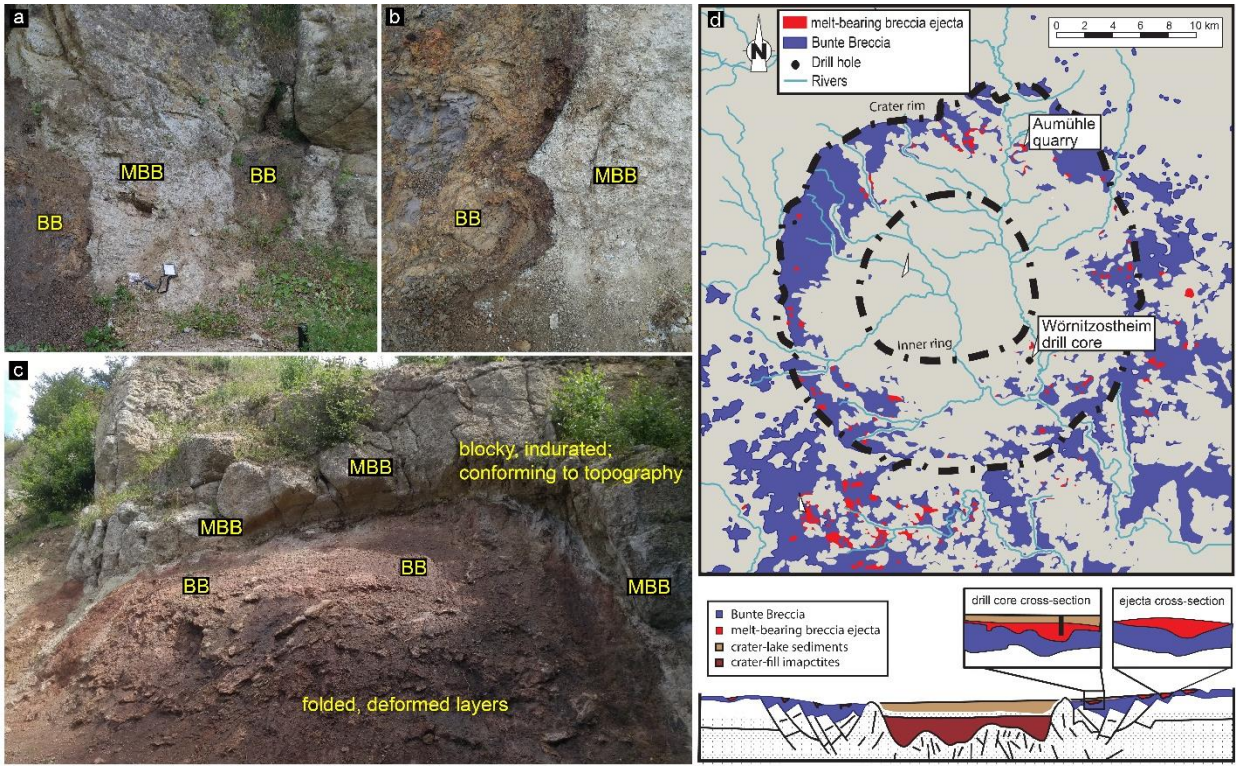

Figure 4.1. a) Bunte Breccia (BB; dark brown/red) and melt-bearing breccia (MBB; light grey) in contact along the east wall of Aumühle quarry. Note the sharp and undulating contact. Handheld tablet shown for scale. b) Zoom image of (a) showing the sharp contact. c) Cross-section of the contact. The melt-bearing breccia (MBB) overlies the Bunte Breccia (BB), conforming to its topography. The difference in erosional character of the two units are shown: the melt-bearing breccia (MBB) is blocky and well-indurated; the Bunte Breccia is a slope-forming lithology and/or with poorly-consolidated materials. Though brecciated, original layering is retained in the Bunte Breccia. d) Geological map of Ries impactites (modified after Hüttner and Schmidt-Kaler, 1999) with a graphical representation of the ejecta units in cross-section. The sample location of Aumühle quarry is shown.

4.3 Methods

Our sampling efforts focused on the Aumühle quarry, 3 km inside the northeastern crater rim (Fig. 4.1d), at the best-known exposure of the Bunte Breccia/melt-bearing breccia contact. Twenty samples (ten samples each of melt-bearing breccia and Bunte Breccia) were collected. Exposures of the Bunte Breccia in this location are composed of sedimentary rocks from Keuper and Liassic/Dogger Formations. The sampled Bunte Breccia outcrop at Aumühle quarry (Fig. 4.1) is comprised of sedimentary materials, largely shaley mudstones, and though brecciated from transport, often retain original sedimentary structures. One sample from a monomict, brecciated Malmian limestone megablock was also acquired from Iggenhausen (22 km from the crater center) for further comparison of pre-impact materials. Impact melt-bearing breccia was also sampled at Aumühle quarry (Fig. 4.1).

4.3.1. Powder X-ray Diffraction (pXRD)

Six samples of Bunte Breccia and 10 samples of melt-bearing breccia matrix from ejecta deposits at the from Aumühle quarry were prepared for pXRD. Disaggregated, powdered sample material was isolated to the <2 μm size-fraction by suspension and centrifugation, and separate aliquots were saturated with $CaCl_2$ and KCl. Two of these samples were further separated to the <0.2 μm size-fraction. Ca-saturated samples were analyzed at 54% relative humidity (RH) and then glycolated. K-saturated samples were analyzed at 0% RH (110^o C), followed by 54% RH analyses, and then dehydrated by heating at 300^o C and 550^o C. Samples were analyzed after each treatment using a Rigaku Rotaflex RU-200B series X-ray diffractometer, equipped with a rotating anode (Co K- α source operated at 160 mA and 45 kV) and a graphite monochromator. Scans were performed from 2 to 42^o 2θ at a step size of 0.02^o 2θ.

Smectite compositions and the type and amount of interstratified clay minerals were identified by modeling XRD patterns based on theoretical calculations built into the modeling software Sybilla (unpublished software). The percentage of layers for each clay mineral phase constituent, as well as the octahedral and interlayer iron content, can be adjusted via fit parameters. The Reichwete (R) ordering of layer interstratification was also adjusted – indicating the probability of finding a given layer depending on a preceding layer – to obtain better fits of the measured pattern to a simulated pattern. These fitting parameters yield the weight percentage of each constituent mineral phase.

4.3.2 Reflectance spectrometry

ASD TerraSpec handheld point spectrometer (as an active detection, with provided light source) contains three sensors measuring the visible (VIS; 0.35-0.74 μm), near-infrared (NIR; 0.74-1.0 μm), and shortwave infrared (SWIR; 1.0-2.5 μm) ranges. Data was collected on hand samples of Bunte Breccia and the matrix of melt-bearing breccia from ejecta deposits at the Aumühle quarry. Spectral resolution is 9.8 nm at 1400 nm wavelength and 8.1 nm at 2100 nm.

4.3.3 Electron Microprobe Analysis (EMPA)

Three polished thin sections of Bunte Breccia samples and 57 of the melt-bearing breccia from Aumühle quarry were examined in both transmitted and reflected light. (Many melt-bearing breccia samples acquired through other field excursions to Aumühle quarry were also studied.) The thin sections were then carbon-coated and analyzed using the JEOL JXA-8530F Hyperprobe at the Earth and Planetary Materials Analysis (EPMA) laboratory at the University of Western Ontario. Wavelength dispersive X-ray spectrometry (WDS) was employed to obtain quantitative geochemical data and produce element maps. Element map data were collected at 15 kV accelerating voltage, 100 nA probe current, and 10 ms dwell time. Ca, Fe, K, Mg, Na were

collected using WDS while Si, Al, P, Ti, and Zr were collected using an energy dispersive X-ray spectrometer (EDS). Quantitative spot analyses of glasses and clay minerals were collected using WDS at 15 kV accelerating voltage, 10 nA probe current, and 5 um spot size.

4.4 Results

4.4.1 Reflectance spectroscopy

Laboratory spectra from the melt-bearing breccia matrix and Bunte Breccia show that the groundmass of both lithologies are comprised of a variety of smectitic clay minerals, as compared to USGS library spectra (Fig. 4.2a). The spectra show hydration (H_2O-related) absorptions present at ~1.4 μm and ~1.9 μm and metal-hydroxyl bonding (ν-OH) indicated by 2.2–2.3 μm features, indicative of smectitic composition (Fig. 4.2; Bishop et al., 2008; Clark et al., 1990). The matrix of the melt-bearing breccia is spectrally characterized by both sharp and broad 2.21 μm absorption features (e.g., Fig. 4.5c) resulting from the presence of either Al-OH or Si-OH bonds, or both. An Si-OH bond is expected due to the dominant composition and glassy nature of the impact melt; the spectral shapes at the ~ 2.2 μm absorption are consistent with montmorillonite, kaolinite, amorphous silica, or an intimate mix of these clay mineral phases. The spectral shape is most consistent with montmorillonite, though an additional shoulder or weak Al, Fe/Mg-OH band at 2.24 – 2.29 μm is often present. These spectral features are consistent with Al-montmorillonite and Fe-montmorillonites. A weak ~2.34 shoulder is also observed, consistent with a calcite contribution. Similar to the spectra from the melt-bearing breccia, those of the Bunte Breccia show both sharp and broad or coupled ~2.2 μm features. The Bunte Breccia spectra also often exhibit contributions from the presence of Fe/Mg-OH bonds and carbonate. The deeper absorptions at ~ 0.9 μm, similar to the shape of nontronite, may

indicate higher Fe^{3+} content as compared to the melt-bearing breccia samples; the overall shape of the Bunte Breccia spectra from the ~0.6 – 1.2 μm may be related to a ferrous (Fe^{2+}) component. It should be noted that the major absorption features of the spectra (indicated by vertical, broken lines in Figure 4.2) are broadly consistent between Bunte Breccia and melt-bearing breccia samples.

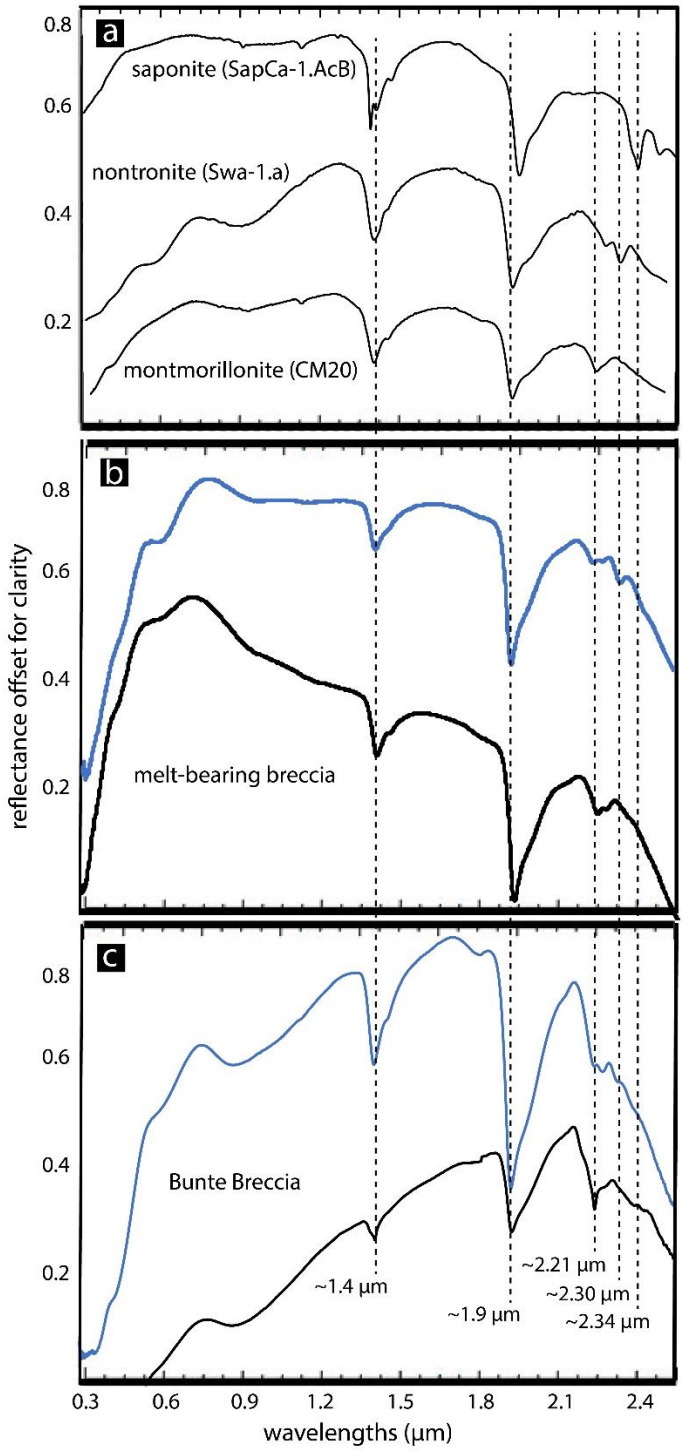

Figure 4.2. a) USGS library VNIR-SWIR spectra (Clark et al., 2007) of smectites are shown for comparison. Vertical dashed lines compare spectral features, including: hydration (H_2O)-related absorptions present at ~1.4 μm and ~1.9 μm; Si-OH and/or Al-OH features at ~2.21 μm; Fe-OH

features at ~2.29 μm; Mg-OH features at ~2.32 μm, and; $CaCO_3$ features at ~2.34 μm. b) Spectra from melt-bearing breccia samples showing ~2.29 and weak ~2.2 μm features (blue spectrum), and the more common broad ~2.21 μm features (black spectrum), generally spectrally consistent with montmorillonite. c) Broad (blue spectrum) and sharp (black spectrum) ~2.2 features with weak ~2.29 μm and strong ~2.34 μm shoulders are generally observed in Bunte Breccia spectra, as shown. The deeper absorptions at ~0.9 μm, similar to the shape of nontronite, may indicate higher Fe content as compared to the melt-bearing breccia samples. All spectra are offset by reflectance for clarity.

4.4.2 powder X-ray diffraction (pXRD)

The pXRD data indicates that the clay mineral phases from the melt-bearing breccias and Bunte Breccia are much more complex than is apparent in the reflectance spectroscopy data; they are comprised of compositionally variable smectites with differing types and amounts of interlayered material. Powdered samples were separated to the <2 μm size-fraction to isolate the clay mineral species for an in-depth and focused examination of the minerals and interlayered material. The observations from the individual XRD reflections that comprise the patterns are given in d-spacing – the distance between two adjacent mineral planes or layers. The basal plane (001) of phyllosilicates give a d-spacing value indicative of a particular mineral species; the <2 μm size-fraction Ca-saturated samples show very strong 001 reflections with d-spacings that confirm smectite composition (Brindley and Brown, 1980). A *d*(001) of 1.5 nm for Ca-saturated samples treated with 54% relative humidity is observed at ~ 6º 2θ (e.g., Fig. 4.3). When treated with ethylene glycol (EG)-solvation, the shifted 001 reflection (~ 5.2º 2θ) shows a d-spacing of ~ 1.5 nm – 1.7nm (Fig. 4.3); this is a swelling/expansion consistent with the low layer charge (higher

CEC) indicative of smectites (Brindley and Brown, 1980) that absorb two layers of ethylene glycol. Peaks at 0.85 – 0.86 nm also represent glycolated smectites, and are present in the clay minerals from all three sample types. However, important differences in the XRD patterns between the Bunte Breccia and the melt-bearing breccia samples show a spectrum of mineralogic complexities and varying crystallinities.

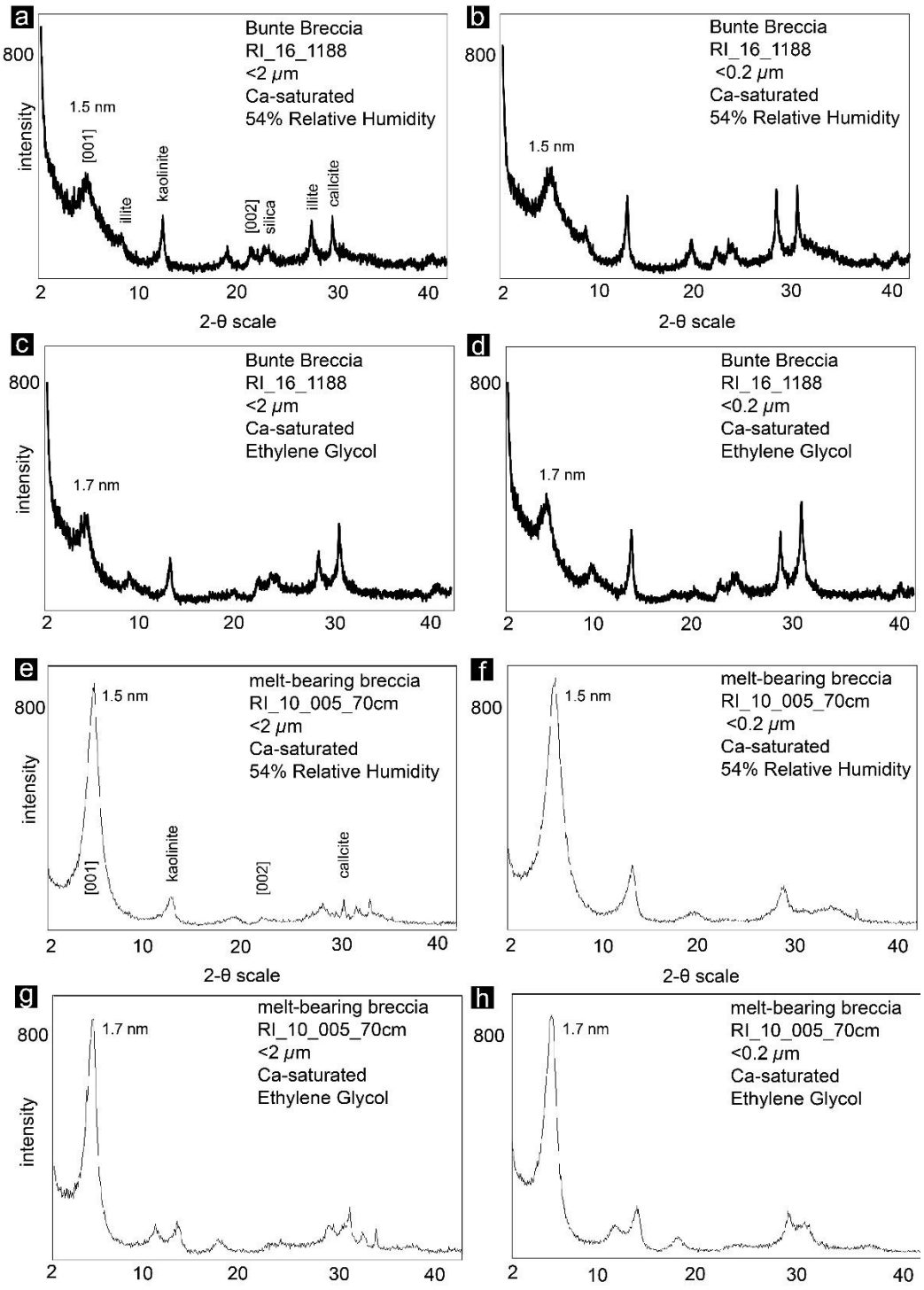

Figure 4.3. a–h) pXRD patterns of Bunte Breccia and melt-bearing breccia samples are shown for <2 μm and <0.2 μm size-fractions treated with Ca-saturation. The patterns represent two treatments, performed in the order of 54% relative humidity (RH) then ethylene glycol (EG)-

solvation. The change in diffraction pattern appears most strongly about the basal (001) position; the *d*(001) of the 54% RH-treated samples is 1.5 nm, and when treated with ethylene glycol (EG)-solvation, the *d*(001) shifts to 1.7nm, confirming the swelling smectite mineralogy. a–d) In the Bunte Breccia samples, the ~ 1.0 nm peak indicative of an illitic component (I/S) is most apparent in the 54% RH treatment. Note that little change occurs between the <2 μm and <0.2 μm size-fractions except for greater intensity kaolinite peaks (e.g., ~20º 2θ). e–h) The melt-bearing breccia samples show more pronounced kaolinite peaks in the <0.2 μm size-fraction and the calcite peaks disappear. Peaks at ~ 0.9 nm represent glycolated smectites. Note the more muted peaks and drastically less low-angle asymmetry, as compared to the Bunte Breccia patterns.

4.4.2.1 Bunte Breccia samples

The <2 μm size-fraction separated XRD patterns of the shaley mudstones of the sampled Bunte Breccia outcrop samples show that they are mineralogically complex. The sharp XRD peaks (Figs. 4.3a–d) are indicative of high crystallinity. Figure 4.3a indicates the various mineral phases that give rise to XRD peaks in the Bunte Breccia samples; kaolinite, quartz, calcite, and illite peaks are present among the indicative 00l smectite peaks. In the expanded (ethylene glycol-solvated) Ca-saturated samples, interlayered illite is observed with a ~1.0 nm peak (Fig. 4.3c).

The change in diffraction patterns occurs most strongly around the basal (001) position for both Ca and K-saturated samples; K-saturated samples were taken through progressive dehydration/heat and rehydration treatments (e.g., Fig. 4.4) to assess the change about the 001 peak position and shape due to interlayered materials. Smectite clay minerals are sensitive to heat-driven dehydroxylation due to the cation content, and occupancy and vacancy, of the sites in the

octahedral sheets (Brindley and Brown, 1980). Thus, the change about the 001 peak in response to the treatments identifies the octahedral cations and allows an assessment of the interlayer species based on the heat resistance of the materials (Brindley and Brown, 1980; Heller-Kallai, 1980; Derkowski et al., 2012). Hydration of the Bunte Breccia samples followed by heating to 110 ºC produced a ~1.01 nm collapse, consistent with mixed-layer smectites. The XRD patterns of successive heat treatments show that any hydroxylated interlayers are destroyed at heating to 300 ºC; the 001 superstructure and other peaks are present most strongly when hydrated to 54% relative humidity (Fig. 4.4a). Kaolinite peaks at ~0.7 nm and *d*(002) at 0.358 nm as well as the broad 001 peak are destroyed at heating to 550º C, indicating that the interlayered material is of a kaolinitic composition.

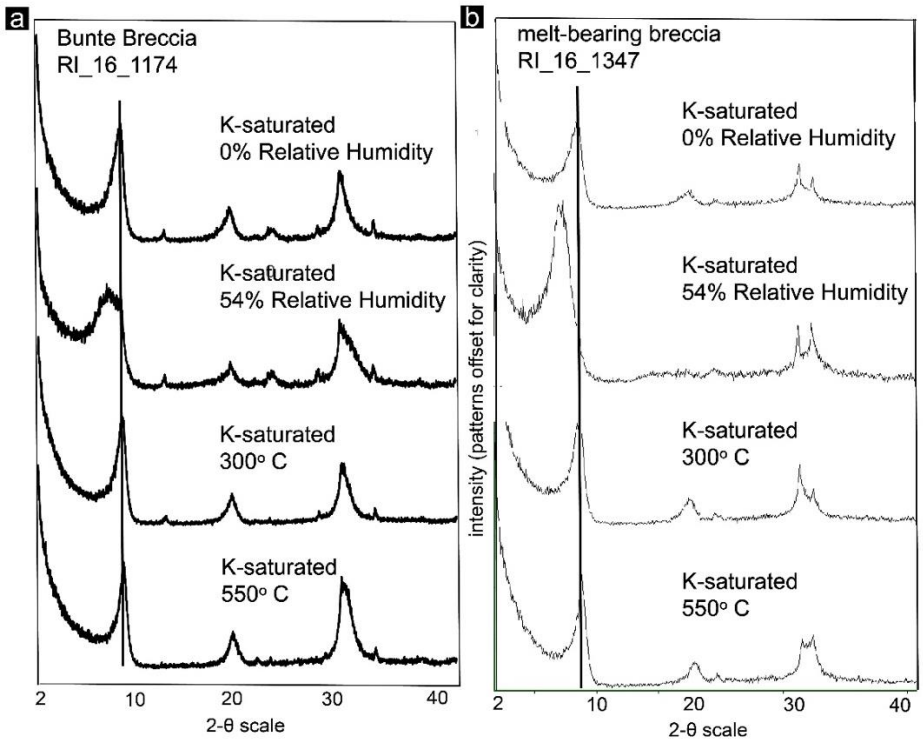

Figure 4.4. a–b) Representative pXRD patterns are shown for clay-size fraction (<2 μm), K-saturated separates. The patterns represent four treatments, performed in the order of top to bottom.

The change in diffraction pattern appears most strongly about the basal (001) position, with the shift in successive treatments as shown. a) Sample from the Bunte Breccia. The 001 peak broadens significantly with hydration; subsequent heating produces nearly complete collapse. High and low-angle asymmetry of the 001 peak indicates some hydroxy interlayering is present, but not appreciable amounts to prevent collapse. Kaolinite peaks collapse at heating to 300º C. Quartz and illite are also present. Modeling of the pattern indicates low interlayer iron and interlayered kaolinite. b) Patterns from a melt-bearing breccia sample. The 001 peak does not swell considerably with treatment (54% RH) and retains a sharper peak shape as compared to the Bunte Breccia samples in (a), but does broaden, indicating hydroxy interlayering. The nearly complete collapse with subsequent heating, however, nearly complete collapse upon heating treatments indicates the limited amount of or partially-formed hydroxy-interlayered material.

The kaolinitic nature of the Bunte Breccia material is observed in the XRD patterns of materials subject to further size-fraction-separation (<0.2 μm; Fig. 4.3). The samples were further separated to the <0.2 μm size fraction to discern if finer-grained, interlayered material contributes different mineral phases than those of the larger clay-fraction. In the <0.2 μm size fraction of the Bunte Breccia samples, there is a more pronounced collapse of peaks due to kaolinite (Figs. 4.3b–d), indicating that a finer-grained component of the Bunte Breccia clays is kaolinitic.

The compositional interpretations are supported and quantified by modeling of the XRD patterns (see Table 4.1). The shaley mudstones of the Bunte Breccia are mineralogically complex at the <2 μm size fraction, yielding modeled compositions of dioctahedral smectites with interlayered illite and kaolinite; varying amounts of these mineral phases are present in the samples

(e.g., multiple smectite, illite, chlorite, and kaolinite interlayers). Peaks indicative of the modeled interlayered illite are most strongly present in in the Ca-saturated samples (e.g., Fig. 4.3). The high interstratification as specified by the modeling is shown in the XRD patterns as: low 001 peak height (as compared to the high slope of the low-angle side of the peak and the higher-order 00l reflections); low- and high-angle 001 peak asymmetry (Figs. 4.3a–d); and the change of peak shape through the K-saturation treatment series (Fig. 4.4a) (as shown by Brindley and Brown, 1980; Ferrage et al., 2005). The modeling is consistent with generally very low interlayer iron, but interlayer content is high, indicating other cations occupy the octahedral sites.

4.4.2.2 Melt-bearing breccia samples

High interstratification or interlayered materials are also observed in the melt-bearing breccia samples, evidenced by: the expansion and collapse of the 001 peak in XRD patterns produced from the K-saturated and heat-treated melt-bearing breccia samples (Fig. 4.4b); non-rational XRD peak intervals (also indicating random interstratification as opposed to well-ordered layers); and low-angle 001 peak asymmetry (as shown by Brindley and Brown, 1980). The 001 peak asymmetry observed (Figs. 4.3g–h; Fig. 4.4b) is consistent with previous modeling of mixed-layer smectites, having one well-ordered layer (compositionally 70% of the structure) and randomly-interstratified materials (comprising 30%) (Ferrage et al., 2005). Many of the melt-bearing breccia samples have kaolinite peaks at ~0.7 nm and *d*(002) at 0.358 nm. The kaolinite peaks and the broad 001 peak are destroyed at heating to 550 ºC, indicating kaolinitic interlayers, as observed in the Bunte Breccia samples. Some samples did not show the indicative kaolinite peaks, but the 001 peak was still somewhat broad; this indicates that other materials are present, such as partially-developed hydroxyl layers (Brindley and Brown, 1980; Georgiadis et al., 2019).

When further separated to the <0.2 μm size-fraction, more pronounced kaolinite peaks are observed – indicating that a smaller size-fraction of the material is comprised of kaolinitic material – and calcite peaks disappear (e.g., Figs. 4.3f–h). In the expanded (ethylene glycol-solvated) Ca-saturated samples, interlayered illite is observed in some of the melt-bearing breccia samples as a ~ 1.0 nm peak.

Modeling of the melt-bearing breccia XRD patterns show that the samples are not consistent with monomineralic montmorillonite. Modeling indicates expanding two-layer dioctahedral smectites – sometimes high in interlayer and octahedral Fe – with varying amounts of interlayering (Table 4.1). Illite and/or kaolinite interlayering are good fits for modeling in many of the samples; hydroxy interlayering is otherwise indicated as the interlayered material that expands the 001 peak structure upon hydration treatments. Compared to the Bunte Breccia samples, the melt-bearing breccia samples show less interlayering, observed as: less 001 peak change with less peak asymmetry upon hydration (Fig. 4.4b); and greater 001 peak height relative to higher-order 00l peaks (Figs. 4.3e–h). A further important difference is that the melt-bearing breccia samples are also are not as well-crystallized (e.g., broader peaks and more muted general pattern; Fig. 4.3).

Table 4.1. Summary of the observed clay mineralogy. The *d*(001) listed are those of the Ca-saturated, ethylene glycolated treatments. Cation chemistry and percent and type of interlayered material is derived from EMPA WDS and XRD pattern modeling. Modeled compositions are listed as a representative range.

Sample location	Mineralogy and occurrence	d(001) and shape	Modeled composition [a]
Bunte Breccia	Comparatively well-ordered, higher crystallinity Al-smectites interlayered with kaolinite, illite, and hydroxy interlayers; strong and well-crystalized illitic and calcite components; highly interstratified and high turbostraticism No secondary alteration – except for minimal Fe oxidation observed at the contact with melt-bearing breccia – nor mineral or glass clast replacement observed	d(001): (~1.726 – 1.744 nm) ≤0.2 μm 001 peak shows little change from <2 μm; ≤0.2 μm shows strongest kaolinite component	Dioctahedral smectite with kaolinite and illite (K/S, R1); two-layer smectites with kaolinite (K/S/S, R1) interlayered illite, smectite, and chlorite (I/S/S/Ch, R1)
Melt-bearing breccia	Dioctahedral smectites (consistent with Al- and Fe-montmorillonites) with little turbostractic stacking; some samples are interlayered with hydroxy and/or Fe-rich materials, some show a strong illitic component; kaolinite and calcite usually present Complete groundmass alteration and variable replacement of glass and granitic clasts by smectites Highly variable textures and crystallinities	d(001): (~1.698) changes in ≤0.2 μm indicates kaolinite in smaller size-fraction, calcite in larger	Dioctahedral smectite with variable kaolinite and illite (K/S, R1)

[a] Abbreviations are defined as follows: S = smectite layer; K/S = kaolinite/smectite; I/S = illite/smectite; R = Reichweite ordering.
[b] See Wemmer, 2008

4.4.3 Electron Microprobe Analysis (EMPA)

Wavelength dispersive X-ray spectrometry (WDS) data from a subset of melt-bearing breccia and Bunte Breccia samples studied in thin section indicate that the clay minerals exist in continuum compositions between mineral end-members, likely ranging from Al – Fe-rich montmorillonite ± illite, kaolinite, and chlorite depending on Al, Fe, and Mg substitutions in the octahedral sites. The geochemical point data obtained from WDS integrates a ~ 5 μm analysis spot;

the data obtained by each spot analysis necessarily integrates the geochemistry from the clay-size fraction (<2 μm) and the finer-grained component (<0.2 μm size-fraction crystallites), and thus, the interlayer material. Geochemical trends differentiate the sample types, as shown in Figure 4.5. The composition of Bunte Breccia clay minerals is a range of Fe-dominant Al/Fe clay minerals with less than 20% Mg (Fig. 4.5). This may be consistent with the overall shapes observed from reflectance spectra (e.g., Fig. 4.2) indicating a higher Fe content. Al/Si ratios of the Bunte Breccia samples (0.47) are consistent with an Fe-rich montmorillonite; the ~2 wt % K is consistent with the XRD findings of a strong illite and kaolinite components.

The melt-bearing breccia samples show a compositional range from montmorillonite to nontronite, with as much as ~60% Fe:Al and as much as ~15% Mg (Fig. 4.5). Generally, the melt-bearing breccias are most consistent with an Al or Al/Fe clay mineral having varying amounts of Fe filling octahedral sites and small amounts (≤ 15%) of Mg-hydroxy interlayering. An Fe-smectite with an intimate mixture of clay mineral and/or other mineral phases or materials (e.g., e.g., hydroxy material, very fine-grained chlorites, zeolites, illite, or kaolinite) is consistent with the observed Al/Si ratio of 0.38 and ~ 1.4 wt % K. The geochemical data supports the observations and XRD results showing that the melt-bearing breccia clay minerals are compositionally diverse Al/Fe/Mg smectites (Table 4.1).

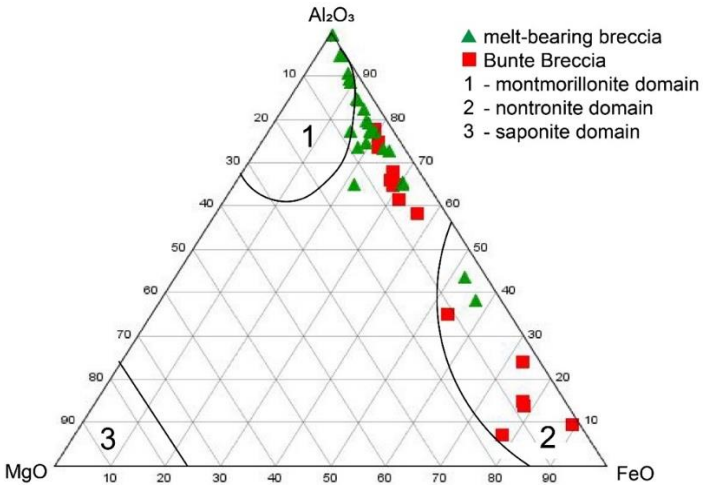

Figure 4.5. EMPA WDS geochemical data from thin sections of melt-bearing breccia and Bunte Breccia samples, as indicated, plotted in an Al_2O_3/MgO/FeO ternary diagram. Smectite domains are provided. The melt-bearing breccia data (green triangles) yields a composition consistent with Al-dominant, mixed Al/Fe montmorillonite. Bunte Breccia data (red squares) have an Fe-dominant, mixed Al/Fe composition.

Backscattered electron imaging and EMPA WDS element-specific maps of the samples (e.g., Fig. 4.6) provides a spatial representation for the mineralogy observed from the reflectance spectroscopy and the XRD data. As shown in Figure 4.6a, Bunte Breccia samples are commonly have calcite-dominant clasts supported by groundmass comprised largely of clay phases. The Si, Al, and Fe-specific WDS maps (Figs. 4.6b–d) show that the Al clay-rich groundmass supports angular, brecciated clasts. The fuzzy-textured clays lack mineral growth textures but instead display a flow-texture that appears to wrap the angular clasts (Fig. 4.6e); this is consistent with clay minerals that are plastically-deformed with brittle clast disaggregation during emplacement as suggested by Pietrek and Kenkmann (2016).

The melt-bearing breccias are groundmass-supported, dominated by clay minerals and fine-grained "clayey" materials (up to ~70 vol%; Osinski, 2004). Alteration textures observed in the melt-bearing breccia indicate a variable replacement of clasts with secondary mineralization, including glass clasts and minerals from granitic clast inclusions (e.g., Figs. 4.6f–j). Much of the groundmass is comprised of fuzzy-textured clay minerals, consistent with an Al/Fe smectite (Figs. 4.6g–i); many of the clay mineral crystallites are sub-μm in apparent size. Calcite is commonly observed in the melt-bearing breccia groundmass, but Figure 4.6 shows that much of the groundmass in this sample has been replaced by space-filling secondary clay minerals. This sample also shows the commonly-observed abundance of mineral fragments, crystallites, and zeolites.

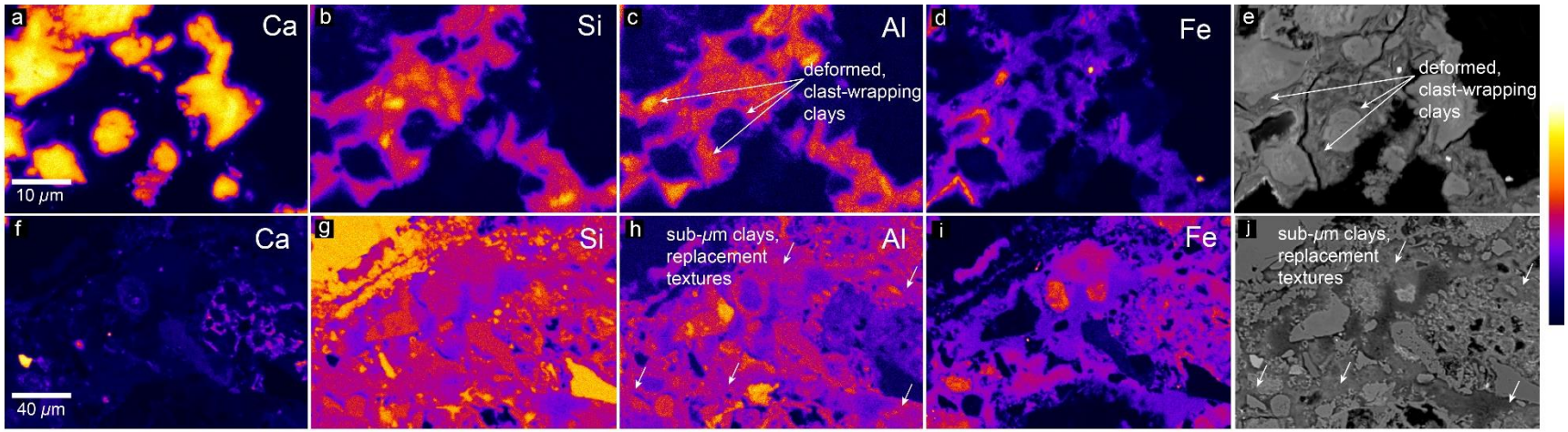

Figure 4.6. a–d) EMPA WDS element-specific maps, as indicated, for a representative Bunte Breccia sample. a) Ca-specific WDS map shows qualitative Ca abundances; as is common in the Bunte Breccia, calcite it a dominant mineral phase. b–c) Si and Al-specific maps show the smectite-rich groundmass, supporting angular brecciated clasts. e) Backscattered electron image of the element maps in (a) – (d). Clay minerals in the matrix display flow-textures that appears to wrap the angular clasts. f–j) EMPA WDS element-specific maps, as indicated, for a representative melt-bearing breccia sample. The lack of Ca and abundance of Si, Al, and Fe as displayed in the respective element-specific maps shows the prevalence of smectite, which is Al and Fe-rich. j) Backscattered electron image of the element maps in (f) – (j). Angular, rounded, and flow-textures clasts are present, and much of the groundmass and clasts have been replaced by secondary minerals.

4.5 Discussion

The pre- and syn/post-impact clay minerals observed in this study are comprised of complex, interstratified smectites, despite their very different origins. Interstratified minerals or materials in mixed-layer smectites represent intermediate products of mineral transformation known to occur in diagenetic or hydrothermal environments; this transformation is a direct dissolution of primary smectite into the crystallization of the mixed-layer smectite (Środoń, 1999; Srodoń, 1980). In this study, we show that the smectites of the melt-bearing breccia groundmass are comprise various interlayers, including kaolinite, illite, and high Fe/Mg hydroxy compounds. The origin and formation conditions of the clay minerals investigated in this study – and the difficulties in discerning pre-impact clay minerals from those of impact origin – is discussed below.

4.5.1 Origin and formation conditions of impact-generated and pre-impact clay minerals at Ries

4.5.1.1 Impact-generated clay minerals of the ejecta melt-bearing breccia

The origin of clay minerals in ejecta impactites is poorly-understood and little-studied. Impact-hydrothermal processes have been suggested as a formation mechanism for some portion of the melt-bearing breccia groundmass (Newsom et al., 1986; Osinski et al., 2004; Sapers et al., 2017). However, the nature and genesis of an ill-defined "clayey" groundmass – which comprises up to 70 vol% of these impactites – is not well-understood. Osinski et al. (2004) performed an extensive study on the melt-bearing breccia and concluded that groundmass clay minerals and other mineral phases represent the alteration products of a series of impact melt products. If the majority of the groundmass was indeed of impact melt origin, the metastable

glasses would have quickly devitrified and recrystallized into poorly-crystalline, stable clay mineral phases (Osinski et al., 2004) – a known nucleation and crystal growth process in the alteration of volcanic glasses (Marshall, 1961). The crystallization of clays from glass devitrification has been described in glass-bearing volcanic deposits as a two-stage process: (1) spherules form, hydrous minerals begin to crystallize, and oxidation occurs due to initial rapid cooling and water loss; and (2) clay minerals are crystallized at somewhat lower temperatures (Drewes, 1963). Under these conditions, clay minerals would similarly be produced by post-impact alteration of impact glass via devitrification/recrystallization due to the aqueous diffusion of cations in the still-hydrous state of the deposit (Naumov, 2005). However, even if no additional fluids or heat are introduced into the system, hydrated glasses continue to devitrify. (For Mars, this is important as devitrification can continue for ~10^9 years after their formation; Marshall, 1961). This process is likely important for the formation processes for the complex, interstratified clay minerals identified in this study.

The complex nature of the ejecta melt-bearing breccia clay minerals identified in this study are consistent with the interstratified clay mineral composition of the ejecta melt-bearing breccias at depth, recovered from Otting (Chapter 3 and Wörnitzoshtheim (Chapter 3; Sapers et al., 2017) cores. These studies have all shown that – exposed at the surface and at depth – the ejecta melt-bearing breccias comprise compositionally diverse and complex Al/Fe/Mg smectites (Table 4.2). This suggests that a formation and alteration mechanism for the groundmass clay minerals other than surficial weathering should be considered. While there is evidence that hydrothermal processes were active in these deposits (e.g., Newsom et al., 1986; Osinski et al., 2004; Sapers et al., 2017) an outstanding question for the ejecta melt-bearing breccias is the potential longevity of a hydrothermal system for the relatively thin (tens of meters) deposits to

alter as extensively as observed. An extensive hydrothermal system was present in the Ries crater-fill deposits due to a post-impact crater lake that sustained the system, critical for trapping shock-induced heat and providing a water source (Osinski et al., 2013); however, apparently no such source was present overlying ejecta deposits. Given that up to ~ 70 vol% of the clayey groundmass is inconsistent with a hydrothermal origin (e.g., Osinski et al., 2004), a mechanism other than hydrothermal alteration should also be considered. Our findings show that the clay minerals of the ejecta melt-bearing breccias formed under complex alteration processes that were sustained for long enough to accommodate the smectite dissolution/crystallization transformation into the observed mixed-layer forms.

We suggest a formation process as follows for at least some size-fraction of the clay minerals observed; this process involves a two-step or continuum initial alteration process, dominated by autometamorphism – the recrystallization of molten rock through strictly endogenous volatiles – and glass devitrification/recrystallization, that formed the complex, interlayered smectites of the groundmass observed in this study. In the first step, the clay minerals crystallize as smectites through the interaction of available volatiles with shock-disordered aluminosilicates – in silica-supersaturated conditions from impact melt (e.g., Naumov, 2005) – and the aqueous diffusion of cations (mainly Fe, Mg) from the glass (Naumov, 2005) and Fe and Mg-bearing basement clasts. A second or continuum dissolution-crystallization would result in layer transformation (e.g., Delvaux et al., 1990). We suggest that devitrification/recrystallization of impact glass and autometamorphism of the hot deposit immediately following emplacement may have formed the initial smectites, then cations were continuously made available in the system through a second or continuum cooling phase of devitrification/recrystallization, as is described for the closed-system alteration of volcanic glass-

bearing deposits (e.g., Drewes, 1963). In this system – even in the absence of an external water source – the kaolinitic, illitic, and hydroxy interlayering of the melt-bearing breccia smectites form due to a partial polymerization of dissolved, and subsequently intercalcated cations (Al^{3+}, Mg^{2+}, and Fe^{3+} oligomers; as described by Georgiadis et al., 2019). We suggest that the cation availability for the formation of smectites with variable kaolinite and illitic interlayering is consistent with an aluminosilicate-supersaturated system present in the melt-bearing breccia just after emplacement. This is plausible if: (1) the cryptocrystalline clays and the silicate glass crystallites present in the melt-bearing groundmass are quenched remnants of impact melt (Osinski et al., 2004); and (2) clay minerals were produced through *in situ* recrystallization/devitrification of the groundmass impact glass (Naumov, 2005).

Naumov (2005) compares the cationic availability afforded by impact glass devitrification to well-known hydrothermal alteration processes. For example, hydrothermal experiments have shown that the amount of Al available in the system is crucial to the formation of mixed-layer K/S or I/S; when all other parameters are kept the same, excess Al reacts with smectite to proceed in the formation of K/S, and a lack of Al forms I/S (Srodon, 1980). Regarding the clay minerals of the melt-bearing breccia, this is consistent with silicification (higher SiO_2 activity) and allitization (higher Al_2O_3 activity) as correlated with high clay mineral crystallinity (Zhang et al., 2017). Furthermore, this is consistent with the modeled Al and K/S and I/S compositions of the relatively well-crystalized melt-bearing breccia clay minerals. Silicification and allitization would be a natural process in an aluminosilicate-supersaturated system; excess Al supplied to the system during the crystallization of the interlayered material could have resulted in a preferential formation of kaolinitic material, as observed in as interlayered constituents of the groundmass smectites. Reflectance spectroscopy indicates a

dioctahedral montmorillonite with Al and Fe occupying octahedral sites (2.21 μm-dominant absorptions features and spectral contributions from high Fe/Mg metal-OH bands at 2.24 – 2.30 μm, e.g., Fig. 4.5c); these results are consistent with previous reflectance spectroscopy of Tornabene et al.. (2013) and indicate that Al, Fe, and Mg are likely to be variably present in the smectite octahedral sites.

The devitrification/recrystallization of impact glass is a sustained, long-term process, and was likely present over time with other post-impact alteration processes. Indeed, the compositionally diverse Al, Fe, and Mg smectites that have been identified in the Ries ejecta melt-bearing breccias were formed by a variety of post-impact alteration processes, including: devitrification/recrystallization; autometamorphism; post-impact hydrothermal alteration; and surficial weathering, where exposed (Newsom et al., 1986; Osinski et al., 2004; Sapers et al., 2017). As described by Osinski et al. (2004), textural evidence within the groundmass show that these clay minerals produced through these various processes cross-cut each other. Table 4.2 provides a list of the clay mineral phases observed in the Ries ejecta melt-bearing breccia deposits, along with those observed in the Bunte Breccia in this study for comparison.

Table 4.2. Compilation of clay mineral phases that have been observed in the melt-bearing breccias and Bunte Breccia of the Ries ejecta deposits.

Sample location	Mineralogy and occurrence	d(001) and shape	Modeled composition [a]	Dominant process
Bunte Breccia	Al-smectites interlayered with kaolinite, illite, and hydroxy interlayers; highly interstratified and high turbostraticism; strong and	d(001): ~1.726 – 1.744 nm [b] ≤0.2 μm 001 peak	Dioctahedral smectite with kaolinite and illite (K/S, R1); two-	Pre-impact sedimentary [c]

	well-crystalized illitic and calcite components [b] No secondary alteration – except for minimal Fe oxidation observed at the contact with melt-bearing breccia – nor mineral or glass clast replacement observed	shows little change from <2 μm; ≤0.2 μm shows strongest kaolinite component	layer smectites with kaolinite (K/S/S, R1) interlayered illite, smectite, and chlorite (I/S/S/Ch, R1)	
Melt-bearing breccia, surficially exposed, thin deposits (m-to-10s of m) in present-day exposures	Comparatively well-ordered, higher crystallinity dioctahedral smectites (consistent with Al- and Fe-montmorillonites) with little turbostractic stacking; some samples are interlayered with hydroxy and/or Fe-rich materials, some show a strong illitic component; strong to weak kaolinite, weak calcite usually present [b] Complete groundmass alteration and variable replacement of glass and granitic clasts by smectites; fracture-lining, vesicle fillings, groundmass replacement, pervasive replacement of glass clasts [d]; flow-textures and globules, partially-coalesced globules; compositionally and texturally variable; both very fine-grained and platy textures [e]	d(001): ~1.65 [d] – 1.698 [b] ≤0.2 μm 001 peak shows little change from <2 μm	Dioctahedral Al/Fe smectite with variable kaolinite and illite (K/S, I/S, R1)	Local, spatially-restricted hydrothermal; autometasomatism; devitrification; variable surficial weathering overprint [d]
Melt-bearing breccia (70 – 90 m depth); upper Wörnitzostheim core	Smectite with an illitic component, calcite [d] Fracture lining, vesicle fillings, groundmass replacement [d,f]	d(001): ~1.25 nm [d]		Hydrothermal [d]
Melt-bearing breccia (~300 m depth); lower Wörnitzostheim core	Al/Fe smectite [f] with an illitic component, calcite, zeolites (phillipsite, erionite, analcime) [d]; chlorite and goethite [f]	d(001): ~1.25 nm [d,f]		Hydrothermal [d]; autometasomatism; devitrification [f]
Degassing pipe interiors from quarry exposures [f]	Poorly-crystallized, compositional continuum between nontronite, saponite, and montmorillonite ± chlorites; turbostractic stacking, highly (randomly) interlayered with hydroxy or chloritic materials; very little evidence of other mineral	d(001): (~1.46 – 1.59 nm) ≤0.2 μm 001 peak broadening due to chloritic material	mixed-layer dioctahedral; mixed-layer trioctahedral smectites; up to 20% interlayered chlorite (C/S); small	Hydrothermal; autometasomatism; devitrification [f]

	phases at the <2 μm size-fraction [f] Thin (~20 μm coating) in degassing pipe interiors; surrounding alteration halos; pipes are densely clustered in observed outcrops [f]		amounts of kaolinite possible (R0/R1)	

[a] Abbreviations are defined as follows: C/S = chlorite/smectite; K/S = kaolinite/smectite; I/S = illite/smectite; R = Reichweite ordering.

[b] this study

[c] See Wemmer, 2008

[d] See Sapers et al., 2017

[e] See Osinski et al., 2004

[f] See Caudill et al., *in press*

4.5.1.2 Comparison of impact-generated clay minerals to the pre-impact clay minerals of the Bunte Breccia

Several indicators are generally used to distinguish detrital smectites from authigenic (e.g., smectites formed from the alteration of glass; Iacoviello et al., 2012), including textural habit and chemical composition (Chamley, 1989; Hillier, 1995; Singer, 1984). Aluminous smectites are likely to be categorized as detrital or as weathering products, particularly if flaky textures are present (Setti et al., 2000; Ehrmann et al., 2005; Fesharaki et al., 2007). For the case of the melt-bearing breccia groundmass, however, lithologic context and textural evidence (e.g., Osinski et al., 2004) indicates a formation via *in situ* alteration from impact glass (with a variety of other syn/post-impact alteration processes). Several distinctions may be drawn between the melt-bearing breccia clay minerals and the Bunte Breccia clay minerals examined in this study, as follows:

- The mineralogical complexity of the Bunte Breccia samples (e.g., Fig. 4.5a) and the poorly-ordered nature of the smectites (as observed through laboratory treatments and XRD) is consistent with a detrital terrigenous origin. Although both the Bunte Breccia and

melt-bearing breccia smectites show turbostraticism in the XRD analyses, the muted 001 peaks (as compared to the melt-bearing breccia (Fig. 4.3), low-angle 001 peak asymmetry (Figs. 4.3a–d), and irrational peak intervals indicate that the Bunte Breccia smectites have less interlayer order and coherency than compared to the melt-bearing breccia smectites. This is consistent with lessened turbostraticism in smectites of authigenic origin (e.g., in melt-bearing breccias), as compared to a higher layer-stacking disorder in detrital-origin smectites (e.g., in Bunte Breccia), as described by Hover et al. (1999).

- The predominance of other mineral phases (e.g., illite, calcite, kaolinite) in the Bunte Breccia at the <2 μm size-fraction suggests formation through complex physical weathering processes consistent with its detrital provenance. (The melt-bearing breccia, by comparison, is less stratified and smectite-dominant.)
- Textural evidence also distinguishes the two materials: sub-μm-scale textures and correlative element-specific WDS maps show the morphology of the cryptocrystalline and replacement textures of the melt-bearing breccia smectites (Figs. 4.6e–j), and the clast-wrapping flow-textures of the Bunte Breccia clay minerals (Figs. 4.6f–j) that are indicative of their emplacement.
- Geochemical and textural variations in a deposit also point to an authigenic origin as opposed to detrital, as circulating fluids differentially alter deposits *in situ*; these have been observed in the ejecta melt-bearing breccias at Aumühle quarry as an increase in illite in localized zones of the melt-bearing breccia (where illite was found to be dominantly interlayered with smectite, and spatially-variable kaolinite; Sapers et al., 2017), and as platy, space-filling smectite occurrences (Newsom et al., 1986; Osinski et al., 2004).

It is important to note the absence of reflectance spectroscopy from the above list; the consistency of the spectral signatures between the sample types examined in this study (Fig. 4.2) offers little definitive differences between the clay minerals of the deposit types, in contrast to the detailed XRD patterns that reveal important variations in clay mineralogy, crystallinity, and interlayer structure (Figs. 4.3 and 4.4). It has not yet been shown that reflectance spectroscopy can detect interlayered materials within the structure of swelling clay minerals; these components of the minerals are likely to be under the limits of detection for the technique. Typically, shifts in absorption bands of reflectance data are attributed to interlayer cation vibrations, but the interlayered material is not characterized or quantified (e.g., Bishop and Murad, 2004). Laboratory analyses that enable a characterization of their complex mineralogic nature, including interlayer materials, and that provide sub-μm-scale textural evidence (e.g., Fig. 4.6) are necessary to distinguish the pre-impact clay minerals from those of impact-origin. Although these datasets allow a comparison of these clay minerals and provide insight into their formation processes, this is largely possible because the geologic context of the clay minerals investigated in this study is known. Structural and compositional variations of smectites are not mutually exclusive to a given formation setting. The complex variation of smectites and other clay minerals formed through impact processes are likely very difficult to differentiate from those of a detrital or weathering origin in the absence of laboratory techniques, as described in this study; even with the best terrestrial laboratory techniques and instruments, their origins are likely not possible to discern in the absence of adequate geologic context. This difficulty is inherent in determining clay mineral provenance. For example, hydrothermal environments have been shown to yield a complex series of clay minerals formed in nearly identical conditions yet are compositionally

variable due to the thermal variance over time, which in turn influences the geochemistry of the environment through evolving circulating fluids (Tardy and Duplay, 1994). As discussed by Tardy et al. (1987), even an apparently monomineralic smectite, formed in any environment, may not be adequately evaluated as a product of the average chemical composition of millions of individual particles, covering a range of chemical formulas. In fact, mixed-layer clay minerals are likely to be highly underestimated and the mineralogy misidentified due to their difficulty in detection (Środoń, 1999; Delvaux et al., 1990; Hughes et al., 1993; Cuadros et al., 1994). These inherent difficulties in discerning specific clay mineral species and assigning provenance explains the debate on the origin and formation conditions of the clay minerals in the melt-bearing breccias at the Ries. Discerning clay mineral provenance on Mars is even more difficult, given: (1) the obvious limitations in orbitally-based or rover-based investigatory methods, and (2) that the clay-rich regions on Mars preserve several different, overlapping geologic settings that have been proposed to have formed the clay minerals, including the under-appreciated impact-related terrains.

4.5.2 Implications for Mars

On Mars, extensive clay minerals have been observed in the ancient Noachian southern highlands (e.g., Bibring et al., 2006; Carter et al., 2015; Ehlmann and Edwards, 2014); these regions also have expansive, purportedly water-carved valley systems. Thus, the observed mineralogy and morphology have been used as evidence to invoke an ancient climate that supported surface-stable liquid water, mobilized by run-off, and even precipitation (Bibring et al., 2006; Ehlmann et al., 2008; Mustard et al., 2005). However, the occurrence of clay minerals is not limited to any one landform, but clay minerals are observed throughout the heavily-cratered southern highlands. Of note is the global spatial distribution of clay minerals, present

circumferential to some of the largest Martian impact basins (e.g., Hellas and Isidis; Tornabene et al., 2013). It is generally accepted that clay minerals associated with impact craters were formed pre-impact in deep subsurface environments and are subsequently exhumed by the impact process (Ehlmann et al., 2011; Michalski et al., 2015, 2017). Although impact-hydrothermal processes have been indicated as a potential formation mechanism for Fe/Mg clay minerals (e.g., Marzo et al., 2010; Osinski et al., 2013b; Newsom, 1980; Allen et al., 1982; Sun and Milliken, 2015), it is generally assumed that this is limited to observations of these minerals in crater central uplifts (Ehlmann et al., 2013) or in distinct megabreccia blocks, fractures, or ridges (Fairén et al., 2010).

Schwenzer and Kring (2013) modeled impact-hydrothermal alteration assemblages based on martian meteorite mineralogy as a proxy for crustal composition; this study found that smectite and chlorite would likely be produced at depth, and at the surface, alteration of the melt sheet would also likely produce clay minerals and chlorite. Hagerty and Newsom (2003) also modeled hydrothermal alteration produced by an impact into basaltic Martian crust (accounting for composition, atmosphere, temperature, and pressure), and predicted virtually identical mineral assemblages to those found at the analogous Lonar Lake impact structure, India; the Fe/Mg smectite saponite was the most abundant alteration mineral predicted, by an order of magnitude, with celadonite, and various Al-oxy-hydroxides. This study and others (Table 4.2; e.g., Newsom et al., 1986; Osinski et al., 2004; Sapers et al., 2017) at Ries show that compositionally diverse Al/Fe/Mg smectites are produced by syn/post-impact processes – critically, even in the ejecta deposits – including, but not limited to hydrothermal processes (as discussed below). The implications for Mars of impact-related alteration in the ejecta is significant in the Noachian terrains that have many overlapping and large (>100 km in diameter)

impact craters, ejecta blankets, and distal ejecta dispersed over great distances. The Isidis basin is a ~1900 km-diameter impact basin formed during the Late Noachian (~3.96 Ga; Caprarelli and Orosei, 2015) that significantly altered the surface of Mars, as did the Hellas impact event and countless others during the Noachian and Pre-Noachian (Frey, 2003). The proximal ejecta of these large impacts could have extended to nearly global scales (Tornabene et al., 2013 and references therein). We suggest that the distribution of clay minerals in Noachian terrains surrounding the largest impact basins may be analogous to those observed in this study of the Ries ejecta impactites; namely that these clay minerals could have been produced by those impact events.

The alteration and resultant secondary mineral products of impactites produced at such a vast scale is not generally recognized as a source of the enigmatic clay minerals dominant in Noachian crust. However, we show that compositionally diverse, abundant (up to perhaps 70 vol%) Al/Fe/Mg smectites formed in thin melt-bearing breccia deposits that would have cooled quickly, without appreciable exogenous volatiles. Autometamorphism and devitrification, therefore, may have been the dominant alteration processes that produced the abundant clay minerals in the thin (tens of m in depth) deposits of the Ries ejecta melt-bearing breccias, as these processes occur in the absence of an external water and heat source. This is particularly significant for Mars given the assertion that Al smectites are indicative of a water-involved surficial weathering horizon (Bishop et al., 2018). As suggested by Tornabene et al. (2013), autometamorphic reactions (including solid-state devitrification) may be the dominant impact alteration process forming smectitic clay minerals on Mars under cold and very dry conditions. As impact-related alteration processes (hydrothermal as well as autometamorphism and devitrification) largely operate regardless of climatic conditions, a warm and wet climate need

not be invoked to explain their presence even at global scales (Osinski and Tornabene, 2017). Noachian crustal materials were massively recycled, brecciated, transported, completely transformed, and altered due to heavy impact cratering; we suggest that impactites are likely to be an important source of hydrated silicates in the Noachian crust.

To develop a more accurate understanding of Mars through its mineralogy, all plausible clay mineral formation mechanisms should be considered. As shown in this study, impact-excavated clay minerals or those of detrital origin may be very difficult to distinguish from those generated by impact-related processes when removed from geologic context and in the absence of laboratory techniques necessary to examine the interlayer constituents of swelling clay minerals. As such, discerning clay minerals on Mars presents an especially difficult challenge. This provides a strong rationale for (1) *in situ* investigation to adequately characterize geologic context, both regional and local, and to confirm orbital data-derived interpretations, and (2) return of well-characterized samples to Earth for laboratory analyses. NASA's upcoming Mars 2020 rover mission will have the opportunity to satisfy both these conditions and employ a methodological approach to discerning clay mineral provenance. The Mars 2020 rover will be exploring deltaic deposits within Jezero Crater (Fassett and Gouge, 2017; Williford et al., 2018) that are incredibly clay-rich, as are the surrounding geologic terrains; a potential extended mission will explore the crater rim and Jezero ejecta deposits (and potentially those from Isidis) (Farley et al., 2018). The deltaic deposits will likely be representative of regional rocks – including transported materials from impactites – and *in situ* impactites are likely to be encountered. We therefore suggest that the clay mineral phases observed in this study and those of previous studies at the Ries and other impact structures (Table 4.2; e.g., Sapers et al., 2017; Osinski et al., 2004; Simpson et al., 2018; Hagerty and Newsom, 2003) could be could be used

as a reference for consideration of impact-related provenance when interpreting clay minerals *in situ* during the Mars 2020 mission.

References

Allen, C.C., Gooding, J.L., and Keil, K., 1982, Hydrothermally altered impact melt rock and breccia: Contributions to the soil of Mars: Journal of Geophysical Research, doi: 10.1029/jb087ib12p10083.

Bibring, J.-P., Langevin, Y., Mustard, J.F., Poulet, F., Arvidson, R., Gendrin, A., Gondet, B., Mangold, N., Pinet, P., Forget, F., Berthé, M., Bibring, J.-P., Gendrin, A., Gomez, C., et al., 2006, Global Mineralogical and Aqueous Mars History Derived from OMEGA/Mars Express Data: Science, v. 312, p. 400–404, doi: 10.1126/science.1122659.

Bishop, J.L., Fairén, A.G., Michalski, J.R., Gago-Duport, L., Baker, L.L., Velbel, M.A., Gross, C., and Rampe, E.B., 2018, Surface clay mineral formation during short-term warmer and wetter conditions on a largely cold ancient Mars: Nature Astronomy, doi: 10.1038/s41550-017-0377-9.

Bishop, J.L., Lane, M.D., Dyar, M.D., and Brown, A.J., 2008, Reflectance and emission spectroscopy study of four groups of phyllosilicates: smectites, kaolinite-serpentines, chlorites and micas: Clay minerals, doi: 10.1180/claymin.2008.043.1.03.

Brindley, G.W. and Brown, G., 1980, X-Ray Diffraction Procedures for Clay mineral Identification: Mineralogical Society, p. 305–356.

Caprarelli, G., and Orosei, R., 2015, Probing the hidden geology of isidis planitia (mars) with

impact craters: Geosciences (Switzerland), doi: 10.3390/geosciences5010030.

Carter, J., Bernard, S., Horgan, B., and Quantin, C., 2019, Organic matter preservation potential at the ExoMars 2020 landing site: a preliminary assessment, in EPSC-DPS Joint Meeting 2019, p. Vol. 13, EPSC-DPS2019-445-1.

Carter, J., Loizeau, D., Mangold, N., Poulet, F., and Bibring, J.P., 2015, Widespread surface weathering on early Mars: A case for a warmer and wetter climate: Icarus, doi: 10.1016/j.icarus.2014.11.011.

Chamley, H., 1989, Clay mineral Sedimentology:, doi: 10.1007/978-3-642-85916-8.

Clark, R.N., King, T.V. V., Klejwa, M., Swayze, G. a., and Vergo, N., 1990, High spectral resolution reflectance spectroscopy of minerals: Journal of Geophysical Research, v. 95, p. 12653, doi: 10.1029/JB095iB08p12653.

Clark, R.N., Swayze, G.A., Wise, R., Livo, K.E., Hoefen, T.M., Kokaly, R.F., Sutley, S.J., Survey, U.S.G., and Title, S., 2007, USGS Digital Spectral Library splib06a: U.S. Geological Survey, p. Digital Data Series 231, http://speclab.cr.usgs.gov/spectral.lib06.

Cuadros, J., Delgado, A., Cardenete, A., Reyes, E., and Linares, J., 1994, Kaolinite/montmorillonite resembles beidellite: Clay minerals and Clay minerals, doi: 10.1346/CCMN.1994.0420517.

Delvaux, B., Herbillon, A.J., Dufey, J.E., and Vielvoye, L., 1990, Surface properties and clay mineralogy of hydrated halloysitic soil clay minerals. I: Existence of interlayer K + specific sites : Clay minerals, doi: 10.1180/claymin.1990.025.2.01.

Derkowski, A., Drits, V.A., and McCarty, D.K., 2012, Nature of rehydroxylation in dioctahedral 2:1 layer clay minerals: American Mineralogist, doi: 10.2138/am.2012.3871.

Drewes, H., 1963, Geology of the Funeral Peak Quadrangle, California, on the east flank of Death Valley: Geological Survey professional paper, p. 1–75.

Ehlmann, B.L., Berger, G., Mangold, N., Michalski, J.R., Catling, D.C., Ruff, S.W., Chassefière, E., Niles, P.B., Chevrier, V., and Poulet, F., 2013, Geochemical consequences of widespread clay mineral formation in Mars' ancient crust: Space Science Reviews, v. 174, p. 329–364, doi: 10.1007/s11214-012-9930-0.

Ehlmann, B.L., and Edwards, C.S., 2014, Mineralogy of the Martian Surface: Annual Review of Earth and Planetary Sciences, v. 42, http://www.annualreviews.org/doi/abs/10.1146/annurev-earth-060313-055024.

Ehlmann, B.L., Mustard, J.F., Fassett, C.I., Schon, S.C., Head III, J.W., Des Marais, D.J., Grant, J. a., and Murchie, S.L., 2008, Clay minerals in delta deposits and organic preservation potential on Mars: Nature Geoscience, v. 1, p. 355–358, doi: 10.1038/ngeo207.

Ehlmann, B.L., Mustard, J.F., Murchie, S.L., Bibring, J.P., Meunier, A., Fraeman, A.A., and Langevin, Y., 2011, Subsurface water and clay mineral formation during the early history of Mars: Nature, doi: 10.1038/nature10582.

Ehrmann, W., Setti, M., and Marinoni, L., 2005, Clay minerals in Cenozoic sediments off Cape Roberts (McMurdo Sound, Antarctica) reveal palaeoclimatic history: Palaeogeography, Palaeoclimatology, Palaeoecology, doi: 10.1016/j.palaeo.2005.06.022.

Engelhardt, W. v., 1972, Shock produced rock glasses from the Ries crater: Contributions to Mineralogy and Petrology, v. 36, p. 265–292, doi: 10.1007/BF00444336.

Engelhardt, W. V., Arndt, J., Fecker, B., and Pankau, H.G., 1995, Suevite breccia from the Ries crater, Germany: Origin, cooling history and devitrification of impact glasses: Meteoritics, v. 30, p. 279–293, doi: 10.1111/j.1945-5100.1995.tb01126.x.

Von Engelhardt, W., 1990, Distribution, petrography and shock metamorphism of the ejecta of the Ries crater in Germany-a review: Tectonophysics, v. 171, p. 259–273, doi: 10.1016/0040-1951(90)90104-G.

von Engelhardt, W., and Graup, G., 1984, Suevite of the ries crater, Germany: Source rocks and implications for cratering mechanics: Geologische Rundschau, v. 73, p. 447–481, doi: 10.1007/BF01824968.

Fairén, A.G., Chevrier, V., Abramov, O., Marzo, G.A., Gavinc, P., Davila, A.F., Tornabene, L.L., Bishop, J.L., Roush, T.L., Gross, C., Kneissl, T., Uceda, E.R., Dohm, J.M., Schulze-Makuch, D., et al., 2010, Noachian and more recent phyllosilicates in impact craters on Mars: Proceedings of the National Academy of Sciences of the United States of America, doi: 10.1073/pnas.1002889107.

Farley, K., Stack Morgan, K., and Williford, K., 2018, Jezero-Midway interellipse traverse mission concept:, https://marsnext.jpl.nasa.gov/workshops/2018-10/PRESENTATIONS/LSW4_TraverseMission_M2020ProjSci_v2.pdf.

Fassett, C.I., and Gouge, T.A., 2017, Hydrological Modeling of the Jezero Crater Outlet-

Forming Flood, in Lunar and Planetary Science Conference, p. 2037.

Ferrage, E., Lanson, B., Sakharov, B.A., and Drits, V.A., 2005, Investigation of smectite hydration properties by modeling experimental X-ray diffraction patterns: Part I: Montmorillonite hydration properties: American Mineralogist, doi: 10.2138/am.2005.1776.

Fesharaki, O., García-Romero, E., Cuevas-González, J., and López-Martínez, N., 2007, Clay mineral genesis and chemical evolution in the Miocene sediments of Somosaguas, Madrid Basin, Spain: Clay minerals, doi: 10.1180/claymin.2007.042.2.05.

Forget, F., Wordsworth, R., Millour, E., Madeleine, J.B., Kerber, L., Leconte, J., Marcq, E., and Haberle, R.M., 2013, 3D modelling of the early martian climate under a denser CO 2 atmosphere: Temperatures and CO 2 ice clouds: Icarus, doi: 10.1016/j.icarus.2012.10.019.

Frey, H. V, 2003, Buried impact basins and the earliest history of Mars: Sixth Intern. Conf. Mars, Pasadena, Ca.,.

Georgiadis, A., Dietel, J., Dohrmann, R., and Rennert, T., 2019, What are the nature and formation conditions of hydroxy-interlayered minerals (HIMs) in soil? J. Plant Nutr. Soil Science, v. 000, p. 1–15, doi: 10.1002/jpln.201900283.

Gough, D.O., 1981, Solar interior structure and luminosity variations: Solar Physics, doi: 10.1007/BF00151270.

Graup, G., 1978, Das Kristallin im Nordlinger Ries. € Petrographische Zusammensetzung und Auswurfmechanismus der kristallinen Trummermassen; Struktur des kristallinen € Untergrundes und Beziehungen zum Moldanubikum: Stuttgart: Enke Verlag, p. 190.

Hagerty, J.J., and Newsom, H.E., 2003, Hydrothermal alteration at the Lonar Lake impact structure, India: Implications for impact cratering on Mars: Meteoritics and Planetary Science, doi: 10.1111/j.1945-5100.2003.tb00272.x.

Heller-Kallai, L., 1980, Dehydroxylation of Dioctahedral Phyllosilicates: Clay minerals and Clay minerals, doi: 10.1346/ccmn.1980.0280505.

Hillier, S., 1995, Erosion, Sedimentation and Sedimentary Origin of Clay minerals, in Origin and Mineralogy of Clay minerals, doi: 10.1007/978-3-662-12648-6_4.

Hörz, F., 1982a, Ejecta of the ries crater, Germany: Special Paper of the Geological Society of America, doi: 10.1130/SPE190-p39.

Hörz, F., 1982b, Geological Implications of Impacts of Large Asteroids and Comets on the Earth: v. 190, 39-55 p., doi: 10.1130/SPE190.

Hörz, F., Ostertag, R., and Rainey, D.A., 1983a, Bunte Breccia of the Ries: Continuous deposits of large impact craters: Reviews of Geophysics, v. 21, p. 1667–1725, doi: 10.1029/RG021i008p01667.

Hörz, F., Ostertag, R., and Rainey, D.A., 1983b, Bunte Breccia of the Ries: Continuous deposits of large impact craters: Reviews of Geophysics, v. 21, p. 1667, doi: 10.1029/RG021i008p01667.

Hover, V.C., Walter, L.M., Peacor, D.R., and Martini, A.M., 1999, Mg-smectite authigenesis in a marine evaporative environment, Salina Ometepec, Baja California: Clay minerals and Clay minerals, doi: 10.1346/CCMN.1999.0470302.

Hughes, R.E., Moore, D.M., and Reynolds, R.C., 1993, Kaolin Genesis and Utilization, in H Murray, W Bundy, C.H. ed., Clay mineral. Soc., Boulder, Colorado, p. 291–323.

Huttner, R., 1969, Bunte Trummermassen und Suevit. (Multi-colored, fragmented material and suevite.): Geologica Bavarica, v. 61, p. 142–200.

Hynek, B., 2016, The great climate paradox of ancient Mars: Geology, doi: 10.1130/focus102016.1.

Iacoviello, F., Giorgetti, G., Nieto, F., and Memmi, I.T., 2012, Evolution with depth from detrital to authigenic smectites in sediments from AND-2A drill core (McMurdo Sound, Antarctica): Clay minerals, doi: 10.1180/claymin.2012.047.4.07.

Kenkmann, T., Collins, G.S., and W??nnemann, K., 2012, The Modification Stage of Crater Formation, in Impact Cratering: Processes and Products, p. 60–75, doi: 10.1002/9781118447307.ch5.

Laskar, J., Correia, A.C.M., Gastineau, M., Joutel, F., Levrard, B., and Robutel, P., 2004, Long term evolution and chaotic diffusion of the insolation quantities of Mars: Icarus, v. 170, p. 343–364, doi: 10.1016/j.icarus.2004.04.005.

Marshall, R.R., 1961, Devitrification of natural glass: Bulletin of the Geological Society of America, doi: 10.1130/0016-7606(1961)72[1493:DONG]2.0.CO;2.

Marzo, G.A., Davila, A.F., Tornabene, L.L., Dohm, J.M., Fairén, A.G., Gross, C., Kneissl, T., Bishop, J.L., Roush, T.L., and McKay, C.P., 2010, Evidence for Hesperian impact-induced hydrothermalism on Mars: Icarus, v. 208,

http://linkinghub.elsevier.com/retrieve/pii/S0019103510001156.

Michalski, J.R., Cuadros, J., Bishop, J.L., Darby Dyar, M., Dekov, V., and Fiore, S., 2015, Constraints on the crystal-chemistry of Fe/Mg-rich smectitic clay minerals on Mars and links to global alteration trends: Earth and Planetary Science Letters, v. 427, p. 215–225, doi: 10.1016/j.epsl.2015.06.020.

Michalski, J.R., Glotch, T.D., Friedlander, L.R., Darby Dyar, M., Bish, D.L., Sharp, T.G., and Carter, J., 2017, Shock metamorphism of clay minerals on Mars by meteor impact: Geophysical Research Letters, doi: 10.1002/2017GL073423.

Morrison, R H and Oberbeck, V.R., 1978, No Title, in Proceedings of Lunar and Planetary Science, p. 3763–3785.

Mustard, J.F., Poulet, F., Gendrin, A., Bibring, J.P., Langevin, Y., Gondet, B., Mangold, N., Bellucci, G., and Altieri, F., 2005, Olivine and Pyroxene Diversity in the Crust of Mars: Science, v. 307, http://www.jstor.org.proxy1.lib.uwo.ca/stable/3841768.

Muttik, N., Kirsimaee, K., and Vennemann, T.W., 2010, Stable isotope composition of smectite in suevites at the Ries crater, Germany: Implications for hydrous alteration of impactites: Earth and Planetary Science Letters, v. 299, p. 190–195, doi: 10.1016/j.epsl.2010.08.034.

Muttik, N., Kirsimaee, K., Somelar, P., and Osinsk, G.R., 2008, Post-impact alteration of surficial suevites in Ries crater, Germany: Hydrothermal modification or weathering processes? METEORITICS & PLANETARY SCIENCE, v. 43, p. 1827–1840, doi: 10.1111/j.1945-5100.2008.tb00646.x.

Naumov, M. V., 2005, Principal features of impact-generated hydrothermal circulation systems: Mineralogical and geochemical evidence: Geofluids, v. 5, p. 165–184, doi: 10.1111/j.1468-8123.2005.00092.x.

Newsom, H.E., 1980, Hydrothermal alteration of impact melt sheets with implications for Mars: Icarus, v. 44, p. 207–216, doi: 10.1016/0019-1035(80)90066-4.

Newsom, H.E., Graup, G., Iseri, D.A., Geissman, J.W., and Keil, K., 1990, The formation of the Ries Crater, West Germany; Evidence of atmospheric interactions during a larger cratering event: Geological Society of America Special Papers , v. 247, p. 195–206, doi: 10.1130/SPE247-p195.

Newsom, H., Graup, G., Sewards, T., and Keil, K., 1986, Fluidization and hydrothermal alteration of the Suevite deposit at the Ries Crater, West Germany, and implications for Mars: Journal of Geophysical Research, v. 91, p. E239–E251, doi: http://dx.doi.org/10.1029/JB091iB13p0E239.

Nisbet, E.G., and Sleep, N.H., 2001, The habitat and nature of early life: Nature, doi: 10.1038/35059210.

Osinski, G.R., 2005, Hydrothermal activity associated with the Ries impact event, Germany: Geofluids, v. 5, p. 202–220, doi: 10.1111/j.1468-8123.2005.00119.x.

Osinski, G.R., 2004, Impact melt rocks from the Ries structure, Germany: An origin as impact melt flows? Earth and Planetary Science Letters, v. 226, p. 529–543, doi: 10.1016/j.epsl.2004.08.012.

Osinski, G.R., Banerjee, N.R., Cockell, C.S., Flemming, R., Izawa, M.R.M., McCutcheon, J., Parnell, J., Preston, L.J., Pickersgill, A.E., Pontefract, A., Sapers, H.M., and Southam, G. Impact-generated hydrothermal systems on Earth and Mars:, file:///Files/60/60b5a1cc-4483-4fcb-b58f-176b8a16170f.pdf.

Osinski, G.R., Grieve, R. a. F., and Spray, J.G., 2004, The nature of the groundmass of surficial suevite from the Ries impact structure, Germany, and constraints on its origin: Meteoritics & Planetary Science, v. 39, p. 1655–1683, doi: 10.1111/j.1945-5100.2004.tb00065.x.

Osinski, G.R., Grieve, R.A.F., and Tornabene, L.L., 2012, Excavation and Impact Ejecta Emplacement, in Impact Cratering: Processes and Products, p. 43–59, doi: 10.1002/9781118447307.ch4.

Osinski, G.R., and Tornabene, L.L., 2017, The role of impact events play in redistributing and sequestering water on Early Mars, in American Geophysical Union, Fall Meeting 2017, p. P33C–2885.

Osinski, G.R., Tornabene, L.L., Banerjee, N.R., Cockell, C.S., Flemming, R., Izawa, M.R.M., McCutcheon, J., Parnell, J., Preston, L.J., Pickersgill, A.E., Pontefract, A., Sapers, H.M., and Southam, G., 2013a, Impact-generated hydrothermal systems on Earth and Mars: Icarus, v. 224, p. 347–363, doi: 10.1016/j.icarus.2012.08.030.

Osinski, G.R., Tornabene, L.L., Banerjee, N.R., Cockell, C.S., Flemming, R., Izawa, M.R.M., McCutcheon, J., Parnell, J., Preston, L.J., Pickersgill, A.E., Pontefract, A., Sapers, H.M., and Southam, G., 2013b, Impact-generated hydrothermal systems on Earth and Mars: Icarus, v. 224, http://linkinghub.elsevier.com/retrieve/pii/S0019103512003491.

Osinski, G.R., Tornabene, L.L., and Grieve, R.A.F., 2011, Impact ejecta emplacement on terrestrial planets: Earth and Planetary Science Letters, v. 310, p. 167–181, doi: 10.1016/j.epsl.2011.08.012.

Pietrek, A., and Kenkmann, T., 2016, Ries Bunte Breccia revisited: Indications for the presence of water in Itzing and Otting drill cores and implications for the emplacement process: Meteoritics and Planetary Science, v. 51, p. 1203–1222, doi: 10.1111/maps.12656.

Pohl, J., Stöffler, D., Gall, H., and Ernstson, K., 1977a, The Reis Impact Crater, in Impact and explosion cratering, p. 343–404.

Pohl, J., Stöffler, D., Gall, H., and Ernstson, K., 1977b, The Ries impact crater, in Impact and explosion cratering, p. 343–404.

Poulet, F., Bibring, J.-P., Mustard, J.F., Gendrin, a., Mangold, N., Langevin, Y., Arvidson, R.E., Gondet, B., Gomez, C., Berthé, M., Erard, S., Forni, O., Manaud, N., Poulleau, G., et al., 2005, Phyllosilicates on Mars and implications for early martian climate: Nature, v. 438, p. 623–627, doi: 10.1038/nature04274.

Quantin-Nataf, C., Carter, J., Mandon, L., Balme, M., Fawdon, P., Davis, J., Thollot, P., Dehouck, E., Pan, L., Volat, M., Millot, C., Breton, S., Loizeau, D., and Vago, J.L., 2019, ExoMars at Oxia Planum, Probing the aqueous-related Noachian environments, in Ninth International Conference on Mars 2019, p. 2089.

Sapers, H.M., Osinski, G.R., Flemming, R.L., Buitenhuis, E., Banerjee, N.R., Tornabene, L.L., Blain, S., and Hainge, J., 2017a, Evidence for a spatially extensive hydrothermal system at

the Ries impact structure, Germany: Meteoritics & Planetary Science, v. 52, p. 351–371.

Sapers, H.M., Osinski, G.R., Flemming, R.L., Buitenhuis, E., Banerjee, N.R., Tornabene, L.., Blain, S., and Hainge, J., 2017b, Evidence for a spatially extensive hydrothermal system at the Ries impact structure, Germany: Meteoritics & Planetary Science, v. 52.

Schaal, R.B., and Horz, F., 1977, Shock Metamorphism of Lunar and Terrestrial Basalts: Proceedings of the Lunar Science Conference, v. 2, p. 1697–1729, http://articles.adsabs.harvard.edu/cgi-bin/nph-iarticle_query?1977LPSC....8.1697S&data_type=PDF_HIGH&whole_paper=YES&type=PRINTER&filetype=.pdf.

Schmieder, M., Kennedy, T., Jourdan, F., Buchner, E., and Reimold, W.U., 2018, A high-precision40Ar/39Ar age for the Nördlinger Ries impact crater, Germany, and implications for the accurate dating of terrestrial impact events: Geochimica et Cosmochimica Acta, v. 220, p. 146–157, doi: 10.1016/j.gca.2017.09.036.

Schwenzer, S.P., and Kring, D.A., 2013, Alteration minerals in impact-generated hydrothermal systems - Exploring host rock variability: Icarus, doi: 10.1016/j.icarus.2013.06.003.

Setti, M., Marinoni, L., Galindo, A.L., and Huertas, A.D., 2000, Compositional and morphological features of the smectites of the sediments of CRP-2/2A, Victoria Land Basin, Antarctica: Terra Antarctica,.

Siegert, S., Branney, M.J., and Hecht, L., 2017, Density current origin of a melt-bearing impact ejecta blanket (Ries suevite, Germany): Geology, doi: 10.1130/G39198.1.

Simpson, S.L., Osinski, G.R., Longstaffe, F.J., Kring, D.A., Schmieder, M., Svensson, M., and Gulick, S.P.S., 2018, Characterization of impact glass alteration and associated secondary clay mineralogy through the upper Chicxulub peak ring, in 49th Lunar and Planetary Science Conference, p. 2083.

Singer, A., 1984, The paleoclimatic interpretation of clay minerals in sediments - a review: Earth Science Reviews, doi: 10.1016/0012-8252(84)90055-2.

Squyres, S.W., and Kasting, J.F., 1994, Early mars: How warm and how wet? Science, doi: 10.1126/science.265.5173.744.

Srodon, J., 1980, Synthesis of mixed-layer kaolinite/smectite: Clay minerals & Clay minerals, v. 28, p. 419–424.

Środoń, J., 1999, NATURE OF MIXED-LAYER CLAY MINERALS AND MECHANISMS OF THEIR FORMATION AND ALTERATION: Annual Review of Earth and Planetary Sciences, doi: 10.1146/annurev.earth.27.1.19.

Stähle, V., 1972, Impact glasses from the suevite of the N??rdlinger Ries: Earth and Planetary Science Letters, v. 17, p. 275–293, doi: 10.1016/0012-821X(72)90287-7.

Stahle, V., and Otterman, J., 1977, Ries-Forschungsbohrung 1973: Zeolithisierung der Gaser im Suevit und Petrographie der Beckensuevite und Gangbreccien: Geologica Bavarica, v. 73, p. 191–217.

Sturm, S., Wulf, G., Jung, D., and Kenkmann, T., 2013, The ries impact, a double-layer rampart crater on earth: Geology, v. 41, p. 531–534, doi: 10.1130/G33934.1.

Sun, V.Z., and Milliken, R.E., 2015, Ancient and recent clay mineral formation on Mars as revealed from a global survey of hydrous minerals in crater central peaks: Journal of Geophysical Research E: Planets, v. 120, p. 2293–2332, doi: 10.1002/2015JE004918.

Tardy, Y., and Duplay, J., 1994, Stability Fields of Smectites and Illites Including Glauconites as a Function of Temperature and Chemical Composition: Developments in Sedimentology, doi: 10.1016/S0070-4571(08)70438-2.

Tardy, Y., Duplay, J., and Fritz, B., 1987, Stability of smectites and illites as a function of temperature and chemical compostion, in Proc. Int. Meeting of Geochemistry of Earth Sciences and Processes of Mineral Formation, Granada, p. 461–494.

Tornabene, L.L., Osinski, G.R., McEwen, A.S., Boyce, J.M., Bray, V.J., Caudill, C.M., Grant, J.A., Hamilton, C.W., Mattson, S., and Mouginis-Mark, P.J., 2012, Widespread crater-related pitted materials on Mars: Further evidence for the role of target volatiles during the impact process: Icarus, v. 220, http://linkinghub.elsevier.com/retrieve/pii/S0019103512002047.

Tornabene, L.L., Osinski, G.R., McEwen, A.S., Wray, J.J., Craig, M.A., Sapers, H.M., and Christensen, P.R., 2013a, An impact origin for hydrated silicates on Mars: A synthesis: AN IMPACT ORIGIN FOR HYDRATED SILICATES: Journal of Geophysical Research: Planets, v. 118, http://doi.wiley.com/10.1002/jgre.20082.

Tornabene, L.L., Osinski, G.R., McEwen, A.S., Wray, J.J., Craig, M.A., Sapers, H.M., and Christensen, P.R., 2013b, An impact origin for hydrated silicates on Mars: A synthesis: Journal of Geophysical Research E: Planets, v. 118, p. 994–1012, doi: 10.1002/jgre.20082.

Wemmer, K., 2008, Provenance of siliciclastic sediments (Permian to Jurassic) in the Central European Basin: Zeitschrift der Deutschen Gesellschaft für Geowissenschaften, v. 159/4, p. 641–650.

Williford, K.H., Farley, K.A., Stack, K.M., Allwood, A.C., Beaty, D., Beegle, L.W., Bhartia, R., Brown, A.J., de la Torre Juarez, M., Hamran, S.-E., Hecht, M.H., Hurowitz, J.A., Rodriguez-Manfredi, J.A., Maurice, S., et al., 2018, The NASA Mars 2020 Rover Mission and the Search for Extraterrestrial Life, in From Habitability to Life on Mars, doi: 10.1016/b978-0-12-809935-3.00010-4.

Wordsworth, R.D., 2016, The Climate of Early Mars: Annual Review of Earth and Planetary Sciences, doi: 10.1146/annurev-earth-060115-012355.

Wordsworth, R., Forget, F., Millour, E., Head, J.W., Madeleine, J.B., and Charnay, B., 2013, Global modelling of the early martian climate under a denser CO 2 atmosphere: Water cycle and ice evolution: Icarus, doi: 10.1016/j.icarus.2012.09.036.

Wordsworth, R.D., Kerber, L., Pierrehumbert, R.T., Forget, F., and Head, J.W., 2015, Comparison of "warm and wet" and "cold and icy" scenarios for early Mars in a 3-D climate model: Journal of Geophysical Research E: Planets, doi: 10.1002/2015JE004787.

Zahnle, K., Arndt, N., Cockell, C., Halliday, A., Nisbet, E., Selsis, F., and Sleep, N.H., 2007, Emergence of a habitable planet: Space Science Reviews, doi: 10.1007/s11214-007-9225-z.

ZHANG, Z.Y., Huang, L., LIU, F., WANG KUANG, Mi., LING FU, Q., and Zhu, J., 2017, The properties of clay minerals in soil particles ftom two ultisols, China: Clay minerals and Clay

minerals, v. 65, p. 273–285.

Chapter 5: CanMars mission Science Team operational results: Implications for operations and the sample selection process for Mars Sample Return (MSR) [2]

5.1 Introduction

Robotic exploration of the surface of Mars has transformed our understanding of past and present processes on the Red Planet and, perhaps more importantly for the future of exploration of the solar system, have provided a human-level view of the surface, sparking public imagination about discoveries and forging a path for human exploration. A highly successful sequence of Mars surface missions (e.g., Mars rovers Spirit, Opportunity, and Curiosity) has provided science results supporting the habitability of early Mars and have motivated Mars Sample Return (MSR) as the next major phase for Mars exploration (Beaty et al., 2019). These missions have also led to increasing sophistication in robotic science operations, which MSR will build on. The Viking landers were the first successfully landed assets on Mars and operated from 1976 to 1982 (Klein, 1998). Viking 1 landed in Chryse Planitia and Viking 2 in Utopia Planitia, both conducting soil analyses and collecting weather data. The Viking missions were critical to test the feasibility of science operations via landed assets on the Martian surface. In 1997, the Mars Pathfinder Sojourner rover demonstrated a low-cost mission, returning weather data and images for an extended, nearly 3-month mission, critically demonstrating the value of mobility

[2] Caudill, C.M., Pontefract, A., Osinski, G. R., Tornabene, L. L., Xie, T., Mittelholz, A., Poitras, J., Simpson, S., Svensson, M., Grau, A. G., Godin, E., Pilles, E., Francis, R., Williford, K., Tuite, M., Battler, M., Hipkin, V., Haltigin, T., and the 2015 & 2016 Science Team members (2019) CanMars mission Science Team operational results: Implications for operations and the sample selection process for Mars Sample Return (MSR), Planetary and Space Science, 172, 43-56.

with respect to achieving science objectives (Golombek et al., 1997). Then in 2004, the Mars Exploration Rovers (MER) Spirit (Arvidson et al., 2006) and Opportunity landed (Squyres et al., 2006); Spirit landed in Gusev Crater, finding evidence of past water before it became stuck in a sand trap to end the mission in 2010; Opportunity landed in Meridiani Planum on January 24, 2004, immediately finding hematite "blueberries", the source of the Fe signatures that had been observed by Mars Global Surveyor. The discovery of these iron concretions, as well as festoon cross-lamination indicative of shallow subaqueous flows, revealed that subsurface water had likely been substantial in Mars' past (Grotzinger et al., 2005; Squyres et al., 2006). Having roved more than 33 km, Opportunity arrived at the 22-km diameter Endeavor Crater in 2011, currently exploring a potential water-carved valley feature until the mission ended on June 2018. The Phoenix lander mission successfully completed a 5-month mission in 2008 studying polar processes and is no longer in operation (Smith et al., 2009). The only currently active landed mission on Mars is the Curiosity rover (or Mars Science Laboratory, MSL) which landed in August 2012 as a next-generation rover (Grotzinger et al., 2012). It landed in Gale Crater to explore hypothesized fluvial and lacustrine deposits in the floor and as a transect of a mounded sedimentary section known as Mount Sharp. MSL has made key discoveries such as the detection of organic material (that is, molecular structures containing carbon) and is still exploring Mount Sharp (Freissinet et al., 2015).

The next NASA Mars rover mission has a novel task unique among the rovers that have been previously deployed, with new goals focused on identifying and acquiring samples of astrobiological significance. The NASA Mars 2020 rover mission is focused on determining past habitability of ancient Mars (during the first billion years of its history) and searching for evidence of past or present life (Mustard et al., 2013), and is the first in a series of planned

missions for Mars Sample Return (MSR). Similarly, the guiding science objectives of the ESA ExoMars rover, also set for launch in 2020, are focused around the search for past or present life and characterization of water/ice and its geochemistry if present (Vago et al., 2017). The ExoMars rover will be capable of drilling 2 m into the subsurface, a depth at which it is thought that organic molecules are shielded from detrimental surface oxidative processes and cosmic radiation, thus enabling their detection (Kminek and Bada, 2006). The search for organic compounds is key for astrobiological investigations, as these structures make up the basic building blocks of all known life processes.

As the fate of any rover is precarious post-landing, and mission funding requires shortened time-critical observations, results, and interpretations, pre-mission analogue studies are fundamental to ensure that procedures are thoroughly vetted and the best possible approach to mission operations are determined. To this end, the 2015–2016 CanMars Mars Sample Return Analogue Deployment (MSRAD) employed simulated instrumentation with the same basic mission goals, new and current operational and workflow procedures, and rover power and uplink/downlink data constraints as is planned for Mars 2020. An overview of the analogue mission campaign and team structure, which included Mission Control (Science and Planning Team operations (for Planning Team operations, see Pilles et al. (2017) which drove the mission at Western), Canadian Space Agency (CSA) Mars Exploration Rover (MESR) Operations Team (conducting rover uplinks at CSA headquarters Saint-Hubert, Quebec), the independent Field Validation Science Team, and the field team (managing on-site operations in Hanksville, Utah; see Caudill et al., 2019) is detailed by Osinski et al. (2019). Here, we outline the procedural and workflow operations of a rover mission Science Team and detail how the daily derived science influenced sol-by-sol plans, thus resulting in targeting and acquiring samples for cache.

Assessment of the accuracy of the data and interpretations reached by the remote Science Team was assessed in four ways:

- After the mission activity was completed, members of the remote Science Team visited the field site to walk the rover traverse, detailing the variances between rover-derived science and interpretations and field observations (Caudill et al., 2019);
- Samples were collected from the field site which were then analyzed with gold-standard laboratory instrumentation and compared with rover-derived results (Caudill et al, 2019);
- The Field Validation Team independently investigated the site using traditional field geology methods, which were compared to the remote robotic methods with important geologic and operational outcomes (Beaty et al., 2019), and;
- Documentarians recorded the activities of both the Science and Planning teams, documenting data-based interpretations and the subsequent decisions made throughout the mission; this documentation was assessed post-mission (and is available for future analogue or real missions) for assessments of decision complexities, team dynamics, and overall efficacy (Bednar et al., 2019).

5.2 Science Operations Construct

The CanMars-MSRAD analogue mission was built on a collaboration between the Centre for Planetary Science and Exploration (CPSX) at the University of Western Ontario (Western) and Canadian Space Agency (CSA). Past CPSX-led planetary analogue missions have been held across North America focused on advancing the science to influencing operations of robotic and future human exploration (e.g., (Marion et al., 2012; Osinski et al., 2010). The CanMars deployment was conceived as a 5-week field and operational test (held in November 2015 and November 2016) for the Mars 2020 sample cache rover mission, resulting in the most realistic

known MSR rover analogue mission to-date (Osinski et al., 2019). The MSL-scale Mars Exploration Rover (MESR) was deployed to a scientifically relevant Mars analogue sedimentary field site (detailed in Tornabene et al., 2019), with integrated mast-mounted imagers, a robotic arm equipped with a micro-imager and sampling system, and integrated and stand-in instruments. Osinski et al. (2019) provide a comprehensive overview of the MESR platform and science instruments used. Briefly, the science instruments included: a Raman spectrometer stand-in for the Scanning Habitable Environments with Raman & Luminescence for Organics & Chemicals (SHERLOC); an X-ray fluorescence (XRF) spectrometer stand-in for the Planetary Instrument for X-ray Lithochemistry (PIXL) with micro-focus camera (Simpson et al., 2017); three separate instruments as stand-ins for SuperCam, namely a Raman (Mittelholz et al., 2016), Laser-induced breakdown (LIBS; Svensson et al., 2017), and visible-infrared (VIS-IR; Bina et al., 2017) spectrometers; and a remote micro-imager (RMI) and mast-mounted cameras (Godin et al., 2017). The SHERLOC stand-in Raman is capable of detecting potential biomarkers *in situ*, with the suite of spectrometers used to test and evaluate the depositional model at each new site to understand habitability potential. CanMars flight rules for the SuperCam stand-ins Raman, LIBS, and VIS-IR allowed usage as remote instruments, meaning data could be acquired on targets up to 12 m away (similar to the expected range for Mars 2020 SuperCam Raman and VIS-IR) and 7 m (the maximum range of MSL ChemCam LIBS) from the rover (Francis et al., 2016). Out-of-simulation field operation of these instruments is documented by Caudill et al. (2019, b).

Rover-derived data and Science Team analysis and interpretations drove the daily, or sol-by-sol, plan; this analogue mission was therefore high fidelity as real-time, remote spectroscopic (geochemical, mineralogical, and imaging) data was integral to the simulation. The construct of

this analogue mission was built on current MSL mission operations and traverse strategies, while acting as a test-bed for further development of those procedures for future missions. The mission scenario included various constraints modeled after MSL, including rover traverse limitations and resource costs as well as strict adherence to data uplink and downlink 'windows' and operational schedules. Although the Science Team did not adhere to Mars time (common for the start of Mars rover missions to maximize operations during daylight), a daily schedule of morning (7:00–10:00) and evening (19:00–22:00) operations was held for three weeks each in November 2015 and November 2016. The 2016 mission deployment was a continuation of the 2015 deployment. The knowledge transfer supporting the continuation of the mission was conducted through: individual team member and instrument team reports; conference abstracts; archived data and interpretations and results presentations; pre-mission training sessions to prepare new team members, and; the use of Slack in both deployments.

5.2.1 Science Objectives

The CanMars mission was science-driven and thus, the main goals can be summarized as two main science objectives: 1) collect and rank samples for cache and return with highest potential for preservation of organic-rich carbon (using Total Organic Carbon (TOC) as a proxy for evaluation of this test); and 2) assess paleoenvironmental habitability potential and history of water at the site. These science objectives are derived from Mars 2020 science objectives (Mustard et al., 2013) which itself is based on the E2E-iSAG report (McLennan et al., 2011). CanMars entailed similar mission objectives to that of Mars 2020, including the characterization and cache of samples with the most significant contributions to the understanding of life and its chemical precursors, surface materials and processes, and planetary and atmospheric evolution. CanMars was also a field-test for Mars 2020 operations and sought to advance the operational

concepts of a MSR mission. The CanMars instrumentation, tasks, and goals are related to the MEPAG goals as shown in Figure 5.1. Full mission success was outlined as collecting two or more scientifically significant samples guided by *in situ* investigations as outlined in the Mars Exploration Program Analysis Group (MEPAG, 2015) document. MEPAG provides a methodology to address the high-level goals of habitability (MEPAG goal 1; Mars 2020/E2E-iSAG objective A) and history of water (MEPAG Goal III, Mars 2020/ E2E-iSAG objective B), including the following sub-goals:

- Goal I, Investigation A1.2. Constrain prior water availability with respect to duration, extent, and chemical activity;
- Goal I, Investigation A1.3. Constrain prior energy availability with respect to type (e.g., light, specific redox couples), chemical potential (e.g., Gibbs energy yield), and flux;
- Goal I, Investigation A1.4. Constrain prior physicochemical conditions, emphasizing temperature, pH, water activity, and chemical composition;
- Goal I, Investigation A2.1. Identify conditions and processes that would have aided preservation and/or degradation of complex organic compounds, focusing particularly on characterizing redox changes and rates in surface and near-surface environments;
- Goal III, Investigation A1.1. Determine the role of water and other processes in the sediment cycle;
- Goal III, Investigation A1.3. Characterize the textural and morphologic features of rocks and outcrops.

It should be noted that the MEPAG document also outlines the need to determine if environments are currently habitable coupled with investigations of evidence for extant life. In

keeping with a realistic analogue scenario with its potential impact to future Mars missions, only ancient habitability was considered, and current life at the analogue site was discounted.

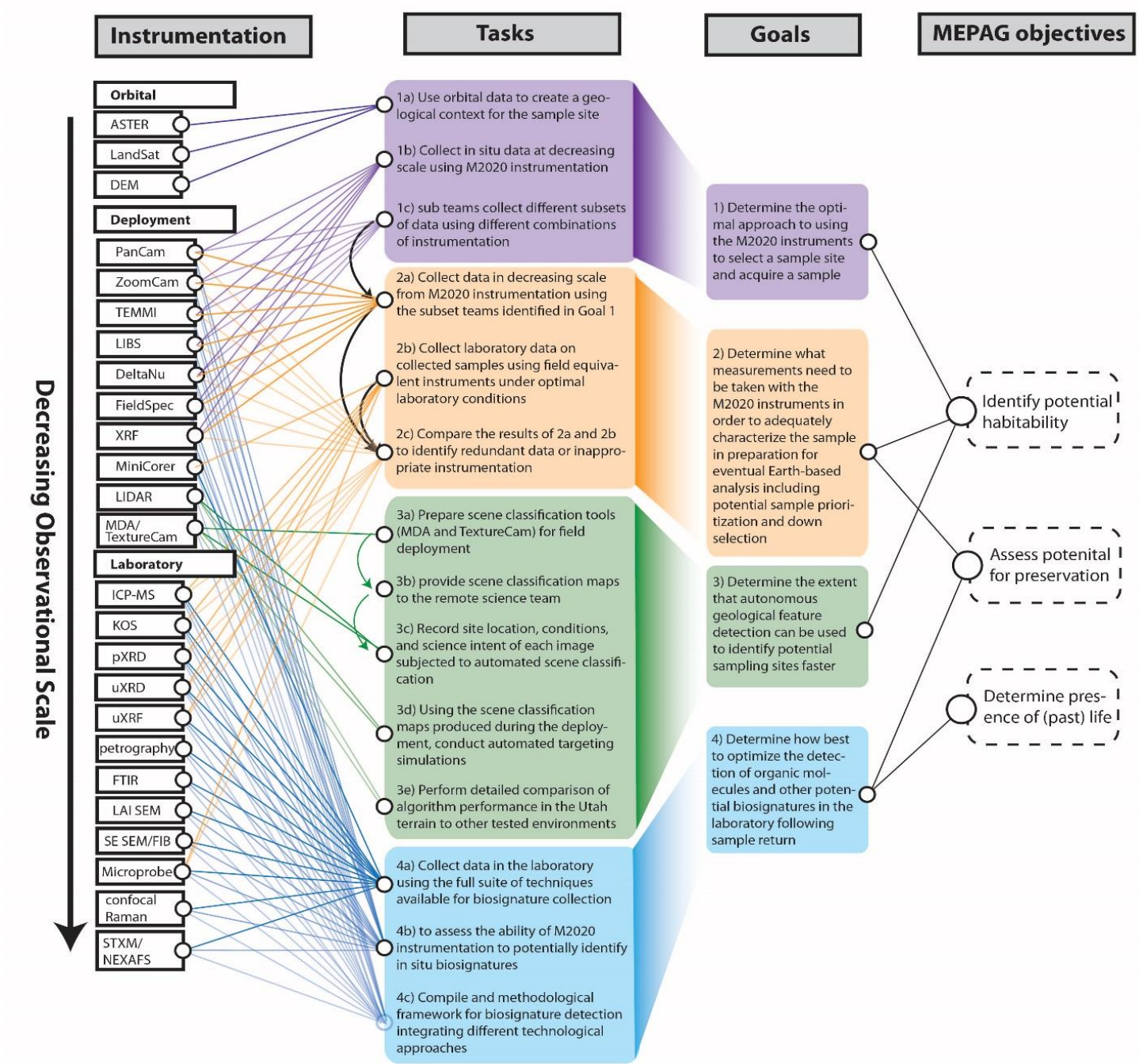

Figure 5.1. Summary of proposed instrument linkages to the CanMars mission requirements and overall MEPAG objectives.

5.3 Pre-mission planning

Several months prior to "landing" and the official analogue mission start in 2015, the mission control team (including Science and Planning Teams) met for several planning meetings to identify and then investigate potential Regions of Interest (ROIs) within the landing ellipse (a ~5.2 by 1.6 km-area). The team developed a number of working geological hypotheses based on remote sensing datasets (see Morse et al., 2019; Tornabene et al., 2019). The Science Team was provided with a set of regional (covering a 15 km^2 area) and landing site-specific data, mimicking the datasets that would be available for remote science of a landing site on Mars. These datasets served as the only guide for initial operations and site research; the field site was concealed from the mission control team so that the analogue mission scenario remained fully in-simulation, or "in-sim". These datasets, their Martian equivalents, and spectroscopic processing are detailed by Tornabene et al. (2019); briefly, datasets available to the Science Team included: Advanced Spaceborne Thermal Emission and Reflection Radiometer (ASTER; 15-90m/pixel) datasets (Fig. 5.2a); multispectral visible to thermal infrared Landsat 8 Operational Land Imagery (OLI; 15-60m/pixel) (Fig. 5.2b); a 10 m/pixel digital elevation model (DEM) (Fig. 5.2c); and a high-resolution visible-near infrared Quickbird image (60cm/pixel) (Fig. 5.2d–e). Here we summarize the general use of those datasets to inform pre-mission science and strategic planning.

The Landsat enhanced bands 7, 5, 3 (Fig. 5.2a) were overlain on the high-resolution Quickbird image as well as the DEM, providing a framework for the regional geologic interpretation. The Landsat data in this band combination is useful as clays and carbonates are highlighted by band 7 (covering SWIR 2.1–2.3 μm range for which minerals in these groups have major absorption features) and band 3 highlights iron oxidation. Band 5 measures the near

infrared, or NIR, which is especially important for vegetation as those wavelengths are scattered back into the atmosphere. Note the magenta in the basinal areas, consistent with clays and carbonates, the paucity of green, and the abundance of blue, consistent with iron oxidation (Fig. 5.2a). Based on ASTER TIR emissivity, bands 10, 11, 12 (Fig. 5.2b), the landing ellipse and its regional surroundings were interpreted to be dominated by a spectral signature consistent with silica-rich materials (indicated by black). ASTER and Landsat multispectral data analyses (covered in detail by Tornabene et al., 2019) led to the interpretation that the landing ellipse had minimal vegetation with silica and carbonate-bearing deposits, abundant ferric oxides, and likely having clay minerals and sulfates. In visible imagery, within the basin, alternating red, white, and blue layers were present underlying sinuous ridges. Geomorphological and morphometrical analyses was performed on the ridges including curvature, continuity of cross-sectional profile across ridge segments, and sinuosity (Figs. 5.2c–d). The ridges were determined to have a strong morphometric similarity to terrestrial inverted paleochannels (i.e., 1.2–1.5 sinuosity; Williams et al., 2011). Combining with the km-scale data (Figs. 5.2a–b) with the m-scale morphology provided by the Quickbird image and DEM (Figs. 5.2c–d), the team hypothesized there was a domed feature (mountain, volcanic edifice, or other feature) to the west of the landing ellipse, with the landing ellipse located in a sedimentary basin having sinuous ridges. Regional extensional tectonism was proposed as a potential mechanism having formed the dome and basin. The team proposed that the ridges were inverted topography, where ancient, inverted paleochannels were likely capped by either resistant fluvial or igneous rocks. The underlying basin materials were thought to be dominated by silica-rich lithologies having various oxidation states, which reflects changes to the environmental conditions over the geologic history of the site (Pontefract et al., 2017). Light-toned whitish deposits are exposed on the basin floor, which

the Science Team proposed could be comprised of volcanic ash, lacustrine evaporates, or other diagenetic or alteration products. Shallow sea or lacustrine deposits, both prior to and after the emplacement of a channel system, would indicate a variable influx of water in wetter climates followed by the present-day erosional regime. A geological map, based on remote sensing data and data acquired during the 2015 mission, is provided in Figure 5.2f.

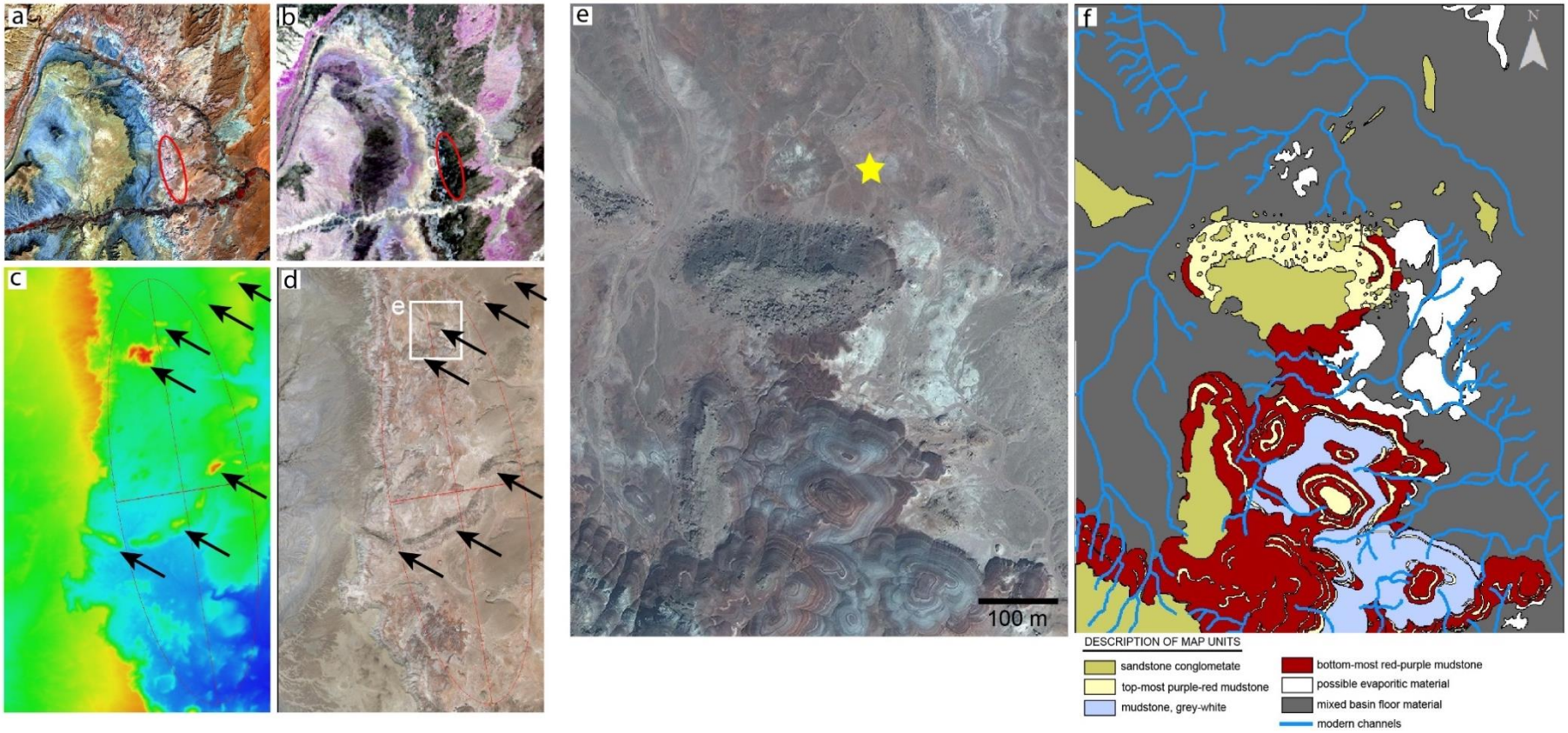

Figure 5.2. a) Regional Landsat 8 OLI (15-60m/pixel) with bands 7 (R), 5 (G), 3 (B) colour infrared image. A local stretch was applied. Blues indicate the presence of ferric oxides (band 3) and magenta indicates the presence of clay minerals and carbonates (band 7). Note the lack of green, which indicates vegetation (band 5). (See Tornabene et al. (2019) for spectral analysis.) The red circle indicates the landing ellipse, which is ~ 5.2 by 1.6 km. b) Regional ASTER TIR (15-90m/pixel, bands 10 (8.125 – 8.475 μm),

11 (8.475 um – 8.825 μm), 12 (8.925 – 9.275 μm)) colour composite. Magenta indicates sulfate-bearing; light blue indicates carbonate-bearing; black indicates silica-dominated; light yellow indicates clay-rich. Same scale as (a). See Tornabene et al. (2019) for spectral interpretations. c) and d) The landing ellipse (~ 5.2 by 1.6 km) is indicated by the red outline, shown on c) a 10 m/pixel DEM and d) a high-resolution Quickbird image (60cm/pixel). Nearly continuous ridges to discontinuous ridge segments are highlighted by black arrows; sinuosity of the ridges features was measured as 1.21 for the northern-most ridge segments and 1.33 for the southern ridge, as indicated in the image. White box in (d) indicates the spatial extent for the immediate landing site shown in (e). e) Close-up of Quickbird image (60cm/pixel) image of the landing site and field area. Yellow star indicates the position of the landing site. f) Geologic map of the field area, following "landing," representing pre-mission data and interpretations and data acquired from the 2015 mission cycle. Same extent and scale as (d). North is up in all images.

As is commonly the case for actual missions, the Science Team was permitted to use terrestrial analogues to help support and develop their hypotheses. The dominant terrestrial analogue used for the field site was the Painted Desert, Arizona, which has multi-coloured layered lacustrine units indicative of periods of variable fluid and sediment influx (e.g., Harris et al., 1997). Regional uplift and basin and range-style extension contributed to the Painted Desert depositional environment (Hendricks, 1985, Arizona Soils). One hypothesis for the landing site was that regional tectonics similarly resulted in sedimentation and fluvial transport from the higher terrain in the west, draining into the area of the landing ellipse. Until landing and rover investigations during the 2015 mission cycle, the hypothesis of volcanic domes to the west and volcanic infilling of channels to the east could not be ruled out. Following landing in 2015, a portion of an inverted channel was investigated (Fig. 5.2e). It was found that the capping unit was a fluvial clastic sandstone as opposed to volcanic material (Fig. 5.2f). However, the team discovered upon ground operation investigations that volcanism was important to the geologic history of the site, present in the form of massive ash fall having comprised at least some component of the siltstone units. The discoveries from remote rover operations are described in the following sections. The putative ancient fluvial and lacustrine systems of our field site were deemed highly favorable for habitability and, with burial and preservation due chiefly to the capping unit, of significance for the preservation of organic matter (Pontefract et al., 2017).

Prior to the start of the 2016 deployment, the mission control team again held a series of meetings to revisit the geological interpretations as determined by investigations of the imagery and the results and interpretations from the 2015 rover operations. The team reviewed the last sol's data (from the previous year) and began planning high-level, treed, potential sol paths – these were long-term mission scenarios that acted as a guide for the mission, to be revisited and

updated as the 2016 mission proceeded and new rover data was acquired. This long-term, mission overview planning protocol is similar to Campaign Planning processes currently being developed for Mars 2020 operations, where high-level sol paths are edited as new areas are explored and characterized in depth (Francis et al., 2018).

In the days leading up to both 2015 and 2016 missions, the team participated in a one-day "dry-run" of operations. A mock-scenario constructed, covering both daily operational shifts, to allow the team to practice the daily operations workflow within the smaller instrument teams and the larger Science and Planning teams. This exercise was important for allowing team members to understand their roles and responsibilities, and for the leadership to assess any gaps and unmet needs of the mission and team.

5.4 Science Team Operations

5.4.1 Operational procedures

Science Team operational procedures proved to have a direct impact on the timeliness, focus, and relevancy of sol-by-sol data interpretation, and hence discussion and next sol, or n+1, plans. The detailed daily operational schedule and related discussion is provided by Osinski et al. (2019). The Science Team worked together in one room, which facilitated discussion even during data processing and interpretation. Geochemistry and spectral/mineralogy datasets on their own are necessarily incomplete to describe the geologic context for a given set of daily targets, which may include rocks of differing lithologies, dust or debris coverings, and/or weathering rinds, as well as soil, dust, or erosional material. Moreover, a great deal of the large amount of data acquired daily may have had little impact with respect to the discussion of next-sol planning when combined with the other data interpretations. These problems were mitigated

by easy, quick consultations between the individual science instrument teams during the initial stages of analysis, essentially building a context for the n-1 scene and narrowing down the data which was most important for that context. For example, while the Raman and VIS-IR spectroscopy teams developed targeted data analysis based on preliminary XRF and LIBS results from those teams, imaging teams provided morphologic, micro-textural, and contextual information, along with mast-mounted camera images giving insight into structures or reference to geologic contacts. The interplay among the instrument teams was critical for timely interpretations. Among the science operational procedures, encouragement of this collaboration during data processing was instrumental in moving the Science Team quickly towards science discussion and meeting the time-sensitive n+1 plan uplink window.

The Science Team discussion for n+1 planning was guided by the Science Team Lead (STL), who took arguments and interpretations into account while ensuring that mission goals were addressed with every targeting and sample selection campaign. New targets were chosen based on observations and interpretations provided by the ongoing data synthesis of previous sols; repeat targets were often discussed but rarely planned, balancing mission goals of a thorough context at each location with the ever-present push to traverse toward new terrain for sampling opportunities. Upon choosing new targets, the distance and traversability were determined using the CSA MESR software Apogy (Sapers et al., 2016; Pilles et al. 2019; Osinski et al., 2019), which allowed for planning of the next or multiple next sols based on rover constraints. Data and energy constraints were considered for the desired use of any instruments or sampling functions. We found that a procedural deadline was necessary for this nominal plan, as discussion of next sol planning was often heated and lengthy. Upon delivery of a nominal plan to the Planning Team, they offered a number of possible traverse scenarios given time, data,

energy, and traversability constraints (see Pilles et al., 2019). Discussion followed to produce a final plan by 10 pm that satisfied the science goals of the mission within engineering constraints.

5.4.2 Strategies for best Science Team operations

The most productive operational procedures in terms of priority sampling opportunities came about from Science and Planning teams independently constructing multi-sol, long-term plans as decision trees (e.g., Fig. 5.3). Preparation for sampling required ground-in-the-loop (localization and data gathered from consecutive sols) as a Light Detection and Ranging (LIDAR) cm-scale resolution workspace was generated for precise rover arm placement opportunities on the following sol (Zylberman et al., 2016). Sampling via the drill corer or scoop and analyses with contact instruments, such as the XRF and micro-focus camera stand-in for the rover arm-mounted Mars 2020 PIXL instrument, required a LIDAR workspace for such precision activities. Consequently, use of these tools and instruments was costly in terms of mission time, often requiring multiple sols of data collection to sufficiently characterize a lithology before sampling was considered. A “walk-about” traverse strategy, rover exploration reconnaissance involving long traverses with minimal data acquisition as detailed by Pilles et al. (2019), cleverly mitigated the potential waste of precious mission time due to activities that required human decision-making. In this strategy, multiple remote science targets were visited per sol with the autonomous capability to end the drive with the construction of a LIDAR workspace at a precise location, which prepared for next-sol sampling while returning data on future potential sample sites, as is shown in the sample planning diagram in Figure 5.3. Preparation for sampling during “walkabouts”, therefore, required the Science Team to develop strategic multi-sol plans (e.g., Fig. 5.3) that included multiple targets and sampling sites with “if-then” decision trees based on priority sample ranking. The sample ranking was based on mission goals, where we determined

the potential for a sample to have total organic carbon (TOC) from previous sols data return and the depositional model. Once these complex and multi-sol nominal plans were detailed, an effectual interplay between the science and planning teams lead to the final walk-about plans.

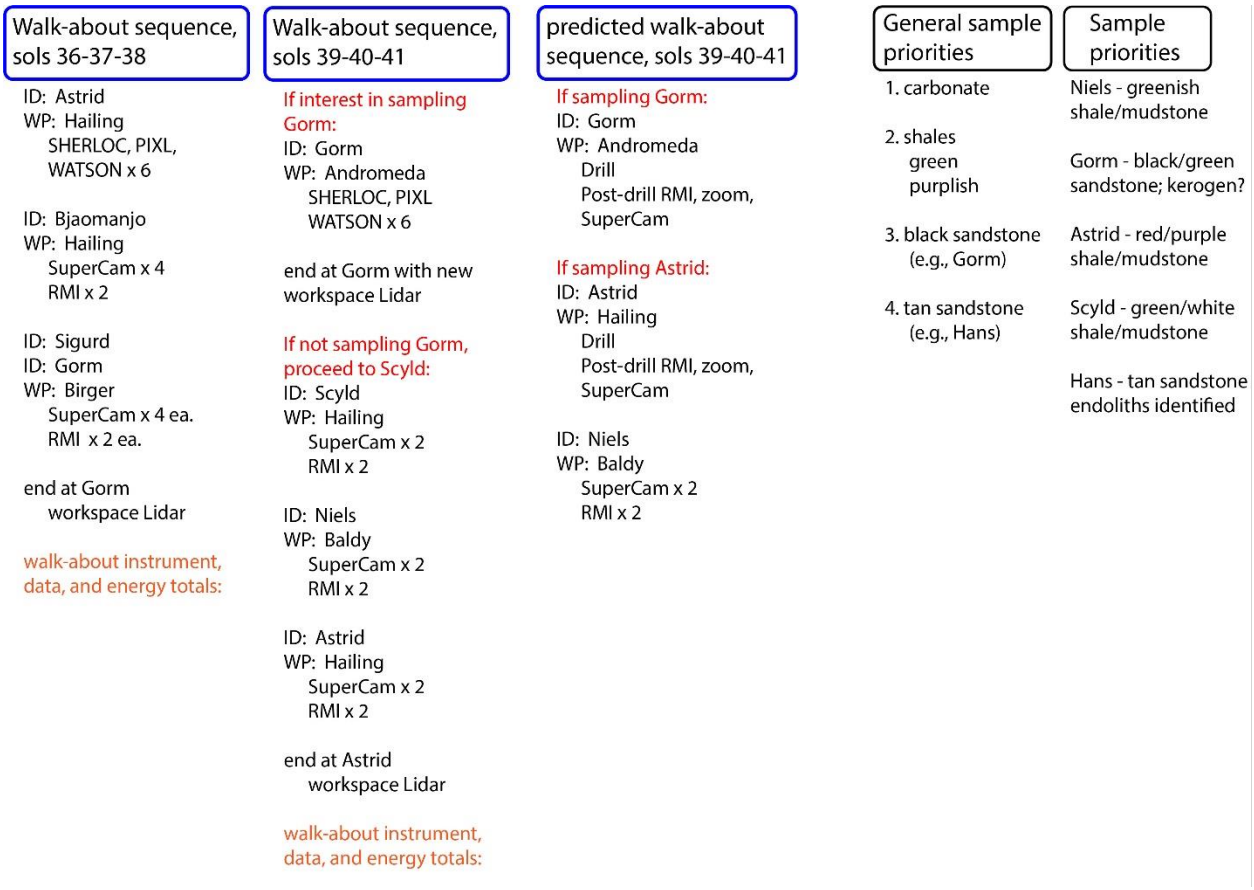

Figure 5.3. In-sim treed, multi-sol plans with sample priorities, representing a typical whiteboard sketch of planning and pre-planning during each shift. “ID” is the name given of a feature of interest (FOI), generally a rock, outcrop, or specific spot in the regolith. This was the sequence planned for sols 36 – 38, with *if-then* statements in the plan for the following sequence plans. “WP” is the waypoint, or the name given for the location of the rover from which the analyses or image is taken. FOI locales are indicated in Figure 5.3. Walk-about planning allows for many

sites to be investigated with pre-planned end-of-sol at a potential sampling FOI. Notes that workspace LIDAR is requested at the end of the multi-sol plans, as this sets up for use of contact instrumentation (e.g., SHERLOC Raman, drill) which requires ground-in-the-loop. Sample priorities, as formed through the site depositional model and defined by the science objectives, are always indicated to guide plans. The sample priorities acted as scientific hypotheses and were continually edited with acquisition of new data and interpretations as the mission progressed.

When choosing scientifically significant targets for n+1 sol or multi-sol plans, the Science Team had other tactical allowances in-play that allowed us to meet mission goals. For example, imaging and "blind targeting," where autonomous data was collected at a known location but on an unknown target, both utilized rover-relative and site geographic coordinates by azimuth and elevation (see also Pilles et al., 2019). This allowed post-drive imagery (e.g., panoramas, zooms, or higher resolution images) as well as targeted remote science (e.g., XRF or Raman). As discussed by Francis et al. (2016) and Francis et al. (2019), such autonomous targeting allowances for the CanMars mission constraints was modeled after MSL visual target tracking (VTT) and actual ChemCam capabilities (Francis et al., 2016). The Science Team used this strategy to collect data on lithologies, soils, and erosional material for geologic characterization, essential to our understanding the history of fluvial processes and climate of the site. Along with acquiring scientifically significant samples, such collection of data enroute to potential sample sites allowed the Science Team to achieve "full success" by meeting multiple MEPAG goals. These tactical strategies were critical for collecting data during consecutive days dedicated to driving and served as a data-rich approach to filling the energy and data budget of a time and distance-limited plan.

5.4.2.1 Pre-planned strategic traverse days

Strategic planning days were used during the CanMars mission to give the team a break from tactical planning to focus on the huge volume of data return and develop and strengthen depositional mode1 and working hypotheses. During each strategic day, pre-planned activity sequences covering a full sol were uplinked to the rover (see Pilles et al., 2019). Strategic traverse days were built into the mission plan, but were necessarily kept as flexible calendar days, to be implemented to coincide with long traverses or other scenarios that were easily pre-planned with a minimum of data return (Pilles et al., 2019). During these days, both the Science and Planning teams broke from normal operations and met in groups with the intention of bringing together multiple perspectives (e.g., science, engineering) and therefore fresh insights to the mission-acquired observations and interpretations. Each group was given a set of tasks based on the experience and specialization of members in the group. Panoramas, zooms, and mast-mounted camera images were stitched and overlain for the purposes of making facies and geomorphological maps, measuring the true height of outcrops, and determining fluvial-lacustrine successions with basin geometries. Primary sedimentary textures and structures such as bedding, cross-bedding (e.g., mapping shown in Fig. 5.3 for outcrops in units #1 and #7), grains, clasts, and apparent porosity were mapped. At the end of the shift, the entire team met to present results, for discussion, and to further develop the depositional model (Fig. 5.3), discussed in the following section. Although the data return from the rover's activities was sparse on these days, the model and stratigraphic columns developed informed sample selection decisions throughout the mission.

In summary, the strategic traverse days were important for the team to make better short- and long-term tactical decisions and may provide an option for strategic planning for Mars 2020

and future rover missions operations. The CanMars analogue mission, relatively accurately representing an end-to-end mission scenario, presented an ideal opportunity to experiment with new models and mission approaches which are too costly to test during extraplanetary missions.

5.4.3 Development of the depositional model

Similar to sedimentary facies models used as basic tools in MER and MSL missions to investigate layered sedimentary sequences (e.g., Edgar et al., 2017) , the depositional model developed during CanMars describes the geologic setting of the region and the implications to sampling selection. The depositional model was a synthesis of imagery and digital terrain models, elucidating sedimentary facies, contacts, stratigraphy, and general architecture of the site, which was learned through paleo current or slope indicators, basinal centers and edges, and unconformities. These observations led to interpretations about the influence of diagenetic histories that either promoted or inhibited biologic activity in particular facies or lithologies. Hence, a large volume of data was synthesized into a predictive model which guided Science Team decisions for long-term planning, afforded by the collective teamwork on the strategic traverse days.

The depositional model provided the Science Team with predictive power to strategically plan the general traverse of the mission, focused primarily on a layered, multi-colored siltstone unit that was not reached until the third week of 2016 operations. Based on the mineralogical and geochemical data, geologic context, and textural evidence, the Science Team proposed that the lowermost white and red layers of the siltstone sequence (Fig. 5.4, unit 4) were likely the same, but influenced by diagenesis, where a variable water table post-emplacement resulted in redox changes. The green layers (Fig. 5.4, unit 5) were in contact with intermittent, high energy lenticular sandstones (Fig. 5.4, unit 7), indicating very low energy environment was present

before a rising water table increased the fluvial activity and sediment influx rate. Mineralogy of the green siltstone was dominated by smectites, with yellowish alteration, a “popcorn” erosional texture, and gypsum present throughout the unit. The team interpreted that nontronite and the green color of the unit may indicate diagenesis, where microbially-mediated weathering resulted in reduced iron in anoxic sediments. Sparse, isolated, cm-scale white material within the siltstones was found to be evaporitic lenses comprised of gypsum and were interpreted in the model to have formed where water only breached the surface during periods where the water table was lower. As the rover traversed up-section through the landing site, the model predicted that the green and/or red-black layers represented a redox sensitive lake (supported by the presence of evaporites), with a potentially microbially-mediated reducing depositional environment (green) and a potentially very high concentration of organic carbon (purple-black). We suggested that these units experienced low sedimentation rates which tends to increase TOC, and even though some amount of ash fall was introduced, very little clastic dilution took place to lower potential TOC (Ding et al., 2015). With low sedimentation rates, redox conditions become an important factor in the preservation of TOC (Ding et al., 2015).

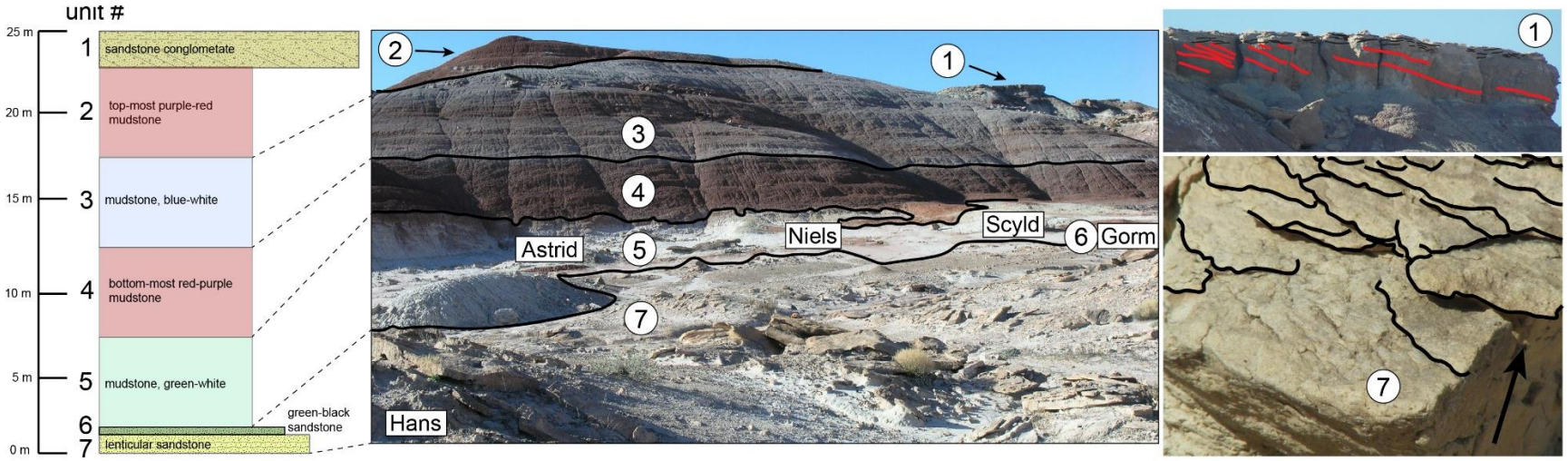

Figure 5.4. Final depositional model and stratigraphic column of the analogue site as produced during the mission. This model guided the planning of the rover traverses to reach desired sampling sites. The input of the model included facies and geomorphological maps, outcrop and feature height and extent measurements, and constructing basin geometries. Primary sedimentary textures and structures such as cross-bedding were mapped directly on to zoom or other imagery, as shown for units #1 and #7. Unit #1 shows cross-bedding in the direction of fluid flow; Unit #7 shows planar cross-bedding (and potentially flaser bedding) as stacked, thin bedding planes, viewed in the direction of fluid flow. Major features of interest (FOIs) and sampling sites are indicated by target name. The model remained fluid, allowing for changes in working hypotheses with regard to lithologic interpretation and boundaries, facies changes, etc. For regional location, see the yellow star in Figure 5.1e.

5.4.4 Sample Priorities

Sample selection for the CanMars mission was governed by two main science objectives: 1) collect and rank samples for cache and return with highest potential for preservation of ancient biosignatures from organic-rich carbon, and; 2) assess paleoenvironmental habitability potential and history of water at the site. Mission requirements regarding sampling (as indicated MSRAD guidelines; see Osinski et al., 2019) indicated one cached sample for minimum mission success, two cached for full success, and three cached as a "stretch". During the 2015 and 2016 CanMars mission cycles, 8 total samples were acquired and cached (four each cycle). Table 5.1 describes the samples, their relative rankings for priority return samples, and the science rationale for each sample. The Science Team ranked the siltstones highest priority based chiefly on the geologic context and interpretation of these units as marginal lacustrine facies, as such a depositional environment would most likely to have organic carbon and potentially biosignature preservation (Figs. 5.5a–c). We were unable to obtain organic carbon signatures in-sim with the Raman, however, and the team recognized that the preservation of ancient biosignatures is highly dependent on the weathering state and general preservation of the lithologies. The sandstone conglomerate (Figs. 5.5d–e) sample was rated as the third priority return sample (above the older sandstone units) due to the potential to retain micro-paleofossils. Table 5.1 presents the 8 cached samples and highest priority return samples chosen based on rover-derived observations and analyses, with 1 being highest priority.

Caudill et al. (2019) provides the post-mission laboratory analyses of these samples, including the total organic carbon (TOC) of a sample suite of the field site and the in-sim cached and ranked samples (Table 5.1). Laboratory Raman revealed that the samples in this study either do not contain kerogen (Raman-detectable form of organic carbon), or do not contain it at

detectable levels (Caudill et al., 2019). Solvent extraction Gas Chromatography Mass Spectrometry (GC-MS) showed that the sandstones had the highest TOC of the in-sim cached samples, but the level of TOC (at <0.03 wt%) was 100 times less than is considered organic-rich for sedimentary rock (Boggs, 2006). Potential explanations for the lack of TOC in the field site may include either a low primary productivity due to the oligotrophic nature or anoxic conditions (perhaps with the influx of ash) of the depositional environment, unfavorable preservation conditions (e.g., ash or other inorganic sedimentation influx to the lacustrine siltstone units; high clastic sedimentation rates in the sandstone units preventing biomass accumulation), or both.

Table 5.1. Priority rankings, descriptions, testable hypotheses, and science rationale of the samples acquired and investigated throughout the CanMars mission. The samples are ranked beginning at most desirable based on the characterization of the lithologic unit. This chart represents the rankings developed by the Science Team throughout the mission; not all desired samples were acquired. See Figure 5.4 for location information.

general lithologic units	**hypothesis test**	**2015 samples**	**2016 samples**	**sampling priorities**	**science rationale**
potatoes (tuff)	Carbonates or concretions? If a Raman signature for carbonates or kerogen was demonstrated, it would be ranked highest (such signal was not detected).		no sample acquired		Carbonates would be lower than shales in TOC, but preserve organic and inorganic carbon together. A return sample would allow isotopic paleothermometry, and may preserve microbial fossils or mats.

green siltstone	Lithology, depositional environment, and organic carbon potential was determined by geologic context, color, and mineralogy. Potential kaolinite, muscovite, and nontronite were observed, and montmorillonite-illite were observed with high confidence. Gypsum was identified (strong peaks, high certainty). Potential nontronite - indicates the weathering of volcanics with microorganisms involved in reduction of iron when soils undergo anoxia (producing the reduced form of the clay mineral).		Niels	1	Marginal lacustrine facies are ranked highest for highest total organic carbon (TOC) and biosignature preservation. Ranking is difficult, as the preservation is highly dependent on the weathering state and general preservation of the lithologies. In an attempt to acquire the most 'fresh' sample possible, we disturbed the surfaces with the rover wheels, which provided an exposure deeper than would have been possible with the rock abrasion tool (RAT). High Na levels in bright white material suggests halite may be present; elevated salinity in these environments may encourage chemical stratification, which in turn favors preservation of organic matter. Dysoxic to anoxic conditions result from exhaustion of free oxygen by oxidation of organic matter in the isolated deep zone of the lake. The darker green coloration, geochemistry, and mineralogy indicate a reduced depositional environment, and therefore representative of the best paleohabitability.
purple/red siltstone	Geochemically, this unit appears to be similar to the underlying white unit. It is clay-rich and very weathered, with the same shrink-swell erosional character. Purple coloration (with geochemistry similar to green layer) may indicate habitability (as black coloration indicates an even more reducing environment than represented by the green shales). Fe-oxides (hematite) and Fe-oxyhydroxides (ferrihydrite) were observed.		Astrid	2	Purple-red siltstones may indicate high TOC and/or oxidized conditions in a low energy environment with possibility to preserve organic matter. Preservation pathways are known in oxide and oxyhydroxide minerals. Purple-black bands may represent cm-scale windows of very well preserved organic carbon, and may indicate habitability as dark coloration indicates an even more reducing environment than represented by the green shales.
"black" sandstone	Could be an organic rich sandstone. This was targeted for biosignatures, but instead graphite was identified by Raman, and is very different from the kerogen signature that would indicate organic carbon If a Raman signature for kerogen was demonstrated, it would		no sample acquired		Could be an organic rich sandstone. High TOC sand units in a fluvial environment could be overbank or crevasse splay deposits with potential for organic and biosignature preservation, though ranked lower than marginal lacustrine facies (shales).

	be ranked highest (such signal was not detected). VIS-IR suggested that Fe and Mg-rich clay minerals were present.				
sandstone conglomerate	Imaging microfossils and cross stratification possible. Will fulfill goals to study history of aqueous environments at the site.	Thrymheim		3	Trough cross stratification and soft sediment deformation features with embedded clasts that were multi-colored, well-rounded, high sphericity pebble to gravel-sized. Potential for microfossils within the conglomerate clasts. Fulfills goals of assessing the history of fluvial activity at the site and the stratigraphic column for broader geologic characterization.
sandstone	Identify biomarkers identified from endolithic communities.		Hans	4	Carotenes were identified *in situ* with Raman, which are indicative of endolithic communities within the rock. This step-wise approach including identifying a rock likely to have preserved endolithic pigments, abrading the rock with the RAT, then confirming with Raman. The carotene pigments do not represent biomarkers from ancient life (i.e., kerogens), but more recent life (extant or extinct). Desert varnish is observed as a weathering product on the sandstones, indicated by dark coloration, mm-sized thickness of the coating, and very high Fe and Mg.
white siltstone	Lithology, depositional environment, and organic carbon potential to be determined by geologic context, color, and mineralogy.	Gimli		5	Gray shale bleached/weathered and/or volcanic ash – least likely to preserve organic material, but fills the stratigraphic column for geologic characterization.
sandstone	Identify biomarkers identified from endolithic communities (such signal was not detected).	Alfheim		6	Sandstone which would fill out the stratigraphic column for geologic characterization.
white/green siltstone, erosional face	Lithology, depositional environment, and organic carbon potential to be determined by geologic context, color, and mineralogy.		Scyld (with green)	7	The sample was not fresh, but taken from a highly erosional face. Although the underlying lithology might be ranked higher for TOC, the state of preservation likely negatively affected biopreservation.
regolith sample	Sample would fill the stratigraphic column for geologic characterization pertaining to the erosional regime and material transport.	Fenrir		8	The last sample in priority is the regolith sample, as it would not give *in situ* information not is likely to preserve biosignatures.

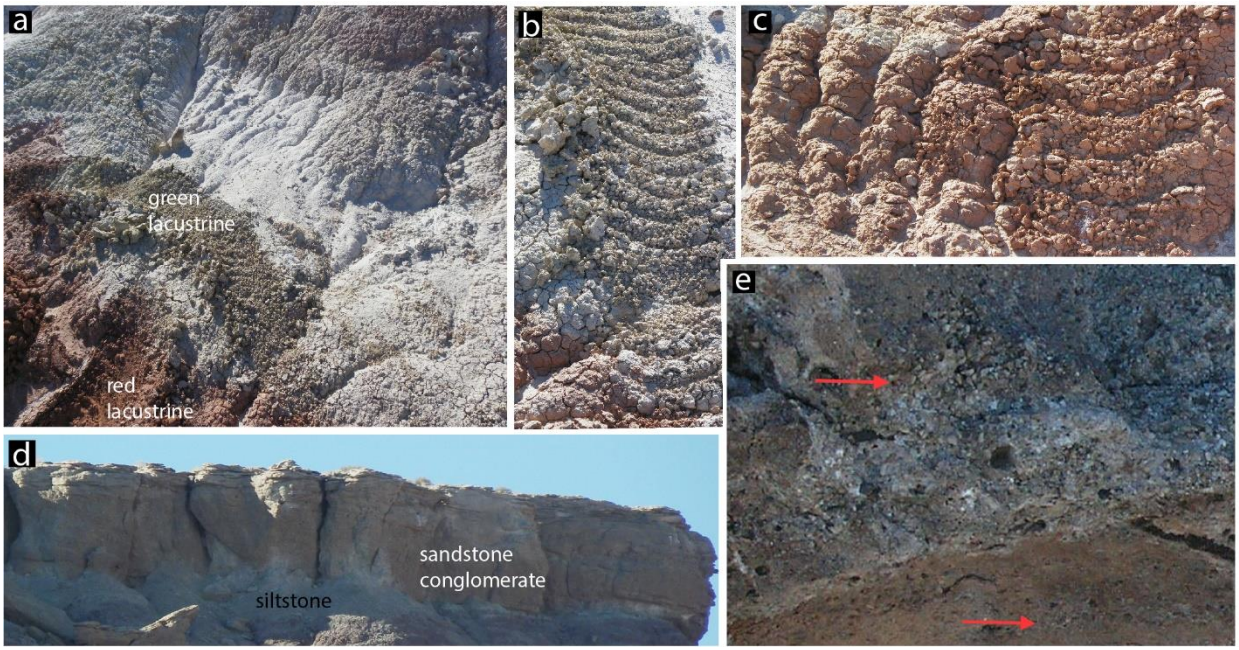

Figure 5.5. a) Sampling context for the first and second priority samples (Table 5.1). Rover wheels were used to disturb the surface in an attempt to sample below the cm-thick erosional surface. b) Sampling location for Niels, green siltstone (unit # 5 in Fig. 5.2). Montmorillonite-dominated green siltstone with yellowish alteration present and a popcorn erosional texture, and gypsum is ubiquitous throughout the unit and as erosional lenses. Potential nontronite as well as the green color may indicator microbially-mediated weathering, producing reduced iron in anoxic sediments. The darker green coloration likely indicates a microbially-mediated reducing depositional environment, and therefore representative of the best paleo-habitability. c) Sampling location for Astrid, red siltstone with dark purple lenses (unit # 4 in Fig. 5.2). The purple coloration is geochemically and mineralogically similar to the green layer (also smectite-rich) and may indicate habitability as dark coloration indicates an even more reducing environment than represented by the green shales. d) Zoom image of the conglomerate – clastic sandstone capping unit (unit # 1 in Fig. 5.2) showing cross stratification and in contact with siltstones. e)

Fallen block of the sandstone conglomerate unit shown in (d) and sampling location of Thrymheim. Two bands of embedded clasts are shown by red arrows, which are multi-colored, well-rounded, high sphericity pebble to gravel-sized clasts. This was sampled for potential for microfossils within the conglomerate clasts and further fulfills goals of assessing the history of fluvial activity at the site and the stratigraphic column for broader geologic characterization.

4.4.5 Post-mission site visit

A fundamental advantage of using an actual field site in analogue mission simulations is the ability to physically explore the field site post-mission to assess the validity and understand the limitations of remote science. Following CanMars mission operations in November 2016, the mission control team visited the rover deployment site near Hanksville, Utah, with the intent of geologically assessing the field site. The team first walked the path of the full mission traverse, only then fully comprehending how little ground can be covered by a rover versus a human and how little of the area it is possible to assess via remote science. The overall lack of awareness of the surroundings – which included missing outcrops and other key details that were just out of the view of the rover's imagery – serves as a caution with regard to over-interpretation of remote science. Given line-of-site, time, and traversability limitations, thorough investigation of a geologic site is a difficult task. Upon visiting the site, the mission control team realized that part of the stratigraphy was missing from the depositional model because it was out of view from the rover traversable terrain. It is important to note that mineralogic, textural, and contextual clues that may be obvious to a field geologist do not always appear evident in spectroscopy data; in available context and scale, imagery is often insufficient for textural and other contextual clues

to differentiate lithologies when mineralogy and chemistry are similar (e.g., an ash-fall tuff versus a very fine-grained sandstone; a volcanic breccia versus an impact breccia). Some minerals were only locally present throughout the field site and proved to be difficult to target. For example, the post-mission analysis indicated the presence of jarosite, interpreted as a common alteration product of the white-grey-green lacustrine unit and the source of the orange alteration observed during the mission. Sulfates (gypsum), Ca-phosphates (brushite), and Fe-oxides and Fe-oxyhydroxides are important indicators of paleoconditions and are important for metabolically-significant organisms that can be formed via a biologically-induced and controlled process (Gramp et al., 2010; Lucas and Prévôt, 1984; Mojzsis and Arrhenius, 1998); thus, jarosite may have been an important finding during the mission. Only after the field visit did the team suggest that the siltstone sequence may have formed as an acid-saline lake; jarosite is an important environmental indicator and was important for ancient Mars as conditions became more arid.

5.5 Lessons learned – Optimal Science Team operational procedures

An important outcome from a procedural standpoint was the collaboration among the various teams. Data analysis and interpretation were heavily communicated between the science instrument and imaging teams, providing holistic and targeted analyses. Mineral identification, lithologic classifications, or other data trends were verified and corroborated by other instrument teams, providing useful and meaningful interpretation. This real-time collaboration also afforded the most efficient data processing and interpretation, which is critical when scientific evidence is intended to dictate next-sol planning. Furthermore, this process allowed the team over time to develop best-strategies to maximize the efficient use of the available instruments in planning, including, for example: the pre-planned use of all reasonable arm-bound instruments when

deployed; expending traversable distance and data and time allowance enroute to a target, and; ending a sol plan with remote spectroscopic observations as well as a LIDAR scan to allow sampling if the returned data showed it was warranted (e.g., Fig. 5.3). A dynamic collaboration between the Science and Planning teams was also vital to the mission success. When coordinating single sol plans, but especially for the complex multi-sol plans, members from the Planning and Science Teams were in direct communication, moving between both control rooms. Combined workflows and advanced hardware and software capabilities are being explored for use in flight missions (e.g., Deans et al. 2012) to allow disparate, remote planetary mission teams to work together in real time. We suggest such research and testing has real power to better integrate dispersed international teams and partners and produce better, more efficient science. Furthermore, we suggest that Science Team Leads (STLs) or other leadership recognize that team members participating remotely (e.g., by phone and/or web-enabled conferencing software) will generally not engage and collaborate as fluidly as those present together in mission control, and strategies should be considered to ensure collaborative space at all levels of participation.

The success of analogue and flight missions depends on team member contribution and participation. Given the intense and difficult science discussions and planning with high-stakes decisions based on limited time and science, it is critical to create a collaborative atmosphere. A culture should be cultivated wherein team members are empowered and expected to speak up about ideas and interpretations, with no penalties for being wrong but accepting of criticism. We suggest that operational schedules include time for instrument team presentations as well as presentations by individuals; this may include scheduled breaks during Tactical planning for individual team members to expand on ideas or prepare graphics to be presented at that planning meeting.

Data processing and interpretation, as well as subsequent next-sol planning, is time-limited both per sol and over the course of a mission; it is thus imperative to implement efficient strategies for Science Team operations and plan implementation. The walkabout rover traverse strategy, along with multi-sol plans with complex decisions trees, was found to be the optimal strategy for choosing sampling sites. Nested decision trees were important for the Science Team, with ranked sample priorities and science rationale for each, to match the traverse scenarios constructed by the Planning Team (e.g., Fig. 5.3). Pilles et al. (2019) provide further discussion on the walkabout and other traverse strategies. This strategy allowed for exploration and data acquisition of many sites, while setting up for n+1 sampling, and furthermore forcing the Science Team to detail potential sampling sites, providing sampling rationales and ranking the potential samples early in the mission. The walkabout planning approach was also discussed by Yingst et al. (2017) who studied best operational approaches to rover-based site characterization and sample cache and improving overall efficiency. The multi-sol planning scenarios implemented in CanMars are also similar to current the MSL extended mission operations, where 3 to 5 tactical planning days occur per week, facilitating customary terrestrial schedules for the team (that is, not on Mars-time) and necessitating multi-sol planning.

Daily report writing with standardized templates for data interpretations and presentations are one avenue for efficient and fluid daily planning operations. One major lesson from the CanMars experiment is the need for structured reports written by each instrument team and team members in major positions. These reports carry the details of the previous planning day and the context of the larger campaign. Having mechanisms in place for transfer and curation of data proved to be equally important; all Science Team members should be able to search for, and understand, the daily data downlink and interpretations from each instrument team. These data documents should

be standardized with predictable and readily ingestible formats. During MSL operations, daily report writing is fundamental to the transfer of knowledge from planning sol to the next, written by instrument Payload Downlink Leads (PDLs), Payload Uplink Leads (PULs), and the Long Term Planner. We suggest that a greater number of roles produce daily reports, perhaps every individual participating in operations if only for the next person working the shift of the same role. However, the team found that it would be more beneficial if the reports and data documents were indexable to a database, keyword-enabled and searchable. This is likely far more effective than individual report writing as it allows any team member to search on specific targets, analyses, or interpretations without combing through various reports; one other issue with many reports is that information can be in conflict, given the very fast pace of Tactical planning. Organization and ease of access is difficult to overstate given the time constraints on daily rover mission operations.

The strategic traverse days were very well spent, as the development of the depositional model guided the sampling and the ultimate direction of the mission. The model allowed predictive power, extending interpretations up-section through stratigraphy and comprehensively linking individual sites to form a geologic construct. We suggest that future missions consider similar scheduled collaborative space where team members have an opportunity to review planned sol paths, data and interpretations, and assure daily operations are advancing overall mission goals. An analogous process in being implemented for Mars 2020 mission operations, where multiple teams will participate in overview planning sessions removed from Tactical, or daily, rover planning (Francis et al., 2018).

5.6 Lessons learned – instrumentation

The search for evidence of ancient life is one of the most challenging objectives of current and future Mars exploration. During CanMars, Raman spectroscopy provided the unique opportunity to identify biosignatures and mineralogy. Raman results were frequently decisional with respect to selecting destinations and observation sites for the rover, and in one case, Raman spectra were used in a conditional sequencing plan where the detection of kerogen signatures would have triggered actions to set up for sampling at the detection site, had that signal been detected (see Francis et al, 2019). In future missions, a similar conditional sequencing function could offer suggestions on adjusting collecting time and laser power based on the former data quality, for Raman and perhaps other spectrometers – adapting the instrument parameters in real-time as developed by Thompson et al. (2014). This would enhance the quality of data with little use of the daily budget of time and energy, given a remote-sensing Raman instrument as is provided by the Mars 2020 SuperCam instrument (Wiens, et al., 2016). Autonomous targeting (e.g., AEGIS, Francis et al., 2016) and other advanced autonomous capabilities and associated workflow adjustments (e.g., multi-sol plans with tiered sampling decision trees; post-measurement high resolution imagery or other target confirmation) is a crucial capability to develop for remote rover operations (Francis et al., 2019). Although the Mars 2020 SHERLOC Raman represents the best instrument for the search of organics, it is a time-intensive arm-mounted proximity instrument requiring ground-in-the-loop.

Remote spectrometers (in this exercise, the stand-in SuperCam LIBS, VIS-IR, and Raman) were used in the plan for nearly every sol, and the arm-mounted instruments were used less frequently. Arm-mounted proximity instruments (the PIXL stand-in XRF and the SHERLOC stand-in Raman, as well the RAT tool and micro-imagers) required ground-in-loop

(or, communication with and decision-making by scientists on Earth) and, thus, due to the time constraints these were only used where previously acquired data led the team to the decision to plan a LIDAR scan and deploy the arm. A LIDAR scan was necessary for precise placement of the arm. Our experience during CanMars is that the use of these instruments requires careful planning with multi-sol planning operations. Importantly, our study demonstrates that spectrometers having remote capabilities are ideal for use in rover missions, greatly increasing the speed of operations and the amount of data that can be acquired. This has also been the experience of the MSL team, where ChemCam (having LIBS and RMI instruments) has proven to be extremely useful and often the most utilized instrument for geochemical observations (Maurice et al., 2016). This is due in part to its mast-mount and remote capabilities, as well as the capacity to provide geomorphologic context with the remote micro-imager. Such remote spectrometry tools further lend themselves well to the increased data throughput that onboard science autonomy can produce (Francis et al., 2017). As suggested by Wiens et al. (2016), the MSL remote instrument suite has proven to be extremely useful in the capacity to provide geomorphologic context and in efficiency.

Given the limited mobility of the rover, additional imagers would always be more beneficial. Micro-imagers are a powerful tool to give geologic context to broader imagery and data observations, and stereo imagery is an important tool to give spatial context for placement of the rover arm. However, we found that multispectral imagers would move rover mission operations forward significantly. With only visible imagery to rely on, it proved easy to misidentify features based on colour, or miss small outcrops completely. This limitation was particularly apparent in CanMars when a small, finely-layered green siltstone bed was missed by the rover team due to image resolution and lighting issues; this outcrop was significant as it was

a rare “fresh” siltstone outcrop not covered by cm-scale popcorn-textured erosional material. Multispectral imaging would mitigate lighting effects and allow mineralogically distinct outcrops and other features to be more easily detected. The Mars 2020 SuperCam instrument will be an improved version of MSL ChemCam, with an expanded Infrared passive Spectrometer (IRS; Bernardi et al., 2017), and along with the PanCam Infrared Spectrometer (ISEM; Korablev et al., 2017) will provide multi-spectral data covering 0.3–2.8 μm wavelengths, ideal to differentiate clay minerals, carbonates, and sulfates. Although this is a significant step forward for data collection and remote geological assessments, a full VIS–SWIR (0.35–2.5 μm) imaging spectrometer would provide the greatest data return for rover-based imaging and spectroscopy, as well as the greatest efficiency in daily decision-making and planning. An imaging spectrometer through the SWIR range allows for pixel-by-pixel mapping of molecular vibrations associated with clay minerals, carbonates, and sulphates. Based on the CanMars mission, we suggest that such a dataset would tremendously increase planning efficiency, though the constraint of data volume is always an issue. Mars 2020’s MastCam-Z will provide imaging spectrometry from 0.4–1.0 μm (Bell et al., 2016), which provides the spectral range to discern ferric and ferrous iron..

The micro-imager TEMMI was an underutilized instrument in this mission due to its placement on the arm (Bourassa et al., 2019), which therefore required a LIDAR workspace and ground-in-the-loop for its use. However, a longer mission would certainly have allowed heavier use of this instrument, as the textural and morphologic information from micro-imaging provided vital geologic context for interpretations. Imagers should therefore be equipped with remote micro-zoom capabilities to maximize their use. Additionally, imagers having stereo imaging capabilities in this field scenario would have allowed for more expeditious decision-making

particularly when assessing outcrops for sampling, mitigating the need for multiple sols to acquire LIDAR workspaces. We suggest that the most useful imagers should be multispectral, micro-zoom, and capable of acquiring stereo images (which are ideally stitched via automated pipeline), while also enabling remote observations (that is, not bound to arm constraints).

As the CanMars field site was in a sedimentary setting, with soft, highly friable lithologies, it became apparent that a scoop would have been beneficial, with the capability to analyze and image the material post-scoop. A scoop tool would have given access to the shallow subsurface in a way that was not within mission parameters; though the Mars 2020 rover will not have a scoop, it will be equipped with a tool for sampling regolith and soft materials. In an attempt to access a fresh surface of the siltstones beneath the several cm-thick popcorn-textured erosional cover, we disturbed the surfaces of green (Fig. 5.4 unit #5) and purplish-red siltstones (Fig. 5.4 unit #4) with the rover wheels, which provided an exposure deeper than would have been possible with the RAT. This introduces other issues though, as debated by the Science Team, including possible contamination from the wheels. A rock hammer or rock splitting tool would also have been ideal, but the thick erosional cover of the siltstone units highlights the need for tools to explore soft sediments. As discussed by Backes et al. (2011), drill bits (having several abrading bit types) and a coring and caching system position the Mars 2020 rover well to meet science goals; however, removing larger surfaces (perhaps via scoop) and obtaining a smooth surface (via splitting or percussion tool) is still in need of investigation.

Pre-mission readiness should include instrument tests and instrument training sessions for the entire Science Team. This point is critical for efficient and effective operations and cannot be overstated. Flight missions of course require instrument validation tests, but we suggest that analogue missions should operate in the same way. Well-designed pre-mission tests using a

variety of samples (e.g., multiple rock types containing different biosignatures) are essential to better understand the capabilities of instruments. For example, Raman was vital but many of the sites in the field area were dominated by clay minerals, and thus complementary geochemical plots from XRF data and VIS-IR-derived mineralogy proved critical to interpretations. The LIBS instrument was used as a low energy option to remove dust or other materials from the surface, but it can be destructive. Indeed, there was concern during the mission that the heat of many LIBS analyses might influence the reliability of Raman results. (This is still the preferred option, though, as the contact RAT requires ground-in-the loop with multiple sols invested in a target, which is costly for any non-sampling site.) We recommend that both flight and analogue missions include extensive pre-mission training for Science Team personnel and engineers, working closely together under a variety of mission-relevant scenarios, to help the team better understand the context of the data, the broader meaning of results and interpretations, and therefore the best use of the entire instrument suite in exploration and operations to serve their science goals.

The 2016 CanMars deployment saw the preliminary implementation of Virtual Reality (VR) technology in mission control. This technology enabled the creation of an immersive virtual environment based on both the provided remote sensing data and ground-based rover-obtained data. If further developed, this technique for observing remote locations could allow for faster feature recognition, and a better understanding of the scale of observed features by members of the mission control team (Morse et al., 2019). Caudill et al. (2019) describes the post-mission geological study and field validation of the CanMars field site and noted the inherent problem in conceptualizing and discerning scale: the true sense of location and relation of the rover to outcrops, formations, and traversable areas remained abstract to the CanMars

Science Team. While VR immersive technology may not likely be feasible for analogue missions, the technology is being developed for use in Mars 2020.

Finally, the development of advanced pre-processing software built-in to the data downlink pipeline would facilitate a faster and more simplified evaluation of data. As management of the Science Team was largely an exercise in managing very limited time budgets and a significant amount of data and details, we deem that such a technological advancement to expedite data processing and interpretation is vital for best outcomes for rover-based missions. These software programs would be instrument-specific, providing the Science Team with a more streamlined data analysis window. Such automated ground segment processing could enhance both the speed of analysis and mission progress, and the completeness of scientific analysis on operational timescales, by providing more complete information to science operations teams quickly. Although pre-processing software is already in use for flight instruments in rover missions, such sophisticated capabilities were not available to CanMars or likely any such future analogue mission. As such, the immense time commitment required for data processing, interpretation, collaboration, preparation for team presentations, and synthesizing these from all instrument teams, should not be discounted. We suggest that future analogue missions carefully consider these time constraints and build in appropriate time to the operational schedule, even if the planning timeline is extended from that of a flight mission.

5.7 Conclusions

The CanMars analogue mission provided the opportunity for the most detailed, in-depth field and operational trials of an MSR mission to-date, vetting mission management and procedures, workflows, instrumentation, and the complex interplay of multiple teams (Osinski et al., 2019). Laboratory analyses of the “returned” samples as well as a post-mission, *in situ* field analysis

revealed that the remote, in-sim mission operations team were able to characterize the lithologies and assess the geologic context and stratigraphic sequence. However, this simulated mission highlights the limitations of rover-based science. Some limitations are inherent (e.g., rover mobility, terrain traversability, line-of-sight) yet others may be mitigated by development of advanced instrumentation and data processing. We suggest the development of pre-processing data pipelines to enhance data return, lessen the daily Science Team workload, and expedite interpretations and next-sol planning. We further suggest that the single most useful additional instrumentation for CanMars would have been multispectral, micro-zoom, and stereo imagers. This would mitigate lighting effects, allowing for the quick and more accurate identification of outcrops of interest, and mitigate the inefficiency of multi-sol ground-in-the-loop to acquire LIDAR workspaces for sampling.

The most valuable asset that the CanMars Science Team had during the mission was each other. Tactical planning for a rover mission is necessarily very difficult – a large team of people with sometimes differing ideas, opinions, and observations must come together to make mission-critical decisions with very little time for science, discussion, or planning. Thus, an intentional operational structure must be employed to maintain a fast-paced flow that still requires all members to participate – intentional space must be created for team members to feel they can voice ideas that are independent of the majority. Real-time collaboration among team members afforded the most efficient data processing and interpretation, which is critical when scientific evidence is intended to dictate next-sol planning. During the CanMars mission, it was found that the optimal approach to remote geologic characterization of a site included a series of autonomous targeting and conditional sequencing functions combined with a walkabout traverse strategy (see Francis et al., 2019; Pilles et al., 2019), built on the development of a depositional

model through intentional space for collaborative science (e.g., the strategic traverse days). Fostering an environment of real-time collaborations among the individual Science Teams during processing, interpretation, and presentation of data allowed for a more robust and streamlined approach to daily science operations; close collaborations and synergy between the science and planning teams also was found to be an optimal use of the very limited time of daily planning.

We suggest that closely-simulated end-to-end analogue missions should be implemented for any future planetary rover mission to vet operational procedures, scientific instrumentation, and hardware and software. Such an opportunity further provides training to mission scientists and engineers to make the best use of limited time and resources. Additionally, the geologic characterization of the field site through the CanMars mission highlights the need for terrestrial analogue studies, having mission objectives as well as instrumentation specific to upcoming missions to guide the search for exploration sites. For example, although the site near Hanksville, Utah, utilized in this study is an excellent analogue for inverted channels on Mars (e.g., Williams et al., 2011) a rover-based mission at an analogous exploration site on Mars may have similar difficulties detecting high levels of organic carbon. Investigating redox couples and potential reducing conditions pre-mission in a similar site may mitigate these concerns. Such considerations need urgent attention; it is the hope that this study and similar continued research into analogous environments on Earth and Mars will assist in site selection for best potential biosignature preservation and detection.

Finally, it is clear that beyond vetting operational workflows and instrumentation, closely-simulated, pre-mission training is imperative for science and planning teams. Such training sessions properly prepares the team and ensures full utilization of the team members and their

time, and hence vital mission time, and produces the best return on investment from the time of rover deployment. The Mars 2020 Science Team has begun simulated mission training for the Science Team, which was born out of the experience of CanMars and its predecessors. The Rover Operations Activities for Science Team Training (ROASTT) program is designed to prepare the Mars 2020 Science Team for the decision-making processes required to achieve the mission's objectives from the first day of ground operations (Francis et al., 2018). The ROASTT team is developing and implementing a series of field and mission operations training exercises, introducing new operational procedures, including Campaign Planning (high-level sol path planning), Campaign Implementation (strategies and sol path planning on the timeline of one week) and abbreviated Tactical timelines (daily operations and planning is carried out in a shortened timeline, as compared to MSL operations). The training of a team not only supports the best return in the first few days or weeks of a mission but sets the entire mission up for success. We found that a best practice is for early pre-mission simulated or analogue mission training to reveal gaps in operational procedures, staffing, or expertise, experience, or understanding of the team. This provides time for all team members to adequately prepare for the complexities of operations and science in a unique mission environment, as they will not likely be afforded the time to do so after the start of the mission. Pre-mission simulations should include: sessions to familiarize the entire team with instrumentation, including presentations with practical examples of the capabilities and limitations of the instruments and data acquired – this is vital to full-team participation in planning and science decision-making; “dry run” planning and walk-through scenarios to allow the team to collectively put this knowledge in play, and; operational simulations true to the real mission working groups and timelines to allow for the leadership to observe team dynamics within the operational construct – this allows a valuable

opportunity to change operational procedures as necessary and assess the needs of the team. Ultimately, pre-mission training and analogue missions allow a team to vet operational workflows and procedures, which are best implemented in advance of flight missions.

References

Aller, R.C., 2013. Sedimentary Diagenesis, Depositional Environments, and Benthic Fluxes, in: Treatise on Geochemistry: Second Edition. pp. 293–334. doi:10.1016/B978-0-08-095975-7.00611-2

Antonenko, I., Osinski, G.R., Battler, M., Beauchamp, M., Cupelli, L., Chanou, A., Francis, R., Mader, M.M., Marion, C., McCullough, E., Pickersgill, A.E., Preston, L.J., Shankar, B., Unrau, T., Veillette, D., 2013. Issues of geologically-focused situational awareness in robotic planetary missions: Lessons from an analogue mission at Mistastin Lake impact structure, Labrador, Canada. Adv. Sp. Res. 52, 272–284. doi:10.1016/j.asr.2012.11.024

Arvidson, R.E., Squyres, S.W., Anderson, R.C., Bell, J.F., Blaney, D., Brückner, J., Cabrol, N.A., Calvin, W.M., Carr, M.H., Christensen, P.R., Clark, B.C., Crumpler, L., Des Marais, D.J., de Souza, J.A., d'Uston, C., Economou, T., Farmer, J., Farrand, W.H., Folkner, W., Golombek, M.P., Gorevan, S., Grant, J.A., Greeley, R., Grotzinger, J., Guinness, E., Hahn, B.C., Haskin, L., Herkenhoff, K.E., Hurowitz, J.A., Hviid, S., Johnson, J.R., Klingelhöfer, G., Knoll, A.H., Landis, G., Leff, C., Lemmon, M., Li, R., Madsen, M.B., Malin, M.C., McLennan, S.M., McSween, H.Y., Ming, D.W., Moersch, J., Morris, R. V., Parker, T., Rice, J.W., Richter, L., Rieder, R., Rodionov, D.S., Schröder, C., Sims, M., Smith, M., Smith, P., Soderblom, L.A., Sullivan, R., Thompson, S.D., Tosca, N.J., Wang, A., Wänke,

H., Ward, J., Wdowiak, T., Wolff, M., Yen, A., 2006. Overview of the Spirit Mars Exploration Rover Mission to Gusev Crater: Landing site to Backstay Rock in the Columbia Hills. J. Geophys. Res. E Planets. doi:10.1029/2005JE002499

Backes, P., Younse, P., DiCicco, M., Hudson, N., Collins, C., Allwood, A., Paolini, R., Male, C., Ma, J., Steele, A., Conrad, P., 2011. Experimental results of rover-based coring and caching, in: IEEE Aerospace Conference Proceedings. doi:10.1109/AERO.2011.5747263

Beaty, D.W., Hipkin, V.J., Caudill, C.M., Hansen, R.F., Hausrath, E.M., Maggiori, C., McCoubrey, R., Parrish, J.C., Ralston, S.J., 2019. Geological Evaluation of the MSRAD Field Site by a Human Field Party: Implications for Rover-based Exploration Operations and for the Future Human Exploration of Mars. Planetary and Space Science, 171, p. 34-49.

Bednar, D. J., Hawkwell, J., King, D., Battler, M., Kerrigan, and M., Osinski, G. R., 2019. Documentation processes during the CanMars mission: Observations and recommendations for future application in analogue and planetary missions. Planetary and Space Science, 174, p. 14-20.

Bina, A., Cao, F., Poitras, J.T., Tornabene, L.L., Caudill, C.M., Osinski, G.R., 2017. 2016 CanMars MSR analogue mission: Visbile/Near-Infrared spectral and mineralogical results based on a “stand-in” spectrometer for Mars 2020 Supercam VIS-IR, in: Lunar and Planetary Science XLVIII.

Bourassa, M., Osinski, G. R., Tornabene, L. L., Caudill, C., Christoffersen, P., Daly M., Godin, E., Pilles, E. A., and Ryan, C. 2019. TEMMI, a Three-dimensional Exploration Multispectral Microscope Imager for planetary-exploration missions. Planetary and Space Science 165:57–74.

Caudill, C. M., Osinski, G. R., Pilles, E. A., Sapers, H. M., Duff, S., Laugton, J., O'Callaghan, J.,

Sapoco, R., Tolometti, G., Tuite, G., Williford, K., Xie, T., 2019. Field and laboratory validation of remote rover operations Science Team findings: The CanMars Mars Sample Return analogue mission, Planetary and Space Science, 165, 250-259.

Clay minerals Society (CMS), 2016. The Clay minerals Society Glossary of Clay mineral Science. Chantilly, VA.

Cloutis, E.A., Hawthorne, F.C., Mertzman, S.A., Krenn, K., Craig, M.A., Marcino, D., Methot, M., Strong, J., Mustard, J.F., Blaney, D.L., Bell, J.F., Vilas, F., 2006. Detection and discrimination of sulfate minerals using reflectance spectroscopy. Icarus 184, 121–157. doi:10.1016/j.icarus.2006.04.003

Compton, J.S., 1991. Origin and diagenesis of clay minerals in the Monterey Formation, Santa Maria Basin Area, California. Clay minerals Clay mineral Miner. 39, 449–466. doi:10.1346/CCMN.1991.0390501

Crowley, J.K., Williams, D.E., Hammarstrom, J.M., Piatak, N., Chou, I.-M., Mars, J.C., 2003. Spectral reflectance properties (0.4–2.5 μm) of secondary Fe-oxide, Fe-hydroxide, and Fe-sulphate-hydrate minerals associated with sulphide-bearing mine wastes. Geochemistry Explor. Environ. Anal. 3, 219–228. doi:10.1144/1467-7873/03-001

Das, S., Hendry, M.J., Essilfie-Dughan, J., 2011. Transformation of two-line ferrihydrite to goethite and hematite as a function of pH and temperature. Environ. Sci. Technol. 45, 268–275. doi:10.1021/es101903y

Ddani, M., Meunier, A., Zahraoui, M., Beaufort, D., El Wartiti, M., Fontaine, C., Boukili, B., El Mahi, B., 2005. Clay mineralogy and chemical composition of bentonites from the Gourougou volcanic massif (northeast Morocco). Clay minerals Clay mineral Miner. 53, 250–267. doi:10.1346/CCMN.2005.0530305

Deans, C., Lees, D.S., Smith, T., Cohen, T.E., Morse, T.F., Fong, T.W., 2012. Field testing next generation ground data systems for future missions, in: Lunar and Planetary Science Conference. Woodlands, Texas, p. 95.

Ding, X., Lui, G., Zha, M., Huang, Z., Goa, C., Lu, X., Sun, M., Chen, Z., Liuzhuang, X., 2015. Relationship between total organic carbon content and sedimentation rate in ancient lacustrine sediments, a case study of Erlian basin, northern China, 149, p. 22-29.

Edgar, L.A., Gupta, S., Rubin, D.M., Lewis, K.W., Kocurek, G.A., Anderson, R.B., Bell, J.F., Dromart, G., Edgett, K.S., Grotzinger, J.P., Hardgrove, C., Kah, L.C., Leveille, R., Malin, M.C., Mangold, N., Milliken, R.E., Minitti, M., Palucis, M., Rice, M., Rowland, S.K., Schieber, J., Stack, K.M., Sumner, D.Y., Wiens, R.C., Williams, R.M.E., Williams, A.J., 2017. Shaler: In situ analysis of a fluvial sedimentary deposit on Mars. Sedimentology. doi:10.1111/sed.12370

Forsman, J.P., Hunt, J.M., 1958. Insoluble organic matter (kerogen) in sedimentary rocks. Geochim. Cosmochim. Acta 15, 170–182. doi:10.1016/0016-7037(58)90055-3

Fortin, D., Leppard, G.G., Tessier, A., 1993. Characteristics of lacustrine diagenetic iron oxyhydroxides. Geochim. Cosmochim. Acta 57, 4391–4404. doi:10.1016/0016-7037(93)90490-N

Francis, R., Pilles, E., Osinski, G. R., McIsaac K. Gaines, D., and Kissi, J. (2018) Utility and applications of rover science autonomy capabilities: Outcomes from a high-fidelity analogue mission simulation. Planetary and Space Science, 170, p. 52-60.

Francis, R., Cross, M.D.G., Kerrigan, M.C., Osinski, G.R., 2016. Exploration and Decision-Making Rules and Resources on the 2015 CanMars MSR Analogue Mission: An Analogue for Mars 2020 Rover Operations. 47th Lunar Planet. Sci. Conf. doi:10.1038/ngeo2474.

Francis, R., Estlin, T., Doran, G., Johnstone, S., Gaines, D., Verma, V., Burl, M., Frydenvang, J., Montaño, S., Wiens, R.C., Schaffer, S., Gasnault, O., DeFores, L., Blaney, D., Bornstein, B., 2017. AEGIS autonomous targeting for ChemCam on Mars Science Laboratory: Deployment & results of initial Science Team use. Sci. Robot. 7.

Francis, R., Estlin, T., Gaines, D., Bornstein, B., Schaffer, S., Verma, V., Anderson, R., Burl, M., Chu, S., Castano, R., Thompson, D., Blaney, D., De Flores, L., Doran, G., Nelson, T., Wiens, R., 2016. AEGIS autonomous targeting for the Curiosity rover's ChemCam instrument, in: 2015 IEEE Applied Imagery Pattern Recognition Workshop, AIPR 2015. doi:10.1109/AIPR.2015.7444544

Freissinet, C., Glavin, D.P., Mahaffy, P.R., Miller, K.E., Eigenbrode, J.L., Summons, R.E., Brunner, A.E., Buch, A., Szopa, C., Archer, P.D., Franz, H.B., Atreya, S.K., Brinckerhoff, W.B., Cabane, M., Coll, P., Conrad, P.G., Des Marais, D.J., Dworkin, J.P., Fairén, A.G., François, P., Grotzinger, J.P., Kashyap, S., Ten Kate, I.L., Leshin, L.A., Malespin, C.A., Martin, M.G., Martin-Torres, F.J., Mcadam, A.C., Ming, D.W., Navarro-González, R., Pavlov, A.A., Prats, B.D., Squyres, S.W., Steele, A., Stern, J.C., Sumner, D.Y., Sutter, B., Zorzano, M.P., 2015. Organic molecules in the Sheepbed Mudstone, Gale Crater, Mars. J. Geophys. Res. Planets 120, 495–514. doi:10.1002/2014JE004737

Godin, E., Caudill, C.M., Osinski, G.R., 2017. Imagery as a multi-scale investigation tool during the CanMars 2016 MSR analogue mission, in: Lunar and Planetary Science XLVIII. p. 1933.

Golombek, M.P., Cook, R.A., Economou, T., Folkner, W.M., Haldemann, A.F.C., Kallemeyn, P.H., Knudsen, J.M., Manning, R.M., Moore, H.J., Parker, T.J., Rieder, R., Schofield, J.T., Smith, P.H., Vaughan, R.M., 1997. Overview of the Mars Pathfinder Mission and

Assessment of Landing Site Predictions. Science (80-.). 278, 1743–1748. doi:10.1126/science.278.5344.1743

Gramp, J.P., Bigham, J.M., Jones, F.S., Tuovinen, O.H., 2010. Formation of Fe-sulfides in cultures of sulfate-reducing bacteria. J. Hazard. Mater. 175, 1062–1067. doi:10.1016/j.jhazmat.2009.10.119

Greenberger, R.N., Mustard, J.F., Ehlmann, B.L., Blaney, D.L., Cloutis, E.A., Wilson, J.H., Green, R.O., Fraeman, A.A., 2015. Imaging spectroscopy of geological samples and outcrops: Novel insights from microns to meters. GSA Today 25, 4–10. doi:10.1130/GSATG252A.1

Grishin, S.I., Bigham, J.M., Tuovinen, O.H., 1988. Characterization of Jarosite Formed upon Bacterial Oxidation of Ferrous Sulfate in a Packed-Bed Reactor. Appl. Environ. Microbiol. 54, 3101–3106.

Grotzinger, J.P., Arvidson, R.E., Bell, J.F., Calvin, W., Clark, B.C., Fike, D.A., Golombek, M., Greeley, R., Haldemann, A., Herkenhoff, K.E., Jolliff, B.L., Knoll, A.H., Malin, M., McLennan, S.M., Parker, T., Soderblom, L., Sohl-Dickstein, J.N., Squyres, S.W., Tosca, N.J., Watters, W.A., 2005. Stratigraphy and sedimentology of a dry to wet eolian depositional system, Burns formation, Meridiani Planum, Mars. Earth Planet. Sci. Lett. doi:10.1016/j.epsl.2005.09.039

Grotzinger, J.P., Crisp, J., Vasavada, A.R., Anderson, R.C., Baker, C.J., Barry, R., Blake, D.F., Conrad, P., Edgett, K.S., Ferdowski, B., Gellert, R., Gilbert, J.B., Golombek, M., Gómez-Elvira, J., Hassler, D.M., Jandura, L., Litvak, M., Mahaffy, P., Maki, J., Meyer, M., Malin, M.C., Mitrofanov, I., Simmonds, J.J., Vaniman, D., Welch, R. V., Wiens, R.C., 2012. Mars Science Laboratory mission and science investigation. Space Sci. Rev. 170, 5–56.

doi:10.1007/s11214-012-9892-2

Harms, J.C., 1979. Primary Sedimentary Structures. Annu. Rev. Earth Planet. Sci. 7, 227–248. doi:10.1146/annurev.ea.07.050179.001303

Harris, A.G., Tuttle, E., Tuttle, S.D., 1997. Geology of National Parks. Kendall/Hunt Publishing Company.

Hong, H., Fang, Q., Zhao, L., Schoepfer, S., Wang, C., Gong, N., Li, Z., Chen, Z.Q., 2017. Weathering and alteration of volcanic ashes in various depositional settings during the Permian-Triassic transition in South China: Mineralogical, elemental and isotopic approaches. Palaeogeogr. Palaeoclimatol. Palaeoecol. 486, 46–57. doi:10.1016/j.palaeo.2016.12.033

Huang, W.L., Longo, J.M., Pevear, D.R., 1993. An experimentally derived kinetic model for smectite-to-illite conversion and its use as a geothermometer. Clay minerals Clay mineral Miner. 41, 162–177. doi:10.1346/CCMN.1993.0410205

Huff, W.D., 2016. K-bentonites: A review. Am. Mineral. doi:10.2138/am-2016-5339

Klein, H.P., 1998. The search for life on Mars: What we learned from Viking. J. Geophys. Res. 103, 28463–28466. doi:10.1029/98JE01722

Kminek, G., Bada, J.L., 2006. The effect of ionizing radiation on the preservation of amino acids on Mars. Earth Planet. Sci. Lett. 245, 1–5. doi:10.1016/j.epsl.2006.03.008

Korablev, O.I., Dobrolensky, Y., Evdokimova, N., Fedorova, A.A., Kuzmin, R.O., Mantsevich, S.N., Cloutis, E.A., Carter, J., Poulet, F., Flahaut, J., Griffiths, A., Gunn, M., Schmitz, N., Martín-Torres, J., Zorzano, M.-P., Rodionov, D.S., Vago, J.L., Stepanov, A. V., Titov, A.Y., Vyazovetsky, N.A., Trokhimovskiy, A.Y., Sapgir, A.G., Kalinnikov, Y.K., Ivanov, Y.S., Shapkin, A.A., Ivanov, A.Y., 2017. Infrared Spectrometer for ExoMars: A Mast-

Mounted Instrument for the Rover. Astrobiology 17, 542–564. doi:10.1089/ast.2016.1543

Lefort, A., Williams, R., Korteniemi, J., 2015. Inverted Channel. Encycl. Planet. Landforms.

Leger, P.C., Trebi-Ollennu, A., Wright, J.R., Maxwell, S.A., Bonitz, R.G., Biesiadecki, J.J., Hartmann, F.R., Cooper, B.K., Baumgartner, E.T., Maimone, M.W., 2005. Mars Exploration Rover Surface Operations: Driving Spirit at Gusev Crater. Pasadena, CA, USA.

Lucas, J., Prévôt, L., 1984. Synthèse de l'apatite par voie bactérienne à partir de matière organique phosphatée et de divers carbonates de calcium dans des eaux douce et marine naturelles. Chem. Geol. 42, 101–118. doi:10.1016/0009-2541(84)90008-1

Marion, C., Osinski, G.R., Abou-Aly, S., Antonenko, I., Barfoot, T.D., Barry, N., Bassi, A., Battler, M., Beauchamp, M., Bondy, M., Blain, S., Capitan, R.D., Cloutis, E.A., Cupelli, L., Chanou, A., Clayton, J., Daly, M., Dong, H., Ferrière, L., Flemming, R.L., Flynn, L., Francis, R., Furgale, P., Gammel, J., Garbino, A., Ghafoor, N., Grieve, R.A.F., Hodges, K., Hussein, M., Jasiobedzki, P., Jolliff, B.L., Kerrigan, M.C., Lambert, A., Leung, K., Mader, M., McCullough, E., McManus, C., Moores, J.E., Ng, H.K., Otto, C., Ozaruk, A., Pickersgill, A., Pontefract, A., Preston, L.J., Redman, D., Sapers, H., Shankar, B., Shaver, C., Singleton, A., Souders, K., Stenning, B., Stooke, P., Sylvester, P., Tripp, J., Tornabene, L.L., Unrau, T., Veillette, D., Young, K., Zanetti, M., 2012. A Series of Robotic and Human Analogue Missions in Support of Lunar Sample Return. 43rd Lunar Planet. Sci. Conf. Abstract #2333.

Marshall, C.P., Leuko, S., Coyle, C.M., Walter, M.R., Burns, B.P., Neilan, B. a, 2007. Carotenoid analysis of halophilic archaea by resonance Raman spectroscopy. Astrobiology 7, 631–643. doi:10.1089/ast.2006.0097

Maurice, S., Clegg, S.M., Wiens, R.C., Gasnault, O., Rapin, W., Forni, O., Cousin, A., Sautter,

V., Mangold, N., Le Deit, L., Nachon, M., Anderson, R.B., Lanza, N.L., Fabre, C., Payré, V., Lasue, J., Meslin, P.-Y., Léveillé, R.J., Barraclough, B.L., Beck, P., Bender, S.C., Berger, G., Bridges, J.C., Bridges, N.T., Dromart, G., Dyar, M.D., Francis, R., Frydenvang, J., Gondet, B., Ehlmann, B.L., Herkenhoff, K.E., Johnson, J.R., Langevin, Y., Madsen, M.B., Melikechi, N., Lacour, J.-L., Le Mouélic, S., Lewin, E., Newsom, H.E., Ollila, A.M., Pinet, P., Schröder, S., Sirven, J.-B., Tokar, R.L., Toplis, M.J., d'Uston, C., Vaniman, D.T., Vasavada, A.R., 2016. ChemCam activities and discoveries during the nominal mission of the Mars Science Laboratory in Gale crater, Mars. J. Anal. At. Spectrom. 31, 863–889. doi:10.1039/C5JA00417A

McLennan, S.M., Sephton, M.A., Allen, C., Allwood, A.C., Barbieri, R., Beaty, D.W., Boston, P., Carr, M., Grady, M., Grant, J., Heber, V.S., Herd, C.D.K., Hofmann, B., King, P., Mangold, N., Ori, G.G., Rossi, A.P., Raulin, F., Ruff, S.W., Sherwood Lollar, B., Symes, S., Wilson, M.G., 2011. Planning for Mars Returned Sample Science: Final report of the MSR End-to-End International Science Analysis Group (E2E-iSAG).

MEPAG, 2015. Mars Scientific Goals, Objectives, Investigations, and Priorities, in: Hamilton, V. (Ed.), White Paper Posted June, 2015 by the Mars Exploration Program Analysis Group (MEPAG) at Http://mepag.nasa.gov/reports.cfm. pp. 1–74.

Mittelholz, A., Maloney, M., Osinski, G.R., 2016. The Use of Raman Spectroscopy for the 2015 CanMars MSR Analogue Mission. 47th Lunar Planet. Sci. Conf.

Morse, Z.R., Harrington, E., Christopherson, P., Hill, P.J., Newman, J., Choe, B., Tornabene, L.L., Osinski, G.R. (2018) The Use of GIS and Immersive Technologies in the CanMars Mars Sample Return Analogue Mission; Advantages for Science Interpretation and Operational Decision-Making. Planetary and Space Science, 168, 15-26.

Mojzsis, S.J., Arrhenius, G., 1998. Phosphates and carbon on Mars: Exobiological implications and sample return considerations. J. Geophys. Res. 103, 28495–28511. doi:10.1029/98je02141

Mustard, J., Adler, M., Allwood, A., Bass, D., Beaty, D., Bell, J., Brinckerhoff, W., Carr, M., Des Marais, D., Drake, B., Edgett, K., Grant, J., Milkovich, S., Ming, D., Murchie, S., Onstott, T., Ruff, S., Sephton, M., Steele, A., Treiman, A., 2013. Report of the Mars 2020 Science Definition Team. Mars Explor. Progr. Anal. Gr. 155–205.

Nachon, M., Clegg, S.M., Mangold, N., Schröder, S., Kah, L.C., Dromart, G., Ollila, A., Johnson, J.R., Oehler, D.Z., Bridges, J.C., Le Mouélic, S., Forni, O., Wiens, R.C., Anderson, R.B., Blaney, D.L., Bell, J.F., Clark, B., Cousin, A., Dyar, M.D., Ehlmann, B., Fabre, C., Gasnault, O., Grotzinger, J., Lasue, J., Lewin, E., Léveillé, R., McLennan, S., Maurice, S., Meslin, P.Y., Rapin, W., Rice, M., Squyres, S.W., Stack, K., Sumner, D.Y., Vaniman, D., Wellington, D., 2014. Calcium sulfate veins characterized by ChemCam/Curiosity at Gale crater, Mars. J. Geophys. Res. E Planets 119, 1991–2016. doi:10.1002/2013JE004588

Osinski, G. R., Battler, M., Caudill, C., Francis, R., Kerrigan, M., Pilles, E., Pontefract, A., Tornabene, L. L., Allard, P., Bakambu, J. N., Balachandran, K., Beaty, D., Bednar, D., Bina, A., Bourassa, M., Cao, F., Christoffersen, P., Choe, B., Cloutis, E., Cote, K., Cross, M., D'Aoust, B., Draz, O., Duff, S., Dzamba, T., Fulford, P., Godin, E., Goordial, J., Grau, A., Haid, T., Haltigin, T., Harrington, E., Harrison, T., Hawkswell, J., Hickson, D., Hill, P., Hipkin, V., Innis, L., King, D., Kissi, J., Li, Y., Lymer, B., Maggiori, C., Maloney, M., Marion-Beauchamp, C., Maris, J., Mcfadden, S., McLennan, S., Mittelholz, A., Morse, Z., Newman, J., O'Callaghan, J., Pascual, A., Patel, P., Picard, M., Pritchard, I., Poitras, J.,

Ryan, C., Sapers, H., Silbur, E., Simpson, S., Svensson, M., Tolometti, G., Uribe, D., Wilks, R., Williford, K., Xie, T., and Zylberman, W. (2019) The CanMars Mars Sample Return Analogue Mission. Planetary and Space Science 166:110–130.

Osinski, G.R., Antonenko, I., Barfoot, T., Ghafoor, N., Jolliff, L., Sylvester, B., 2010. An analogue mission in support of MoonRise and other sample return missions to the South Pole–Aitken basin, in: Annual Meeting of the Lunar Exploration Analysis Group. Washington, D. C., p. 3047.

Osinski, G.R., Francis, R., Haltigin, T., Kerrigan, M.C., Pontefract, A., Silber, E.A., Tornebene, L.L., 2016. Overview of the 2015 CanMars Mars Sample Return Analogue Mission. 47th Lunar Planet. Sci. Conf. Abstract #2616.

Pilles, E. A., Cross, M., Caudill, C., Francis, R., Newman, J., Bourassa, M., Hipkin, V., Battler, M., Silber, E., McLennan, S., Williford, K., Haltigin, T., Kerrigan, M., and Osinski, G. R. 2019. Exploring new models for improving planetary rover operations efficiency through the 2016 CanMars Mars Sample Return (MSR) Analogue Deployment. Planetary and Space Science 165:250–259.

Pontefract, A., Tornebene, L.L., Haltigin, T., Kerrigan, M., Duff, S., Barry, N., Osinski, G.R., 2017. Science overview for the 2015 CanMars MSR Analogue Mission: the evolution from pre-mission hypotheses to in-situ science, in: 47th Lunar and Planetary Science Conference. Woodllands, Texas.

Ryan, C.H., Haid, T.M., Osinski, G.R., Tornabene, L.L., 2016. 2015 CanMars MSR Analogue Mission: The Utilization of the Three-Dimensional Exploration Multispectral Microscopic Imager (TEMMI) for In Situ Analysis. 47th Lunar Planet. Sci. Conf.

Sapers, H.M., Pilles, E., Francis, R., Osinski, G.R., Cross, M., Allard, P., 2016. Mars Sample

Return Analogue Mission: Daily Activity Planner Enhanced by Environment Simulation Software. 47th Lunar Planet. Sci. Conf.

Showstack, R., 2011. Mars Opportunity rover finds gypsum veins. Eos (Washington. DC). doi:10.1029/2011EO510003

Simpson, S., Duff, S., O' Callaghan, J., Caudill, C.M., Osinski, G.R., 2017. 2016 CanMars Analogue Mission: Insights into the utility of X-ray fluorescence spectrometry for the identification of paleoenvironments suitable for ancient biopreservation, in: 47th Lunar and Planetary Science Conference. p. 2175.

Smith, P.H., Tamppari, L.K., Arvidson, R.E., Bass, D., Blaney, D., Boynton, W. V, Carswell, A., Catling, D.C., Clark, B.C., Duck, T., Dejong, E., Fisher, D., Goetz, W., Gunnlaugsson, H.P., Hecht, M.H., Hipkin, V., Hoffman, J., Hviid, S.F., Keller, H.U., Kounaves, S.P., Lange, C.F., Lemmon, M.T., Madsen, M.B., Markiewicz, W.J., Marshall, J., McKay, C.P., Mellon, M.T., Ming, D.W., Morris, R. V, Pike, W.T., Renno, N., Staufer, U., Stoker, C., Taylor, P., Whiteway, J.A., Zent, A.P., 2009. H2O at the Phoenix landing site. Science 325, 58–61. doi:10.1126/science.1172339

Squyres, S.W., Arvidson, R.E., Bollen, D., Bell, J.F., Brückner, J., Cabrol, N.A., Calvin, W.M., Carr, M.H., Christensen, P.R., Clark, B.C., Crumpler, L., Des Marais, D.J., d'Uston, C., Economou, T., Farmer, J., Farrand, W.H., Folkner, W., Gellert, R., Glotch, T.D., Golombek, M.P., Gorevan, S., Grant, J.A., Greeley, R., Grotzinger, J., Herkenhoff, K.E., Hviid, S., Johnson, J.R., Klingelhöfer, G., Knoll, A.H., Landis, G., Lemmon, M.T., Li, R., Madsen, M.B., Malin, M.C., McLennan, S.M., McSween, H.Y., Ming, D.W., Moersch, J., Morris, R. V., Parker, T., Rice, J.W., Richter, L., Rieder, R., Schröder, C., Sims, M., Smith, M., Smith, P., Soderblom, L.A., Sullivan, R.J., Tosca, N.J., Wänke, H., Wdowiak, T.,

Wolff, M.J., Yen, A.S., 2006. Overview of the Opportunity Mars Exploration Rover Mission to Meridiani Planum: Eagle Crater to Purgatory Ripple. J. Geophys. Res. E Planets. doi:10.1029/2006JE002771

Svensson, M.O., Maloney, M., Duff, S., Osinski, G.R., 2017. Laser induced breakdown spectroscopy (LIBS) as a simulated stand-off geochemical analysis instrument in the CanMars 2016 MSR analogue mission, in: Lunar and Planetary Science XLVIII. p. 1511.

Thompson, D.R., Allwood, A., Assad, C., Flanery, D., Hodyss, R., Knowles, E., Wade, L., 2014. Adaptive sampling for rover x-ray lithochemistry, in: International Symposium on Artificial Intelligence, Robotics, and Automation in Space. Montreal, Canada.

Tornabene L. L., Battler, M., Choe, B., and Osinski, G. R., 2019. An orbit-based remote sensing geological assessment of the CanMars Mars Sample Return Analogue Deployment (MSRAD) landing site situated in the Henry Mountains Basin, near Hanksville, Utah. Planetary and Space Science, 173, p. 14-34.

Vago, J.L., Westall, F., Pasteur Instrument Teams, Landing S, Coates, A.J., Jaumann, R., Korablev, O., Ciarletti, V., Mitrofanov, I., Josset, J.-L., De Sanctis, M.C., Bibring, J.-P., Rull, F., Goesmann, F., Steininger, H., Goetz, W., Brinckerhoff, W., Szopa, C., Raulin, F., Westall, F., Edwards, H.G.M., Whyte, L.G., Fairén, A.G., Bibring, J.-P., Bridges, J., Hauber, E., Ori, G.G., Werner, S., Loizeau, D., Kuzmin, R.O., Williams, R.M.E., Flahaut, J., Forget, F., Vago, J.L., Rodionov, D., Korablev, O., Svedhem, H., Sefton-Nash, E., Kminek, G., Lorenzoni, L., Joudrier, L., Mikhailov, V., Zashchirinskiy, A., Alexashkin, S., Calantropio, F., Merlo, A., Poulakis, P., Witasse, O., Bayle, O., Bayón, S., Meierhenrich, U., Carter, J., García-Ruiz, J.M., Baglioni, P., Haldemann, A., Ball, A.J., Debus, A., Lindner, R., Haessig, F., Monteiro, D., Trautner, R., Voland, C., Rebeyre, P., Goulty, D.,

Didot, F., Durrant, S., Zekri, E., Koschny, D., Toni, A., Visentin, G., Zwick, M., van Winnendael, M., Azkarate, M., Carreau, C., the ExoMars Project Team, 2017. Habitability on Early Mars and the Search for Biosignatures with the ExoMars Rover. Astrobiology 17, 471–510. doi:10.1089/ast.2016.1533

Van Daele, M., Moernaut, J., Silversmit, G., Schmidt, S., Fontijn, K., Heirman, K., Vandoorne, W., De Clercq, M., Van Acker, J., Wolff, C., Pino, M., Urrutia, R., Roberts, S.J., Vincze, L., De Batist, M., 2014. The 600 yr eruptive history of Villarrica Volcano (Chile) revealed by annually laminated lake sediments. Bull. Geol. Soc. Am. 126, 481–498. doi:10.1130/B30798.1

Vítek, P., Jehlička, J., Edwards, H.G.M., Osterrothová, K., 2009. Identification of β-carotene in an evaporitic matrix-evaluation of Raman spectroscopic analysis for astrobiological research on Mars. Anal. Bioanal. Chem. 393, 1967–1975. doi:10.1007/s00216-009-2677-0

Wiens, R.C., Maurice, S., Mccabe, K., Cais, P., Anderson, R.B., Beyssac, O., Bonal, L., Clegg, S., Deflores, L., Dromart, G., Fischer, W.W., Forni, O., Gasnault, O., Grotzinger, J.P., Johnson, J.R., Martinez-Frias, J., Mangold, N., McLennan, S., Montmessin, F., Rull, F., Sharma, S.K., Sautter, V., Lewin, E., Cloutis, E., Poulet, F., Bernard, S., McConnochie, T., Lanza, N., Newsom, H., Ollila, a., Leveille, R., Le Mouélic, S., Lasue, J., Melikechi, N., Meslin, P.-Y., Misra, a., Grasset, O., Angel, S.M., Fouchet, T., Beck, P., Bridges, N., Bousquet, B., Fabre, C., Pinet, P., Benzerara, K., Montagnac, G., 2016. The Supercam Remote Sensing Instrument suite for Mars 2020. 47th Lunar Planet. Sci. Conf. 8–9.

Williams, R.M.E., Irwin, R.P.I., Zimbelman, J.R., Chidsey, T.C., J., Eby, D.E., 2011. Field guide to exhumed paleochannels near Green River,Utah: Terrestrial analogs for sinuous ridges on Mars, in: Garry, W.B., Bleacher, J.E. (Eds.), Analogs for Planetary Exploration: Geological

Society of America Special Paper 483. The Geological Society of America, pp. 483–505.

Yingst, R.A., Berger, J., Cohen, B.A., Hynek, B., Schmidt, M.E., 2017. Determining best practices in reconnoitering sites for habitability potential on Mars using a semi-autonomous rover: A GeoHeuristic Operational Strategies Test. Acta Astronaut. 132, 268–281. doi:10.1016/j.actaastro.2016.12.018

Yuan, W., Liu, G., Luo, W., Li, C., 2016. The Influence of Volcanic Ash Sediments on the Formation of Lacustrine Organic-Rich Shale in Ordos Basin, Central China, in: AAPG Annual Convention and Exhibition. Calgary, Alberta, Canada, p. 90259.

Zylberman, W., Hickson, D., Haid, T., Osinski, G.R., 2016. 2015 CANMARS MSR Analogue Mission: The Key-Role of LIDAR in Rover Navigation and Potential for Future Missions. 47th Lunar Planet. Sci. Conf. Abstract #1041.

Chapter 6: Discussion

6.1 Investigations of clay-bearing impactites at the Ries impact structure as a planetary analogue for deciphering clay mineral provenance on Mars

In this thesis, the clay-bearing rocks of the Ries impact structure, Germany, were investigated as planetary analogues. The complexities of discerning clay mineral species and provenance is evident – whether they are analyzed within a standard laboratory setting or remote rover operations. Like clay minerals on Earth, Martian clay minerals of the Noachian are likely to have formed under a variety of conditions, but their strong association with heavily cratered Southern Highlands and surrounding the largest impact structures on the surface (Fig. 6.1; Fig. 1.1) suggests an impact-related origin for at least some of the clay minerals observed (see Chapter 4). As our work at Ries shows, a variety of clay mineral species are likely to be produced by impact-related processes and subsequent alteration. Smectites – as well as clay mineral phases of similar composition that are not well-constrained (Osinski et al., 2004) – are produced *in situ* through a variety of impact-related processes. This work (Chapter 4) indicates that recrystallization/devitrification of impact glass and autometamorphism may be the most important processes that developed abundant Al/Fe/Mg smectites in the thin ejecta melt-bearing breccia deposits at Ries, given the absence of a long-lived water and heat source. Through these processes, smectites would have crystallized at the surface or subsurface. Evidence of impact-hydrothermal alteration has been shown in the Ries ejecta melt-bearing breccia as well, consistent with a dioctahedral (Al/Fe) smectite (Newsom, 1980; Newsom et al., 1986; Osinski et

al., 2004; Osinski, 2005; Sapers et al., 2017); this thesis also shows that compositionally complex Al/Fe/Mg smectites are produced via early volatile loss through post-emplacement (Chapter 3). Table 4.2 in Chapter 4 provides a detailed summation of the clay mineral phases (including interlayer composition, associated mineral assemblages, and occurrence) that have been observed in the Ries melt-bearing breccia, specifically in the ejecta deposits. In Table 6.1 below, we provide clay mineral phases that have been identified in other pertinent terrestrial impact-generated deposits; Fe/Mg smectite is a common impact-related alteration product in terrestrial craters, occurring locally and observed with dioctahedral Al-smectite (Naumov, 2005). This chapter will summarize the findings of this thesis, highlighting the likely formation conditions of the impactite clay minerals observed in the Ries ejecta melt-bearing breccias. We will then discuss the implications of those findings on clay-bearing deposits on Mars.

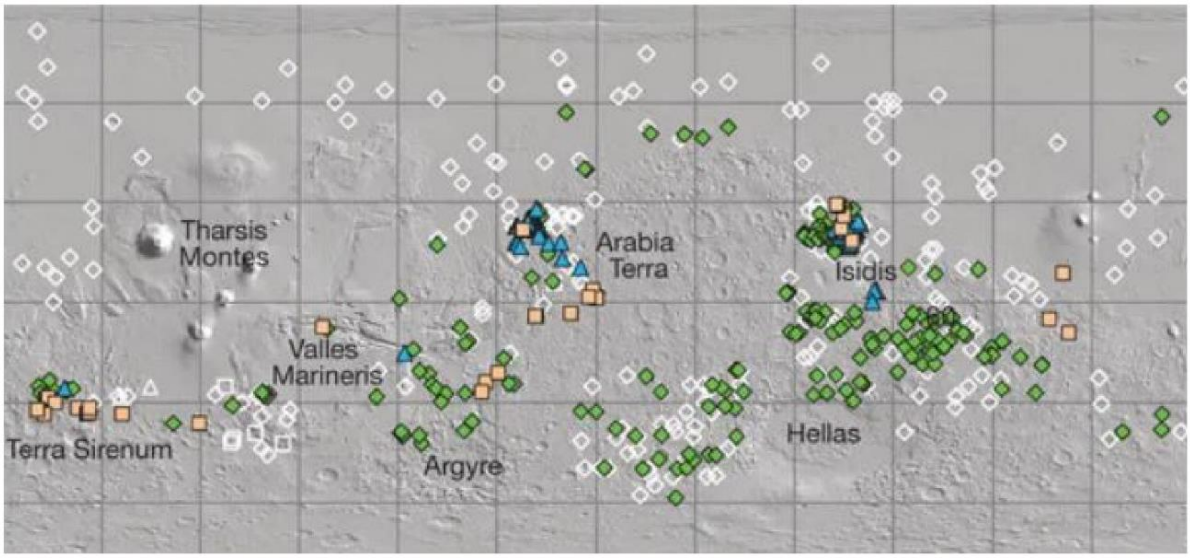

Figure 6.1. Clay minerals and associated mineral assemblages on Mars derived from CRISM data by Ehlmann et al. (2011). The data is categorized by major assemblages as indicated; open polygons indicate CRISM targets where clay minerals were not identified. Note the prevalence of clay minerals distributed circumferential to large basin impact structures (i.e., Hellas, Argyre, and Isidis). Modified after Ehlmann et al. (2011).

Table 6.1. Compilation of terrestrial impact structures and settings where impact-generated clay mineral phases have been observed. Clay mineral phases listed includes composition, mineral species, type, texture, and interlayered and constituent materials, as information is available. Note the prevalence of Fe/Mg smectites (dioctahedral Fe-smectites are nontronites; trioctahedral Mg-smectites are saponites) as the observed clay mineral phase. (Clay minerals in impact structures other than Ries and Chicxulub were originally compiled by Hagerty and Newsom, 2003). These are non-diagnostic observations of minerals produced by meteorite impact.

Impact structure and sample setting	Clay mineral phases	Reference
Ries melt-bearing breccia (surficially exposed): *fracture lining, vesicle fillings, groundmass replacement, pervasive replacement of glass clasts*	~1.65 nm Al-smectite with illitic components [a] relatively well-ordered, moderate crystallinity dioctahedral smectites with turbostractic stacking; interlayered with hydroxy materials; Al/Fe smectite ± illite, ± kaolinite [b] flow-textures and globules, partially-coalesced globules; compositionally and texturally variable; both very fine-grained and platy textures [c] smectite, illite, chlorite [a, b, c, d]	[a] Sapers et al. (2017) [b] This study; Chapters 3 and 4 [c] Osinski et al. (2004) [d] Newsom et al. (1986)
Ries melt-bearing breccia (70 – 90 m depth): *fracture lining, vesicle fillings, groundmass replacement*	~1.25 nm smectite with minor illitic component [a] Fe-smectite with chlorite [b]	[a] Sapers et al. (2017) [b] This study; Chapters 3 and 4

Ries melt-bearing breccia (~300 m depth): *pervasive replacement of glass and mineral clasts*	~1.25 nm smectite with an illitic component, chlinochlore [a]	[a] Sapers et al. (2017)
Degassing pipes of Ries melt-bearing breccia: *lining pipe interiors and as alteration halos*	~1.46 – 1.59 nm Al/Fe/Mg, Fe/Mg mixed dioctahedral and trioctahedral smectites in intermediate/ continuum compositions (nontronite, saponite, montmorillonite); poorly crystalized, turbostractic-stacked; crystallite 2 μm – <0.2 μm; interlayering and finer-grained component consistent with chloritic or Mg-hydroxy material [b]	[b] This study; Chapters 3 and 4
Chicxulub upper peak ring (629 – 714 m depth): *ubiquitous secondary phase in altered glass clasts, within the groundmass occurring along fractures and completely replacing spherulitic clasts*	Fe/Mg smectite (saponite or nontronite) with hydroxy-interlayer material; replaces glass and spherulitic clasts, with a budding, globular texture; poorly-crystalline palagonite-like phase replacing glass clasts	Simpson et al. (2018)
Lonar Lake: *replacement in vugs and vesicles*	Saponite, celadonite	Hagerty and Newsom (2003)
West Clearwater: *localized occurrence, not specified*	Saponite, Nontronite	Allen et al. (1982)
Mistastin: *replacement in vugs and vesicles*	Fe-montmorillonite	Grieve (1975)
Manicouagan: *replacement in vugs and vesicles*	Saponite, Nontronite	Allen et al. (1982)
Sudbury: *replacement in vugs and vesicles*	Saponite, Nontronite	Allen et al. (1982)

6.1.1 Identifying clay minerals and deciphering their complex formation in terrestrial impactites

Naumov (2005) found that – accounting for target rock type – terrestrial craters shared a similar hydrothermal mineral assemblage including clay minerals (often smectites, chlorites, and mixed-layer smectites/chlorites; Table 6.1). (If carbonate rocks are significant, however,

widespread carbonate-quartz-sulfide assemblages are present and clay minerals are rare.) The proposed reason for this uniformity of secondary mineralization among impact structures in varying target lithologies is that the systems typically produce altering fluids that are weakly alkaline to near-neutral pH due to the supersaturation of silica in the form of shock-disordered aluminosilicates (Naumov, 2002, 2005). Investigation of the Lonar Lake Crater, India, has offered a more specific analogue to Martian crustal lithology, dominated by mafic – ultramafic basalts, and further provides insight into expected impact-induced alteration products on Mars. The Lonar event impacted a basaltic target with a composition similar to that of Martian meteorites; drill core from the basaltic impact breccias show that the dominant alteration product is saponite (Fe/Mg smectite), with minor celadonite (Fe-rich phyllosilicate) and carbonate (Hagerty and Newsom, 2003). Schwenzer and Kring (2013) modeled impact-hydrothermal alteration assemblages based on martian meteorite mineralogy as a proxy for crustal composition. Similar to the findings by Naumov (2005) for terrestrial craters, Schwenzer and Kring (2013) found that smectite and chlorite would likely be produced at depth, and at the surface, alteration of crater-fill impact melt sheets would also likely produce clay minerals and chlorite.

The degassing pipe-associated alteration in the melt-bearing breccia at the Ries – chloritic-composition hydroxy-interlayered Al/Fe/Mg smectites in the ejecta, and zeolite-dominated alteration in the crater fill (Chapter 3) – correlates broadly to impact-hydrothermal alteration regimes as described by (Naumov, 2005). Higher temperature phases (e.g., chlorite and hydrated Fe-Ca-Al silicates) are expected to form early in impact-hydrothermal systems but are likely to be overprinted by smectite-dominated retrograde reactions due to later cooling and other alteration phases (Naumov, 2005; Tornabene et al., 2013; Sapers et al., 2017; Osinski et al.,

2004; Naumov, 2002). In fact, Naumov (2005) observed that hydrothermally-altered impact deposits are always characterized by a retrograde sequence of alteration minerals due to the predictable cooling path and other post-impact processes.

Many impact-generated hydrothermal systems produce two alteration regimes (Naumov, 2005): a shallow smectite-dominated zone and a deeper chlorite-anhydrite zone. A general order of mineral crystallization in these zones is indicative of a uniform decrease of the temperature of formation: the smectites (saponite, then montmorillonite) and zeolites crystalize first, followed by analcime, Fe-montmorillonite, and calcite; the chlorite crystalizes first in the deeper regime, followed by lower-temperature replacements of chlorite + anhydrite + calcite (Naumov, 2005). The alteration assemblage of the ejecta degassing pipes is dominated by Al and Fe/Mg smectites and represents the lower-temperature (~160–200 °C; Naumov, 2005 and references therein) trend of addition of Mg and alkalis. High-resolution laboratory techniques were used in this study to identify chloritic-composition hydroxy-interlayered smectites (Chapters 3 and 4), which has been thus far absent from the literature regarding impact-generated hydrothermal systems. The formation of hydroxy interlayers, or partially-formed hydroxy interlayers, is a common intermediate form between smectite and chlorite (Hazen et al., 2013).

The higher-temperature alteration assemblage of the crater-fill degassing pipes is dominated by Ca-zeolites + sulfates and minor calcite, representing enrichment of silica and Ca. The silica enrichment of the higher-temperature alteration regime (~300–350 °C; Naumov, 2005 and references therein), is proposed to be due to higher activities of silica in the hydrothermal solution as it interacts with greater proportions of shock-disordered aluminosilicates and lower pH conditions. Following this model, the crater-fill deposits at the Ries were supersaturated in silica due to the volume of impact melt material and the far greater longevity of hydrothermal

activity, as compared to the melt-bearing ejecta deposits. Thus, the silica and Ca-rich zeolites that line the crater-fill degassing pipes represent the early alteration regimes of the crater-fill deposits. Likewise, the smectite alteration assemblage of the ejecta degassing pipes is representative of the early alteration regimes of (as described by Naumov, 2005); an increase in the Na/Ca ratio (in comparison to the alteration of the crater-fill) is caused by a lower temperature regime, having greater salinity, which favors the crystallization of alkalis over calcium. The formation and alteration of the degassing pipes are likely an early and distinct process and series of events; yet, discerning their formation allows a more complete understanding of the early conditions and post-impact alteration of ejecta impact melt-bearing breccia.

One main consideration of the ejecta degassing pipes – and indeed, the abundance of impact-generated clay minerals in the groundmass of the ejecta melt-bearing breccia – is the volatile source necessary to mineralize degassing pipe interiors and alteration halos. For the crater-fill melt-bearing breccia at the Ries, pervasive alteration was facilitated by a long-lived water source – the post-impact crater lake – and also retained a substantially higher volume of melt than that of the locally emplaced, discontinuous deposits of the ejecta (Osinski, 2005). However, the lack of an apparent long-lived water and heat source in the thin ejecta melt-bearing breccias, coupled with the volumetrically significant (up to ~ 70%) clay minerals that comprise the groundmass, requires an alternative to hydrothermal processes as a sole alteration mechanism. Indeed, much of the groundmass is inconsistent with a hydrothermal formation (Newsom et al., 1986; Osinski et al., 2004). As discussed in Chapter 4, we describe a two-step or continuum initial alteration process, dominated by autometamorphism – the recrystallization of molten rock through strictly endogenous volatiles – and glass devitrification/recrystallization,

that formed the complex, interlayered smectites of the groundmass observed in the melt-bearing breccia groundmass. A first stage of impactite alteration is a pervasive autometasomatism of impact melt-bearing bodies during the initial and progressive stages of cooling (Naumov, 2005). The melt-bearing breccia is initially emplaced at ~750 – 900 °C, with the impact melt still molten (Osinski et al., 2004) and under annealing conditions, retaining the heat necessary for the initial stages of alteration of the deposit. In the model that we propose (see Chapters 3 and 4), the clay minerals crystallize as smectites through the interaction of available volatiles with shock-disordered aluminosilicates – in silica-supersaturated conditions from impact melt (e.g., Naumov, 2005) – and the aqueous diffusion of cations (mainly Fe, Mg) from the glass (Naumov, 2005) and Fe and Mg-bearing basement clasts. It is this aqueous diffusion and the initial devolatilization of the deposit that may have been the origin of the degassing pipes within in deposit. (As discussed in Chapter 3, a source other than the volatile-rich, underlying Bunte Breccia is necessary, given that this deposit is not present for the volatile source of the degassing pipes found in the Wörnitzostheim and Nördlingen drill cores.) In this model, cations would have been continuously made available in the system through a second or continuum cooling phase of devitrification/recrystallization, as is described for the closed-system alteration of volcanic glass-bearing deposits (e.g., Drewes, 1963). These processes likely liberated and mobilized the cations necessary for the mineralization of the degassing pipes. In this system – even in the absence of an external volatile and heat source – interlayering of the smectites form due to a partial polymerization of dissolved, and subsequently intercalated cations (Al^{3+}, Mg^{2+}, and Fe^{3+} oligomers; as described by Georgiadis et al., 2019). Hydrated glass and other minerals in the melt-bearing breccia were recognized by Newsom et al. (1986) as a likely source of volatiles for the formation of the degassing pipes. Hildreth and Fierstein (2012) found that

recrystallization/devitrification of glass within the melt-rich volcanic ignimbrite deposit in the Navarupta-Katmai, Alaska, volcanic field liberated gas, just after emplacement and over extended time periods; the fumarole pipes at Navarupta-Katmai are described as discrete altered zones, formed from focused gas ascent gathered from within the tuff, from volatiles that were interstitially-trapped during emplacement and more that were liberated by devitrification (Hildreth and Fierstein, 2012, and discussed in Chapter 3). We suggest that these fumaroles and their formation mechanisms are similar to the degassing pipes at Ries based on the strong similarities in the morphology, size in cross-section, vertical depth extent, secondary mineral alteration, and elutriation (as well as lithologic character of the host in terms of porosity, melt content, grain and clast size, as described by Hildreth and Fierstein 2012). We therefore suggest the following sources of volatiles for the formation of the degassing pipes and initial alteration of the ejecta melt-bearing breccia deposit: (1) liberation of volatiles from rapidly devolatilizing and crystallizing glass upon initial cooling (and may have provided an initial starting point for the formation of degassing pipes, as suggested in the formation of volcanic fumarole pipes; Hildreth and Fierstein, 2012); (2) volatiles entrained within impactites during initial mobilization and flow-emplacement of the discontinuous ejecta unit – these volatiles will also be lost through early convective cooling; (3) variable autometamorphism or other alteration of entrained shock-disordered, volatile-bearing rocks (e.g., amphiboles and biotites in the basement-derived rocks); and (4) water at the contact, or released through a degassing of an underlaying volatile-rich layer (i.e., the sedimentary-derived Bunte Breccia), where present, due to contact with the hot melt-bearing breccia.

Even in the absence of long-term surficial aqueous activity, our work indicates that impactites alter over time to produce somewhat predictable alteration products (as suggested by

Naumov, 2005, and shown in Table 6.1). Devolatilization, autometamorphism, and devitrification/recrystallization processes operate even with little or no surface water, groundwater, or appreciable ice bodies, and thus may have implications for the composition of impactites and the formation degassing pipes on volatile-poor rocky bodies like Ceres and Vesta (as discussed in Chapter 3). We show that compositionally diverse, abundant Al/Fe/Mg smectites comprise ejecta impactites, having formed without appreciable exogenous volatiles. Autometamorphism and devitrification, therefore, may have been the dominant alteration processes that produced the abundant clay minerals of the Ries ejecta melt-bearing breccias. We suggest that these findings also have significant implications for the ancient clay-bearing terrains on Mars.

6.1.2 Implications for clay mineral formation on Mars

On Mars, it is generally considered that the presence of clay-bearing units indicates climatic conditions during the Noachian and Early Hesperian Eras that supported near-neutral to mildly-acidic liquid water stability at the surface and near-surface (e.g., Bishop et al., 2017; Bishop and Rampe, 2016). Observed Fe^{3+} smectite-bearing stratigraphic units (Michalski and Dobrea, 2007; Bishop et al., 2008, 2017; Wray et al., 2008; Bishop and Rampe, 2016) are interpreted as aqueous alteration of the crust by endogenic processes involving meteoric water, and representative of ancient warm, wet conditions (Bishop and Rampe, 2016). When the Fe-smectite units are observed in association with deposits rich in Al-smectite, kaolinite, poorly-crystalline clay mineral phases, and other hydrated silica phases (Fig. 6.1; Loizeau et al., 2012; Bishop and Rampe, 2016; Bishop et al., 2017; Ehlmann et al., 2011), they are interpreted as leached weathering horizons resulting from a climatic shift from a toward a colder, drier climate

(Bishop and Rampe, 2016). Some workers, however, have suggested that similar products (particularly Fe/Mg smectites ± chlorites) observed on Mars' surface are likely to have been produced in the subsurface through impact-induced hydrothermal alteration (e.g., Allen et al., 1982; Newsom, 1980; Tornabene et al., 2013; Sun and Milliken, 2015; Ehlmann, Mustard, Murchie, et al., 2011b; Ehlmann et al., 2013; Michalski et al., 2015). In fact, Ehlmann et al. (2009) suggested that impact-induced hydrothermal alteration was likely necessary to explain the widespread distribution of Fe/Mg smectites in Noachian terrains. This study (Table 6.1; Chapters 3 and 4) and others (e.g., Newsom et al., 1986; Osinski et al., 2004; Sapers et al., 2017) at Ries show that compositionally diverse Al/Fe/Mg smectites are produced by syn/post-impact processes – critically, even in the ejecta deposits. We suggest that similar alteration products should be considered in impact deposits – in the region of the crater, in impact ejecta, in impact-related features like hydrothermal vents (e.g., degassing pipes) and alteration-filled fractures, and potentially as materials present in stratigraphy, with no apparent connection to a source crater – on other terrestrial bodies. Impacts into targets with silica-rich crusts will result in the devitrification of thermodynamically unstable impact glasses and a supersaturation of silica in the form of shock-disordered aluminosilicates (Naumov, 2005, and as discussed in previous sections); this process is therefore likely to be similar between Earth and Mars. The implications of devitrification and autometamorphism having produced abundant smectites in the Ries ejecta deposits, without appreciable exogenous water and heat sources, may be significant for the presence of smectites on Mars; Mars likely has abundant impact glasses (e.g., Schultz and Mustard, 2004; Osinski et al., 2011; Tornabene et al., 2013; see Chapter 1) produced by many overlapping and large (>100 km in diameter) impact events, having dispersed ejecta at global scales. This suggests that smectites observed on Mars may not necessarily indicate either: (1) a

water-involved surficial weathering horizon (as suggested by Bishop and Rampe, 2016); or (2) impact-related alteration constrained solely to hydrothermal processes. Even in the absence of long-term surficial aqueous alteration, our work indicates that impactites alter over time to produce somewhat predictable alteration products (Table 6.1). In the case of a "cold, dry" Mars, hydrated impact glasses would devitrify and form smectitic clay minerals at a vast scale, spatially and temporally; though it is recognized (Tornabene et al., 2013a) that in the absence of heat and aqueous activity alteration via devitrification may extend over periods on the order of 10^9 years (Marshall, 1961). Many overlapping impact events over millennia, with overlapping melt-bearing breccia ejecta deposits (see Chapter 1), and globally-dispersed impact ejecta, may result in secondary clay minerals from devitrified impactites observed in strata-bound deposits and reworked by other processes within detrital deposits.

The impact-origin for clay minerals on Mars is not only plausible but could rectify the disconnect between mineralogic observations (e.g., Bibring et al., 2006; Carter et al., 2015; Ehlmann and Edwards, 2014; Bishop and Rampe, 2016; Bishop et al., 2017) and the modeling of the climate of Mars during the time the clay minerals were produced (e.g., Hynek, 2016). This disconnect is a difficult conundrum for Mars science. On the one hand, geomorphological evidence in the form of vast water-carved valley systems (Craddock and Howard, 2002) has been proposed as indicating Earth-like conditions in the Noachian Era – with long-term atmospheric stability and precipitation that recharged surface-water and presumably produced the widespread aqueous, ambient-temperature clay minerals at the surface. However, several factors point to an unlikely scenario for long-term "warm, wet" conditions on Early Mars: (1) the thermophysical reality of the low solar flux – the sun was only 75% as luminous as today (Gough, 1981), and Mars is 50% farther from the sun than Earth; (2) inefficiency of CO_2 as a primary greenhouse

gas (Forget et al., 2013; Wordsworth et al., 2013) means that it is unlikely for Early Mars to attain and sustain temperatures necessary for surface-water stability (Wordsworth, 2016; Palumbo and Head, 2018); and (3) the strongly chaotic obliquity cycles of Mars that have likely forced ice ages and prevented long periods of climatic stability (Laskar et al., 2004).

Various scenarios have been proposed to reconcile the abundant geological evidence of surface-stable liquid water at the Martian surface with the likely nature of the early climate (Baker et al., 1990; Craddock and Howard, 2002; Stepinski and Coradetti, 2004; Wordsworth et al., 2015; Ramirez and Craddock, 2018; Cassanelli and Head, 2019). Yet, even when climate models assume an early "warm and wet" Mars, water is dominated by ice and snow in the polar regions and does not explain the formation and distribution of water-carved valley networks (Palumbo and Head, 2018). A solution to the formation of valley networks in a climate with only transient warm, wet periods has been presented by Fastook and Head (2015) and Grau Galofre et al. (2018): Noachian ice sheets provided a huge reservoir of potential melt water, with subglacial hydrologic systems capable of forming the observed fluvial and lacustrine features. Furthermore, Fastook and Head (2015) and Grau Galofre et al. (2018) use morphologic modeling of Martian terrain and that of terrestrial analogues to show that transient warm, wet periods were not necessary to force on otherwise predicted "cold and icy" climate.

It has been suggested that the most likely scenario for surface water availability for the formation of valley networks is through punctuated, short-term, transient phases of warm temperatures in an otherwise "cold and icy" climate (Head and Marchant, 2014; Wordsworth et al., 2015; Palumbo and Head, 2018). However, the scenario of transient periods of surficial water availability may not entirely explain the presence of the widespread clay minerals in Noachian terrains. Bishop et al. (2018) provided a geochemical model in support of the formation of

surficial dioctahedral (Al/Fe^{3+}) smectite within the windows of short-term, warm climatic events. Mineralogic evidence in support of this model are the lacustrine clay minerals observed by NASA's Mars Science Laboratory rover (MSL; Grotzinger et al., 2012) in Gale Crater – Al-rich, Fe^{3+}-bearing dioctahedral smectite – that are proposed to have formed through episodic fluctuations in water levels linked with short-term atmospheric cycling (Fedo et al., 2017; Stein et al., 2017; Gwizd et al., 2018). However, the majority of the smectites at Gale Crater and throughout the Noachian terrains are Fe/Mg smectites. Furthermore, the presence of Al-smectites is not restricted to lake beds or other water-formed landforms but are widespread. Present geochemical models may still be insufficient to describe the origin of clay minerals on Mars if a major component of Noachian geologic activity is not recognized: impact cratering. The model of clay mineral formation provided by Bishop et al. (2018) suggests that the formation of Fe/Mg smectites are restricted to subsurface hydrothermal environments. We make the case in this thesis for the likelihood that some, and perhaps the majority, of the clay minerals observed in the Noachian terrains of Mars were produced through various impact-related processes (hydrothermal and otherwise). Geologic evidence indicates that impact cratering played an active role in producing new crustal materials on Mars over millennia (e.g., many overlapping preserved impact structures and ejecta; megabreccia observed in stratigraphic exposures); compelling evidence from Earth suggests that impacts not only fundamentally alter planetary crusts but play an active role in the evolution of a body's atmosphere and biosphere (Grieve, 1993). Impact processes mobilize, melt, and concentrate volatile-bearing materials, accommodate pore space and fractures, and provide long-lived heat (for potentially tens of thousands to millions of years; Abramov and Kring, 2007, 2004) with the capacity to circulate volatiles concomitant with large-scale mineral alteration. However, these processes largely

operate regardless of climatic conditions, the recognition of impact-generated clay minerals may allow for a more accurate view of Mars' past, and avoid the propensity to accommodate warm, wet climatic conditions to explain the vast presence of clay minerals on Noachian surfaces.

6.2 Exploration strategies and approaches to *in situ* rover-based investigations of impactites

One main goal of this thesis is to incite new ways of thinking about the variety of complex processes – including impact cratering – that produced materials observed on the surface of Mars. There is, perhaps, no better way to understand the metacognition of the Mars scientist, and the resultant science questions and subsequent investigations, than to test exploration strategies through a fully-simulated mission to Mars. The CanMars experiment allowed for complex, multi-faceted lessons to be learned regarding rover-based operational procedures as well as the necessity for preparedness of the specific geology that will be explored via landed missions on Mars (Chapter 5; Osinski et al., 2019; Francis et al., 2016). The lessons-learned include the difficulties in properly characterizing the geologic context and the inherent difficulty in identifying and adequately characterizing smectite clay minerals. The characterization of pre-, syn-, and post-impact clay minerals from Ries impact structure in this thesis also demonstrates this difficulty; hydrothermal or otherwise impact-generated clay minerals are very difficult to differentiate from detrital clay minerals, particularly in the absence of high-resolution laboratory techniques. To account for these difficulties – and get the greatest value from a mission like Mars 2020 – we found that terrestrial analogues that model the expected materials as closely as possible should be studied and approaches developed for remote investigations of those materials. During remote rover investigations, as we gain more knowledge about a particular rock type or setting, it provides an opportunity to expand on our

understanding of local environments and larger geologic and planetary systems. To arrive at this deeper understanding, it is critical to maintain the willingness to adapt previous models and avoid the inertia of previous intellectual frameworks and group-thinking. This principle is inherent in any space exploration mission, but is worth continually reminding ourselves as a scientific community considering the immensity of the task and the considerable number of individuals working together to face that task. It is in this spirit that we suggest that a methodological approach for detecting impactites – materials that are typically under-studied and may be under-appreciated in their volumetric and geologic significance on Mars – be folded into the framework of a larger exploration strategy. Below, we seek and to consolidate our findings from *in situ* field investigations of impactite materials and Mars-analogous terrain and to provide an exploration framework that we hope will be useful for identifying and characterizing impactites on Mars.

6.2.1 In situ detection of impactites and clay minerals on Mars

Investigations during the Columbia Hills campaign by the Mars Exploration Rover (MER; 2004 – 2018) Spirit provided an excellent example of *in situ* characterization of a potential impactite and associated clay minerals. The Spirit team was able to interpret and characterize altered impactites using the onboard instrument suite (Arvidson et al., 2008), including the Miniature Thermal Emission Spectrometer (Mini-TES; used for determining spectral signatures of minerals; Silverman et al., 2003), Mössbauer Spectrometer (MB; identified iron-bearing minerals; Klingelhöfer et al., 2003), and Alpha-particle X-Ray Spectrometer (APXS; provided elemental chemistry; Rieder et al., 2003). The data provided by these instruments supported the impactite interpretation of the Assemblee clastic rocks at Columbia

Hills, Mars, based on the following lines of evidence: the presence of Fe-poor amorphous glasses that were relatively high in siderophile elements (Clark et al., 2007a; Ming et al., 2008); a spectral interpretation of the mineral maskelynite (diaplectic plagioclase glass; Clark et al., 2007); bulk elemental data having a compositional match to that of the regional geology (as discussed in Arvidson et al., 2008 and Tornabene et al., 2013); rock textures including angular mineral and lithic clasts, though rounded clasts were also present. It is also noteworthy that the Assemblee rocks were observed as being fractured and potentially vesicular (Clark et al., 2007). The siderophile elements observed may indicate a contribution from the impactor (Palme, 1982; Grieve, 1987); however, caution should be exercised when assessing for an extraterrestrial component as the impactor is vaporized in larger impact events; even in smaller impact events, the geochemical signature of the impactor may have been subsequently altered or otherwise weathered (Koeberl, 1998).

At the Assemblee outcrop, a ferric-sulfate-rich material was also investigated (Squyres et al., 2006). Compositional profiles (including SiO_2, Al_2O_3, and cations Mg, K, and Ca, with enriched Mg) and stoichiometry suggest the presence of montmorillonite or mineral phases that are compositionally similar (e.g., amorphous or poorly crystalline "clayey, smectite-like" material, or a more complexly altered or interlayered smectite) (Clark et al., 2007). However, concrete identification for smectite clay minerals *in situ* remained elusive, as the indicative signatures in reflectance spectra for clay minerals lay outside of the range of Mini-TES.

Following the successful MER missions, MSL carried an X-ray Diffractometer (XRD) to Mars for the first time (Blake et al., 2012). An XRD is an instrument that allows for direct identification of minerals by detecting the interaction between their crystalline structure and the incidence angle of diffracted X-rays. This instrument is key to the identification of minerals *in*

situ by a rover on Mars; therefore, we will briefly describe the instrument and the data it produces (see also, Chapters 3 and 4). Incoming X-rays produced by the instrument are scattered in a wave pattern upon interacting with the basal planes of a mineral; most waves are cancelled out by destructive interference, but the others add constructively at an angle equal to a multiple of the wavelength of the incoming X-ray source (known as Bragg's Equation; Bragg, 1914). Theta (θ) represents the angle of both the incoming and diffracted beam, or the constructive X-rays. The 2θ angle and intensities of the diffracted X-rays are recorded as an X-Y plot, yielding a two-dimensional "XRD pattern" (see Brindley and Brown, 1980; Chapters 3 and 4 of this thesis and figures therein). As described by Blake et al. (2012), capabilities of MSL's Chemistry and Mineralogy (ChemMin) XRD are enhanced from that of the MER rover payload, as compositional data alone does not allow for the observation of specific mineral species which are sensitive to the precise temperature, pressure, and chemical conditions of their formation.

MSL's ChemMin combines powder XRD and X-ray Fluorescence (XRF) instruments and has been hugely successful at identifying the mineralogy and measuring elemental abundance of the surface materials analyzed by the mission. The SAM (Sample Analysis at Mars) instrument evolved gas analyses (EGA) supports the mineralogical findings by providing data on the nature of the octahedral sheets of the clay minerals (Bristow et al., 2018). By heating the materials in its oven, SAM allows dehydroxylation experiments, as is commonly performed in terrestrial laboratories as a step-wise approach to discern smectite species, interlayering, and complexities of superstructure XRD peaks. Smectites are sensitive to heat-driven dehydration conditions which cause dehydroxylation at known temperatures dependent on the octahedral site occupancy of cations (Brindley and Brown, 1980). For the clay minerals detected in the Murray

Formation mudstones in Gale Crater, multiple peak H_2O releases suggested that both dioctahedral (Al-rich) and trioctahedral (Mg-rich) smectites were present (Bristow et al., 2018).

These observations represent incredibly innovative instrumentation and techniques to discern clay mineralogy *in situ* on Mars. The XRD data provides measurements directly from the mineral structure, and thus provides definitive mineralogical data that cannot be derived from other datasets alone, notably, reflectance spectroscopy. As discussed in Chapters 3 and 4 (and a major outcome of those findings), it has not yet been shown that reflectance spectroscopy can detect interlayered materials within the structure of swelling clay minerals; these components of the minerals are likely to be under the limits of detection for the technique. Typically, shifts in absorption bands of reflectance data are attributed to interlayer cation vibrations, but the interlayered material is not characterized or quantified (e.g., Bishop and Murad, 2004). *In situ* ground-truthing of the mineralogy is necessary to confirm the decades of excellent, yet, largely orbital data-derived interpretations about the surface and the past of Mars. Though advances like ChemMin have provided detailed data on the mineralogy from the Martian surface, challenges remain. Due to the necessarily limited scope of a spacecraft-bound instrument, some fundamental clay mineral analysis techniques are still only possible in the terrestrial laboratory setting. For example, the inability to separate clays (<2 μm constituents) from the bulk material resulted in XRD peak overlap with pyroxenes in the sample, preventing crystallographic and chemical characterization of the Murray Formation clay minerals by MSL (Bristow et al., 2018). Furthermore, MSL's ChemMin XRD has a limited angular range of 5° to 50° 2θ with <0.35° 2θ resolution. This range is indeed sufficient to identify and quantify virtually all minerals. However, given the inherent difficulty in characterizing clay minerals, the <5° 2θ range, specifically, 2° – 5°, greatly assists in assessing the shape of the low-2θ 001 smectite peak (the

basal mineral plane of smectite) that often provides critical information about the nature of the smectite and interlayered materials (see Chapters 3 and 4, and figures therein). SAM's EGA instrument on MSL allows for thermal manipulation of samples, which provides incredible insight into the nature of the clay minerals; however, it is the change of the XRD pattern with step-wise, controlled heating/dehydration and rehydration treatments, following cation-saturation of the material, that yields analysis of the nature of the interlayered material when present within the expanded smectite layers (Georgiadis et al., 2019; Brindley and Brown, 1980).

It is clear that the instruments aboard Spirit, Opportunity, and MSL have proved very effective at data acquisition and synthesis for the identification and characterization of rock types on Mars, including impactites. However, the characterization of impactites, as with their clay mineral constituents, is often not an easy or straightforward task even in Earth laboratories. As suggested by Tornabene et al. (2013), a systematic approach may be adopted by Mars 2020 (and other future rover missions like ESA's ExoMars), similar to that of Spirit, Opportunity, and MSL, to best support or falsify an impactite-origin hypothesis for a given lithologic target. A methodological approach to characterizing impactites using MSL instruments is presented by Tornabene et al. (2013); based on this approach, we make similar recommendations for impactite characterization with the instruments that will be aboard the Mars 2020 rover.

6.2.2 Methods for rover-based identification of impactites

The Mars 2020 instrument suite includes SuperCam (Wiens et al., 2017; see also Chapter 5), built as an improved version of MSL's Chemistry Camera suite (ChemCam) with the added capabilities of remote Raman spectroscopy and passive reflectance spectroscopy in the visible – short-wave infrared range (VISIR; Bernardi et al., 2017). These are both a first for Mars rover-

based instruments. The extended detection of the spectral range to VISIR is a significant improvement, as 0.3 – 2.8 μm wavelengths are ideal to differentiate clay minerals (e.g., Chapters 3 and 4), carbonates, and sulfates (Clark et al., 1990, 2007b; Bishop and Murad, 2005; Bishop et al., 2008, 2017). A laser-induced breakdown spectroscopy (LIBS) instrument is included to provide quantitative elemental composition, and the Remote Micro-Imager (RMI) will provide context imaging for the targets of the various SuperCam instruments. The rover mast imager and spectrometer MastCam-Z will provide imaging spectrometry from 0.4 to 1.0 μm (Bell et al., 2016), producing image data that will differentiate ferric and ferrous iron. The Mars 2020 payload will also have the first microfocus X-ray fluorescence (XRF) instrument, Planetary Instrument for X-ray Lithochemistry (PIXL; Allwood et al., 2015), capable of producing elemental chemistry "maps" – these element maps are much like those commonly produced by laboratory electron microprobe instruments (e.g., see Chapter 3). PIXL's micro-XRF can resolve textures up to sub-mm-scale, similar to that of a geological hand lens (Allwood et al., 2015). The Scanning Habitable Environments with Raman & Luminescence for Organics & Chemicals (SHERLOC) is an arm-mounted, Deep UV (DUV, 248.6 nm) Raman spectrometer, designed to identify mineralogy and specifically, the distribution and type of organics, if present (Beegle et al., 2015). Much like SuperCam's RMI, SHERLOC also has an imager – the Wide Angle Topographic Sensor for Operations and eNgineering (WATSON) – capable of μm-scale imaging of the target. The Mars 2020 rover will not have an XRD instrument nor the capability to detect and measure isotopic signatures as with MSL's SAM instrument, as the exploration strategy shifted away from bulk measurements to higher-resolution, spatially-coordinated measurements (e.g., instrument-coordinated imagers and element maps). The exploration framework for the Mars 2020 mission is based on the search for rock textures and microstructures, with the

expressed goal of studying fine-scale compositional and textural variations that may have preserved evidence of biosignatures (Williford et al., 2018).

The search for sites of astrobiological relevance requires an enormous effort to characterize both regional and local geology. Indeed, a motivation for the Mars 2020 mission is to characterize, collect, and cache samples that represent the geological diversity for eventual return to Earth (Williford et al., 2018). The Mars 2020 landing site is within Jezero Crater, which acted as a catch basin for fluvial deposits during the Early Hesperian/Late Noachian; the crater rim was breached by a flow and fluvially-transported sediments were deposited on the crater floor (Goudge et al., 2017). It is thought these deposits may have a high likelihood of supporting life during a warmer, wetter past, and may have preserved evidence of past life. The deltaic deposits on Jezero Crater floor hold tantalizing clues of Fe/Mg smectite and putatively sedimentary carbonates, indicative of neutral-alkaline aqueous conditions and thus having a high habitability potential (Ehlmann et al., 2008a; Ehlmann et al., 2008b; Ehlmann et al., 2009; Goudge et al., 2015). However, the area of the landing site is incredibly geologically diverse and additionally offers the opportunity to understand the evolution of Mars through access to deep, Early Noachian terrain (Bramble et al., 2017). In the planned extended mission (Farley et al., 2018), the rover would traverse out of the crater through the breach in the rim and encounter the following deposit types: (1) megabreccia exposures: clay-rich breccia that may have been excavated from the Isidis impact event (Chapter 1, Fig. 1.1), and thus record ancient geologic conditions (Mustard et al., 2007); (2) Mid-Noachian to Early Hesperian clay-rich ridges that may have formed as mineralized veins by circulating groundwater (Saper and Mustard, 2013; Pascuzzo et al., 2019); (3) kaolinite, carbonate, and sulfate-bearing materials that are stratigraphically-bound and thus may reveal the composition and temperature of ancient

groundwater and/or ancient climates (Mustard et al., 2007; Quinn and Ehlmann, 2019); (4) Late Hesperian to Early Amazonian fluviolacustrine clay mineral deposits (Goudge et al., 2018; Ehlmann et al., 2008a); and (5) impactites produced by the Jezero impact event.

Given the geological setting of the Mars 2020 mission, particularly if the extended traverse through the crater rim is pursued, it will become necessary to properly identify and characterize impactites. The Jezero impactites will likely be present in a number of settings, including: (1) detrital material on the crater floor carried by fluvial deposits from the eroding crater rim and terraces (see Chapter 1, Fig. 1.5 for crater schematic); (2) *in situ* crater-fill impactites, if exposed below the deltaic and other post-impact deposits; (3) allochthonous monomict or polymict lithic crystalline breccias (e.g., Chapter 1, Fig. 1.4b) and monomict megablocks (m - >100m-scale) in the region of the outer terraces, crater rim, and just beyond the crater rim; (4) polymict melt-bearing breccias (e.g., Chapter 1, Fig. 1.4c–d) within the crater and beyond the crater rim; and (5) parautochthonous monomict or polymict Bunte-Breccia-type breccia (e.g., Chapter 1, Fig. 1.4f) of the continuous ejecta deposits beyond the crater rim, found stratigraphically below the melt-bearing breccia (e.g., Chapter 1, Fig. 1.4a). Identification of characteristics to determine potential impact-origin using the instrument suite aboard Mars 2020 is provided in Table 6.2; identification of impactite clay mineral phases is provided in Table 6.1. Below, we suggest a method of investigation to determine the impactite origin of lithologies or materials. This simplified investigation method is not meant to provide an exhaustive list of criteria, but rather a guide to augment current intellectual frameworks with respect to *in situ* investigations and larger geologic systems on Mars. A large-to-small-scale investigatory framework is presented as follows:

1. Local and regional geologic context:

a. Autochthonous impactites are found in the immediate vicinity to their host crater (Fig. 6.2) and are, thus, relatively straightforward to identify. These rocks near the crater rim are faulted and fractured but lack shock metamorphism, and although uplifted and displaced, generally retain their original stratigraphic relationships (Grieve and Therriault, 2012). Note that multiple overlapping impact events may obscure obvious relationships between impactites as well as their crater of origin. Unlike those in the rim area, autochthonous impactites in the crater central uplift are shocked, with mineralogic evidence of shock metamorphism, including shatter cones (Grieve and Therriault, 2012).

b. Impact melt rocks from a coherent melt sheet may line the crater floor and terraces and display columnar jointing (Fig. 6.2; Osinski et al., 2018); although columnar jointing is a classic volcanic igneous structure, those derived from impact melt may show evidence of grading from glassy melt clasts (bottom), clast-rich glassy to very fine-grained melt rock, and clast-poor, fine-grained melt rock (Osinski et al., 2012). Melt-poor or melt-free allochthonous lithic breccias may also be observed as grading into melt-bearing breccias in the crater fill deposits. If the crater-fill deposits are eroded and the crater floor is exposed, allochthonous lithic breccias and melt rocks can be observed within dikes (Fig. 6.2).

c. Allochthonous rocks also occur as megablocks proximal to a host crater, and as distal megabreccias and lithic breccias (Fig. 6.2). These breccias are highly variable in terms of clast size (< 1mm and larger), clast angularity, sorting, and level of shock (Grieve and Therriault, 2012), and are excellent first-indicators of a

potential impactite (particularly when the original impact crater has been obscured or the deposit is distal from the host crater). In the ejecta, impact melt rocks and melt-bearing breccias and melt-poor to melt-free lithic breccias occur as discrete lithologies, often in sharp contact (Fig. 6.2; Chapter 1, Fig. 1.4a; Osinski, 2006). This is a distinctive contact in ejecta deposits: discontinuous distribution of melt-bearing breccias – emplaced as a flow – overlies a continuous melt-poor or melt-free unit of lithic breccias (Fig. 6.2; Chapter 1, Fig. 1.2c and Chapter 4, Fig. 4.1d).

d. Post impact-hydrothermal features, like vugs and degassing pipes, may be present in the crater-fill impact melt rocks (e.g., Hagerty and Newsom, 2003, and references therein) and the melt-bearing breccias of the crater interior and ejecta (Chapters 3 and 4).

2. Hand sample-scale textural observations: Shatter cones are the only diagnostic shock-deformation feature visible at the hand sample-scale (Table 6.2) (Dietz, 1960; French and Koeberl, 2010; Osinski and Ferrière, 2016).

    a. Hand sample-scale observations of impact melt-bearing impactites: Melt-bearing breccias have a variable matrix – glassy, devitrified glass, and/or crystalline (fine, medium or coarse-grained) (Grieve and Therriault, 2012) with a wide range of microscopic textures (Floran et al., 1978; Osinski et al., 2004). Shocked and unshocked clasts of mixed target rock and fragments are supported by the matrix (Fig. 6.2); flow-banded (schlieren) textures and larger flow-textured glass clasts (Fig. 6.2; Osinski et al., 2018; Chapter 1, Fig. 1.4 d–e) may also be present. Importantly, PIXL will be able to observe groundmass textures of impact melt-bearing impactites, including: clast-rich – clast poor varieties with vitric/glassy

groundmass ± quench crystals, vesicles, intermingling melt particles; clastic groundmass with angular, broken melt particles (Osinski et al., 2012)

3. Minerals: high-pressure polymorphs (e.g., coesite and stishovite (from quartz) (Stöffler, 1971; Stähle et al., 2008) and wadsleyite and ringwoodite (from olivine), though these have only been identified in meteorites; Ferriere and Osinski, 2012; Ohtani et al., 2004; Fritz and Greshake, 2009); diaplectic glass (Stoffler and Langenhorst, 1994); products of melting, representing mixed mineral compositions, or monomineralic melts (e.g., lechatelierite; Keil et al., 1997), commonly present with quench crystallites or microlites of pyroxene, plagioclase, and olivine (Osinski et al., 2012); "clayey" or poorly-crystallized clay mineral phases (Table 6.1; Osinski et al., 2004; Sapers et al., 2017; Newsom, 1980; Newsom et al., 1986, and references therein; Chapters 3 and 4).
4. Geochemistry: Atypical isotopic ratios and elevated concentrations of specific siderophile elements are considered useful as initial cosmic indicators or initial characterization of a meteoric contribution (Palme et al., 1978; Wolf et al., 1980; Koeberl et al., 2007) – though, this assessment is complicated by the variety of possible projectile compositions, relies on localized enrichment as compared to low background crustal values, and is diluted and often heterogeneously distributed in impactites (Goderis et al., 2012). It is generally accepted that impact melt rocks have a relatively homogenous major element geochemistry as compared to the original target material (Palme et al., 1979; Osinski et al., 2012), though geochemical homogeneity in impact-melted crystalline rock may not always be the case (e.g., Marion and Sylvester, 2010; Osinski et al., 2018). Heterogenous melting, mixing, and rapid cooling means that fractionation rarely occurs (Osinski et al., 2012).

Table 6.2. Diagnostic and non-diagnostic indicators for shock-metamorphism and meteorite impact (French and Koeberl, 2010 and references therein) and the method of detection with Mars 2020 instrumentation. The detection method listed as "orbitally-derived" relies on supportive datasets; those listed as "terrestrial laboratory required" are not currently possible to derive *in situ*.

Diagnostic indicators	Detection method
Preserved meteorite fragments	SuperCam RMI; MastCam-Z
Chemical projectile signatures	SuperCam LIBS; PIXL
Isotopic projectile signatures	*terrestrial laboratory required* [a]
Shatter cones	SuperCam RMI; MastCam-Z
High-pressure (diaplectic) mineral glasses	SuperCam LIBS, Raman; PIXL; SHERLOC
High-pressure mineral phases	SuperCam LIBS, Raman; PIXL; SHERLOC
High-temperature glasses and melts	SuperCam LIBS, Raman, RMI; PIXL; SHERLOC, WATSON
Planar fractures (PFs) in quartz	*terrestrial laboratory required*
Planar deformation features (PDFs) in quartz	*terrestrial laboratory required*
Non-diagnostic indicators	**Detection method**
Circular morphology	*orbitally-derived*
Circular structural deformation	*orbitally-derived*
Circular geophysical anomalies	*orbitally-derived*
Fracturing, brecciation, and megabreccias	SuperCam RMI; MastCam-Z; orbital imaging

Kink banding in micas	*terrestrial laboratory required*
Mosaicism in crystals	*terrestrial laboratory required*
Pseudotachylite and pseudotachylitic breccias	SuperCam RMI; MastCam-Z
Igneous rocks and glasses	SuperCam LIBS, Raman, RMI; PIXL; SHERLOC
Groundmass textures of impact melt rock or melt-bearing impactites	SuperCam RMI; PIXL; WATSON
Spherules and microspherules	PIXL
Indicative clay mineral phases; see Table 6.1	SuperCam LIBS, Raman; PIXL; SHERLOC; see Table 6.1 [a]

[a] Note that isotopic analyses and XRD-derived identification of clay minerals would be possible with MSL's SAM EGA instrument suite but are not present in the Mars 2020 instrument suite.

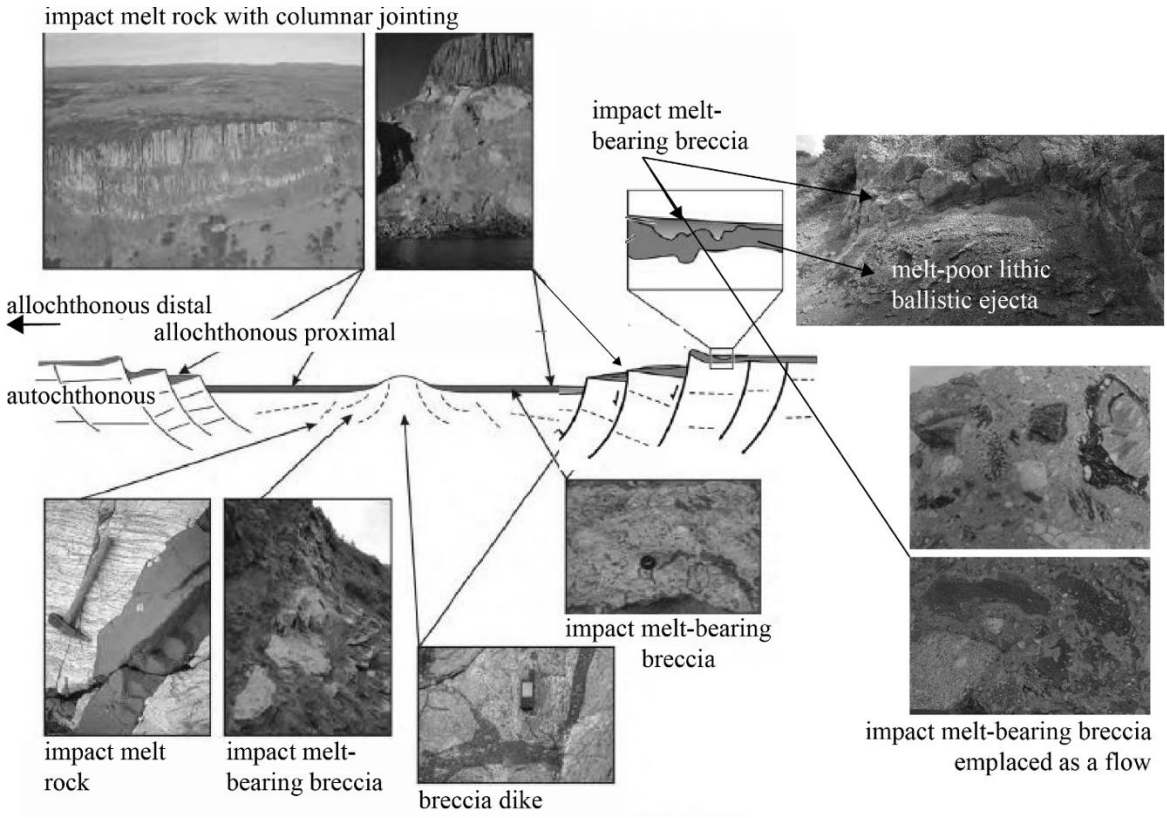

Figure 6.2. Schematic diagram of a typical complex impact structure shown with the locations and images of impactites (modified after Osinski and Grieve, 2012).

For rover-based investigations, the best apparent approach to investigate potential impactite origin may be through the assessment of the following: geologic context; outcrop-scale stratigraphic relationships and hand sample-scale textural observations; and geochemical, mineralogical, and micro-textural evidence as acquired by PIXL and SuperCam (Table 6.2). The PIXL micro-XRF will be a powerful tool to distinguish sub-mm-scale rock texture and correlate morphology to chemistry. Therefore, PIXL may be used to identify glassy and particulate groundmass with intermingling textures – evidence that the groundmass remain molten during and following deposition (Osinski et al., 2012). Indicative shock-metamorphism in minerals (e.g., diaplectic glass, kink banding in micas, mosaicism in crystals, planar deformation features, and planar fractures in minerals; Table 6.2) are typically some of the best criteria for the identification of impact-origin of materials, but their observation requires microscopy (Engelhardt and Bertsch, 1969; Stoffler and Langenhorst, 1994; Grieve et al., 1996; Morrow, 2007). Given the high erosion of the breached Jezero Crater rim and terraces, impact-related features like melt dikes (e.g., Fig. 62.) and degassing pipes (e.g., Chapter 3) may be exposed and observable by the Mars 2020 rover team. Unless shatter cones are observed, an impact-origin may be difficult to definitively identify. Indeed, without microscopic evidence, even terrestrial impact craters or materials of impact-origin have been historically, and remain, difficult to identify (French, 2004). Nevertheless, the consideration of the very likely presence of these

materials throughout the ancient Martian crust necessitates a planned approach for their identification.

6.3 Conclusions

It is suggested that the recognition of the full range of impact-related materials – and their potential superposition in mineral assemblages of varied terrains in the Noachian regions – is necessary for a complete, more accurate view of Mars' past geologic and climatic history. The opportunity to investigate impactites will likely be presented to the upcoming Mars 2020 mission. In the Mars 2020 landing ellipse and extended traverse, Fe/Mg smectites have been identified in the fluviolacustrine intra-crater deposits of Jezero Crater, and in the ejecta within breccias, megabreccia/megablocks, and as strata-bound mounds (e.g., Mustard et al., 2009); we suggest that varied and complex impact-generated clay mineral assemblages are also likely abundant. Furthermore, pre-impact clay minerals may have been excavated by the Isidis and Jezero impact events (and likely many other obscured impacts in the intervening time period). Thick sequences of strata-bound Al-phyllosilicates overlie Fe/Mg-smectites as light-toned layered deposits in the ExoMars landing site region of Oxia Planum, and Fe/Mg-smectites cover at least 80% of the landing ellipse surface area (Quantin at al., 2016); these mineral assemblages, which include amorphous hydrated silica, present in stratigraphic sequence have been dated from early – late Noachian and have been interpreted as recording a warm, wet climatic period with alkaline water, followed by an era of acid leaching. We suggest that the ExoMars rover landing site presents an incredible opportunity to investigate a regionally extensive clay-bearing member (that potentially extends to Mwarth Vallis; Vago et al., 2017) for evidence of their true origin: sedimentary (authigenic, detrital or diagenetic), authigenic impact-generated, or otherwise.

The clay mineral phases that have been observed in terrestrial impact environments (e.g., Table 6.1) could be used as a reference for consideration of impact-related provenance when interpreting clay minerals *in situ* during the Mars 2020 and ExoMars rover missions. As shown in this study, impact-excavated clay minerals or those of detrital or weathering origin may be very difficult to distinguish from those generated by impact-related processes when removed from geologic context and in the absence of laboratory techniques necessary to examine the interlayer constituents of swelling clay minerals. As discussed in Chapter 4, impact-generated clay minerals are complex and varied, as with clay minerals formed in other settings. It is important to note that reflectance spectroscopy offered little definitive differences between the detrital and impact-generated clay minerals in that study, in contrast to the detailed XRD patterns that revealed important variations in clay mineralogy, crystallinity, and interlayer structure. Due to the necessarily limited scope of a spacecraft-bound instrumentation, some fundamental clay mineral analysis techniques that provide critical information about the nature of the smectite and interlayered materials are still only possible in the terrestrial laboratory setting. As such, discerning clay mineral provenance on Mars presents an especially difficult challenge. The findings of this thesis argues for: (1) *in situ* ground-truthing of Martian clay mineralogy to confirm (largely orbital data-derived) interpretations about the surface and the past of Mars; (2) a methodological approach to discern geologic context and characterization of clay minerals that includes potential impactite origin; and (3) a strong rationale for the return of well-characterized samples to Earth for laboratory analyses.

References

Abramov, O., and Kring, D.A., 2004, Numerical modeling of an impact-induced hydrothermal

system at the Sudbury crater: Journal of Geophysical Research E: Planets, v. 109, doi:10.1029/2003JE002213.

Abramov, O., and Kring, D. a., 2007, Numerical modeling of impact-induced hydrothermal activity at the Chicxulub crater: Meteoritics & Planetary Science, v. 42, p. 93–112, doi:10.1111/j.1945-5100.2007.tb00220.x.

Allen, C.C., Gooding, J.L., and Keil, K., 1982a, Hydrothermally altered impact melt rock and breccia: Contributions to the soil of Mars: Journal of Geophysical Research, doi:10.1029/jb087ib12p10083.

Allen, C.C., Gooding, J.L., and Keil, K., 1982b, Hydrothermally altered impact melt rock and breccia: Contributions to the soil of Mars: Journal of Geophysical Research, v. 87, p. 10083–10101, doi:10.1029/JB087iB12p10083.

Allwood, A., Clark, B., Flannery, D., Hurowitz, J., Wade, L., Elam, T., Foote, M., and Knowles, E., 2015, Texture-specific elemental analysis of rocks and soils with PIXL: The Planetary Instrument for X-ray Lithochemistry on Mars 2020, *in* IEEE Aerospace Conference Proceedings, doi:10.1109/AERO.2015.7119099.

Arvidson, R.E. et al., 2008, Spirit Mars Rover Mission to the Columbia Hills, Gusev Crater: Mission overview and selected results from the Cumberland Ridge to Home Plate: Journal of Geophysical Research E: Planets, doi:10.1029/2008JE003183.

Baker, V.R., Kochel, R.C., Laity, J.E., and Howard, A.D., 1990, Spring sapping and valley network development: Special Paper of the Geological Society of America, doi:10.1130/SPE252-p235.

Beegle, L. et al., 2015, SHERLOC: Scanning habitable environments with Raman & luminescence for organics & chemicals, *in* IEEE Aerospace Conference Proceedings, v.

2015- June, doi:10.1109/AERO.2015.7119105.

Bell, J.F., Maki, J.N., Mehall, G.L., Ravine, M.A., Caplinger, M.A., and Team, M.-Z., 2016, Mastcam-Z: Designing a Geologic, Stereoscopic, and Multispectral Pair of Zoom Cameras for the Nasa Mars 2020 Rover, *in* 3rd International Workshop on Instrumentation for Planetary Missions,.

Bernardi, P., Maurice, S., McCabe, K., Caïs, P., Wiens, R.C., Robinson, S., Perez, R., Parès, L.P., Newell, R., and Réess, J.-M., 2017, The supercam instrument on the NASA Mars 2020 mission: optical design and performance, doi:10.1117/12.2296230.

Bibring, J.-P. et al., 2006, Global Mineralogical and Aqueous Mars History Derived from OMEGA/Mars Express Data: Science, v. 312, p. 400–404, doi:10.1126/science.1122659.

Bishop, J.L., Fairén, A.G., Michalski, J.R., Gago-Duport, L., Baker, L.L., Velbel, M.A., Gross, C., and Rampe, E.B., 2018, Surface clay mineral formation during short-term warmer and wetter conditions on a largely cold ancient Mars: Nature Astronomy, doi:10.1038/s41550-017-0377-9.

Bishop, J.L., Lane, M.D., Dyar, M.D., and Brown, A.J., 2008, Reflectance and emission spectroscopy study of four groups of phyllosilicates: smectites, kaolinite-serpentines, chlorites and micas: Clay minerals, doi:10.1180/claymin.2008.043.1.03.

Bishop, J.L., Michalski, J.R., and Carter, J., 2017, Infrared and Raman Spectroscopies of Clay minerals, *in* Gates, W.P., Kloprogge, J.T., Madejová, J., and Bergaya, F. eds., Developments in Clay mineral Science, Developments in Clay mineral Science, p. 482–591.

Bishop, J.L., and Murad, E., 2004, Characterization of minerals and biogeochemical markers on Mars: A Raman and IR spectroscopic study of montmorillonite: Journal of Raman Spectroscopy, doi:10.1002/jrs.1173.

Bishop, J.L., and Murad, E., 2005, The visible and infrared spectral properties of jarosite and alunite: American Mineralogist, doi:10.2138/am.2005.1700.

Bishop, J.L., and Rampe, E.B., 2016, Evidence for a changing Martian climate from the mineralogy at Mawrth Vallis: Earth and Planetary Science Letters, doi:10.1016/j.epsl.2016.04.031.

Blake, D. et al., 2012, Characterization and calibration of the CheMin mineralogical instrument on Mars Science Laboratory: Space Science Reviews, doi:10.1007/s11214-012-9905-1.

Bragg, W.H., 1914, XCVII. The intensity of reflexion of X rays by crystals : The London, Edinburgh, and Dublin Philosophical Magazine and Journal of Science, doi:10.1080/14786440508635159.

Bramble, M.S., Mustard, J.F., and Salvatore, M.R., 2017, The geological history of Northeast Syrtis Major, Mars: Icarus, doi:10.1016/j.icarus.2017.03.030.

Brindley, G.W. and Brown, G., 1980, X-Ray Diffraction Procedures for Clay mineral Identification: Mineralogical Society, p. 305–356.

Bristow, T.F. et al., 2018, Clay mineral diversity and abundance in sedimentary rocks of Gale crater, Mars: Science Advances, doi:10.1126/sciadv.aar3330.

Brown, G., Brindley, G.W., 1980, Crystal structures of clay minerals and their Xray identification: Journal of Mineralogical Society, p. 305- 356., doi:10.1016/j.jenvman.2011.05.031.

Carter, J., Loizeau, D., Mangold, N., Poulet, F., and Bibring, J.P., 2015, Widespread surface weathering on early Mars: A case for a warmer and wetter climate: Icarus, doi:10.1016/j.icarus.2014.11.011.

Cassanelli, J.P., and Head, J.W., 2019, Assessing the formation of valley networks on a cold

early Mars: Predictions for erosion rates and channel morphology: Icarus, doi:10.1016/j.icarus.2018.11.020.

Clark, B.C. et al., 2007a, Evidence for montmorillonite or its compositional equivalent in Columbia Hills, Mars: Journal of Geophysical Research E: Planets, doi:10.1029/2006JE002756.

Clark, R.N., King, T.V. V., Klejwa, M., Swayze, G. a., and Vergo, N., 1990, High spectral resolution reflectance spectroscopy of minerals: Journal of Geophysical Research, v. 95, p. 12653, doi:10.1029/JB095iB08p12653.

Clark, R.N., Swayze, G.A., Wise, R., Livo, K.E., Hoefen, T.M., Kokaly, R.F., Sutley, S.J., Survey, U.S.G., and Title, S., 2007b, USGS Digital Spectral Library splib06a: U.S. Geological Survey, p. Digital Data Series 231.

Craddock, R.A., and Howard, A.D., 2002, The case for rainfall on a warm, wet early Mars: Journal of Geophysical Research: Planets, v. 107, p. 5111, doi:10.1029/2001JE001505.

Dietz, R.S., 1960, Meteorite impact suggested by shatter cones in rock: Science, doi:10.1126/science.131.3416.1781.

Drewes, H., 1963, Geology of the Funeral Peak Quadrangle, California, on the east flank of Death Valley: Geological Survey professional paper, p. 1–75.

Ehlmann, B.L. et al., 2009a, Identification of hydrated silicate minerals on Mars using MRO-CRISM: Geologic context near Nili Fossae and implications for aqueous alteration: Journal of Geophysical Research E: Planets, v. 114, doi:10.1029/2009JE003339.

Ehlmann, B.L. et al., 2009b, Identification of hydrated silicate minerals on Mars using MRO-CRISM: Geologic context near Nili Fossae and implications for aqueous alteration: Journal of Geophysical Research, v. 114.

Ehlmann, B.L. et al., 2008a, Orbital identification of carbonate-bearing rocks on Mars: Science, doi:10.1126/science.1164759.

Ehlmann, B.L., Berger, G., Mangold, N., Michalski, J.R., Catling, D.C., Ruff, S.W., Chassefière, E., Niles, P.B., Chevrier, V., and Poulet, F., 2013, Geochemical consequences of widespread clay mineral formation in Mars' ancient crust: Space Science Reviews, v. 174, p. 329–364, doi:10.1007/s11214-012-9930-0.

Ehlmann, B.L., and Edwards, C.S., 2014, Mineralogy of the Martian Surface: Annual Review of Earth and Planetary Sciences, v. 42.

Ehlmann, B.L., Mustard, J.F., Fassett, C.I., Schon, S.C., Head III, J.W., Des Marais, D.J., Grant, J. a., and Murchie, S.L., 2008b, Clay minerals in delta deposits and organic preservation potential on Mars: Nature Geoscience, v. 1, p. 355–358, doi:10.1038/ngeo207.

Ehlmann, B.L., Mustard, J.F., Murchie, S.L., Bibring, J.P., Meunier, A., Fraeman, A.A., and Langevin, Y., 2011a, Subsurface water and clay mineral formation during the early history of Mars: Nature, doi:10.1038/nature10582.

Ehlmann, B.L., Mustard, J.F., Murchie, S.L., Bibring, J.-P., Meunier, A., Fraeman, A. a., and Langevin, Y., 2011b, Subsurface water and clay mineral formation during the early history of Mars: Nature, v. 479, p. 53–60, doi:10.1038/nature10582.

Engelhardt, W. v., and Bertsch, W., 1969, Shock induced planar deformation structures in quartz from the Ries crater, Germany: Contributions to Mineralogy and Petrology, v. 20, p. 203–234, doi:10.1007/BF00377477.

Farley, K., Stack Morgan, K., and Williford, K., 2018, Jezero-Midway interellipse traverse mission concept.:

Fastook, J.L., and Head, J.W., 2015, Glaciation in the Late Noachian Icy Highlands: Ice

accumulation, distribution, flow rates, basal melting, and top-down melting rates and patterns: Planetary and Space Science, doi:10.1016/j.pss.2014.11.028.

Fedo, C. et al., 2017, Facies analysis and basin architecture of the upper part of the Murray formation, Gale crater, Mars, *in* 48th Lunar and Planetary Science Conference, Woodlands, TX, p. abstract 1689.

Ferriere, L., and Osinski, G.R., 2012, Shock metamorphism, *in* Pierazzo, G.R.O. and E. ed., Impact Cratering: Processes and Products, Blackwell Publishing, p. 105–124.

Floran, R.J., Grieve, R.A.F., and Phinney, W.C., 1978, Manicouagan impact melt, Quebec; 1, stratigraphy, petrology and chemistry: Journal of Geophysical Research, v. 83, p. 2737–2759.

Forget, F., Wordsworth, R., Millour, E., Madeleine, J.B., Kerber, L., Leconte, J., Marcq, E., and Haberle, R.M., 2013, 3D modelling of the early martian climate under a denser CO 2 atmosphere: Temperatures and CO 2 ice clouds: Icarus, doi:10.1016/j.icarus.2012.10.019.

Francis, R., Cross, M.D.G., Kerrigan, M.C., and Osinski, G.R., 2016, Exploration and Decision-Making Rules and Resources on the 2015 CanMars MSR Analogue Mission: An Analogue for Mars 2020 Rover Operations: 47th Lunar and Planetary Science Conference, p. Abstract #2735, doi:10.1038/ngeo2474.

French, B.M., 2004, The importance of being cratered: The new role of meteorite impact as a normal geological process: Meteoritics and Planetary Science, doi:10.1111/j.1945-5100.2004.tb00335.x.

French, B.M., and Koeberl, C., 2010, The convincing identification of terrestrial meteorite impact structures: What works, what doesn't, and why: Earth-Science Reviews, v. 98, p. 123–170, doi:10.1016/j.earscirev.2009.10.009.

Fritz, J., and Greshake, A., 2009, High-pressure phases in an ultramafic rock from Mars: Earth and Planetary Science Letters, doi:10.1016/j.epsl.2009.10.030.

Georgiadis, A., Dietel, J., Dohrmann, R., and Rennert, T., 2019, What are the nature and formation conditions of hydroxy-interlayered minerals (HIMs) in soil? J. Plant Nutr. Soil Science, v. 000, p. 1–15, doi:10.1002/jpln.201900283.

Goderis, S., Paquay, F., and Claeys, P., 2012, Projectile Identification in Terrestrial Impact Structures and Ejecta Material, *in* Impact Cratering: Processes and Products, doi:10.1002/9781118447307.ch15.

Goudge, T.A., Milliken, R.E., Head, J.W., Mustard, J.F., and Fassett, C.I., 2017, Sedimentological evidence for a deltaic origin of the western fan deposit in Jezero crater, Mars and implications for future exploration: Earth and Planetary Science Letters, doi:10.1016/j.epsl.2016.10.056.

Goudge, T.A., Mohrig, D., Cardenas, B.T., Hughes, C.M., and Fassett, C.I., 2018, Stratigraphy and paleohydrology of delta channel deposits, Jezero crater, Mars: Icarus, v. 301, p. 58–75, doi:10.1016/j.icarus.2017.09.034.

Goudge, T.A., Mustard, J.F., Head, J.W., Fassett, C.I., and Wiseman, S.M., 2015, Assessing the mineralogy of the watershed and fan deposits of the Jezero crater paleolake system, Mars: Journal of Geophysical Research: Planets, doi:10.1002/2014JE004782.

Gough, D.O., 1981, Solar interior structure and luminosity variations: Solar Physics, doi:10.1007/BF00151270.

Grau Galofre, A., 2018, Insights on the origin and evolution of the Martian valley networks from erosion models: Reconciling climate modeling and geomorphological observations: The University of British Columbia.

Grieve, R.A.., 1993, Impact craters: Lessons from and for the Earth: Vistas in astronmony, v. 36, p. 203–230.

Grieve, R.A.F., 1975, Petrology and chemistry of the impact melt at Mistastin Lake crater, Labrador: Bulletin of the Geological Society of America, v. 86, p. 1617–1629, doi:10.1130/0016-7606(1975)86<1617:PACOTI>2.0.CO;2.

Grieve, R.A.F., 1987, Terrestrial impact structures.: Annual review of earth and planetary sciences. Vol. 15, doi:10.18814/epiiugs/1987/v10i2/001.

Grieve, R.A.F., Langenhorst, F., and Stöffler, D., 1996, Shock metamorphism of quartz in nature and experiment: II. Significance in geoscience: Meteoritics and Planetary Science, doi:10.1111/j.1945-5100.1996.tb02049.x.

Grieve, R.A.F., and Therriault, A.M., 2012a, Impactites: their characteristics and spatial distribution, *in* Pierazzo, G.R.O. and E. ed., Impact Cratering: Processes and Products, Blackwell Publishing, p. 90–105.

Grieve, R.A.F., and Therriault, A.M., 2012b, Impactites: Their Characteristics and Spatial Distribution, *in* Impact Cratering: Processes and Products, doi:10.1002/9781118447307.ch7.

Grotzinger, J.P. et al., 2012, Mars Science Laboratory mission and science investigation: Space Science Reviews, v. 170, p. 5–56, doi:10.1007/s11214-012-9892-2.

Gwizd, S., Fedo, C., Grotzinger, J., Edgett, K., Rivera-Hernandez, F., and Stein, N., 2018, Depositional history of the Hartmann's Valley member, Murray formation, Gale crater, Mars, *in* 48th Lunar and Planetary Science Conference, Woodlands, TX, p. abstract 2150.

Hagerty, Justin J.; Newsom, H.E., 2003, Hydrothermal alteration at the Lonar Lake impact structure, India: Implications for impact cratering on Mars: Meteoritics & Planetary

Science, v. Volume 38, p. 327–478, doi:10.1111/j.1945-5100.2003.tb00272.x.

Hagerty, J.J., and Newsom, H.E., 2003, Hydrothermal alteration at the Lonar Lake impact structure, India: Implications for impact cratering on Mars: Meteoritics and Planetary Science, doi:10.1111/j.1945-5100.2003.tb00272.x.

Hazen, R.M., Sverjensky, D.A., Azzolini, D., Bish, D.L., Elmore, S.C., Hinnov, L., and Milliken, R.E., 2013, Clay mineral evolution: American Mineralogist, v. 98, p. 2007–2029, doi:10.2138/am.2013.4425.

Head, J.W., and Marchant, D.R., 2014, The climate history of early Mars: Insights from the Antarctic McMurdo Dry Valleys hydrologic system: Antarctic Science, doi:10.1017/S0954102014000686.

Hildreth, W., and Fierstein, J., 2012, The Novarupta-Katmai Eruption of 1912 — Largest Eruption of the Twentieth Century: Centennial Perspectives: US Geological Survey Professional Paper, p. 259.

Hynek, B., 2016, The great climate paradox of ancient Mars: Geology, doi:10.1130/focus102016.1.

Keil, K., Stoffler, D., Love, S.G., and Scott, E.R.D., 1997, Constraints on the role of impact heating and melting in asteroids: Meteoritics and Planetary Science, doi:10.1111/j.1945-5100.1997.tb01278.x.

Klingelhöfer, G. et al., 2003, Athena MIMOS II Mössbauer spectrometer investigation: Journal of Geophysical Research E: Planets, doi:10.1029/2003je002138.

Koeberl, C., 1998, Identification of meteoritic components in impactites: Geological Society Special Publication, doi:10.1144/GSL.SP.1998.140.01.11.

Koeberl, C., Shukolyukov, A., and Lugmair, G.W., 2007, Chromium isotopic studies of

terrestrial impact craters: Identification of meteoritic components at Bosumtwi, Clearwater East, Lappajärvi, and Rochechouart: Earth and Planetary Science Letters, doi:10.1016/j.epsl.2007.02.008.

Laskar, J., Correia, A.C.M., Gastineau, M., Joutel, F., Levrard, B., and Robutel, P., 2004, Long term evolution and chaotic diffusion of the insolation quantities of Mars: Icarus, v. 170, p. 343–364, doi:10.1016/j.icarus.2004.04.005.

Loizeau, D., Carter, J., Bouley, S., Mangold, N., Poulet, F., Bibring, J.P., Costard, F., Langevin, Y., Gondet, B., and Murchie, S.L., 2012, Characterization of hydrated silicate-bearing outcrops in Tyrrhena Terra, Mars: Implications to the alteration history of Mars: Icarus, doi:10.1016/j.icarus.2012.03.017.

Marion, C.L., and Sylvester, P.J., 2010, Composition and heterogeneity of anorthositic impact melt at Mistastin Lake crater, Labrador: Planetary and Space Science, doi:10.1016/j.pss.2009.09.018.

Marshall, R.R., 1961, Devitrification of natural glass: Bulletin of the Geological Society of America, doi:10.1130/0016-7606(1961)72[1493:DONG]2.0.CO;2.

Michalski, J.R., Cuadros, J., Bishop, J.L., Darby Dyar, M., Dekov, V., and Fiore, S., 2015, Constraints on the crystal-chemistry of Fe/Mg-rich smectitic clay minerals on Mars and links to global alteration trends: Earth and Planetary Science Letters, v. 427, p. 215–225, doi:10.1016/j.epsl.2015.06.020.

Michalski, J.R., and Dobrea, E.Z.N., 2007, Evidence for a sedimentary origin of a clay minerals in the Mawrth Vallis region, Mars: Geology, doi:10.1130/G23854A.1.

Ming, D.W. et al., 2008, Geochemical properties of rocks and soils in Gusev Crater, Mars: Results of the Alpha Particle X-Ray Spectrometer from Cumberland Ridge to Home Plate:

Journal of Geophysical Research E: Planets, doi:10.1029/2008JE003195.

Morrow, J.R., 2007, Shock-metamorphic petrography and microRaman spectroscopy of quartz in upper impactite interval, ICDP drill core LB-07A, Bosumtwi impact crater, Ghana: Meteoritics and Planetary Science, doi:10.1111/j.1945-5100.2007.tb01063.x.

Mustard, J.F., Ehlmann, B.L., Murchie, S.L., Poulet, F., Mangold, N., Head, J.W., Bibring, J.P., and Roach, L.H., 2009, Composition, morphology, and stratigraphy of Noachian crust around the Isidis basin: Journal of Geophysical Research E: Planets, doi:10.1029/2009JE003349.

Mustard, J.F., Poulet, F., Head, J.W., Mangold, N., Bibring, J.P., Pelkey, S.M., Fassett, C.I., Langevin, Y., and Neukum, G., 2007, Mineralogy of the Nili Fossae region with OMEGA/Mars Express data: 1. Ancient impact melt in the Isidis Basin and implications for the transition from the Noachian to Hesperian: Journal of Geophysical Research E: Planets, v. 112, doi:10.1029/2006JE002834.

Naumov, M. V., 2002, Impact-Generated Hydrothermal Systems: Data from Popigai, Kara, and Puchezh-Katunki Impact Structures, doi:10.1007/978-3-662-05010-1_6.

Naumov, M. V., 2005, Principal features of impact-generated hydrothermal circulation systems: Mineralogical and geochemical evidence: Geofluids, v. 5, p. 165–184, doi:10.1111/j.1468-8123.2005.00092.x.

Newsom, H.E., 1980, Hydrothermal alteration of impact melt sheets with implications for Mars: Icarus, v. 44, p. 207–216, doi:10.1016/0019-1035(80)90066-4.

Newsom, H., Graup, G., Sewards, T., and Keil, K., 1986, Fluidization and hydrothermal alteration of the Suevite deposit at the Ries Crater, West Germany, and implications for Mars: Journal of Geophysical Research, v. 91, p. E239–E251,

doi:http://dx.doi.org/10.1029/JB091iB13p0E239.

Ohtani, E., Kimura, Y., Kimura, M., Takata, T., Kondo, T., and Kubo, T., 2004, Formation of high-pressure minerals in shocked L6 chondrite Yamato 791384: Constraints on shock conditions and parent body size: Earth and Planetary Science Letters, doi:10.1016/j.epsl.2004.08.018.

Osinski, G.R., 2006, Effect of volatiles and target lithology on the generation and emplacement of impact crater fill and ejecta deposits on Mars: Meteoritics & Planetary Science, v. 41, p. 1571–1586, doi:10.1111/j.1945-5100.2006.tb00436.x.

Osinski, G.R., 2005, Hydrothermal activity associated with the Ries impact event, Germany: Geofluids, v. 5.

Osinski, G.R. et al., 2019, The CanMars Mars Sample Return analogue mission: Planetary and Space Science, doi:10.1016/j.pss.2018.07.011.

Osinski, G.R., and Ferrière, L., 2016, Shatter cones: (Mis)understood? Science Advances, doi:10.1126/sciadv.1600616.

Osinski, G.R., and Grieve, R.A.F., 2012, Comparison of Mid-Size Terrestrial Complex Impact Structures: A Case Study, *in* Impact Cratering: Processes and Products, p. 290–305, doi:10.1002/9781118447307.ch19.

Osinski, G.R., Grieve, R.A.F., Bleacher, J.E., Neish, C.D., Pilles, E.A., and Tornabene, L.L., 2018, Igneous rocks formed by hypervelocity impact: Journal of Volcanology and Geothermal Research, v. 353, p. 25–54, doi:10.1016/j.jvolgeores.2018.01.015.

Osinski, G.R., Grieve, R.A.F., Marion, C., and Chanou, A., 2012, Impact Melting, *in* Impact Cratering: Processes and Products, p. 125–145, doi:10.1002/9781118447307.ch9.

Osinski, G.R., Grieve, R. a. F., and Spray, J.G., 2004, The nature of the groundmass of surficial

suevite from the Ries impact structure, Germany, and constraints on its origin: Meteoritics & Planetary Science, v. 39, p. 1655–1683, doi:10.1111/j.1945-5100.2004.tb00065.x.

Osinski, G.R., Tornabene, L.L., and Grieve, R.A.F., 2011, Impact ejecta emplacement on terrestrial planets: Earth and Planetary Science Letters, v. 310.

Palme, H., 1982, Identification of projectiles of large terrestrial impact craters and some implications for the interpretation of Ir-rich Cretaceous/Tertiary boundary layers: Special Paper of the Geological Society of America, doi:10.1130/SPE190-p223.

Palme, H., Gobel, E., and Grieve, R.A.F., 1979, The distribution of volatile and siderophile elements in the impact melt of East Clearwater, *in* Proceedings of Lunar and Planetary Science Conference, p. 2465–2492.

Palme, H., Janssens, M.J., Takahashi, H., Anders, E., and Hertogen, J., 1978, Meteoritic material at five large impact craters: Geochimica et Cosmochimica Acta, doi:10.1016/0016-7037(78)90184-9.

Palumbo, A.M., and Head, J.W., 2018, Early Mars Climate History: Characterizing a "Warm and Wet" Martian Climate With a 3-D Global Climate Model and Testing Geological Predictions: Geophysical Research Letters, doi:10.1029/2018GL079767.

Pascuzzo, A.C., Mustard, J.F., Kremer, C.H., and Ebinger, E., 2019, The formation of irregular polygonal ridge networks, Nili Fossae, Mars: Implications for extensive subsurface channelized fluid flow in the Noachian: Icarus, doi:10.1016/j.icarus.2018.10.020.

Quantin-Nataf, C., Carter, J., Mandon, L., Balme, M., Fawdon, P., Davis, J., Thollot, P., Dehouck, E., Pan, L., Volat, M., Millot, C., Breton, S., Loizeau, D., and Vago, J.L., 2019, ExoMars at Oxia Planum, Probing the aqueous-related Noachian environments, in Ninth

International Conference on Mars 2019, p. 2089.

Quinn, D.P., and Ehlmann, B.L., 2019, The Deposition and Alteration History of the Northeast Syrtis Major Layered Sulfates: Journal of Geophysical Research: Planets, doi:10.1029/2018JE005706.

Ramirez, R.M., and Craddock, R.A., 2018, The geological and climatological case for a warmer and wetter early Mars: Nature Geoscience, doi:10.1038/s41561-018-0093-9.

Rieder, R., Gellert, R., Brückner, J., Klingelhöfer, G., Dreibus, G., Yen, A., and Squyres, S.W., 2003, The new Athena alpha particle X-ray spectrometer for the Mars Exploration Rovers: Journal of Geophysical Research E: Planets, doi:10.1029/2003je002150.

Saper, L., and Mustard, J.F., 2013, Extensive linear ridge networks in Nili Fossae and Nilosyrtis, Mars: implications for fluid flow in the ancient crust: INVERTED LINEAR RIDGE NETWORKS ON MARS: Geophysical Research Letters, v. 40.

Sapers, H.M., Osinski, G.R., Flemming, R.L., Buitenhuis, E., Banerjee, N.R., Tornabene, L.L., Blain, S., and Hainge, J., 2017, Evidence for a spatially extensive hydrothermal system at the Ries impact structure, Germany: Meteoritics and Planetary Science, v. 52, doi:10.1111/maps.12796.

Schultz, P.H., and Mustard, J.F., 2004, Impact melts and glasses on Mars: Journal of Geophysical Research, v. 109, p. E01001, doi:10.1029/2002JE002025.

Schwenzer, S.P., and Kring, D.A., 2013, Alteration minerals in impact-generated hydrothermal systems - Exploring host rock variability: Icarus, doi:10.1016/j.icarus.2013.06.003.

Silverman, S., Peralta, R., Christensen, P., and Mehall, G., 2003, Miniature Thermal Emission Spectrometer for the Mars Exploration Rover, *in* European Space Agency, (Special Publication) ESA SP, doi:10.1117/12.511577.

Simpson, S.L., Osinski, G.R., Longstaffe, F.J., Kring, D.A., Schmieder, M., Svensson, M., and Gulick, S.P.S., 2018, Characterization of impact glass alteration and associated secondary clay mineralogy through the upper Chicxulub peak ring, *in* 49th Lunar and Planetary Science Conference, p. 2083.

Squyres, S.W. et al., 2006, Overview of the Opportunity Mars Exploration Rover Mission to Meridiani Planum: Eagle Crater to Purgatory Ripple: Journal of Geophysical Research E: Planets, v. 111, doi:10.1029/2006JE002771.

Stähle, V., Altherr, R., Koch, M., and Nasdala, L., 2008, Shock-induced growth and metastability of stishovite and coesite in lithic clasts from suevite of the Ries impact crater (Germany): Contributions to Mineralogy and Petrology, doi:10.1007/s00410-007-0252-2.

Stein, N. et al., 2017, Candidate Desiccation Cracks in the Upper Murray Formation, Gale Crater, Mars: 48th Lunar and Planetary Science Conference,.

Stepinski, T.F., and Coradetti, S., 2004, Comparing morphologies of drainage basins on Mars and Earth using integral-geometry and neural maps: Geophysical Research Letters, doi:10.1029/2004GL020359.

Stöffler, D., 1971, Coesite and stishovite in shocked crystalline rocks: Journal of Geophysical Research, doi:10.1029/jb076i023p05474.

Stoffler, D., and Langenhorst, F., 1994, Shock metamorphism of quartz in nature and experiment: I. Basic observation and theory: Meteoritics, doi:10.1111/j.1945-5100.1994.tb00670.x.

Sun, V.Z., and Milliken, R.E., 2015, Ancient and recent clay mineral formation on Mars as revealed from a global survey of hydrous minerals in crater central peaks: Journal of Geophysical Research E: Planets, v. 120, p. 2293–2332, doi:10.1002/2015JE004918.

Tornabene, L.L., Osinski, G.R., McEwen, A.S., Wray, J.J., Craig, M.A., Sapers, H.M., and Christensen, P.R., 2013a, An impact origin for hydrated silicates on Mars: A synthesis: Journal of Geophysical Research E: Planets, v. 118, p. 994–1012, doi:10.1002/jgre.20082.

Tornabene, L.L., Osinski, G.R., McEwen, A.S., Wray, J.J., Craig, M.A., Sapers, H.M., and Christensen, P.R., 2013b, An impact origin for hydrated silicates on Mars: A synthesis: Journal of Geophysical Research E: Planets, v. 118, doi:10.1002/jgre.20082.

Vago, J.L., Westall, F., Pasteur Instrument Teams, Landing S, Coates, A.J., Jaumann, R., Korablev, O., Ciarletti, V., Mitrofanov, I., Josset, J.-L., De Sanctis, M.C., Bibring, J.-P., Rull, F., Goesmann, F., Steininger, H., Goetz, W., Brinckerhoff, W., Szopa, C., Raulin, F., Westall, F., Edwards, H.G.M., Whyte, L.G., Fairén, A.G., Bibring, J.-P., Bridges, J., Hauber, E., Ori, G.G., Werner, S., Loizeau, D., Kuzmin, R.O., Williams, R.M.E., Flahaut, J., Forget, F., Vago, J.L., Rodionov, D., Korablev, O., Svedhem, H., Sefton-Nash, E., Kminek, G., Lorenzoni, L., Joudrier, L., Mikhailov, V., Zashchirinskiy, A., Alexashkin, S., Calantropio, F., Merlo, A., Poulakis, P., Witasse, O., Bayle, O., Bayón, S., Meierhenrich, U., Carter, J., García-Ruiz, J.M., Baglioni, P., Haldemann, A., Ball, A.J., Debus, A., Lindner, R., Haessig, F., Monteiro, D., Trautner, R., Voland, C., Rebeyre, P., Goulty, D., Didot, F., Durrant, S., Zekri, E., Koschny, D., Toni, A., Visentin, G., Zwick, M., van Winnendael, M., Azkarate, M., Carreau, C., the ExoMars Project Team, 2017. Habitability on Early Mars and the Search for Biosignatures with the ExoMars Rover. Astrobiology 17, 471–510. doi:10.1089/ast.2016.1533

Wiens, R.C., Maurice, S., and Perez, F.R., 2017, The SuperCam remote sensing instrument suite for the Mars 2020 rover: a preview: Spectroscopy, v. 32, p. 50.

Williford, K.H. et al., 2018, The NASA Mars 2020 Rover Mission and the Search for

Extraterrestrial Life, *in* From Habitability to Life on Mars, doi:10.1016/b978-0-12-809935-3.00010-4.

Wolf, R., Woodrow, A.B., and Grieve, R.A.F., 1980, Meteoritic material at four Canadian impact craters: Geochimica et Cosmochimica Acta, doi:10.1016/0016-7037(80)90289-6.

Wordsworth, R.D., 2016, The Climate of Early Mars: Annual Review of Earth and Planetary Sciences, doi:10.1146/annurev-earth-060115-012355.

Wordsworth, R., Forget, F., Millour, E., Head, J.W., Madeleine, J.B., and Charnay, B., 2013, Global modelling of the early martian climate under a denser CO 2 atmosphere: Water cycle and ice evolution: Icarus, doi:10.1016/j.icarus.2012.09.036.

Wordsworth, R.D., Kerber, L., Pierrehumbert, R.T., Forget, F., and Head, J.W., 2015, Comparison of "warm and wet" and "cold and icy" scenarios for early Mars in a 3-D climate model: Journal of Geophysical Research E: Planets, doi:10.1002/2015JE004787.

Wray, J.J., Ehlmann, B.L., Squyres, S.W., Mustard, J.F., and Kirk, R.L., 2008, Compositional stratigraphy of clay-bearing layered deposits at Mawrth Vallis, Mars: Geophysical Research Letters, doi:10.1029/2008GL034385.

Appendices

A.1 Field Description: Ries impact structure, degassing pipes

The degassing pipes observed in surficial quarry exposures and drill cores (for locations, see Fig. 3.2a) are vertically-oriented (Fig. 3.3), cm-diameter features with clast-supported and void-space interiors. The clast-rich, fines-poor interiors are lined with fine-grained material that coats the pipe walls and entrained clasts (Figs. 3.2b–c). Entrained clasts with alteration rims include glass clasts at varying levels of alteration and shocked lithic clasts. At Aumühle quarry, alteration emanates from the Bunte Breccia/melt-bearing breccia contact, constricting into cm-wide "proto-pipes" through the melt-bearing breccias. The proto-pipes have vertically-oriented alteration but lack an interior cavity or entrained clasts, and eventually forming degassing pipes as the flow travels vertically (Figs. 3.3a–b). Large (cm–dm-wide), variably altered glass clasts, having mm-wide alteration rims, are bisected by both proto-pipes (Fig. 3.3c) and degassing pipes. At Aumühle, cm to dm-wide alteration halos are present (Fig. 3.3d). Common degassing pipe alteration varies from brown – dark brown, pale and dark green, yellow, or orange (e.g., Figs. 3.2b–c). A degassing pipe was observed in the Wörnitzoshtheim core at 27.5 m depth (~12 m below the lacustrine/melt-bearing breccia contact and ~100 m above the melt-bearing breccia/Bunte Breccia contact). In the Nördlingen 1973 drill core, the observed degassing pipe (at 332 – 336 m depth; ~10 m below the top of the suevite unit) is lined by a white alteration (Fig. 3.4). This white alteration is botryoidal, and a bladed form is also present, infilling veins and capping the botryoidal forms. Table A.1 describes all locations of study and degassing pipes with detailed descriptions.

A.2 Spectral parameters and processing imaging spectrometry

Correction of imaging spectroscopy measurements of outcrops to reflectance included a dark current subtraction and flat field correction followed by a dark object subtraction (e.g., shadowed areas) to remove atmospheric scattering and correction to an in-scene Spectralon reference panel (Greenberger et al., 2016). Laboratory data of samples were calibrated to reflectance line-by-line using a dark current subtraction and image of a Spectralon panel covering the same portion of the field of view as the sample, correcting for the reflectance properties of Spectralon, to remove both instrumental effects and differences in lighting across the field of view. Band depth parameters were computed to create image maps of particular mineral compositions (e.g., Clark and Roush (1984), Pelkey et al. (2007), and Greenberger et al. (2016)). The formulas for the band depth parameters shown in the provided spectral maps are provided in Table A.2 with center wavelength and continuum points. For the presented spectral maps, interactive stretching was applied to set parameters to 0–8% maximum band depths. Spectra were then examined pixel-by-pixel to confirm parameter detections.

Table A.1

Field locations and descriptions of degassing pipes (DP).

Quarries; DP present	Location	Depth	Glass clasts	Density of DP (per m)	Description
Aumühle	3 km inside northeastern crater rim	surface	vesicular, glassy +/- clayey	1 - 5	Within melt-bearing ejecta deposits, inside the crater rim. Alteration pathways are apparent at the contact with BB, where Fe-rich alteration flow into "proto-pipes" to form DP. Glass clasts are also a source of cations, contributing to the degassing pipes and associated alteration as entrained/encountered by DP. Tens of cms-wide, dark brown - red-brown alteration halos present. DP alteration is dark brown - red-brown - yellow-orange - yellow-green in color.
Otting	3.5 km outside of the eastern crater rim	surface	vesicular, glassy +/- clayey	0 - 5	Within melt-bearing ejecta deposits, outside of the crater rim. Outcrops are variably degraded and covered with plant overgrowth; slight variation in color (brown - orange) surrounds some DP as alteration halos. DP alteration is dark brown - yellow-orange - yellow in color.
Altenbürg (south wall)	0.5 km inside the southwestern crater rim	surface	vesicular, glassy +/- clayey	1 - 2	Within melt-bearing ejecta deposits, inside the crater rim. Outcrops are variably degraded and covered with plant overgrowth; alteration halos are not apparent. DP alteration is dark brown - orange-yellow in color.
Drill cores; DP present					
Otting	3.5 km outside of the eastern crater rim	0 – 10 m	vesicular, glassy +/- clayey	unknown	Within melt-bearing ejecta deposits, outside of the crater rim. DP are found from the top of the core to the contact with BB (0 -10 m). Pervasive light-olive green and yellow alteration near the contact with BB.

Nördlingen 1973	2.8 km west of crater center, inside the inner ring	332 – 336 m	vesicular, glassy +/- clayey	unknown	Core is within the crater fill deposits, sampling ~300 m of lacustrine sediments and the high-temperature suevites. DP was observed at 332 – 336 m, ~ 30 m below the lacustrine contact. (BB is not present in the crater fill sequence.) Fe-alteration (brown - red-brown - orange-red) is restricted to localized glass clast alteration. DP alteration is (nearly pure) white in color.
Wörnitzostheim	5 km inside the southeastern crater rim	27.4 – 27.7 m	vesicular, glassy +/- clayey	unknown	Core is within melt-bearing ejecta deposits, inside the crater rim, sampling ~81 m of the melt-bearing breccia (which was overlain by ~20 m of lacustrine sediments). DP was observed at 27.4 – 27.7 m, below the lacustrine contact. (BB is present underlying the melt-bearing breccia but was not sampled by the ~100 m depth core.) DP alteration is brown - light-olive green and yellow in color.
Quarries; DP not present					
Selbronne	6 km outside of the southwestern crater rim	surface	clayey +/- vesicular, glassy		
Altenbürg (northwest wall)	0.5 km inside the southwestern crater rim	surface	clayey		
Unterwilfigen	2 km outside of the western crater rim	surface	clayey		

Notes: Abbreviations are as follows: DP = degassing pipes; MBB = melt-bearing breccia; BB = Bunte Breccia.

Table A.2

Band depth (BD) parameters used for the study in Chapter 3; see Figure 3.5. See Bishop et al. (2017) for references for absorption features indicative of M-OH bonds and mineralogy. R = reflectance at that wavelength. The continua were calculated as a linear regression using given end points; a mean of 3 bands were used for the center wavelength and median of 3 bands were used for each continuum point.

Parameter	Formula	Notes
BD2340	1-R2.34/Continuum (2.286 to 2.352)	C-O combination in carbonates; wavelengths optimized for calcite
BD2300	1-R2.30/Continuum (2.16 to 2.34)	Fe/Mg-OH combination bands; e.g. Fe/Mg clay minerals
BD2210	1-R2.20/Continuum (2.13 to 2.27)	Al-OH, Al/Fe-OH, Al/Mg-OH stretching modes, or Si-OH; e.g., Al-clay minerals or hydrated silica

Curriculum Vitae

Education

- Master of Geoscience (MSc), August 2015
  University of Arizona, Tucson, Arizona, US
- Bachelor of Geoscience (BSc), December 2011
  University of Arizona, Tucson, Arizona, US
- GIS Spatial Analyst Software Program, May 2007
  Asheville-Buncombe Technical College, Asheville, North Carolina

Awards and Recognition

- NSERC Vanier Canada Graduate Scholar; $150,000 Scholarship (2017)
- LPI Early Career Development Award (2017)
- Global Opportunities Award, Western University Field Travel Award (2017)
- Pierazzo International Student Travel Award (2016)
- CSA Recognition for Contributions to 2015 CanMars MESR Rover Analog Mission (2015)
- NASA Special Recognition and Appreciation Award for outstanding MRO research (2011)
- John T. and Ada M. Diederich Educational Trust: $50,000 Scholarship (2000)

Selected Presentations and Interviews

- CBC News: The National interview (July 2019)
  https://www.youtube.com/watch?v=FQjsZlGYzxI&feature=youtu.be
- Science outreach talks and activities with London, Ontario public and catholic middle and high schools, London public libraries, and London Boys and Girls Club (2015 - 2018)
- Invited Research Forum lectures, Centre for Planetary Science and Exploration (CPSX), September 2015; November 2018
- Radio interview discussing Mars, impact cratering, and Mars rover analogue missions, March 2017
  https://gradcastradio.podbean.com/e/gradcast-102-discovering-life-on-utah-with-christy-caudill/
- CPSX Space Camp Lecturer and Activities Leader (2016)
- UA College of Science Invited Lecture Series (2011)
- HiRISE Science Team Meeting, 2010 presentation representing the Impact Cratering Science Theme

Space Fight Projects Experience

Visiting Student Research Scholar, Mars 2020 ROASTT Team

NASA JPL, California Institute of Technology, Pasadena, California

July – September 2018; January – March 2019

Assisted the Mars 2020 Science Office and Mission Systems and Operations Division in the Rover Operations Activities for Science Team Training (ROASTT) program in developing and implementing a series of field and mission operations training exercises. This program is designed to prepare the Mars 2020 Science Team for operations and the decision-making processes required to achieve the mission's objectives once the rover lands on Mars. I received hands-on training in Mars 2020 Mission System architecture and was involved in development of operational processes and procedures; this position followed from my experience in building analogue mission systems, designed to vet rover-based science operational procedures and practices (see *CanMoon Lunar Rover Analogue Deployment* and *CSA-CREATE CanMars Mars Sample Return Analogue Deployment (MSRAD)* listed below in "Analogue field trials").

CIPP team member, HiRISE Uplink Operations planning cycle

Western University, London, Ontario, Canada

June – July 2016

Member of the Western University CIPP ("Co-I of the Pay Period") team, performing HiRISE science image acquisition for one uplink operations cycle. This included six weeks of uplink planning, sequence execution, validation of science objectives, and assisting with daily captioned image releases. This team worked remotely with the HiRISE team and HiRISE Operation Center (HiROC) staff for uplink execution.

Lead geometry processing, HiRISE Downlink Operations Staff

HiROC, Lunar and Planetary Laboratory, University of Arizona
December 2010 - March 2012

Team lead for HiRISE processing and preparation of anaglyph products, including writing sequences for stereo pair acquisition and editing pipelines for processing. Lead of product evaluation for quality and distribution prior to release, which included: observation problems investigation and resolution; reading and providing reports when appropriate; and supervising an undergraduate evaluation team. Participated in imaging campaigns and caption writing for acquired images with the Impact Cratering Science Theme Team.

Research Assistant for HiRISE Science Team
Lunar and Planetary Laboratory, University of Arizona
May 2009 - December 2011

HiRISE image analysis and research under HiRISE PI and supervisor Alfred McEwen that included using ENVI and ISIS for preliminary data processing, and creating a large-scale, global database for study of Martian bedrock outcrops. New HiRISE images were requested and planned in support of this work. SOCET SET was used on stereo pair images to digitize geomorphic features for mathematical analysis (deriving strike and dip approximations on bedding) and in creating DTM products.

Space Fight Projects Experience – Analogue field trials

Technical Assurance Manager / Science-Planning Integrator / Field Validation Lead, CanMoon Lunar Rover Analogue Deployment
August 2019

During the development and implementation of the CanMoon training exercise, I acted in several capacities, including: (1) conceptual development of the mission system and development of end-to-end implementation strategies and constructs; (2) development of training modules for, and gave lectures to, the participants on operational constructs, strategies, instrumentation and data acquisition, and instrument-specific team-building and synergies, and (3) participant in several roles during the exercise, as an out-of-simulation consultant and as an active team member. As Science-Planning Integrator (SPI): Responsible for communications between Planning/Engineering (Rover Operators) and Science (Tactical) teams, to include: ensure activities are planned correctly and that science intent is properly conveyed; quickly inform of any changes to the plan; resolve conflicts and make adjustments to the plan as dictated by science intent, mission goals, and engineering constraints, and; remain flexible and foresee any communication needs between the teams, with knowledge of Planning/Engineering and Science operations and instrument capabilities, constraints, and limitations. As Field Validation Lead: Post-mission, on-site geological characterization in Lanzarote, Spain with sample collection for laboratory analyses and an ongoing comparison study of the in-simulation science versus the field and laboratory science results.

PanCam ISEM Instrument Field Trials, Green River, Utah
November 2017

The field trials represented a test of "geologic" filters and imaging modes with transmission/responses for the Infrared Spectrometer for ExoMars (ISEM) instrument emulator as an international collaboration with the ExoMars PanCam team from the University of St. Andrews, University College London, and Open University. I served as geological support, directing measurements of targets of interest having mineralogical and chemical variation. I also provided interpretations in the field as a first-order examination of the spectral data and geological correlation. I then collected samples for the team of selected targets and performed the follow-up, gold-standard laboratory analyses; mineralogy was determined through pXRD at The Laboratory for Stable Isotope Science (LSIS), Western University.

Science Team Lead, CSA-CREATE CanMars Mars Sample Return Analogue Deployment (MSRAD)
November 2016

Goals: Vet operational, procedural, and sample acquisition workflows of a MSR remote rover mission; Evaluate the efficacy and limitations of a Mars 2020-emulator instrument suite in identifying priority samples. As Science Team Lead (STL): Analogue mission system development, employing known and novel strategies in an operational test-bed environment; I was also lead in development of the daily operational timelines and activities, as I led the Science Team in Mission Control through the daily Campaign and Tactical processes in a high-fidelity science mission to explore Mars analogue terrain with the remotely-operated CSA MESR rover. I ensured collaborative, timely, and effective operations, meeting science objectives under a tight schedule of daily n+1 planning. Necessarily, this leadership required fast-

paced multi-tasking and consistent coordination with the Planning/Engineering team. In this high-fidelity mission scenario, we experienced the necessarily intense and difficult science discussions and planning with high-stakes decisions based on limited time and science. Outcomes: Documentation of a high-fidelity MSR analogue mission with operational lessons learned (Caudill et al., 2019a); post-mission on-site analysis with analogue site characterization (Caudill et al., 2019b). I led the follow-up geologic characterization, which included an on-site geological analysis at the Green River, Utah field site, sample collection for laboratory analyses, and a comparison study of the in-simulation science versus the field and laboratory science results.

XRF Instrument Team Lead, CSA-CREATE "CanMars" Mars Sample Return Analogue Deployment
November 2015

Other Work Experience

December 2016 - Present
Research Assistant, Centre for Planetary Science and Exploration

Editor of the Geological Association of Canada Planetary Sciences Division newsletter;
Manager of the Geological Association of Canada Planetary Sciences Division Twitter feed

March 2012 - August 2015
Geologist/Geoinformatics Systems Specialist
Geoinformatics Deputy Section Chief
Arizona Geological Survey

As a manager of multifaceted team to produce deliverables for national and international geoscience data projects, as well as an acting geological consultant and systems engineer to the projects, I facilitated daily coordination between national partners (namely, all US State Geologic Surveys), web/applications development staff, and contractors, to assist in developing programs, namely the National Geothermal Data System. Through this project, I gained data science experience (including use of open-source GIS, ArcGIS, Postgres/PostGIS, XML, and GitHub) and team management experience, as I was responsible for systems and knowledge transfer and the deliverables to project officers at the National Renewable Energy Laboratory and the US Department of Energy.

Publications

Allender, E. J., Cousins, C. R., Gunn, M. D., **Caudill C. M.** (2020) Multiscale and multispectral characterization of mineralogy with the ExoMars 2020 rover remote sensing payload, Earth and Space Science, doi: 10.1029/2019EA000692.

C.M. Caudill, Pontefract, A., Osinski, G. R., Tornabene, L. L., Xie, T., Mittelholz, A., Poitras, J., Simpson, S., Svensson, M., Grau, A. G., Godin, E., Pilles, E., Francis, R., Williford, K., Tuite, M., Battler, M., Hipkin, V., Haltigin, T., and the 2015 & 2016 Science Team members (2019a) CanMars mission Science Team operational results: Implications for operations and the sample selection process for Mars Sample Return (MSR), Planetary and Space Science, 172, 43-56.

C.M. Caudill, Osinski, G. R., Pilles, E. A., Sapers, H. M., Duff, S., Laugton, J., O'Callaghan, J., Sapoco, R., Tolometti, G., Tuite, G., Williford, K., Xie, T. (2019b) Field and laboratory validation of remote rover operations Science Team findings: The CanMars Mars Sample Return analogue mission, Planetary and Space Science, 165, 250-259.

D. W. Beaty, V. J. Hipkin, **C. M. Caudill**, R. F. Hanson, E. M. Hausrath, C. Maggiori, R. McCoubrey, J. C. Parrish, R. S. Ralston (2019) Geological Evaluation of the MSRAD Field Site by a Human Field Party: Implications for Rover-based Exploration Operations and for the Future Human Exploration of Mars, Planetary and Space Science, 171, 34-49.

E. A. Pilles, M. Cross, **C. M. Caudill**, R. Francis, G. R. Osinski, J. Newman, M. Battler, M. Bourassa, T. Haltigin, V. Hipkin, M. Kerrigan, S. McLennan, E. A. Silber, K. Williford (2019) Exploring new models for improving planetary rover operations efficiency through the 2016 CanMars Mars Sample Return (MSR) analogue deployment, Planetary and Space Science, 165, 250-259.

C.M. Caudill, G.R. Osinski, L.L. Tornabene (2018) Geological Mapping and Interpretation of Bakhuysen Csrater, Mars, Icarus 314, 175-194.

Tornabene, L. L., F.P. Seelos, A. Pommerol, N. Thomas, **C. M. Caudill**, P. Becerra, J.C. Bridges, S. Byrne, M. Cardinale, M. Chojnacki, S. J. Conway, G. Cremonese, C. M. Dundas, M. R. El-Maarry, J. Fernando, C. J.

Hansen, K. Hansen, T. N. Harrison, R. Henson, L. Marinangeli, A. S. McEwen, M. Pajola, S. S. Sutton, and J.J. Wray (2018) Image simulation and assessment of the colour and spatial capabilities of the Colour and Stereo Surface Imaging System (CaSSIS) on the ExoMars Trace Gas Orbiter, Space Sci. Rev., doi:10.1007/s11214-017-0436-7.

C.M. Caudill (2015) Geochemical databases for characterization of K-metasomatized Tertiary units in central-western Arizona. Arizona Geological Survey Digital Information DI-45 (http://repository.azgs.az.gov/uri_gin/azgs/dlio/1662).

C.M. Caudill, L.L. Tornabene, A.S. McEwen, S. Byrne, L. Ojha, S. Mattson (2012) Layered MegaBlocks in the central uplifts of impact craters, Icarus 221, 710-720.

Livio L. Tornabene, Gordon R. Osinski, Alfred S. McEwen, Joseph M. Boyce, Veronica J. Bray, **Christy M. Caudill**, John A. Grant, Christopher W. Hamilton, Sarah Mattson, Peter J. Mouginis-Mark (2012) Widespread crater-related pitted materials on Mars: Further evidence for the role of target volatiles during the impact process, Icarus 220, 348-368.

V. J. Bray, L. L. Tornabene, L. P. Keszthelyi, A. S. McEwen, B. R. Hawke, T. A. Giguere, S. A. Kattenhorn, W. B. Garry, B. Rizk, **C. M. Caudill**, L. R. Gaddis, C. H. van der Bogert (2010), New insight into lunar impact melt mobility from the LRO camera, *Geophys. Res. Lett.*, *37*.

Selected Abstracts

C.M. Caudill, G.R. Osinski, L.L. Tornabene, F.J. Longstaffe (2019) Clay mineralogy of the Ries degassing pipes: the complexities of clay mineral provenance. 50th Lunar and Planetary Science Conference Proceedings.

C.M. Caudill, G.R. Osinski, L.L. Tornabene, F.J. Longstaffe (2018) Degassing pipes at the Ries impact structure as an analogue for crater-related pitted material on terrestrial planets. 49th Lunar & Planetary Science Conference, 2765.

C.M. Caudill, R. N. Greenberger, H. M. Sapers, L. L. Tornabene, G. R. Osinski, B. L. Ehlmann. (2017) Mineralogical and Hyperspectral Mapping of the Ries Ejecta Deposits as a Martian Analogue for Impact Melt Modification. 48th Lunar & Planetary Science Conference, 2426. *(Talk)*

C.M. Caudill, G.R. Osinski, L.L. Tornabene, T. Haltigin, V. Hipkin, M. Battler, S. Duff, J. O'Callaghan, and the 2016 CanMars Team. (2017) CanMars 2016 MSR Analogue Mission Science Overview. 48th LPSC, 1969.

C.M. Caudill, et al. (2017) Relevance of pitted material and impact melt to early Martian hydrothermalism and habitability; Ries ejecta deposits as a Martian Analogue. Fourth Conference on Early Mars 2017, 3086. (*Talk*)

C.M. Caudill, et al. (2016) Impact Cratering Processes as Understood Through Martian and Terrestrial Analog Studies. 49th Annual American Geophysical Union (AGU) Meeting, 189287. (*Talk)*

C.M. Caudill, et al. (2016) Mineralogical and Geochemical Study of Ries Ejecta Deposits as a Martian Analogue for Impact Melt Modification. 79th Annual Meeting of The Meteoritical Society, 6481.

C.M. Caudill, et al. (2016) Geologic Mapping of Bakhuysen Crater, Mars: Analogies to the Ries Impact Ejecta with Insights into Martian Impact Melt. 79th Annual Meeting of The Meteoritical Society, 6474. (*Talk)*

C. M. Caudill, G. R. Osinski, L. L. Tornabene, A. S. McEwen (2016) Geologic Mapping of Bakhuysen Crater, Mars: Insights into Large Basin Impact Cratering Processes, 47nd Lunar & Planetary Science Conference, 2360.

C. M. Caudill, A. Grau Galofre, A. Pontefract, G. R. Osinski (2016) 2015 CanMars MSR Analog Mission: In Situ Geochemical Insights from X-Ray Fluorescence Spectrometry, 47nd Lunar & Planetary Science Conf., 1731.

Caudill, Christy, Richard, Stephen M., Musil, Leah, Sonnenschein, Adrian, and Good, Jessica (2014) National Geothermal Data System: Open Access to Geoscience Data and Digital Technologies. Geological Society of America Annual Meeting in Vancouver, British Columbia, Abstract 250046.

C. Caudill, L.L. Tornabene, A. McEwen, J. Wray (2011) Crater-Exposed Stratigraphy Blocks and Volcanogenic Origin, Mars, 42nd Lunar & Planetary Science Conference.

C. Caudill, L. Tornabene, and A. McEwen (2011) Crater-Exposed Intact Stratigraphy Blocks and Volcanogenic Origin, Planetary Cratering Consortium, held Sept. 14-16, 2011 in Flagstaff, AZ. Abstract #1006. (*Talk*)

L.L, Tornabene; **Caudill, C. M**.; McEwen, A. S.; Osinski, G.; Wray, J. J.; Mustard, J. F.; Skok, J. R.; Marzo, G.; Grant, J. A. (2010) High-resolution morphologic and spectral characteristics of Crater-exposed Bedrock on Mars: Insights into the petrogenesis, stratigraphy and geologic history of the Martian crust. American Geophysical Union, Fall Meeting 2010, abstract #P44B-07.

V.J. Bray, L.L. Tornabene, **C. Caudill**, B. Ray Hawke, T.A. Giguere, A.S. McEwen, L.R. Ostrach, M.S. Robinson. (2009) Impact Melt Deposit Morphology and Distribution on the Moon and Mars, 2009 American Geophysical Union, held Dec. 14, 2009 in San Fransisco, CA.